CORA Cork Open Research Archive
Cartlann Taighde Oscailte Chorcaí

Title	Statistical methods for mapping kinetics together with associated uncertainties in long field of view dynamic PET studies
Authors	Wu, Qi
Publication date	2024
Original Citation	Wu, Q. 2024. Statistical methods for mapping kinetics together with associated uncertainties in long field of view dynamic PET studies. PhD Thesis, University College Cork.
Type of publication	Doctoral thesis
Rights	© 2024, Qi Wu. - https://creativecommons.org/licenses/by-nc-nd/4.0/
Download date	2026-11-16 07:25:42
Item downloaded from	https://hdl.handle.net/10468/16923

UCC
University College Cork, Ireland
Coláiste na hOllscoile Corcaigh

Statistical Methods for Mapping Kinetics Together with Associated Uncertainties in Long Field of View Dynamic PET Studies

Qi Wu

Thesis submitted for the degree of
Doctor of Philosophy



NATIONAL UNIVERSITY OF IRELAND, CORK

SCHOOL OF MATHEMATICAL SCIENCES

July 2024

Head of School: Dr. Kevin Hayes

Supervisors: Prof. Finbarr O'Sullivan
Dr. Jian Huang

Contents

List of Figures iv
List of Tables x
Acknowledgements xiii
Abstract xiv

1 Thesis Introduction and Overview 1
1.1 Introduction 1
1.2 Main Contributions 2
1.3 Publications Related to This Thesis 3
1.4 Thesis Structure 4

2 Quantitation of dynamic total-body PET imaging: recent developments and future perspectives 6
2.1 Introduction 7
2.2 Total-Body PET Studies 9
2.3 Opportunities and Challenges in Dynamic Total-Body PET Imaging 14
2.4 Overview of Dynamic PET Quantitation 15
2.4.1 Basic Equation 15
2.4.2 Region of Interest Versus Voxel-level Analysis 18
2.5 Arterial Input Function 19
2.5.1 Blood Sampling 19
2.5.2 Image-Derived Input Function 21
2.5.3 Population-Based Input Function 22
2.5.4 Model-Based Input Function 22
2.6 Kinetic Model 26
2.6.1 Compartmental Model 26
2.6.1.1 1C Model 27
2.6.1.2 2C Model 27
2.6.1.3 Delay Effect 28
2.6.1.4 Model Selection 29
2.6.2 Patlak Plot 29
2.6.2.1 Selection of t* 30
2.6.2.2 Generalized Patlak 31
2.6.3 Spectral Analysis 32
2.6.4 Non-parametric Analysis 33
2.7 Other Approaches 34

3 A Generalized Linear Modeling Approach to Bootstrapping Multi-frame PET Image Data 36
3.1 Introduction 37
3.2 Methods: Basic Models and Analysis Techniques 39
3.2.1 Statistical Modeling of the Image-Domain Data . . . 39

3.2.2 Bootstrapping Techniques 42
3.2.2.1 Projection-Domain Bootstrap 43
3.2.2.2 Image-Domain Bootstrap: Model-based Approach 43
3.2.2.3 Approximate Image-Domain Bootstrap by Recycling 44
3.2.3 Specification of Unknowns in the Image-Domain Model 45
3.3 Applications to Parametric Imaging 49
3.3.1 Non-Parametric Residue Mapping (NPRM) of Kinetics 50
3.3.2 FDG Brain tumor Study 54
3.3.3 FLT Breast tumor Study 57
3.4 Assessment of Performance 62
3.4.1 1-D Experiments 70
3.4.2 Statistical Interpretation of Simulation Data 74
3.5 Discussion 76

4 Mapping ^{18}F-FDG Kinetics together with Patient-Specific Bootstrap Assessment of Uncertainties: An Illustration with data from a Long-Axial FOV PET/CT Scanner 79
4.1 Introduction 80
4.2 Materials and Methods 81
4.2.1 Patient Scans and Volumes of Interest (VOIs) 81
4.2.2 Parametric Imaging Techniques 82
4.2.2.1 Tissue Residue 82
4.2.2.2 Summary Kinetic Parameters 83
4.2.2.3 Compartmental Model Kinetic Analysis . . 84
4.2.2.4 Non-parametric Residue Mapping (NPRM) of Kinetics 86
4.2.2.5 Bootstrap Assessment of Uncertainty 87
4.2.2.6 Analysis of Fitting VOI Time-Course Data . 87
4.2.3 Statistical Analysis 88
4.2.3.1 Representation of VOI Time-Course Data . 88
4.2.3.2 VOI Kinetics 89
4.2.3.3 DGP Model 90
4.2.3.4 Log-Linear Modelling of VOI SEs 90
4.3 Results 92
4.3.1 Illustration 92
4.3.2 Representation of VOI Time-Course Data 93
4.3.3 VOI Kinetics 96
4.3.4 DGP Model 96
4.3.5 SEs of VOI Kinetics 98
4.4 Discussion 99

5 Shortened Dynamic Imaging Protocols for ^{18}F-FDG PET Scans 107
5.1 Introduction 108

5.2 Materials and Methods 114
5.2.1 Materials 114
5.2.1.1 FDG Brain tumor Study 114
5.2.1.2 FDG Breast tumor Study 115
5.2.2 Kinetic Analysis 116
5.2.3 Machine Learning Methods 116
5.2.4 Population Residue Basis 118
5.2.5 Exponential Extension of Non-parametric Residue . . 119
5.3 Results 121
5.4 Discussion 124

6 Discussion and Conclusions **127**
6.1 Discussion 127
6.2 Conclusions 131

A List of Publications and Presentations by the Author **A1**
A.1 Peer Reviewed Journals A1
A.2 Conference Publications A2
A.3 Conference Presentations A3

Bibliography **B1**

Nomenclature **C1**

List of Figures

2.1 Long axial field of view (LAFOV) PET/CT scanners. A: Biography Vision Quadra (Siemens); B: uEXPLORER (United imaging Healthcare); C: PennPET EXPLORER (University of Pennsylvania). 9
2.2 The number of publications (left y-axis) on the total-body (TB) PET studies (blue) and dynamic TB scanning with the implementation of kinetic analysis (red) for the period from 2019 to 2022. The percentage (right y-axis) of publications relevant to the kinetic model in TB PET is shown as the black line. The data were collected from a search on PubMed on 08/05/2023. 10
2.3 Overview of dynamic PET quantitation. Abbreviations: PET: positron emission tomography; IDIF: image-derived input function; PBIF: population-based input function; ROI: region of interest; FA: factor analysis; SVD: singular value decomposition; PCA: principal component analysis; MA: mixture analysis. 16
2.4 A diagram illustrating the dual blood supply to the liver. (Feng et al. 2020) 18
2.5 Flowchart of typical PBIF and IDIF strategies, along with the PBPM methodology in 2.5.4. (Xiu et al. 2022) 20
2.6 Voxel level quantitative parametric perfusion image with radiotracer delay. (left). ^{15}O-H_2O dynamic images with 5s duration in each time frame after tracer injection. (right series) (Knuuti et al. 2023) 21
2.7 Markov chain model for tracer atom dynamics within the body. Graph representation (left). Transition matrix (right). (Huang & O'Sullivan 2014) 23

3.1 Metabolic Images with image-domain bootstrap assessment of standard errors: Rows 1-3 show the Brain tumor FDG data; 4-6 for the Breast tumor FLT data. The mapped parameters are shown on rows 1&4 – the location of tumor volume of interest (VOI) on the slice is indicated with an arrow. Columns correspond to different metabolic parameters (labeled in yellow) with color bars indicating units - see section 3.3.1 for definitions. Computed standard errors (SE) are on rows 2&5. Rows 3&6 show histograms of the bootstrap sampling distributions of the 95'th percentile of the metabolic parameter in the normal [black] and tumor [red] VOIs. 58

3.2 Diagnostics associated with the Image-Domain Bootstrapping Model (3.2) using the FDG-Brain data. Six plots, labeled (i) to (vi), are shown for each dataset: (i) raw sub-TACs (dots) and fitted models (lines) for the selected basis set - columns of X. (ii) Non-parametric residues corresponding to the fitted model - c.f. (3.10). (iii) Boxplots by time-frame of standardized residuals from the unconstrained least squares fit, $r_{ij}/\hat{\sigma}_i\hat{\phi}_j\hat{h}_{ij}$. The simple, $\hat{\phi}_j^0$ in (3.5), and optimized, $\hat{\phi}_j$, standard deviations are shown as green and red dots. (iv) Boxplots of scaled residuals, $\hat{\epsilon}_{ij} = r_{ij}/\hat{\sigma}_i\hat{\phi}_j$, for each κ-bin (each containing roughly 10000 data points). $\hat{h}_l$-values are shown as red points; the red line is for comparison with unity (zero skewness of bin data). (v) Histogram of the overall distribution of the standardized residuals and its relation to a Gaussian fit (purple curve). Super-imposed are points showing quantiles of standardized residuals from different κ-bins (colored from red to dark blue according to bin order) versus corresponding quantiles of the Gaussian (right y-axis). The quantile pattern for the overall histogram and the Gaussian fit are shown with dashed black and purple lines. (vi) Directional auto-correlation patterns of the normalized residuals, $\hat{\eta}$, as a function of distance in millimeters. X-Y are transverse with Y perpendicular to the scanning bed; Z is the axial direction. 59

3.3 Diagnostics associated with the Image-Domain Bootstrapping Model (3.2) using the FLT-Breast data. Six plots, labeled (i) to (vi), are shown for each dataset: (i) raw sub-TACs (dots) and fitted models (lines) for the selected basis set - columns of X. (ii) Non-parametric residues corresponding to the fitted model - c.f. (3.10). (iii) Boxplots by time-frame of standardized residuals from the unconstrained least squares fit, $r_{ij}/\hat{\sigma}_i\hat{\phi}_j\hat{h}_{ij}$. The simple, $\hat{\phi}_j^0$ in (3.5), and optimized, $\hat{\phi}_j$, standard deviations are shown as green and red dots. (iv) Boxplots of scaled residuals, $\hat{\epsilon}_{ij} = r_{ij}/\hat{\sigma}_i\hat{\phi}_j$, for each κ-bin (each containing roughly 10000 data points). $\hat{h}_l$-values are shown as red points; the red line is for comparison with unity (zero skewness of bin data). (v) Histogram of the overall distribution of the standardized residuals and its relation to a Gaussian fit (purple curve). Super-imposed are points showing quantiles of standardized residuals from different κ-bins (colored from red to dark blue according to bin order) versus corresponding quantiles of the Gaussian (right y-axis). The quantile pattern for the overall histogram and the Gaussian fit are shown with dashed black and purple lines. (vi) Directional auto-correlation patterns of the normalized residuals, $\hat{\eta}$, as a function of distance in millimeters. X-Y are transverse with Y perpendicular to the scanning bed; Z is the axial direction. 60

3.4 Source distribution, $\lambda_{xt} = \sum_{k=1} \alpha_k(x)\mu_k(t)$, for the 2-D simulation experiments. Rows correspond to the FDG-Brain data (A) and FLT-Breast data (B). $\alpha_k(x)$ patterns and attenuation in (i), time-courses for each component, $\mu_k(t)$ (normalized), are in (ii). Flux parameters are in (iii). 64

3.5 Dynamic image-domain source leads to a corresponding projection domain array. Simulated counts are reconstructed and computed metabolic images. Each replicate of the simulation has both non-parametric (projection-domain) and model-based (image-domain) bootstrapping. 64

3.6 Voxel estimates of average standard deviations of flux. The true values are estimated by direct replication, these values are compared to image and projection domain bootstraps for a single replicate. 65

3.7 Schematic for 2-D investigation of Bootstrapping ROI averages. A total of 696 and 676 ROIs are defined for Brain and Breast, respectively. (A) Grids of rectangular ROIs and their size distributions. Estimates of average ROI standard deviations of flux are shown on rows B and C - colors correspond to different ROI sizes. 68

3.8 Scaled spatial patterns (α_j) for source distribution in 1-D experiments (dotted lines); projection domain patterns ($K_\beta \alpha_j$) are also shown (solid lines). Left - FDG studies; Right - FLT studies. Source sub-TACs (μ_j) are in Figure 3.4 A(ii) (FDG) and Figure 3.4 B(ii) (FLT). Colors of α_j's here match the colors of corresponding sub-TACs in Figure 3.8. The solid black line is the attenuation pattern. 71

4.1 Meier-Zierler tissue residue (R) and a decomposition into vascular (R_b), based on consideration of atoms with traveltimes less than 15 seconds in the tissue), in-distribution (R_d) and extracted (R_e) components. These are used to defineassociated metabolic parameters indicated. 83

4.2 MIP maps of NPRM kinetic parameters including associated SEs. SEs are based on the standard deviation of MIP results for each of 25 bootstrap replications. Top-row: CT images for a selected cross-sections through the volume and PET MIP maps at indicted times. 92

4.3 Results of four fitting procedures to the VOI time-course data in Figure 4.2. Data are points, line-colors correspond to methods used [top-left]. Full time course on the left; first minute on the right. 93

4.4 Elements of Bootstrap DGP - equation (4.7). (a) DGP scale, $\hat{\sigma}_e$, versus injected dose per unit tissue voxel, (b) Axially averaged scale, (c) The histogram is the overall residual distribution - pooling residuals regardless of $\hat{\kappa}$ values. The y-axis is in density units. The solid purple line is a standard Gaussian to this histogram. The linear quantile for the standard Gaussian is shown with the dashed purple line. Normal quantile functions (coloured lines) for used in the bootstrap DGP to map simulated Gaussian process variables, η^*_{ij} to the values ϵ^*_{ij} in equation (4.13). Different solid coloured lines (NIH colors from black to red) correspond to quantile transforms over different ranges for the COV measure $\hat{\kappa}$ - black for lowest $\hat{\kappa}$ and red for the largest $\hat{\kappa}$ range. The higher $\hat{\kappa}$ range have quantiles that are linear (Gaussian) on the left and quite flat on the right - this corresponds to a right-skewed error distribution pattern; lower $\hat{\kappa}$ values are more heavy-tailed than a standard Gaussian on the left and right. (d) Boxplot of directional (x-perpendicualar to scan table,z-axial) Spatial Correlation Patterns (ACF) across all studies. 97

4.5 ACF-based measure of Scanner FWHM Resolution. Note this measure takes account of patient specific factors - activity distribution, positioning and movements associated with breathing etc - which may impact the 3-D resolution of data. . . . 99

4.6 Prediction of VOI kinetic standard errors (SE - vertical axes) via a log-linear model prediction ($\hat{\text{SE}}$ - horizontal axes) - formula indicated. Correlations in black are for logarithmic SE values; red for the raw scale. 100
4.7 Contoured images of the reduced objective function in 2C-VOI analysis, $g(\phi_2, \phi_1|\Delta)$ in equation(4.5) with Δ fixed at the optimal value, over a fine grid of values for (ϕ_2, ϕ_1). Darker colors correspond to large values for the objective function. The minimum value of the objective function over the grid is the red point; the value determined by the Broyden-Fletcher-Goldfarb-Shanno algorithm is in blue. Two panels of results for 9 VOIs are shown. The left set is for the VOI data in Figure 4.3; the right set is for a time-course corresponding to a randomly selected voxel in each VOI. Note the colors in each image ranges from the minimum (bright yellow) to a maximum (dark red). In all cases the value of the objective function at the blue point is no bigger than its value at the red point, demonstrating the reliability of the algorithm. . . 101
4.8 Comparison of bootstrap generated voxel-level SEs based on 25 and 100 bootstrap samples - SE_{25} and SE_{100}. Points correspond to 5000 voxels randomly sampled from each VOI. The boxplot shows the relative deviations between SE_{25} and SE_{100}. The mean absolute deviation is on the order of 10% for all parameters. 102
4.9 Pairwise plots for each VOI type of the relation between ^{18}F-FDG flux values (MR_{FDG}) computed using the NP-voxel (vertical-axis) and 2C (horizontal) analysis. Correlation (indicated by: $r = **$) values and best fitting linear regression (solid line) are shown. 103
4.10 Voxel mapping of arrival of ^{18}F-FDG signal. Mapped values are the amplitude-weighted delay values, $\{\delta + \Delta_k, k = 1, 2, ..., K\}$ in equation 4.6. Data are centered so that the mean delay in the LV is zero. Left: Image of coronal scan corresponding to the CT slice in Figure 4.2. The boxplot on the right shows the distribution of mapped delay values by VOI. 105

5.1 Schematic representation of an overview of short-duration dynamic FDG PET scanning protocols. 111
5.2 Diagram of resampled PET-FDG scan data in brain tumour series. First 15 minutes(green), 0-30 minutes(navy) and clinical setting 60-75 minutes(purple). A similar resampling approach was used for the breast series. 115
5.3 Diagram of the use of NPRM to convert 4D dynamic PET data into a set of 3D metabolic images. 116

5.4 The diagram includes models such as regression trees, random forests, and neural networks. 118
5.5 Population residue basis $B_j(t)$ and a sample basis elements $\mu_j(t)$ in a brain tumor study. 120
5.6 Row 1: Attenuation and voxel-level mapping of K_i acquired from the full dynamic data. Rows 2 & 3: Predicted voxel-level metabolic parameter K_i using metabolic information generated from shorter dynamic scans, with acquisition times of 15 and 30 minutes respectively. A neural network and Generalized Additive Model (GAM) are used in the image generation of a breast tumor study. 121
5.7 The boxplot shows the distribution of Flux recovered from a full scan using NPRM, the application of population residue, and the use of population residue with a short acquisition time of 15 minutes. The colors refer to different regions: red for tumor, blue for the whole brain, grey for grey matter, and yellow for white matter. 122
5.8 The comparison of flux values at the regional level. Left column: direct comparison of flux recovered from different methods. Right column: prediction of Flux as described in Section 5.2.4, using GAM and LOOCV. The colors refer to different regions: red for the tumor, blue for the whole brain, grey for grey matter, and yellow for white matter. The correlations shown in black represent overall correlations, the others correspond to their respective colors. 122
5.9 The boxplot shows the distribution of Flow and Flux recovered from a full scan using NPRM, and the use of residue extension with short acquisition times of 15 and 30 minutes. The colors refer to different regions: red for tumors, blue for the whole brain, grey for grey matter, and yellow for white matter. 124
5.10 The comparison of flux values at the regional level. Left column: direct comparison of flux recovered from different methods. Right column: prediction of Flux as described in Section 5.2.5, using GAM and LOOCV. The colors refer to different regions: red for the tumor, blue for the whole brain, grey for grey matter, and yellow for white matter. The correlations shown in black represent overall correlations, the others correspond to their respective colors. 125

List of Tables

2.1 List of reported dynamic studies on total-body PET scanners (uEXPLORER, PennPET Explorer and Biograph Vision Quadra). The corresponding radiotracer, the number of patients (No.), data dimension (voxels, time-frames), subject type, site of scanning and temporal sequences in each cohort are presented. 11
2.2 Characteristics and Challenges/Opportunities of total-body PET scanners. 15
2.3 A summary of major kinetic models used in PET quantitation. 24

3.1 Reliability of Bootstrap Estimates of voxel Standard Deviations for mapped Kinetics in 2-D. Means and maxima of voxel kinetic estimates, averaged over replicates, are shown as $\bar{\mu}_\bullet$ and $\bar{\mu}_\vee$. Mean of voxel standard deviations, averaged over replicates ($\bar{\sigma}_\bullet$) its standard error ($\bar{SE}_\bullet$) and the overall RMSE values, see (3.20), are reported as a percentage of the maximum ($\bar{\mu}_\vee$). Estimates $(\hat{a}, \hat{b}, \hat{c})$ correspond to (3.19). 63
3.2 Reliability of Bootstrap Estimates of Standard Deviations for ROI means of mapped Kinetics. Note approximately 700 ROIs are considered in each case, see Fig 3.7. Means and maxima of ROI-averaged kinetic parameters, averaged over replicates, are shown as $\bar{\mu}_\bullet$ and $\bar{\mu}_\vee$. Mean ROI standard deviation, averaged over replicates ($\bar{\sigma}_\bullet$), its standard error ($\bar{SE}_\bullet$) and the overall RMSE values, computed by ROI version of (3.20), are reported as a percentage of the maximum ($\bar{\mu}_\vee$). Estimates $(\hat{a}, \hat{b}, \hat{c})$ are based on the ROI version of (3.19). . 69
3.3 Reliability of Bootstrap Estimates of voxel Standard Deviations for mapping Kinetics in 1-D based on FBP and ML reconstructed data. Means and maxima of voxel kinetic estimates, averaged over replicates, are shown as $\bar{\mu}_\bullet$ and $\bar{\mu}_\vee$. Mean of voxel standard deviations, averaged over replicates ($\bar{\sigma}_\bullet$), its standard error ($\bar{SE}_\bullet$) and the overall RMSE values, see (3.20), are reported as a percentage of the maximum ($\bar{\mu}_\vee$). Estimates $(\hat{a}, \hat{b}, \hat{c})$ correspond to (3.19). 72
3.4 Analysis of Voxel-level Error Characteristics across all Simulations. The coefficients are for the models in (3.22) and (3.23). The R^2-values only reported for (3.23). Corresponding values for (3.22), are uniformly high (in excess of 90%) 75

4.1 VOI time-course fitting across all 24 studies. Mean and standard deviations of the WRSS deviations between the VOI time-course and the VOI average of voxel-wise (Voxel-NP) and direct NP (VOI-NP) and 2C (VOI-2C) fits of the VOI time-course are shown. Last two columns summarize mean and standard deviation of percent deviations between WRSS values of Voxel-NP and VOI-NP fits, and between Voxel-NP and VOI-2C values. 94

4.2 VOI Kinetics (mean$\pm$ standard deviation) recovered using different methodologies. VOI averaged voxel kinetics are in the top panel; kinetics obtained by analysis of the VOI time-course using the NP model and 2C model are shown in the middle (VOI-NP) and bottom (VOI-2C) panel. Significance of deviations from Voxel-NP values, evaluated by the paired Wilcoxon test, are indicated by $*, **$ and $***$ for p-values less than 0.05, 0.01 and 0.001, respectively. 95

4.3 Comparison with Literature Values for MR_{FDG}, DV and Blood Flow in Different Tissues. c.f. equation (4.4). 106

5.1 RMSE for Flux estimates across different regions and methods compare to true. 125

I, Qi Wu, certify that this thesis is my own work and has not been submitted for another degree at University College Cork or elsewhere. All joint contributions, external references and sources are clearly acknowledged and identified within the contents. I have read and understood the regulations of University College Cork concerning plagiarism and intellectual property.



Qi Wu

Acknowledgements

I would like to take this opportunity to express my sincerest gratitude to everyone who has helped me throughout my journey in completing this PhD thesis.

First and foremost, I would like to express my sincere gratitude to my supervisors Prof. Finbarr O'Sullivan and Dr. Jian Huang, for providing me with opportunities to work on this fascinating project and dedicating their time on me during my PhD journey.

I would like to thank Finbarr for his patience, enthusiasm, horizon, and constructive feedback have been instrumental in the success of my research. I deeply appreciate the opportunity he gave me to collaborate with him and his constant support throughout. Likewise, I cannot express my gratitude enough to Jian, for his continued faith and support over the years. His guidance, advice, and support will be invaluable for my future endeavors.

I am also grateful to the members of my thesis committee. Especially the internal examiner, Dr. Supratik Roy and external examiner, Prof. Winfried Brenner at Charité - Universitätsmedizin Berlin for their insightful comments.

Furthermore, I would like to extend my thanks to our international collaborators in the USA, Switzerland and China. I am grateful to Prof. David A. Mankoff at the University of Pennsylvania and Dr. Mark Muzi at the University of Washington for the clinical datasets and insightful inputs. I also appreciate Prof. Kuangyu Shi and Prof. Axel Rominger at Bern University Hospital for generously sharing their highly valuable datasets on the latest long-axial field of view PET scanner - Siemens Biograph Vision Quadra. Additionally, I thank Prof. Yun Zhou for providing me with the opportunity to intern at United Imaging Healthcare and guiding me in the uEXPLORER Total-Body PET studies.

I am thankful for everyone in Lab 2.11 for contributing an enjoyable environment and priceless PhD experience. Special thanks go to Dr. Zhaoyan Xiu for introducing me to the PET world even before my PhD studies began. Dr. Fengyun Gu, an invaluable colleague and even like my third mentor, who spent significant time with me on various aspects of the work.

In addition, I would like to acknowledge my family, who have been my pillars of strength and support. Their unwavering love and understanding have continually motivated me. Their support has been invaluable in helping me to overcome the challenges and to persevere until the end.

Finally, I acknowledge the financial support from School of Mathematical Sciences, Science Foundation Ireland and National Cancer Institute USA.

Abstract

Positron Emission Tomography (PET) is an essential diagnostic imaging technique in clinical care settings, as well as in medical research. It plays a crucial role in diagnosis, prognosis, treatment planning, and clinical decision-making. PET imaging, a well-established radio-tracer imaging technique, involves injecting a radio-tracer to analyze in-vivo metabolic processes. Dynamic PET scanning provides multiple time frames, offering more detailed metabolic information. However, traditional methods like Patlak and compartmental modeling are commonly used in data obtained from conventional scanners. The use of constant or exponential residue functions may be limited in complex environments, such as diverse tissues or multiple organs. This thesis aims to develop statistical approaches for enhancing and assessing parametric imaging from dynamic PET scans. The Non-Parametric Residue Mapping (NPRM) procedure is established as an entirely automatic process that integrates data-driven segmentation, non-parametric residue analysis, and voxel-level kinetic mapping. A model-based image-domain bootstrapping method is developed with the objective to generate reliable uncertainty estimates, which are crucial for accurate data interpretation and subsequent treatment decisions. This method uses an empirical distribution of re-scaled data and a non-parametric approach for analysis of the spatial correlation structure. Numerical simulations using both direct Filtered Backprojection (FBP) and iterative Maximum Likelihood (ML) reconstructions are considered. Illustrative examples on conventional scanners and Long Axial Field-of-View (LAFOV) PET scanners are conducted. A short-duration dynamic scanning protocol is proposed to enhance the quantitation of a shortened dataset specifically. This protocol utilizes NPRM and machine learning techniques to aim at making short dynamic acquisition protocols clinically feasible.

Chapter 1

Thesis Introduction and Overview

1.1 Introduction

Medical imaging, a revolutionary technology widely used in diagnostics today, encompasses numerous modalities such as X-ray, computed tomography (CT), positron emission tomography (PET), magnetic resonance imaging (MRI), Single Photon Emission Computed Tomography (SPECT), and ultrasound. These advanced technologies allow us to gain a comprehensive understanding of the anatomical structure and physiological function of the human body in vivo. Among these, molecular imaging, primarily encompassing PET and SPECT, is a unique branch of medical imaging that emphasizes visualizing molecular and cellular processes within the body using specific imaging agents. As these techniques do not include anatomical structure imaging, they are typically combined with CT and MRI for registration and anatomical localization (Ganguly et al. 2010). In terms of comparison, PET is considered superior to SPECT due to its finer resolution and the shorter half-life of its radiotracer (Rahmim & Zaidi 2008). In recent years, PET has found extensive clinical and research applications in diverse fields such as oncology, cardiology, and neurology (Hoh 2007, Khalil 2017). It provides valuable quantitative measurements of a diverse range of functional and biological processes, such as tumor metabolism (Weber et al. 2000), proliferation (Peck et al. 2015), blood flow (Kaufmann et al. 1999), and receptor-binding (Gunn et al. 1997), depending on the administered radiotracer. Given the nuanced insights offered by these measurements, PET

imaging contributes significantly to the advancement of precision medicine, a burgeoning field that customizes medical treatment to individual patient characteristics. The potential benefits of PET imaging to precision medicine are profound, potentially revolutionizing our approach to disease diagnosis and treatment (Lammertsma 2017, Mankoff et al. 2019, Zaidi & Karakatsanis 2017). In daily clinical practice, PET imaging is obtained at a single time point and assessed visually or using simple indices, e.g., standardized uptake value (SUV) (Thie 2004). Although these are sufficient for many diagnostic applications, dynamic scans with multiple time frames are implemented in some research avenues for advanced diagnosis, response assessment, therapy management, and tracer development (Tomasi et al. 2012, Wijngaarden et al. 2023).

This thesis primarily focuses on FDG PET dynamic imaging. We apply numerous methods, such as Non-parametric Residue Mapping (NPRM) and image domain bootstrap, to generate accurate kinetic information. We also use machine learning to reduce dynamic scanning time. Our objective is to explore the potential of PET imaging and advance analysis approaches to provide more accurate clinical diagnoses and therapy management.

1.2 Main Contributions

The main contributions of this thesis are as follows:

- An overview of the current status, opportunities and challenges of total body PET imaging.
- An overview of quantification of dynamic PET imaging, including a basic equation to model the measured tissue time activity curve, the arterial input function estimation and kinetic modeling of dynamic PET data.
- Non-parametric Residue Mapping (NPRM) Technique
  - A non-parametric residue mapping procedure is proposed to generate parametric imaging.
  - The applicability of NPRM technique to dynamic PET scanning on the LAFOV PET scanners is assessed.

- Image-Domain Bootstrap Technique
  - A novel image-domain bootstrap model without the reconstruction requirement is developed. This provides a practical mechanism to simulate 4D dynamic PET data efficiently.
  - The utilization of this procedure for evaluating uncertainties of kinetic mapping and regional summaries has been demonstrated.
  - Applicability of this approach to LAFOV PET datasets is assessed.
- Exploration of shortened dynamic protocols using machine learning techniques.
- Several peer-reviewed journals and conference proceedings have been published and the ones relevant to this thesis are in section 1.3. The full publications and conference presentations are listed in Appendix A.

1.3 Publications Related to This Thesis

Related to Chapter 2

1. F Gu, Q Wu. "Quantitation of dynamic total-body PET imaging: recent developments and future perspectives". *European Journal of Nuclear Medicine and Molecular Imaging*, 50:3538-3557, 2023.

Related to Chapter 3

2. F O' Sullivan, F Gu, Q Wu and L D O'Suilleabhain. "A Generalized Linear modeling approach to bootstrapping multi-frame PET image data". *Medical Image Analysis*, 72:102-132, 2021.
3. F Gu, Q Wu, F O' Sullivan, J Huang, M Muzi and D A Mankoff. "An illustration of the use of model-based bootstrapping for evaluation of uncertainty in kinetic information derived from dynamic PET". *IEEE NSS& MIC Records 2019*.

Related to Chapter 4

4. Q Wu, F Gu, L O'Suilleabhain, H Sari, S Xue, K Shi, A Rominger, F O'Sullivan. "Mapping FDG Kinetics together with Patient-Specific Bootstrap Assessment of Uncertainties: An Illustration with data from

a Long-Axial FOV PET/CT Scanner". *Journal of Nuclear Medicine*, 65:971-979, 2024.

5. F O' Sullivan, Q Wu, F Gu, K Shi, L O'Suilleabhain, S Xue and A Rominger. "Mapping FDG Tracer Kinetics and their Uncertainties via the Bootstrap using data from a Long-Axial FOV PET/CT Scanner". *Journal of Nuclear Medicine*, 63(3220), 2022.

Related to Chapter 5

6. Q Wu, F O' Sullivan, M Muzi and D A Mankoff. "An exploration of the prognostic utility of shortened dynamic imaging protocols for PET-FDG scans". *IEEE Nuclear Science Symposium and Medical Imaging (NSS& MIC) Records 2019*.

7. Z Huang, Y Wu, F Fu, N Meng, F Gu, Q Wu, Y Zhou, Y Yang, X Liu, H Zheng, D Liang, M Wang and Z Hu, "Parametric image generation with the uEXPLORER total-body PET/CT system through deep learning". *European Journal of Nuclear Medicine and Molecular Imaging*, 49:2482-2492, 2022.

1.4 Thesis Structure

This thesis is structured as follows:

Chapter 2 provides an overview of the recently developed Long Axial Field of View (LAFOV) scanners, which have emerged as a significant development in the field of medical imaging. This chapter introduces the PET quantitation process and traditional kinetic analysis techniques. The current state of development, potential opportunities, and challenges associated with these innovative LAFOV scanners are discussed. The protocols for reconstructed data, tracers, and quantitation approaches used are summarized.

Chapter 3 introduces the Non-Parametric Residue Mapping (NPRM) technique and the development of a statistical linear model analysis for creating valid bootstrap samples from multi-frame PET image data, particularly in dynamic PET studies with Fluorodeoxyglucose (FDG) and Fluorothymidine (FLT) in brain and breast cancer patients. The quantitative perfor-

mance is assessed by 1-D and 2-D simulation. The accuracy of projection-domain bootstraps and the novel image-domain bootstraps has been evaluated. The uncertainty in kinetic information or complex regional summary is explored.

Chapter 4 examines the NPRM technique and assesses uncertainties using image-domain bootstraps with data obtained from the LAFOV scanner - Biograph Vision Quadra. Comparisons between NPRM and standard 2C modeling corresponding to several key organs and tumor lesions are carefully examined. Kinetics and bootstrap-derived uncertainties are reported for voxel, VOI, and maximum intensity projection maps. NPRM generated kinetic maps were of good quality, well-aligned with the vascular and metabolic patterns. A sample tracer arrival map is also shown.

Chapter 5 outlines various methods to reduce acquisition time in static or dynamic studies, aiming to enhance efficiency without compromising result quality. This chapter specifically focuses on a proposed abbreviated protocol designed to obtain full kinetics. This is accomplished using NPRM and a machine learning scheme, which enables the generation of more precise Ki values. The effectiveness of this protocol has been examined , demonstrating its potential to enhance efficiency and accuracy in clinical studies.

Chapter 6 provides a comprehensive summary of this work, highlighting key findings and major contributions, as well as discussing the potential future developments.

Chapter 2

Quantitation of dynamic total-body PET imaging: recent developments and future perspectives

Abstract

Positron emission tomography (PET) scanning is an important diagnostic imaging technique used in disease diagnosis, therapy planning, treatment monitoring and medical research. The standardized uptake value (SUV) obtained at a single time frame has been widely employed in clinical practice. Well beyond this simple static measure, more detailed metabolic information can be recovered from dynamic PET scans, followed by the recovery of arterial input function and application of appropriate tracer kinetic models. Many efforts have been devoted to the development of quantitative techniques over the last couple of decades. The advent of new-generation total-body PET scanners characterized by ultra-high sensitivity and long axial field of view, i.e., uEXPLORER (United Imaging Healthcare), PennPET Explorer (University of Pennsylvania) and Biograph Vision Quadra (Siemens Healthineers), further stimulate valuable inspiration to derive kinetics for multiple organs simultaneously. But some emerging issues also need to be addressed, e.g., the large-scale data size and organ-specific phys-

iology. The direct implementation of classical methods for total-body PET imaging without proper validation may lead to less accurate results. The published dynamic total-body PET datasets are outlined and several challenges/opportunities for quantitation of such types of studies are presented. An overview of the basic equation, calculation of input function (based on blood sampling, image, population or mathematical model) and kinetic analysis encompassing parametric (compartmental model, graphical plot and spectral analysis) and non-parametric (B-spline and piece-wise basis elements) approaches is provided.

2.1 Introduction

In recent years, positron emission tomography (PET) has a wide range of clinical and research applications in oncology, cardiology and neurology (Hoh 2007, Khalil 2017). It is a unique imaging modality that enables the measurements of a diverse range of functional and biological processes (e.g., tumor metabolism (Weber et al. 2000), proliferation (Peck et al. 2015), blood flow (Kaufmann et al. 1999) and receptor-binding (Gunn et al. 1997)), depending on the administrated radiotracer. In daily clinical practice, PET imaging is obtained at a single time point and assessed visually or using simple indices, e.g., standardized uptake value (SUV) (Thie 2004). Although these are sufficient for many diagnostic applications, dynamic scans with multiple time frames are implemented in some research avenues for advanced diagnosis, response assessment, therapy management and drug/tracer development (Tomasi et al. 2012, Wijngaarden et al. 2023).

Since the 1950s, there have been great advances with PET including the introduction of time-of-flight technologies (Vandenberghe et al. 2016), optimized detectors (Lecomte 2009, Zaidi & Alavi 2007), new radiotracers (Lau et al. 2020), iterative reconstruction algorithms (Vardi et al. 1985, Leahy & Qi 2000) and novel quantitative methods (Muzi et al. 2012, Wang et al. 2020) by a variety of scientists in physics, engineering, chemistry, mathematics and statistics (Nutt 2002, Wacholtz 2011, Jones & Townsend 2017). However, some constraints such as the limited axial coverage still exist (Katal et al. 2022). Currently, the conventional PET/CT systems have a short axial field of view (AFOV) of about $15 \sim 30$ cm and typically only a

specific organ such as the brain is imaged. On these scanners, whole-body (even dynamic) scanning can be performed by a multi-bed scenario, but pitfalls like the missing early-phase data and low temporal resolution limit its wide use (Rahmim et al. 2019).

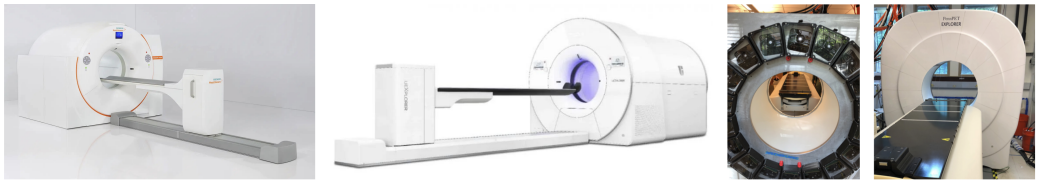
The revolutionary total-body (TB) PET scanners (e.g., uEXPLORER (Badawi et al. 2019*a*), PennPET Explorer (Pantel et al. 2020) and Siemens Biograph Vision Quadra (Alberts et al. 2021)) have been developed to overcome these limitations. Such devices enable the simultaneous image of the entire human body or main organs using a single-bed position. Given their ultra-high sensitivity (10∼40 fold), extended field of view (1∼2m) and enhanced temporal resolution (20∼200 time frames), the potential clinical applications of these innovative technologies have been exploited in different ways to provide better image quality (Spencer et al. 2021, Surti et al. 2020, Alberts et al. 2021, Prenosil et al. 2022), reduce scan time (Liu et al. 2021*c*, Hu et al. 2021, Chen et al. 2022*b*, Wu et al. 2022*c*, Viswanath et al. 2022, Sari et al. 2022*a*), lower the injected dose (Liu et al. 2021*a*, Tan et al. 2022, Zhao et al. 2021, Sachpekidis et al. 2022) and develop new drugs, see (Tan et al. 2020, Slart et al. 2021, Alavi et al. 2022, Katal et al. 2022, Nadig et al. 2021, Viswanath et al. 2021, Filippi et al. 2022) for more descriptions. Next to all the exciting opportunities that arise with TB systems, there remain some challenges. The analysis of large-scale data, especially for dynamic scanning, becomes one of them.

Quantitation of dynamic PET studies could be able to provide additional biological information and the potential benefits have been highlighted in precision medicine (Lammertsma 2017, Mankoff et al. 2019, Zaidi & Karakatsanis 2017). A broad family of quantitative techniques with focus on the recovery of arterial input function and the establishment of tracer kinetic model has been proposed to estimate the kinetic parameters of interest. The other procedures including motion correction and denoising also have some impacts on the estimated kinetics. Many different points of view have been taken in extensive literature and more comprehensive references (Gunn et al. 2001, Tomasi et al. 2012, Muzi et al. 2012, Bertoldo et al. 2014, Veronese et al. 2016, Wang et al. 2020, Dimitrakopoulou-Strauss et al. 2021, Pantel et al. 2022*b*) are suggested for further readings. The aim of this chapter is to provide an overview of the basic principles and model

formulations of the most important strategies for PET quantitation, along with their feasibilities and recent developments for the emerging total-body PET imaging. The future perspectives to further enhance quantitative accuracy are discussed as well.

2.2 Total-Body PET Studies

Since the first total-body human imaging was obtained on the uEXPLORER scanner in Zhongshan hospital (Badawi et al. 2019*a*), the spread of uEXPLORER with other long axial field of view ($>$ 1m) systems has become worldwide. Up to 2022, more than 10 total-body PET/CT scanners, including uEXPLORER, PennPET Explorer and Biograph Vision Quadra, have been installed in China (Lan et al. 2022), the United States (Pantel et al. 2020, Wang et al. 2021*a*) and Europe (Alberts et al. 2021, van Sluis et al. 2022, Sachpekidis et al. 2022).



A: Biograph Vision Quadra B: uEXPLORER C: PennPET EXPLORER

Figure 2.1: Long axial field of view (LAFOV) PET/CT scanners. A: Biography Vision Quadra (Siemens)[1]; B: uEXPLORER (United imaging Healthcare)[2]; C: PennPET EXPLORER (University of Pennsylvania)[3].

The use of such scanners in both clinical (static mode) and research (dynamic mode) settings is emerging. Fig. 2.2 shows the trend for the work in the area of total-body PET from 2019 to 2022. The proportion of dynamic studies with the implementation of kinetic analysis in total-body PET also steadily increases each year.

A list of reported dynamic total-body PET study cohorts along with the specific details is provided in Table 2.1. Several types of subjects were re-

[1] https://www.siemens-healthineers.com/molecular-imaging/pet-ct/biograph-vision-quadra
[2] https://usa.united-imaging.com/products/molecular-imaging/uexplorer/
[3] https://www.med.upenn.edu/pennpetexplorer/

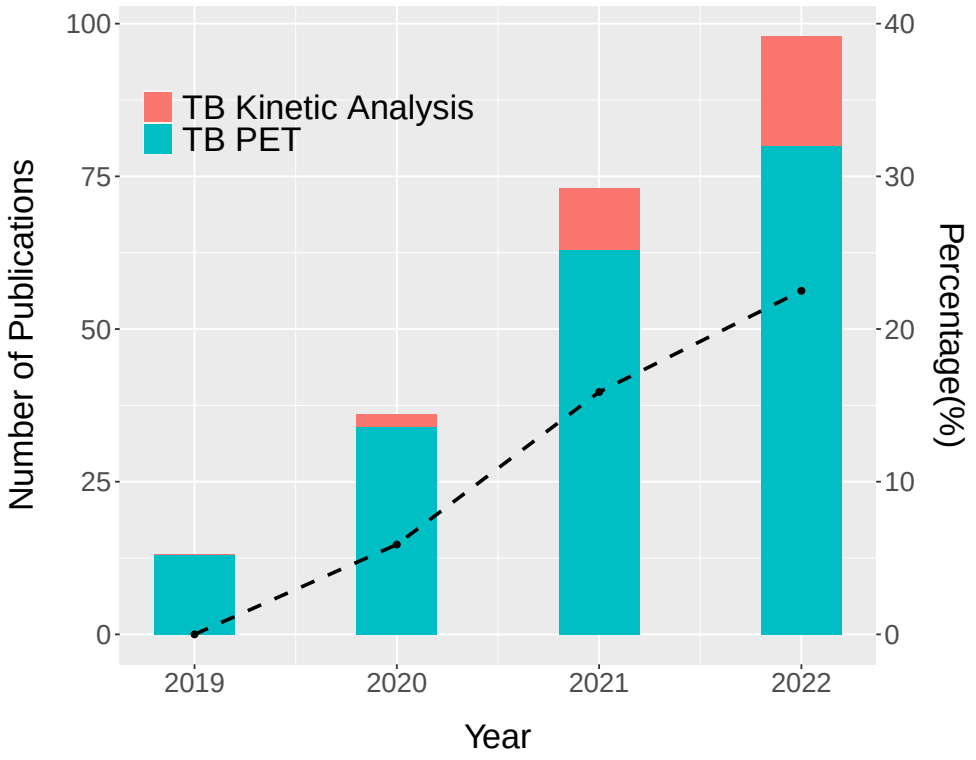


Figure 2.2: The number of publications (left y-axis) on the total-body (TB) PET studies (blue) and dynamic TB scanning with the implementation of kinetic analysis (red) for the period from 2019 to 2022. The percentage (right y-axis) of publications relevant to the kinetic model in TB PET is shown as the black line. The data were collected from a search on PubMed on 08/05/2023.

cruited: healthy volunteers and patients diagnosed with cancer or infected with COVID-19. While the most of scans were done exclusively with the administration of fluorine-18 labeled fluorodeoxyglucose (^{18}F-FDG), there are other radiotracers of interest to be employed, such as ^{68}Ga-FAPI-04 (Chen et al. 2022*a*, 2023*a*, Liu et al. 2023*a*), ^{15}O-H_2O (Andersen et al. 2022), ^{89}Zr-Df-Crefmirlimab (Omidvari et al. 2023, 2022), ^{18}F-Fluciclovine (Abdelhafez et al. 2022) and [^{11}C]methionine (Li et al. 2023). A range of scanning and reconstruction protocols have been applied by different hospitals/institutions, but the magnitude of image voxels is generally on the order of ten million and a more dense sequence is commonly performed at the early time. Although these dynamic datasets may not be consistent, the data analysis should face similar problems that will be discussed carefully in the next section.

Table 2.1: List of reported dynamic studies on total-body PET scanners (uEXPLORER, PennPET Explorer and Biograph Vision Quadra). The corresponding radiotracer, the number of patients (No.), data dimension (voxels, time-frames), subject type, site of scanning and temporal sequences in each cohort are presented.

PET Scanner	Radiotracer	No.	(Voxels, Time frames)	Subject Type	Site	Temporal Sequences	Ref.
uEXPLORER	^{18}F-FDG	1	$(236 \times 236 \times 679, 187)$	Healthy	[a]	$60 \times 1s, 30 \times 2s, 20 \times 3s, 12 \times 10s, 50 \times 30s, 15 \times 120s$	(Zhang et al. 2020*b*)
	^{18}F-FDG	11	$(236 \times 236 \times 679, 97)$	Healthy	[a]	$24 \times 5s, 73 \times 60s$	(Liu et al. 2021*c*)
	^{18}F-FDG	30	$(236 \times 236 \times 679, 60)$	Healthy	[a]	$36 \times 5s, 24 \times 180s$	(Tan et al. 2023, Liu et al. 2021*a*,*b*)
	^{18}F-FDG	35	$(236 \times 236 \times 679, 55)$	Cancer	[a]	$36 \times 5s, 19 \times 180s$	(Lv et al. 2022)
	[^{68}Ga]Ga-DOTA-FAPI-04	19	$(192 \times 192 \times$ NA, NA)	Malignancy	[a]		(Liu et al. 2023*a*)
	[^{68}Ga]Ga-DOTA-TATE	7	$(192 \times 192 \times$ NA, 55)	Cancer	[a]	$36 \times 5s, 19 \times 180s$	(Yin et al. 2023)
	^{18}F-FDG	7	$(192 \times 192 \times 672, 70)$	Cancer	[b]	$30 \times 5s, 15 \times 30s, 25 \times 120s$	(Wu et al. 2022*d*)
	^{18}F-FDG	28	$(192 \times 192 \times 672, 66)$	Healthy/Cancer	[b]	$24 \times 5s, 6 \times 10s, 6 \times 30s, 6 \times 60s, 24 \times 120s$	(Wang et al. 2022*e*)
	^{18}F-FDG	15	$(192 \times 192 \times 673, 25)$	Cancer	[b]	$1 \times 30s, 3 \times 10s, 4 \times 30s, 5 \times 60s, 4 \times 180s, 8 \times 300s$	(Chen et al. 2022*b*)
	^{18}F-FDG	200	$(192 \times 192 \times 673, 98)$	Healthy/Cancer	[b]	$50 \times 2s, 20 \times 10s, 10 \times 30s, 10 \times 60s, 8 \times 300s$	(Huang et al. 2022)
	^{18}F-FDG	13	$(150 \times 150 \times 486, 120)$	Healthy	[c]	$60 \times 1s, 30 \times 2s, 6 \times 10s, 6 \times 30s, 12 \times 120s, 6 \times 300s$	(Wang et al. 2023*b*)

Table 2.1 continued from previous page

	^{18}F-FDG	21	$(150 \times 150 \times 486, 66)$	Healthy/Cancer	[c]	$30 \times 2s, 12 \times 10s, 6 \times 30s, 12 \times 120s, 6 \times 300s$	(Li et al. 2022*a*)
	^{18}F-FDG	10	$(150 \times 150 \times 486, 29)$	Healthy/Cancer	[d]	$6 \times 10s, 2 \times 30s, 6 \times 60s, 5 \times 120s, 4 \times 180s, 6 \times 300s$	(Wang et al. 2021*a*)
	^{18}F-FDG	7	(NA, 120)	COVID-19	[d]	$60 \times 1s, 30 \times 2s, 6 \times 10s, 6 \times 30s, 12 \times 120s, 6 \times 300s$	(Wang et al. 2022*d*)
	^{11}C-Butanol	3		Healthy/Peripheral artery disease	[d]	$12 \times 5s, 6 \times 10s, 6 \times 30s, 5 \times 300s$	(Li et al. 2022*b*)
	^{89}Zr-Df-Crefmirlimab	8	$(512 \times 512 \times$ NA, 46)	Healthy/COVID-19	[d]	$6 \times 60s, 16 \times 30s, 2 \times 60s, 12 \times 120s, 10 \times 300s$	(Omidvari et al. 2023, 2022)
	^{18}F-Fluciclovine	37	$(256 \times 256 \times$ NA, NA)	Cancer	[d]		(Abdelhafez et al. 2022)
	^{18}F-FDG	30	$(360 \times 360 \times 672, 92)$	Cancer	[e]	$30 \times 2s, 12 \times 5s, 6 \times 10s, 4 \times 30s, 25 \times 60s, 15 \times 120s$	(Wang et al. 2022*a*)
	^{68}Ga-FAPI-04	9	$(239 \times 239 \times 679, 92)$	Cancer	[f]	$30 \times 2s, 12 \times 5s, 6 \times 10s, 4 \times 30s, 25 \times 60s, 16 \times 120s$	(Chen et al. 2022*a*)
	^{68}Ga-FAPI-04	13	$(360 \times 360 \times$NA, 92)	Cancer	[f]	$30 \times 2s, 12 \times 5s, 6 \times 10s, 4 \times 30s, 25 \times 60s, 15 \times 120s$	(Chen et al. 2023*a*)
	[^{11}C]methionine	12	(NA, 67)	Multiple myeloma	[f]	$30 \times 2s, 12 \times 5s, 6 \times 10s, 4 \times 30s, 15 \times 60s$	(Li et al. 2023)
PennPET Explorer	^{18}F-FDG	4		Healthy/Cancer	[g]		(Pantel et al. 2020, Viswanath et al. 2020)

Table 2.1 continued from previous page

Biograph Vision Quadra	^{18}F-FDG	12	$(220 \times 220 \times 708, 31)$	Cancer		[h]	$6 \times 10s, 3 \times 20s, 6 \times 30s, 5 \times 60s, 11 \times 300s$	(van Sluis et al. 2022)
	^{18}F-FDG	24	$(440 \times 440 \times 645, 62)$	Cancer		[i]	$2 \times 10s, 30 \times 2s, 4 \times 10s, 8 \times 30s, 4 \times 60s, 5 \times 120s, 9 \times 300s$	(Sari et al. 2022*b*, Alberts et al. 2021, Sari et al. 2022*a*)
	[^{82}Rb]C1	1		Atypical chest pain		[i]		(Caobelli et al. 2023)
	^{15}O-H_2O	5	$(440 \times 440 \times 645, 54)$	Cancer		[j]	$1 \times 5s, 30 \times 1s, 15 \times 2s, 5 \times 10s, 3 \times 20s$	(Andersen et al. 2022)

[*a*] Zhongshan Hospital, Fudan University, Shanghai, China

[*b*] Henan Provincial People's Hospital People's Hospital of Zhengzhou University, Henan, China

[*c*] University of California Davis, California, USA

[*d*] University of California Davis EXPLORER Molecular Imaging Center, California, USA

[*e*] Sun Yat-Sen University Cancer Center, Guangzhou, China.

[*f*] Renji Hospital, Shanghai, China

[*g*] University of Pennsylvania, Philadelphia, USA

[*h*] University of Groningen, Groningen, The Netherlands

[*i*] Bern University Hospital, University of Bern, Bern, Switzerland

[*j*] University of Copenhagen, Denmark

2.3 Opportunities and Challenges in Dynamic Total-Body PET Imaging

As summarized in Table 2.2, the unique characteristics of total-body PET studies bring a series of new challenges and opportunities for improved quantitative accuracy. Details are presented below:

(i) Improved image-derived input function. Due to the long axial field of view of total-body PET scanners, image-derived input functions can be measured from multiple blood pools (e.g., heart ventricle, aorta and artery). Higher temporal resolution (e.g., 1s even 0.1s per early frame) also allows better temporal sampling of the extracted input function (Zhang et al. 2020*b*,*a*, Viswanath et al. 2021).

(ii) Organ-dependent time delay. The arrival time of tracer to different organs is significantly varied, which has been an important factor for accurate total-body kinetics (Feng et al. 2019, 2021, Wang et al. 2021*a*, Wu et al. 2022*b*).

(iii) Tissue-specific kinetics. Each kind of tissue has its own physiological mechanism and some tissues such as the liver, kidney and bladder even exhibit more complex kinetics. Thus, a single kinetic model may not be feasible for multiple organs and appropriate model selection is necessary (Wang et al. 2021*a*,*c*, Wu et al. 2022*b*, Gu et al. 2022).

(iv) Capture fast kinetics. The high temporal sampling imaging provides an opportunity for better investigation of fast kinetics such as the blood volume or blood flow (perfusion), which are potential biomarkers for the prediction of therapy response or survival (Meikle et al. 2021, Gu 2023, Mankoff et al. 2002, Dunnwald et al. 2011).

(v) High-quality dynamic PET images. The increased sensitivity enables the generation of high signal-to-noise (SNR) images, which is greatly beneficial to the quantitation of dynamic imaging at the voxel level, e.g., noise reduction and lesion enhancement. But we need to note the sensitivity along the axial field of view shows the reciprocal U shape (non-uniform) (Lin et al. 2022, Dai et al. 2023, Prenosil et al. 2022). Thus, images have higher variances towards the axial edge, which

needs to be considered carefully.

(vi) Huge data set. It is challenging to store and process such enormous and complex datasets, which may be addressed by some automation forms using more comprehensive approaches (e.g., segmentation) (O'Sullivan 1993, Pedersen et al. 1994, Ahn et al. 2000, Wong et al. 2002*a*, Razifar 2005, Zanderigo et al. 2015) or artificial intelligence (Slart et al. 2021, Matsubara et al. 2022, Cheng et al. 2021, Apostolopoulos et al. 2022, Wang et al. 2021*c*)

Table 2.2: Characteristics and Challenges/Opportunities of total-body PET scanners.

Characteristics	**Challenges/Opportunities**
Multiple organs/tissues	• Tissue-specific kinetics • Large blood pool in FOV • Heterogeneity • Delay Correction
Higher temporal resolution	• Capture fast kinetics
Higher spatial resolution	• Better image quality
Huge data set	• High computational cost

2.4 Overview of Dynamic PET Quantitation

Dynamic PET quantitation is not a single procedure and involves several steps such as the recovery of input function and application of tracer kinetic modeling. The overview of this process is presented in Fig. 2.3. In the following sections, we will introduce the basic principles and some well-established methodologies, also their further developments for the emerging total-body PET imaging (Zhang et al. 2020*b*, Viswanath et al. 2021, Sari et al. 2022*b*).

2.4.1 Basic Equation

Understanding the targeted biochemical pathway is critical for the interpretation of dynamic PET imaging data. It can be approached using the indicator-dilution method built on the seminal work of Meier and Zierler (Meier & Zierler 1954). Assuming the radiotracer's interaction with tissue

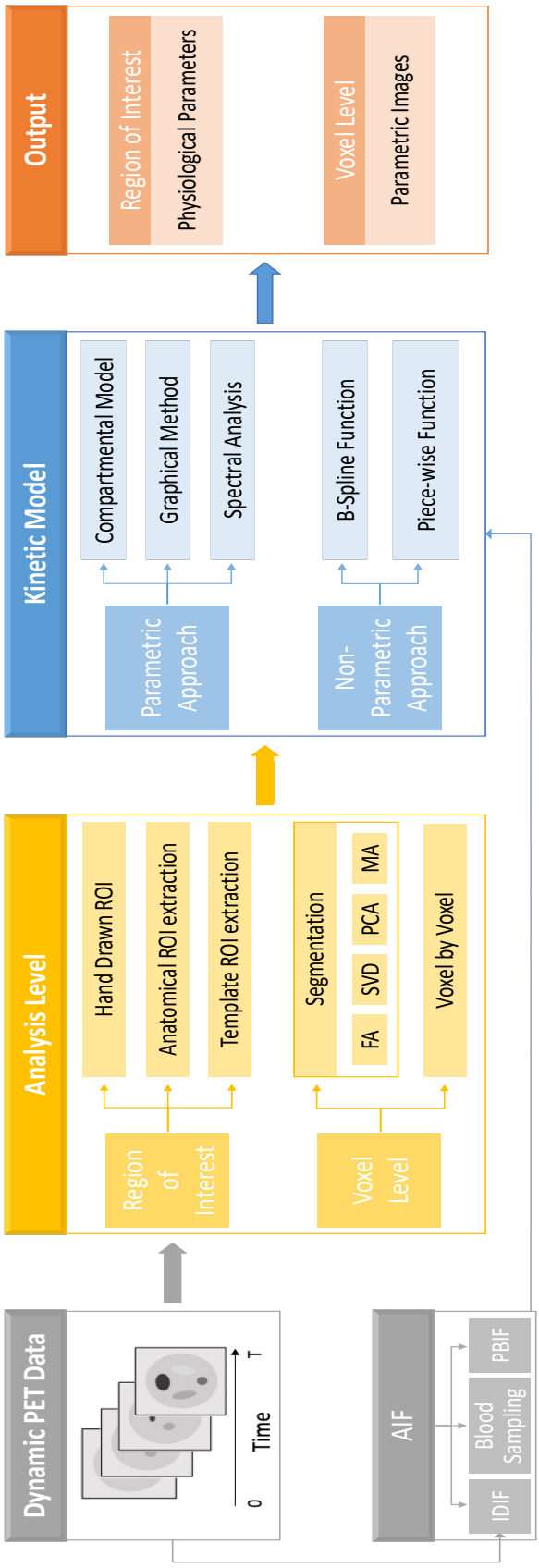


Figure 2.3: Overview of dynamic PET quantitation. Abbreviations: PET: positron emission tomography; IDIF: image-derived input function; PBIF: population-based input function; ROI: region of interest; FA: factor analysis; SVD: singular value decomposition; PCA: principal component analysis; MA: mixture analysis.

is substantially linear and time-invariant (LTI), the vascular network can be regarded as an LTI system with an arterial input. Hence, the measured tissue time activity curve (TAC) - C_T can be expressed as a convolution between the arterial input function (C_p) and tissue residue, also called the impulse response function (R) as in (2.1).

$$C_T(t) = \int_0^t R(t-s)C_p(s)ds \equiv R(t) \otimes C_p(t) \tag{2.1}$$

With the known input function, kinetic analysis is concerned with the estimation of residue and associated kinetic parameters such as flow (K), flux (K_i) and volume of distribution (V_D).

$$K = R(0), \quad K_i = \lim_{t\to\infty} R(t), \quad V_D = \int_0^\infty R\,(t)\,dt \tag{2.2}$$

When the model is applied to PET time-course data, there is typically an adjustment for a biologically important parameter - blood volume (V_B). Moreover, the site to recover the input function may be remote from the tissue, introducing a time delay. The correction is generally accomplished by the inclusion of a delay term (Δ) in the modeling procedure as (2.3). The delay has been found to vary with different voxels/organs/tissues and its correction is necessary (Feng et al. 2019, 2021, Wang et al. 2021*a*, Wu et al. 2022*b*).

$$C_T(t) = V_B C_p(t-\Delta) + (1-V_B)\int_0^t R(t-s)C_p(s-\Delta)ds \tag{2.3}$$

Some specific organs (e.g., liver) receive dual blood supplies from the hepatic aorta and portal vein (Figure2.4) (Chen et al. 1991, Slimani et al. 2008, Materne et al. 2000, Chen & Feng 2004). To account for such an effect, the input function can be expressed as a weighted sum of both supplies (Keiding 2012, Wang et al. 2018, 2021*b*).

$$C_p(t) = (1-f_A)C_{PV}(t) + f_A C_A(t) \tag{2.4}$$

where C_{PV} is the portal vein input and $C_A(t)$ is the aortic input. f_A is the fraction of the hepatic artery to the overall liver blood flow.

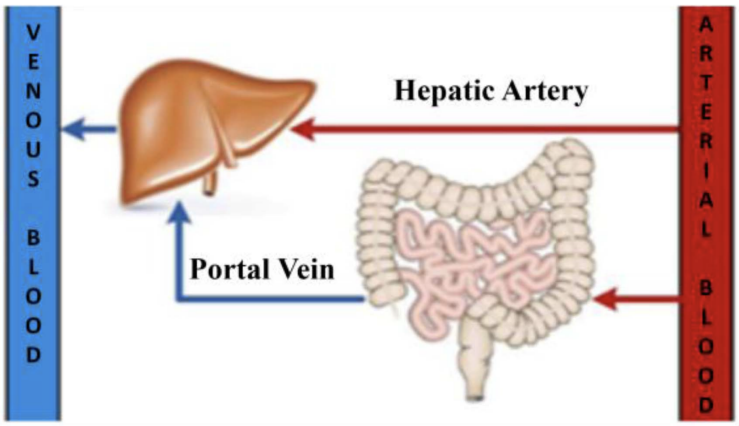


Figure 2.4: A diagram illustrating the dual blood supply to the liver. (Feng et al. 2020)

2.4.2 Region of Interest Versus Voxel-level Analysis

The computation of kinetic parameters can be performed either at the regional or voxel level. Due to the average of the voxel information in a region of interest (ROI), the noise can be reduced dramatically. ROI analysis leads to more robust results, especially in the case of dynamic PET studies, but also introduces some biases when defining ROIs from a template, summed or anatomic images (Bertoldo et al. 2014). An alternate approach to regional estimates is performing analysis at the voxel level and generated parametric images can reveal the heterogeneity of tumors (Muzi et al. 2012). However, many issues need to be considered carefully , such as computational efficiency, selection of appropriate models and noise suppression (Wang et al. 2021*a*).

Total-body PET scanners have the ability to image more organs/tissues using the single-bed position, but the datasets are much bigger and more complex than conventional studies. Multivariate statistical methods including factor analysis (FA) (Ahn et al. 2000), singular value decomposition (SVD) (Zanderigo et al. 2015), principal component analysis (PCA) (Pedersen et al. 1994, Razifar 2005) and mixture analysis (MA) (O'Sullivan 1993) express the dynamic PET data as a weighted sum of image volumes. They enable the identification of organs and structures with different kinetic patterns in a temporal sequence and reduce the temporal and spatial variations of the noise (Svensson et al. 2011). Once the segmentation process is completed, kinetics for each segment TAC (sub-TAC) are calculated and then

mapped back to the original spatial space. These data-driven approaches have the great potential to efficiently handle the complexities and address variable noise issues in dynamic total-body images (Wong et al. 2002*a*).

2.5 Arterial Input Function

For standard PET quantitation, the knowledge of the tracer arterial plasma concentration is required as an arterial input function (AIF). The input function can be derived either from (i) arterial blood samples, (ii) the time course of an ROI drawn on the PET image - image-derived input function (IDIF), or (iii) based on the population-based Input Function (PBIF). Here, we provide a brief introduction to these commonly used and model-based approaches together with their applications in total-body PET studies. A summarized flowchart of IDIF, PBIF and PBPM are given in Figure 2.5. For more details, readers are referred to two recent review papers (Feng et al. 2020, van der Weijden et al. 2023).

2.5.1 Blood Sampling

Arterial blood sampling during dynamic acquisition has been considered as the standard for input function in many references (Graham & Lewellen 1993, Chen et al. 2021*a*, Feng et al. 2015, Sari et al. 2018). But some concerns are also raised; for example, the measured AIF may suffer from some effects (e.g., delay, dispersion and metabolites), which need to be corrected (van der Weijden et al. 2023). This invasive procedure also implies discomfort for the patient (insertion of arterial lines and increased radiation) and additional costs for the analysis of numerous blood samples. Thus, it is typically used for research purposes and not recommended for routine clinical practice.

Manual blood sampling or an automatic blood sampling system (ABSS) (Napieczynska et al. 2018) is generally used to collect arterial blood. However, manual separation of plasma requires decay correction (Chen et al. 1995, Bober 2021), while longer tubing in ABSS introduces higher dispersion effects (Votaw & Shulman 1998) and requires consideration of the blood-to-plasma ratio (Li et al. 2020, Berezhkovskiy et al. 2011). Another

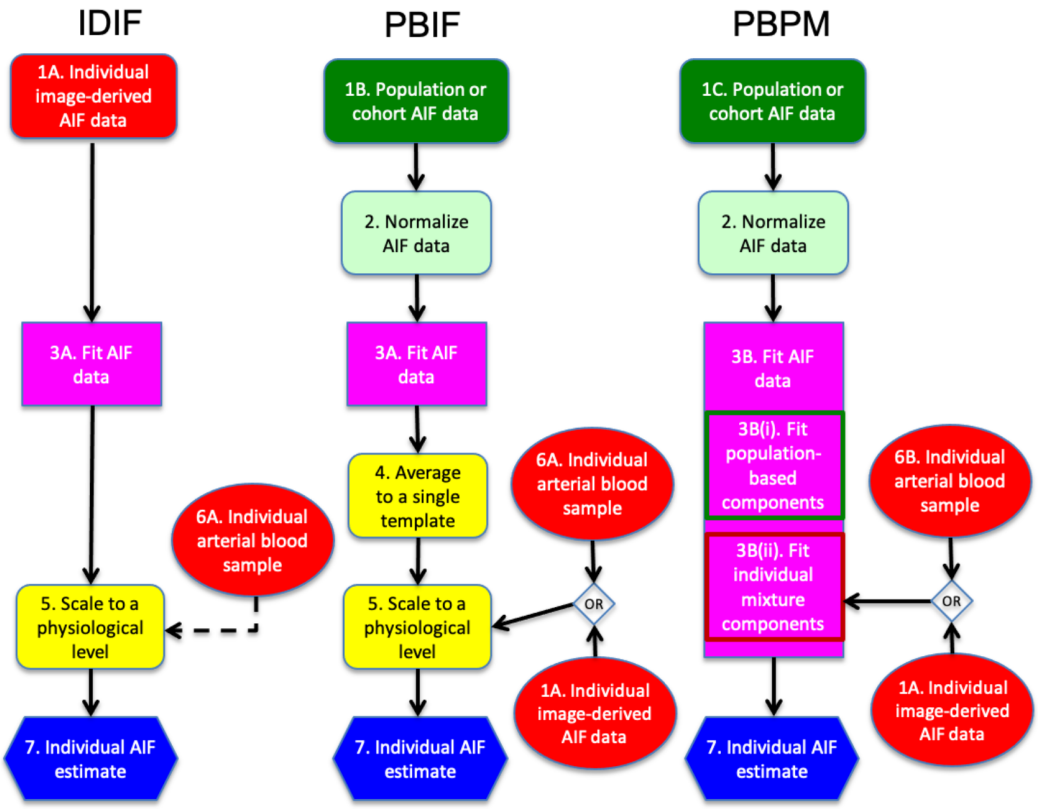


Figure 2.5: Flowchart of typical PBIF and IDIF strategies, along with the PBPM methodology in 2.5.4. (Xiu et al. 2022)

issue with AIF refers to the metabolite analysis. Although there are no blood-based metabolites for some tracers such as ^{18}F-FDG and ^{15}O-H_2O, most tracers produce isotope-labeled metabolites that contaminate the input function. These metabolites can be corrected by some mathematical models, e.g., Hill model (Gunn et al. 1998, Asselin et al. 2007), Power model (Watabe et al. 2000, Meyer et al. 2005) and Exponential models (Huang et al. 1991). A review of the commonly used metabolite-correction approaches is suggested to read for further details (Tonietto et al. 2016).

In practice, it would be more difficult to get the blood sampling for the total-body PET study. For example, both the radial artery and antecubital vein are harder to access due to the long axial field of view (Slart et al. 2021). The long line from the wrist to the sampling site may also cause more serious delay and dispersion issues (van der Weijden et al. 2023). With so many challenges, the first attempt was made by a Denmark group

to get the arterial blood sample for the total-body ^{15}O-H_2O scanning with Quadra (Andersen et al. 2022). And also some preliminary findings on applications of quantitative parametric perfusion imaging shown as Figure 2.6 are reported in (Knuuti et al. 2023). Such clinical trials are expected to be conducted more in the future. On the other hand, some non-invasive techniques (based on image/population/mathematical models) have also been developed as follows.

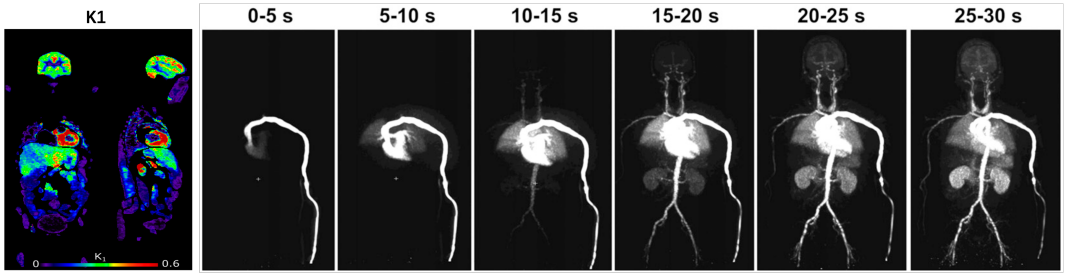


Figure 2.6: Voxel level quantitative parametric perfusion image with radiotracer delay. (left). ^{15}O-H_2O dynamic images with 5s duration in each time frame after tracer injection. (right series) (Knuuti et al. 2023)

2.5.2 Image-Derived Input Function

To obviate the need for blood sampling, input information can also be derived from a region drawn at the blood pool on PET images, referred to as image-derived input function. Due to the limited field of view of conventional PET scanners, sometimes IDIF can only be measured from small vessels such as carotids. However, total-body PET imaging provides multiple choices encompassing the left ventricle, aorta and other big blood vessels (Zhang et al. 2020*b*, Viswanath et al. 2021, Sari et al. 2022*b*). So far, the IDIF recovered from an ROI over the descending aorta (DA) has been the most popular one (Wang et al. 2020). Furthermore, the high spatial and temporal resolutions may also lead to more accurate and less noisy IDIF.

However, the use of IDIF still needs to be investigated carefully in the total-body setting. The whole blood activity concentration can be derived and plasma concentration is impossible to obtain. Reliable results are only generated with radiotracers that do not produce any metabolites, such as ^{18}F-FDG (Bertoldo et al. 2014). Additional corrections to the IDIF are also

important for accurate kinetics (Wang et al. 2023*b*).

2.5.3 Population-Based Input Function

Assuming individuals have the same tracer injection protocol and similar physiological characteristics in a cohort, the population-based input function is generally calculated by averaging and scaling this set of input functions using arterial catheterization invasively (Takikawa et al. 1993). Such a method is probably the most interesting approach for use in clinical practice with many radiotracers, but currently it has been validated almost exclusively for ^{18}F-FDG (Vriens et al. 2009). Several groups have attempted to reduce the dynamic scanning time using the PBIF on the total-body PET scanners (Wu et al. 2022*c*, Sari et al. 2022*a*, van Sluis et al. 2022).

2.5.4 Model-Based Input Function

Model-based descriptions of the arterial samples are usually introduced to obtain continuous and noise-free input functions, which may be helpful to further improve IDIF or PBIF. The most famous models are Feng's model (Feng et al. 1993) and its variation, i.e. tri-exponential model (Parsey et al. 2000), but they both cannot describe the complex behavior of the AIF and account for different injection protocols properly (Tonietto et al. 2015).

Simultaneous estimation of the input function (SIME) is usually used to generate a specific input function by fitting regional TACs simultaneously (Feng et al. 1997, Wong et al. 2001, 2002*b*). Recently, a population-based projection model (PBPM) has been developed which combines population profiling (as in a PBIF approach) with individual arterial input data modeling (as in an IDIF approach). This model incorporates knowledge of injection duration into the fit, allowing for varying injection protocols (Xiu et al. 2022). Another promising model to be applied to the emerging total-body PET imaging is the novel Markov chain model for the representation of the whole-body tracer circulation shown in Figure 2.7 (Huang & O'Sullivan 2014).

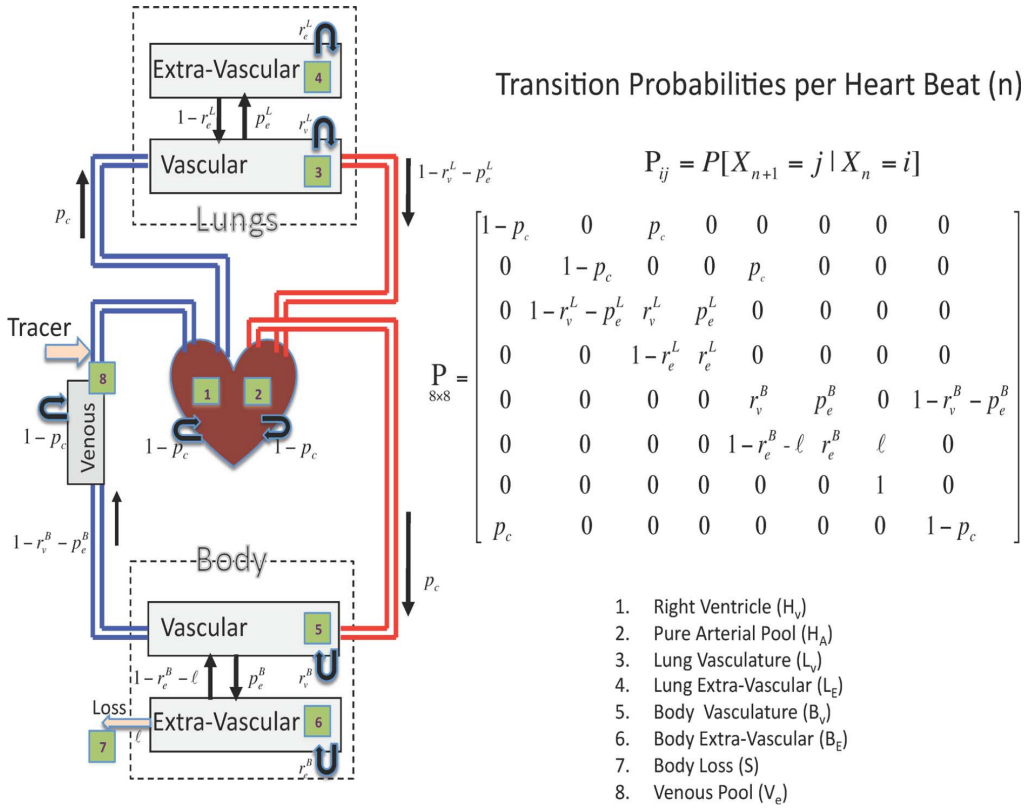


Figure 2.7: Markov chain model for tracer atom dynamics within the body. Graph representation (left). Transition matrix (right). (Huang & O'Sullivan 2014)

Table 2.3: A summary of major kinetic models used in PET quantitation.

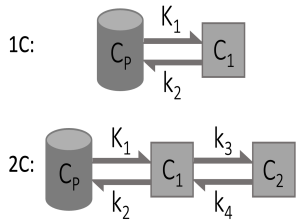
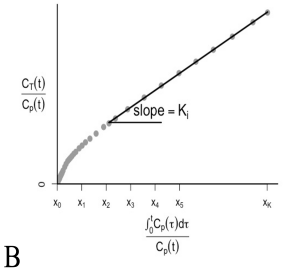
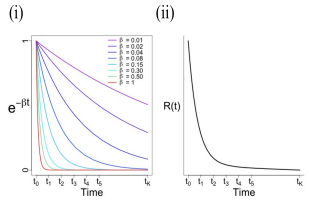
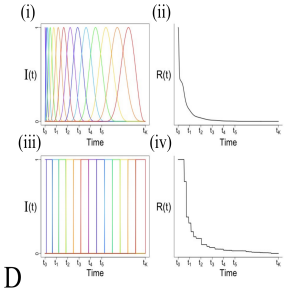
Kinetic Model	Compartmental Model	Patlak Plot	Spectral Analysis	Non-parametric Analysis
Graphical Representation	 A	 B	 C	 D
Formula	1C: $\frac{dC_1(t)}{dt} = K_1 C_p(t) - k_2 C_1(t)$ 2C: $\begin{cases} \frac{dC_1(t)}{dt} = K_1 C_p(t) - (k_2 + k_3) C_1(t) + k_4 C_2(t) \\ \frac{dC_2(t)}{dt} = k_3 C_1(t) - k_4 C_2(t) \end{cases}$	$\frac{C_T(t)}{C_p(t)} = K_i \frac{\int_0^t C_p(\tau)d\tau}{C_p(t)} + C, t \geq t^*$	$C_T(t) = \sum_{j=0}^{J} \alpha_j g_j(t), \alpha_j \geq 0$	$C_T(t) = \sum_{j=0}^{J} \alpha_j f_j(t), \alpha_j \geq 0$
Residue Form	1C: $R(t) = K_1 e^{-k_2 t}$ 2C: $R(t) = K_1(\pi_1 e^{-\theta_1 t} + \pi_2 e^{-\theta_2 t})$	$R(t) = K_i, t \geq t^*$	$R(t) = \sum_{j=0}^{J} \alpha_j e^{-\beta_j t}$	$R(t) = \sum_{j=1}^{J} \alpha_j I_j(t)$
Kinetic Parameters	All	Only K_i	All	All
Computation	Nonlinear Least Square or Maximum Likelihood	Ordinary Least Square	Non-negative Least Square	Quadratic Programming

Table 2.3 continued from previous page

Application to TB PET	Yes	Yes	No	Yes
References	(Feng et al. 2019, 2021, Wang et al. 2021*a*, Liu et al. 2021*b*, Sari et al. 2022*b*, Wu et al. 2022*b*, Omidvari et al. 2023, Li et al. 2023, Chen et al. 2023*a*, Wang et al. 2023*b*, 2022*e*, Yin et al. 2023)	(Zhang et al. 2020*b*, Sari et al. 2022*b*, Wu et al. 2022*a*, Gu et al. 2022, van Sluis et al. 2022, Wu et al. 2022*c*, Chen et al. 2022*b*, Viswanath et al. 2021, Chen et al. 2023*a*, Wang et al. 2022*e*)		(O'Sullivan et al. 2022)

*For details of derivations, see (Gu 2023).

A: One (1C) and two compartmental (2C) models. C_p is the plasma compartment; C_1 and C_2 are tissue compartments.

B: Patlak plot.

C: Spectral Analysis. (i) exponential distribution for different values of β; (ii) the typical residue estimated by spectral analysis.

D: Non-parametric Analysis. (i) general form of B-spline basis elements; (ii) the typical residue estimated by B-spline function; (iii) general form of piece-wise elements; (iv) the typical residue estimated by piece-wise function.

Notations:

$$\begin{cases} \pi_1 = \frac{k_4-\theta_1+k_3}{\theta_2-\theta_1}, \quad \pi_2 = \frac{\theta_2-k_4-k_3}{\theta_2-\theta_1} \\ \theta_1 = \frac{k_2+k_3+k_4-\sqrt{(k_2+k_3+k_4)^2-4k_2k_4}}{2} \qquad g_j(t) = C_p(t) \otimes e^{-\beta_j t} \qquad f_j(t) = C_p(t) \otimes I_j(t),\ I \text{ represents basis function (B-spline or piece-wise form)} \\ \theta_2 = \frac{k_2+k_3+k_4+\sqrt{(k_2+k_3+k_4)^2-4k_2k_4}}{2} \end{cases}$$

2.6 Kinetic Model

Many kinetic models have been well-developed for quantitative PET scanning, but they differ in terms of residue form and produced information (Bertoldo et al. 2014). A summary is shown in Table 2.3. Most of them (e.g., compartmental model, Patlak plot and spectral analysis) are parametric models that generally rely on the necessary assumptions. These are difficult to justify for the heterogeneous tissue region, especially the diverse-tissue study. The non-parametric method without the assumption requirement should be more flexible and indeed have some substantial advantages.

Here we provide an overview of various parametric and non-parametric strategies (see (Gu 2023) for more details of derivations) and summarize their recent developments for total-body PET imaging (Zhang et al. 2020*b*, Feng et al. 2021, Wang et al. 2021*a*, Li et al. 2022*a*, Sari et al. 2022*b*, Wu et al. 2022*b*, Gu et al. 2022, Wu et al. 2022*a*, O'Sullivan et al. 2022). The feasibility, challenge and promise of these methodologies are also discussed.

2.6.1 Compartmental Model

Compartmental modeling forms the basis for tracer kinetics of dynamic PET data. There are two most important models used to derive physiological information in absolute measurement units as shown in Table 2.3A. One tissue compartmental (1C) model with two rate constants (K_1 in ml/min/cm^3 and k_2 in min^{-1}) was developed by Kety (Kety & Schmidt 1948) for quantitative assessment of blood flow (perfusion). Two tissue reversible compartmental (2Cr) model with four rate constants (K_1 in ml/min/cm^3, k_2, k_3 and k_4 in min^{-1}) is mainly used for quantifying receptor-ligand binding studies (Mintun et al. 1984). While k_4 equals 0 (irreversible), it becomes the most famous Sokolov-Huang model (2Ci) generally employed for the quantitation of metabolic rate for glucose (Sokoloff et al. 1977, Phelps et al. 1979, Huang et al. 1980). For more generalized compartmental models and detailed underlying biochemical mechanisms, see (Gunn et al. 2001).

These models are described by a system of first-order time-dependent differential equations, which can be solved by a numerical procedure known as nonlinear least squares (NLS) in order to appropriately estimate the residue

function and associated kinetics. The advantages of compartmental modeling are the reliability and independency on the scanning time. When dealing with very noisy data (e.g., voxel-level analysis), this method has several shortcomings including convergence issues, long computational time and sensitivity to initial estimates due to the nature of NLS (Bertoldo et al. 2014).

2.6.1.1 1C Model

One tissue compartmental model is given by a differential equation as (2.5):

$$\frac{dC_1(t)}{dt} = K_1 C_p(t) - k_2 C_1(t) \tag{2.5}$$

where C_1 represents tissue compartment and C_p is the plasma compartment. Solved by the integrating factor method, the solution is found to be:

$$C_1(t) = \int_0^t K_1 e^{-k_2(t-s)} C_p(s) ds \tag{2.6}$$

Related to the simple basic equation (2.1), the residue function can be expressed as

$$R(t) = K_1 e^{-k_2 t} \tag{2.7}$$

Hence, the parameter of interest - blood flow (perfusion) $= R(0) = K_1$.

2.6.1.2 2C Model

Similar to the 1C model, two tissue compartmental model is represented by a coupled system of differential equations as (2.8).

$$\begin{cases} \frac{dC_1(t)}{dt} = K_1 C_p(t) - (k_2 + k_3) C_1(t) + k_4 C_2(t) \\ \\ \frac{dC_2(t)}{dt} = k_3 C_1(t) - k_4 C_2(t) \end{cases} \tag{2.8}$$

where C_2 is the tissue compartment. By the Laplace transform and its inversion (Trench 2013), the final result is given by:

$$C_T(t) = C_1(t) + C_2(t) = K_1(\pi_1 e^{-\theta_1 t} + \pi_2 e^{-\theta_2 t}) \otimes C_p(t) \tag{2.9}$$

where

$$\begin{cases} \pi_1 = \frac{k_4-\theta_1+k_3}{\theta_2-\theta_1}, \quad \pi_2 = \frac{\theta_2-k_4-k_3}{\theta_2-\theta_1} \\ \theta_1 = \frac{k_2+k_3+k_4-\sqrt{(k_2+k_3+k_4)^2-4k_2k_4}}{2} \\ \theta_2 = \frac{k_2+k_3+k_4+\sqrt{(k_2+k_3+k_4)^2-4k_2k_4}}{2} \end{cases}$$

Again recall the fundamental equation (2.1), residue is a mixture of exponentials as (2.10).

$$R(t) = K_1(\pi_1 e^{-\theta_1 t} + \pi_2 e^{-\theta_2 t}) \tag{2.10}$$

For the irreversible 2C model ($k_4 = 0$), the metabolic flux is focused, that is $K_i = \lim_{t\to\infty} R(t) = \frac{K_1 k_3}{k_2+k_3}$. For the reversible tracers, volume of distribution is calculated as: $V_D = \int_0^\infty R(t)dt = \frac{K_1}{k_2}(1 + \frac{k_3}{k_4})$.

2.6.1.3 Delay Effect

In the routine PET image, IDIF is usually extracted from a nearby arterial blood pool so the time delay between IDIF and the targeted tissue is very short and even negligible. The total-body PET scanner provides several options for IDIF location that may be far away from some tissues. The delay time can be up to 50 seconds and significantly varied to different tissues, which has been an important factor in affecting the kinetic quantification (Feng et al. 2019, 2021, Wang et al. 2021*a*, Wu et al. 2022*b*).

To correct this effect, the delay term is jointly estimated with other parameters in compartmental models. Take 1C model as an example, replacing the residue function in (2.3) by (2.7) gives:

$$C_T(t) = V_B C_p(t-\Delta) + (1-V_B)\int_0^t K_1 e^{-k_2(t-s)} C_p(s-\Delta)ds \tag{2.11}$$

In this setting, (V_B, K_1, $k2$, Δ) are estimated. Similarly for 2C model, (V_B, K_1, $k2$, $k3$, Δ) or (V_B, K_1, $k2$, $k3$, $k4$, Δ) are derived but the estimation procedure is more computationally expensive. Two schemes have been proposed to determine the delay by only the first few minutes data using 1C model (Feng et al. 2019, 2021) or full-time data in arbitrary models (Wang et al. 2021*a*). The former one has been initially demonstrated to be efficient (Wu et al. 2022*b*).

2.6.1.4 Model Selection

The selection of compartmental models (1C, 2Ci, 2Cr) usually depends on the tracer property, the aim of the study, and even the organ or tissue of interest. For example, 1C is generally adopted for ^{15}O-H_2O and 2Cr is used for ^{11}C-Raclopride. As the most commonly used tracer - ^{18}F-FDG, the irreversible model (2Ci) is employed for many organs while its uptake into the liver exhibits reversible characteristics (Keramida et al. 2014). Therefore, we must justify each case carefully for the use of the compartmental model.

The typical quantitation for dynamic PET study is applying a single model, which works well in organ-specific imaging on conventional scanners. However, it may not be suitable for total-body imaging as a single model may not be feasible for various tissues and organs. Wang et al. have reported that a voxel-level model selection strategy based on an Akaike information criterion (AIC) leads to improved total-body parametric imaging (Wang et al. 2021*a*). But there is no doubt that it brings a higher computational burden. Later on a further examination of various compartmental models for multiple organs is implemented at the ROI level (Wu et al. 2022*b*). This study indicates that the applicability of compartmental models for the bladder is questionable.

2.6.2 Patlak Plot

Graphical techniques provide simple ways to estimate the specific kinetic parameters by appropriately transforming the equations of compartmental modeling for irreversible and reversible tracers (Patlak et al. 1983, Logan et al. 1990, Zhou et al. 2010). Here we just focus on the most popular graphical method - Patlak model, for more details about other approaches, we suggest a review article for further reading (Logan 2003). Patlak analysis has been widely applied to dynamic PET imaging due to its simplicity and robustness (Patlak et al. 1983), which is assumed that: (i) the trapping of tracer in studied organs/tissues is completely irreversible; (ii) Patlak plot results in a straight line after the time that steady-state conditions between reversible tissue and plasma compartments are reached. If both assumptions are satisfied, K_i can be estimated easily as the slope of the Patlak plot after the equilibrium time (t^*) using linear regression. The Patlak plot is

given by the expression below:

$$\frac{C_T(t)}{C_p(t)} = K_i \frac{\int_0^t C_p(\tau)d\tau}{C_p(t)} + constant, \quad t \geq t^* \tag{2.12}$$

K_i is computed using a few late time frames of dynamic scanning by a non-iterative strategy - ordinary least square (OLS). Due to the nature of linearity, it should be much faster and less sensitive to noise than NLS and it is therefore appropriate for applications at the voxel level (Tomasi et al. 2012). On the other hand, it must be noted that this approach does not provide any insight regarding the complete profile of tracer kinetics and only a reduced set of parameters (K_i) is obtained.

When adopting the standard Patlak (sPatlak) method for dynamic total-body imaging, many tissues and organs can be studied simultaneously. Single t^* may not be appropriate for the diverse-tissue environment as the equilibrium conditions are probably achieved at different time points. The feasibility of Patlak plot also needs to be justified for certain tissues like the liver, kidney and bladder. These limitations and possible solutions are discussed in detail in the following.

2.6.2.1 Selection of t*

The improper t^* may introduce additional errors in estimated K_i (Choi et al. 1991). A rich literature has explored the choice of t^* for a single organ on short AFOV PET scanners, for example, 20 min for brain (Chen et al. 1998) and 10 min for lung (Coello et al. 2017). Total-body Patlak images are generated with various t^*, from 10 min (Chen et al. 2021*b*), 15 min (Liu et al. 2021*c*), 20 min (Wu et al. 2022*d*) to 30 min (Zhang et al. 2020*b*). But there are no more details about the justifications in these studies.

Recently, an adaptive t^* scheme has been proposed to determine the optimal options for different ROIs or voxels (Wu et al. 2022*a*). It is based on two criteria - max-error and R squared (R^2). Max-error is defined as the worst case error between the predicted value and the true value for all observations on the Patlak plot. The selected t^* is the earliest one so that the max-error is less than a threshold value. This criterion has been employed in PMOD ($Z\ddot{u}rich, Swizerland$) and the default setting of threshold

is 10%. R^2 is a common metric to quantify the goodness of linear fit and a value closer to 1 indicates a better fit, so optimal t^* is determined by the maximum R^2. This procedure has the potential to improve the accuracy of kinetic parameters. However, further investigations in patient cohorts and more sophisticated techniques need to be developed.

2.6.2.2 Generalized Patlak

As described above, the standard Patlak analysis assumes an irreversible 2C model. For total-body imaging, this assumption can be broken by some tissues (e.g., the liver where ^{18}F-FDG may exhibit mild positive uptake reversibility and bladder associated with the complex tracer excretion process) (Choi et al. 1994, Wu et al. 2022*b*,*a*) and tumors (e.g., hepatocellular carcinoma) (Torizuka et al. 1995) so that the sPatlak plot is no longer linear.

To address these issues, a generalized Patlak (gPatlak) method (2.13) based on the reversible 2C model was proposed in 1985 (Patlak & Blasberg 1985), which introduced an additional exponential term characterized by the net efflux (k_{loss}) to account for the effect of tracer dephosphorylation properly.

$$\frac{C_T(t)}{C_p(t)} = K_i \frac{\int_0^t e^{-k_{loss}(t-\tau)} C_p(\tau) d\tau}{C_p(t)} + constant, t \geq t^* \tag{2.13}$$

This model becomes non-linear due to the added exponential term, but it can be solved by applying a basis function to linearize the estimation process (Karakatsanis et al. 2015).

The utility of the gPatlak approach for diverse organs and tissues is first examined by Karakatsanis et al. (Karakatsanis et al. 2015) in multi-bed multi-pass whole-body PET imaging. Then the performance of both standard and generalized Patlak methods has been assessed for multiple organs at the ROI level using a total-body PET study on uEXPLORER (Gu et al. 2022). Results show that gPatlak can bring benefits for the liver, kidney, lung and especially bladder. Thus, it would be also interesting to explore the use of the gPatlak plot for voxel-level analysis in the future.

2.6.3 Spectral Analysis

The residue function in the compartmental model is the single exponential (2.7) or a mixture of exponentials (2.10). It may not have sufficient degrees of freedom to capture full variability in total-body PET data. Spectral Analysis (SA) proposed by Cunningham and Jones in 1993 (Cunningham & Jones 1993) assumes the residue to be the sum of $J+1$ exponential terms.

$$R(t) = \sum_{j=0}^{J} \alpha_j e^{-\beta_j t}, \alpha_j \geq 0, \beta_j \geq 0, \beta_0 = 0 \tag{2.14}$$

Thus, the tissue time course can be expressed as

$$C_T(t) = \sum_{j=0}^{J} \alpha_j e^{-\beta_j t} \otimes C_p(t) \equiv \sum_{j=0}^{J} \alpha_j g_j(t) \tag{2.15}$$

$g_j(t)$ are known with the pre-defined eigenvalues β_j, whereas the amplitudes α_j are estimated by the NLS algorithm. The model structure (e.g., reversibility or irreversibility, number of compartments) is derived from α_j, also called spectrum (Tomasi et al. 2012). The information of macroparameters, such as K, K_i and V_D is obtained as:

$$K = \sum_{j=0}^{J} \alpha_j, \quad K_i = \alpha_0, \quad V_D = \sum_{j=1}^{J} \frac{\alpha_j}{\beta_j} \tag{2.16}$$

Some relevant strategies such as rank-shaping spectral analysis (Turkheimer et al. 2003) and spectral analysis with iterative filter (Veronese et al. 2010) have also been developed in recent years. The main strength of spectral analysis is its flexibility which can be applied to reversible or irreversible tracers, single or multiple compartmental models, and homogeneous as well as heterogeneous systems (Veronese et al. 2016). These characteristics make this method adaptable to various tracers and particularly suitable for total-body PET imaging. But until now, it has not been implemented in this area.

2.6.4 Non-parametric Analysis

Typically the tissue residue is a monotone decreasing function and approximated as nonnegative sums of exponential terms in the compartmental framework. However, the strict monotonicity ($\Delta R(t) < 0$) is not always realistic (Li et al. 1997) and the assumed exponential form may not be reasonable to represent data in which in-vivo biochemistry is not clear (King et al. 1996, Østergaard et al. 1996, 1999, Barrio et al. 2020*b*), especially for the emerging total-body PET imaging (Wu et al. 2022*b*, Gu et al. 2022).

Unlike the methods discussed above, residue can also be estimated by the non-parametric approaches (O'Sullivan et al. 2009, Hawe et al. 2012, O'Sullivan et al. 2014, Chen et al. 2019) and given by:

$$R(t) = \sum_{j=1}^{J} \alpha_j I_j(t), \quad \alpha_j \geq 0 \tag{2.17}$$

Although it has a similar structure as (2.14), I here represents the basis elements, which can be B-spline (O'Sullivan et al. 2009, Chen et al. 2019) or piece-wise function (Hawe et al. 2012, O'Sullivan et al. 2014). This procedure has the ability to adapt to monotone (even exponential) and non-monotone forms as no unrealistic parametric restrictions are imposed.

The non-parametric residue analysis can be implemented rapidly by quadratic programming and has the advantage of providing more accurate kinetic quantitation in multiple tissues. An efficient application of this concept to generate parametric imaging is described as follows.

The non-parametric residue mapping (NPRM) consists of a fully automatic process incorporating data-adaptive segmentation, non-parametric residue analysis of segment data (sub-TAC) and voxel-level kinetic mapping scheme (Gu et al. 2021*a*).

Following the linear structure of mixture model (O'Sullivan 1993), the voxel-level time course (z_i) can be expressed as a non-negative combination of sub-TACs (μ_l). The mechanism enables to address the heterogeneity of voxel-level data.

$$z_i(t) = \sum_{l=1}^{L} \pi_{il} \mu_l(t), \quad \pi_{il} \geq 0, \quad i = 1, 2, ..., N \tag{2.18}$$

where π is the coefficient and N is the number of voxels.

For each sub-TAC, the associated residue is estimated non-parametrically and the parameter of interest - θ (e.g., K, K_i or V_D) can be derived as a function (g) of residue.

$$\mu_l(t) = R_l(t) \otimes C_p(t - \Delta) \Rightarrow \theta_l = g(R_l)$$

The final parametric imaging is obtained as

$$\theta_i = \sum_{l=1}^{L} \pi_{il}\theta_l, \quad i = 1, 2, ..., N \tag{2.19}$$

The NPRM approach has some important features like the flexibility for diverse tissues and consideration of delays for different parts and also the ability to address issues with bladder or injection site (O'Sullivan et al. 2009, 2014, Gu et al. 2021*a*), which make it feasible to be applied to total-body PET studies.

Building on (2.18), an image-domain bootstrap data generation process can be defined by the spatial and temporal patterns of model residuals (O'Sullivan et al. 2021, Gu et al. 2021*b*). It has been used to assess the uncertainty (standard errors) of parametric imaging (Gu et al. 2019*b*). The practicality of simultaneous segmentation, kinetic parameter estimation and uncertainty evaluation has also been demonstrated for a total-body breast cancer patient study on Biograph Vision Quadra (O'Sullivan et al. 2022).

2.7 Other Approaches

All the aforementioned approaches are applied in the image domain, however, they can be incorporated into the reconstruction process to estimate kinetic parameters by modeling projection data (sinogram or list-mode), known as the "direct method" (Kotasidis et al. 2014). The ideas for direct estimation could date back to the 1980s (Snyder 1984, Carson & Lange 1985) and since then many scientists have made great contributions to the progression of this technology for more accurate kinetics than the routine post-reconstruction procedure (Meikle et al. 1998, Kamasak et al. 2005,

Wang et al. 2008, Tsoumpas et al. 2008, Wang & Qi 2009, Rahmim et al. 2009). We suggest a detailed technical review for further reading (Wang & Qi 2013). It is remarkable that direct Patlak has been adopted on commercial scanners and applied to total-body PET studies (Zhang et al. 2020*b*, Sari et al. 2022*b*, Li et al. 2022*c*). But it suffers from similar problems like the non-linearity for specific tissues as mentioned above (Karakatsanis et al. 2016, Gu et al. 2022, Wu et al. 2022*a*).

Another research interest in future work is the implementation of artificial intelligence (AI) for the total-body PET imaging (Matsubara et al. 2022, Li et al. 2021). As a subcategory of AI, deep learning (DL) techniques, e.g., convolutional neural network (CNN) (Zaidi & El Naqa 2021) and generative adversarial network (GAN) (Apostolopoulos et al. 2022), have been extensively used in PET for solving a wide variety of problems involving image reconstruction (Gong et al. 2018, Reader et al. 2020, Häggström et al. 2019), denoising (Cui et al. 2019, Lu et al. 2019), segmentation (Niyas et al. 2021, Guo et al. 2019) as well as quantitation (Gong et al. 2021, Zaker et al. 2022). A few initial attempts have been made to extract the flux (K_i) from total-body PET studies by DL methods (Huang et al. 2022, Li et al. 2022*c*, Wang et al. 2022*c*). More opportunities and challenges facing the adoption of DL in total-body PET quantitation are detailedly discussed in a recent review paper (Wang et al. 2021*c*).

There are a number of PET studies where dynamic scans are used and main organs are included, e.g., whole-body human and preclinical animal imaging. The data structures and characteristics are similar to total-body human studies. Therefore, it is natural to generalize the techniques developed in these studies for quantifying dynamic total-body imaging. For example, (i) generalized and direct Patlak methods are both first examined for multiple organs in whole-body scans (Karakatsanis et al. 2015, Yao et al. 2021, Dias et al. 2021), then applied to total-body imaging (Gu et al. 2022, Zhang et al. 2020*b*, Sari et al. 2022*b*); (ii) the above-mentioned NPRM procedure is demonstrated in the whole-body pregnant macaque studies (Gu et al. 2019*a*) before it is employed to generate total-body parametric imaging (O'Sullivan et al. 2022). Many other perspectives also have excellent potential as tools in the future (Kuntner & Stout 2014, Rahmim et al. 2019).

Chapter 3

A Generalized Linear Modeling Approach to Bootstrapping Multi-frame PET Image Data

Abstract

PET imaging is an important diagnostic tool for the management of patients with cancer and other diseases. Medical decisions based on quantitative PET information could potentially benefit from the availability of tools for the evaluation of associated uncertainties. Raw PET data can be viewed as a sample from an inhomogeneous Poisson process, so there is the possibility of directly applying bootstrapping to raw projection-domain list-mode *data. Unfortunately, this is computationally impractical, particularly if data reconstruction is iterative or the acquisition protocol is dynamic. We develop a flexible statistical linear model analysis to be used with multi-frame PET image data that can create valid bootstrap samples. The technique is illustrated using data from dynamic PET studies with fluoro-deoxyglucose (FDG) and fluoro-thymidine (FLT) in brain and breast cancer patients. As is often the case with dynamic PET studies, image data have been archived without raw list-mode data. Using the bootstrapping technique, maps of kinetic parameters and associated uncertainties are obtained. The quantitative performance of the approach is assessed by simulation. The proposed image-domain bootstrap is found to substantially match the projection-domain alternative. Analysis of results also points to*

a close relation between relative uncertainty in voxel-level kinetic parameters and local reconstruction error. This is consistent with statistical theory.

3.1 Introduction

Positron emission tomography (PET) is a well-established radio-tracer imaging technique, extensively relied on in both secondary and tertiary clinical care settings, as well as in medical research. As the role of quantitative PET in clinical decision making evolves, it is likely that there will be an increasing interest in the availability of practical methods for evaluating uncertainty associated with the results reported for an individual patient. There is already a significant literature on variance assessment for PET. Much of this work has concentrated on the development of analytic approaches based on the linear approximations to the reconstruction process – see, for example, (Alpert et al. 1982, Barrett et al. 1994, Carson et al. 1993, Huesman 1977, Ibaraki et al. 2014, Maitra & O'Sullivan 1998, Qi & Leahy 2000, Tanaka & Murayama 1982, Wang & Gindi 1997). The potential of applying Efron's statistical bootstrap (Efron & Tibshirani 1994) in this setting was described by (Haynor & Woods 1989). There have been a number of contributions - see, for example, (Buvat 2002, Dahlbom 2001, Lartizien et al. 2010, Ibaraki et al. 2014, Kucharczak et al. 2018) - that have attempted to implement variations on this approach. The attraction of the non-parametric bootstrap is that it does not involve detailed analytic assumptions which may be difficult to justify in a real patient study. So far, bootstrapping methods for PET image data have concentrated on re-sampling in the raw measurement domain. We refer to such *list-mode* or *sinogram* sampling techniques as projection-domain methods. The work here is stimulated by (Huang et al. 2020), who used a combination of physical phantom and numerical simulations to develop an image-domain bootstrapping strategy for PET data. The approach is based on a sub-ordinate Gaussian structure, a particular type of Gaussian copula form (Joe 2014), with the ability to capture the Poisson-like nature of voxel-level measurements as well as relevant spatial and temporal covariances. In the context of standard clinical PET-FDG studies, involving imaging over a relatively short duration time frame between 45 and 60 minutes after tracer injection, (Huang et al. 2020) proposed

sub-dividing frame data in order to obtain the near-replicate information needed to estimate unknown parameters in a proposed image-domain simulation model. This technique was illustrated using data from a clinical PET-FDG lung cancer study.

Our work here develops a more flexible procedure for image-domain bootstrapping. This new approach is applicable in situations where there may be a complex temporal structure in the measured PET data — a near-constant temporal structure is intrinsic to the method used in (Huang et al. 2020). In addition the latter work relied on a parametric Gamma-model form to represent the marginal distributions of voxel-level data and a parametric spatial auto-regressive (SAR) form to represent covariance patterns. The method here uses the empirical distribution of re-scaled data and a non-parametric approach for analysis of the spatial correlation structure. The purpose of this report is to describe the modeling techniques involved in a novel image-domain bootstrapping method and to numerically demonstrate its performance relative to the standard projection-domain bootstrapping technique. Similar to (Huang et al. 2020) the proposed approach is only applicable to situations where the PET data have a temporal extent — $e.g.$ dynamic PET studies. In this setting suitable modeling of the dynamic data enables us to identify an associated set of residuals that can be manipulated to construct a viable model-based image-domain bootstrapping procedure.

The technical framework for the methodology is set out section 3.2 with some illustrative examples presented in section 3.3. The examples come from dynamic studies with PET-FDG and PET-FLT in brain and breast-cancer patients. Apart from the distinctive temporal patterns arising in these data, the studies come from different scanners one using a traditional analytic filtered-backprojection (FBP) reconstruction method and the other an iterative maximum likelihood (ML) approach. Residual diagnostics demonstrate how the generalized linear modeling adapts to the varying nature of these studies. A kinetic mapping technique is applied to the bootstrap-simulated datasets in order to produce parametric images of metabolism and associated voxel-by-voxel standard errors. Section 3.4 presents numerical simulation studies, matched to the real data. These studies explore the performance of this novel model-based bootstrapping technique relative to the projection-domain list-mode bootstrapping approach. In addition we ex-

amine if performance is impacted by the nature of the data reconstruction process used. The results are very promising, demonstrating that the efficient model-based image-domain bootstrapping substantially matches the performance of the projection-domain approach, regardless of what data reconstructed scheme is used. The paper concludes with some discussion in Section 3.5.

3.2 Methods: Basic Models and Analysis Techniques

The input data for the approach is a 4-D dynamic PET dataset represented by an $N \times T$ array, $\{z_{ij};\ i = 1, .., N, j = 1, ..., T\}$. Here N represents the number of voxels in the field of view and T is the number of time-frames in the PET acquisition. z_{ij} is the reconstructed PET-measured tracer concentration value at the 3-D voxel co-ordinate, x_i, at a time t_j corresponding to the mid-point of the j'th time-frame of scanning. We begin by providing a formal mathematical description of the model, highlighting the various unknowns that must be estimated before it can be used for bootstrapping.

3.2.1 Statistical Modeling of the Image-Domain Data

Let the true mean and variance of the PET measurement z_{ij} be denoted μ_{ij} and σ_{ij}^2, respectively. The proposed approximation of measurements has the structure of a general linear model in which the error process, while allowed to be non-Gaussian and non-stationary, is linked to a sub-ordinate Gaussian process. The starting point for the specification is a set of data-dependent basis vectors, denoted $X = \{\mu_k, k = 1, 2, ..., K\}$, that have the ability to approximate local mean values, μ_{ij}. The method used to identify X is described in section 3.2.3 below. The statistical model for z_{ij} is expressed as a sum of systematic and random terms. The basic version is given by

$$\begin{aligned} z_{ij} &= \mu_{ij} + \sigma_{ij}\epsilon_{ij} \ ; \ \epsilon_{ij} = Q(\eta_{ij}) \ \text{ with } \ \eta_{ij} \sim N(0,1) \\ \mu_{ij} &= x_j'\alpha_i \ ; \ \sigma_{ij} = \sigma_i\phi_j \ ; \ \sum_{j=1}^{T} \phi_j^2 = T \end{aligned} \tag{3.1}$$

Here x_j is the j'th row of X and α_i is a vector of unknown coefficients. Note that the systematic part of z_{ij}, here μ_{ij}, is approximated by a linear form. The model is referred to as a *generalized linear model* because errors are allowed to be non-Gaussian and the scale factors, σ_{ij}, are not assumed constant (Seber 2015). In (3.1), σ_{ij} is a product of spatial (σ_i) and temporal (ϕ_j) factors. The constraint on ϕ is required for identifiability. A key part of (3.1) is that the error term ϵ_{ij} is related to a sub-ordinate Gaussian variable, η_{ij}, by a (unknown) Q-transform. In statistical parlance, the inverse of Q defines the normal-quantile plot for the collection of measurement errors (R Core Team 2021). We assume Q is strictly monotone and, for identifiability, scaled so that $var(\epsilon_{ij}) = 1$. Monotonicity of Q is a requirement for the distribution of the measurement errors to be well-defined; it does not restrict the flexibility of the model to adapt to arbitrary distributional forms for the error. Strict monotonicity implies that the quantile mapping is invertible. If the model errors have a continuous distribution - a very plausible approximation for PET and many other types of medical imaging data - then Q must be strictly monotone. The sub-ordinate Gaussian η-process, $\eta = \{\eta_{ij}, i = 1, 2, ..., N, j = 1, 2, ..., T\}$, is assumed to have independent temporal components, matching the formal Poisson structure of PET (Vardi et al. 1985), and a common stationary spatial auto-correlation, consistent with physical phantom measurements and simulations, see, for example, (Huang et al. 2020). Note that the concept of using a simple sub-ordinate stationary process, like η here, to describe dependency in multivariate data is well established. (Joe 2014) provides a treatment of many instances which has proved useful in applied statistical work.

While the model in (3.1) can capture non-stationarity (in mean and variance) and rather general correlation patterns, it has limited ability to adapt to the local skewness of PET data. Such skewness is particularly important for iteratively reconstructed PET data. Thus, a more elaborate form of the model is needed for our proposed image-domain bootstrapping procedure. (Scheuermann et al. 2013, Mou et al. 2017) used Gamma-distributions to model the local skewness of iteratively reconstructed PET measurements of scanned physical phantoms. In a Gamma-distribution, the ratio of the mean to the standard deviation is the square-root of the shape parameter. This quantity is inversely proportional to the skewness of the distribution.

As the shape parameter increases, skewness diminishes and the Gamma-distribution formally converges to a Gaussian form. Using the fit of the basic model in (3.1) to define $\tilde{\mu}_{ij}$, $\tilde{\sigma}_i$ and $\tilde{\phi}_j$, we let $\kappa_{ij} = \frac{\tilde{\mu}_{ij}}{\tilde{\sigma}_i \tilde{\phi}_j}$. The refined statistical modeling approach uses κ_{ij} as a surrogate variable for representing deviations from the product form of the variance and the assumed distributional structure. This leads to the generalized linear model

$$\begin{aligned} z_{ij} &= \mu_{ij} + \sigma_{ij}\epsilon_{ij} \;\; ; \;\; \epsilon_{ij} = Q(\eta_{ij}|\kappa_{ij}) \;\; , \;\; \eta_{ij} \sim N(0,1) \\ \mu_{ij} &= x_j'\alpha_i \;\; ; \;\; \sigma_{ij} = \sigma_i\phi_j \; ; \; \sum_{j=1}^{T} \phi_j^2 = T \end{aligned} \tag{3.2}$$

where $Q(\cdot|\kappa)$ is strictly monotone for each fixed κ-value and is assumed to be slowly varying as a function of κ. For identifiability, a scaling constraint involving Q is also required. For this with $h^2(\kappa) = var(Q(\eta|\kappa))$, we require $\sum_{ij} h^2(\kappa_{ij}) = NT$. Obviously, model (3.2) reduces to model (3.1), when the transform Q does not vary with κ. If $Q(\cdot|\kappa)$ corresponded to a scaled Gamma distribution then, based on (Mou et al. 2017), κ would increase with dose or sensitivity. And with increasing κ, Q becomes linear. Indeed model (3.2) will converge to model (3.1), with $Q \equiv 1$, as these factors increase. This is in line with the results reported by (Mou et al. 2017). Thus the structure in (3.2) gives the ability to adapt to distributions that vary from being highly skewed to ones that are substantially Gaussian. In light of this, the model gives the ability to accommodate both the skewed nature of iteratively reconstructed (ML) PET data and the Gaussian nature of analytically reconstructed (FBP) PET scans (Scheuermann et al. 2013, Mou et al. 2017). Regardless of Q, the variance structure specified in the model ensures that with particular choices for σ, ϕ and h, the specification in (3.2) accommodates the situation where variance is directly proportional to the mean - similar to what (Huesman 1977) proposed for PET ROI data. For this, let $h(\kappa)^2$ be proportional to $|\kappa|$, $\phi_j = \tilde{\phi}_j$ and choose σ_i proportional to $\tilde{\sigma}_i$. In this situation, the model in (3.2) could also be viewed within the Gaussian copula framework used by (Lennon & Yuan 2019) to model time-series of count data.

Since the temporal components of the sub-ordinate Gaussian are assumed independent with a common stationary spatial structure, the covariance of η can be written in the form of a tensor product, $\Sigma_N \otimes I_T$, where Σ_N is

a $N \times N$ matrix representing the spatial correlation pattern and I_T is an T-dimensional identity matrix. Spatial stationarity implies that the covariance can be diagonalized using the Fourier transform (Brockwell & Davis 1991), $i.e.$ $\Sigma_N = \mathcal{F}_N^t \Lambda_N \mathcal{F}_N$ where $\mathcal{F}_N$ is the matrix mapping an N-vector to its 3-D sine and cosine Fourier coefficients. The action of $\mathcal{F}_N$ is of course computed using the standard 3D fast Fourier transform (FFT). The matrix Λ_N is diagonal with elements, $\lambda = \{\lambda_i, i = 1, ..., N\}$. λ, which will need to be estimated, has elements corresponding to the discretely sampled 3-D spectral density or power spectrum of η (Brockwell & Davis 1991). While η has a stationary spatial structure, the measurement error in either (3.1) or (3.2) is neither first nor second order stationary in a spatial sense.

It is important to appreciate that even though the model specification in (3.2) has substantial flexibility, it should only be viewed as a device for obtaining reasonable inferences - here the computation of approximate variances of imaging biomarkers. The general context of modelling in science is worth keeping in mind - approximate models, such as (3.2), may not be correct to arbitrary precision but in a practical environment they are still often very useful (Box 1976). Before providing details of how the various unknowns in (3.2) are specified, we describe bootstrapping procedures for PET based on our model and also based on a non-parametric model-free approach.

3.2.2 Bootstrapping Techniques

Bootstrapping is a general statistical technique that may be used to evaluate the sampling distribution of any summary statistic, $e.g.$ a relevant biomarker, that might be of interest. In particular, the bootstrap sample can be used to obtain bias and variance characteristics of the computed summary, and also to formally access associated hypotheses that might be of interest (Efron & Tibshirani 1994). Here we consider two possibilities for creating bootstrap samples for PET data: a well-established Projection-Domain approach and a novel Image-Domain approach developed here. The Image-Domain method uses equations (3.1) and (3.2); the Projection-Domain is based on the raw count data before it has been reconstructed. It is helpful to record the steps involved in bootstrap simulation using these techniques. This is provided below. We also describe a simple recycling scheme that

would be important where it is not practical to retain a large number of bootstrap replications.

3.2.2.1 Projection-Domain Bootstrap

This approach involves random sampling (with replacement) from the number (N_e) of detected events. If events are binned into count arrays, this is equivalent to drawing a random sample from a multinomial distribution with N_e trials and probabilities proportional to the observed counts in a binned array. Each simulated count array is processed to produce a bootstrap reconstruction, z^*. Repeating the process N_B times leads to a projection-domain bootstrap sample, $\mathcal{B}_P = \{z^b, b = 1, 2, ..., N_B\}$. If raw data are binned count arrays before reconstruction, there would also be the possibility to sample bootstrap counts using an inhomogeneous Poisson process with mean values proportional to the observed array counts. While this ensures that the simulated data is fully Poisson and more variable than the multinomial, because such sampling would not correspond to *list-mode* re-sampling, we do not use it here. Note that as the count-rate increases, there will be little percentage difference between counts produced by either sampling method.

3.2.2.2 Image-Domain Bootstrap: Model-based Approach

Let $\hat{X}$, $\hat{\alpha}$, $\hat{\sigma}$, $\hat{\phi}$, $\hat{\kappa}$, $\hat{Q}$ and $\hat{\lambda}$ be the estimated values of the various unknowns in (3.2). Bootstrap simulated data, z^*_{ij}, are generated by first creating an array $\xi^* = \{\xi^*_{ij}, i = 1, ..., N, j = 1, 2.., T\}$ with elements corresponding to a random sample of size NT from a standard Gaussian distribution with mean zero and unit variance. With $\mathcal{F}_N$ representing the normalized 3-D mixed sine and cosine transform (computed by the standard 3-D FFT) and $\hat{\sigma}_{ij} = \hat{\sigma}_i\hat{\phi}_j$, the simulated data are

$$z^*_{ij} = \hat{x}'_j\hat{\alpha}_i + \hat{\sigma}_{ij}\hat{Q}(\eta^*_{ij}|\hat{\kappa}_{ij}) \quad \text{where} \quad \eta^*_{\cdot j} = \mathcal{F}^t_N(\hat{\lambda}^{1/2}\xi^*_{\cdot j}) \tag{3.3}$$

where $\xi^*_{\cdot j}$ and $\eta^*_{\cdot j}$ are the j'th columns of the $N \times T$-dimensional arrays corresponding to ξ^* and η^*. Repeating the process N_B times gives an image-domain bootstrap sample, $\mathcal{B}_I = \{z^b, b = 1, 2, ..., N_B\}$ where z^b is the b'th realization of z^* in equation (3.3).

3.2.2.3 Approximate Image-Domain Bootstrap by Recycling

In practical clinical settings, data retention protocols can mean that raw list-mode data are not routinely archived especially for dynamic studies. In such environments, it is also unlikely that there would be a willingness to retain extensive bootstrap datasets. Hence a simplified alternative to the full image-domain bootstrap is of interest. The proposal here is to retain a set of fitted model α-coefficients for a small number of image-domain bootstrap samples ($N_B^* \ll N_B$) and to base further bootstrap inferences on that dataset - $\mathcal{B}_I^* = \{\alpha^b, b = 1, 2, ..., N_B^*\}$. To justify this, it is important that the coefficients retained are sufficient for the proposed inferences and also that the size of N_B^* is adequate. Under either of the models in (3.1,3.2), any target parameter, θ, associated with the measurable tracer concentration signal ($\mu_{i\cdot} \approx x'\alpha_i$) is readily expressed in terms of the associated model coefficient - $i.e.$ $\theta_i = f(\mu_{i\cdot}) = f(x'\alpha_i) \equiv g(\alpha_i)$. Recall that a basic property of maximum likelihood is that if $\hat{\alpha}_i$ is an optimal estimator of α_i then $\hat{\theta}_i = g(\hat{\alpha}_i)$ is optimal for θ_i, $c.f.$ (Rao 1973). Thus if the errors in (3.1) are Gaussian and a corresponding weighted least squares procedure is used for the estimation of coefficients, the α-coefficient data can be expected to be sufficient in a statistical sense.

We propose a novel *recycling* procedure to help enhance the value of the retained limited data $\mathcal{B}_I^*$. In the approach samples are generated by sampling from $\mathcal{B}_I^*$ a set of say $\tilde{N}_B$ values at each voxel and then, by application of a spatial filtering process, create a recycled bootstrap dataset $\tilde{\mathcal{B}}_I^* = \{\tilde{z}^b, b = 1, 2, ..., \tilde{N}_B\}$ where $\tilde{z}_{ij}^b = x_j'\tilde{\alpha}_i^b$. Importantly, the recycled $\tilde{\mathcal{B}}_I^*$ data is only created at the time that inferences are being considered – so there is no need to retain extensive bootstrap samples. This recycling scheme can be motivated by the fact that the sampling distribution of α-coefficient estimates is approximately Gaussian. Note that since the error terms in (3.1) are independent, Gaussian approximation of the natural weighted least squares estimates of coefficients follows by application of a multivariate version of Lineberg's central limit theorem - see in Theorem 1 (Bardet et al. 2008). The approximation implies a common Gaussian distribution for the deviations $D_i = (\hat{\alpha}_i - \alpha_i)/\sigma_i = [X'WX]^{-1}X'W^{-1/2}\epsilon_{i\cdot}$ where W is the diagonal matrix with elements $w_j \propto \phi_i^{-2}$ for $j = 1, 2, ..., T$. Under model (3.1), D_i is mean zero with covariance $var(D_i) = \Sigma_K = [X'WX]^{-1}$.

D_i is a spatially invariant transformation of the error process and also of the underlying sub-ordinate Gaussian process η. Thus for (3.1) the $N \times K$ array, D, with rows D_i's, is strictly stationary in a spatial sense. Now if the error in (3.1) is exactly Gaussian the covariance of D has the tensor-product form $\Sigma_N \otimes \Sigma_K$, where Σ_N is the spatial covariance of η. Thus simulated realizations of D can be produced by creating a $N \times K$ array whose rows are independent samples from a K-dimensional Gaussian with zero mean vector and covariance Σ_K and then transforming the columns of the array by multiplication by the matrix $\mathcal{F}_N^t \hat{\Lambda}_N^{1/2}$ as in (3.3). So when Gaussian approximation of $\hat{\alpha}$-coefficients is reasonable, bootstrap samples can be produced by

$$\tilde{\alpha}_i^b = \hat{\alpha}_i + \hat{\sigma}_i \tilde{D}_i^b \; ; \quad i = 1, 2, ..., N \; , \; b = 1, 2, ..., \tilde{N}_B \tag{3.4}$$

where $\tilde{D}^b$ is obtained by first sampling, independently for each row, from the distribution of $(\hat{\alpha}_i - \alpha_i)/\sigma_i$ and then filtering, column-by-column, the resulting $N \times K$ dimensional array using $\mathcal{F}_N^t \hat{\Lambda}_N^{1/2}$. Recycling follows this process but uses the empirical distribution of the bootstrap dataset $\mathcal{D}_i^* = \{(\alpha_i^b - \hat{\alpha}_i)/\hat{\sigma}_i, b = 1, 2, ..., N_B^*\}$ for the sampling from the i'th row. An obvious modification of this would be to use the full set of $\mathcal{D}_i^*$'s, $\mathcal{D} = \{(\alpha_i^b - \hat{\alpha}_i)/\hat{\sigma}_i, b = 1, 2, ..., N_B^*, i = 1, 2..., N\}$, for row-wise simulation. This approach would rely more heavily on the accuracy of the Gaussian approximation for its justification.

3.2.3 Specification of Unknowns in the Image-Domain Model

As indicated earlier, the model in (3.2) has a number of unknowns all of which need to be defined before image-domain bootstrapping is possible. We begin by describing how the basis set, X, is specified and after that consider the other elements.

The goal in basis selection is to choose a configuration that is physiologically interpretable and has the ability to approximate the measured time-course data at all voxels in the volume. A clustering scheme is used to identify clusters of time-courses that have self-similar shapes. If a basis can be found to represent the average time-course in such clusters, then it can be expected that a simple scaling of the representation for the average will fit individual time-course data in the cluster. In light of this, the basis selection is opti-

mized so that the set of cluster means are well represented. But because the number of clusters is quite small (typically on the order of 100-200) relative to the number of voxels, evaluation of the objective function for assessment of any candidate basis set based on the reduced cluster-mean data is computationally efficient. A generalized cross-validation criterion is used as an objective function for basis set assessment. Backward elimination, a well-established type of greedy algorithm in statistical model selection (Friedman et al. 2001), is used for the optimization of the basis. In general the initial basis is taken to be the cluster means. However, in the case that the time-course information is well-sampled in time, a physiologically-based modeling process is used so that instead of raw cluster means being used as the initial basis, a set of model-based predictions of the cluster mean time-courses are used. As some clusters may contain a relatively small number of voxels and as a result may be noisy, the modeling step acts as a well-grounded noise suppression scheme. Modeling also enhances the physiologic interpretability of the final set of basis elements selected.

Detailed implementation of the above basis selection scheme substantially follows (O'Sullivan 1993, O'Sullivan et al. 2014). The process is implemented in two steps. The first step applies recursive hierarchical clustering to partition the data into a large set of clusters, $\{C_l, l = 1, 2, ...L\}$, with the property that the data in each cluster has a similar shape pattern: $i.e.$ if $i \in C_l$ then for a suitable constant a_i, $z_{ij} \approx a_i \mu_{jl}$ where $\tilde{\mu}_{jl} = \frac{1}{|C_l|} \sum_{i \in C_l} z_{ij}$ for $j = 1, 2, ..., T$ is the mean time-course for the l'th cluster. Step 2 takes the collection of mean time-course patterns associated with each of these clusters as an initial set of basis elements $X_L = \{\tilde{\mu}_1, ..., \tilde{\mu}_L\}$ and applies a cross-validation guided backwards elimination procedure to construct a final subset $X_K = \{\mu_1, ..., \mu_K\} \equiv \hat{X}$ with the property that voxel-level data can be adequately represented by a non-negative linear combination of the columns of $\hat{X}$. In the case that well-sampled time-course of PET-measured data is acquired and we have access to the time-course of the tracer in the arterial blood, the second step is modified by replacing each of the cluster mean time-courses by a modeled time-course. A non-parametric residue modeling process is used for that. This is reviewed in Section 3.3.1 below. Modeling helps to ensure that the final set of basis vectors satisfies physiological constraints linked to the basic principles of blood-tissue exchange

(Meier & Zierler 1954).

Specification of the Unknowns, apart from X

With X fixed, an unconstrained weighted least squares procedure, with a simple fixed temporal weighting scheme, is used for the estimation of α_i's in (3.1). The simple weighting scheme and associated ϕ-values are

$$w_j^0 = e^{-t_j\zeta} dt_j / \bar{\mu}_j^* \quad , \quad \phi_j^0 \propto 1/\sqrt{w_j^0} \quad \text{for} \quad j = 1, 2, .., T \tag{3.5}$$

Here $\bar{\mu}_j^* = \max(\bar{\mu}_j, m)$ where $\bar{\mu}_j$ is average of the reconstructed concentration values over the j'th time-frame and m is taken to be a fraction (0.1) of the maximum of these $\bar{\mu}_j$ values. The duration of the scan time-frame is dt_j and $e^{-t_j\zeta}$, with ζ the decay constant for the radio-tracer isotope, is the standard tracer decay factor. While the estimates of α_i based on these simple weights may not be optimal, under general conditions weighted least squares estimates are unbiased and also consistent, as the scale of the error diminishes (Seber 2015). In addition the Gauss-Markov theorem tells us that if weighting is inversely proportional to the variance of the measurement error, least squares will have minimum variance among all unbiased estimators (Seber 2015). In practice, unless there is a substantial discrepancy between optimal weights and simplistic weights, the latter will typically be highly efficient – see (Romano & Wolf 2017). In the bootstrapping setting the unbiasedness property of weighted least squares is important as it ensures that the data simulation process is also unbiased. The use of weighted least squares is also helpful in simply justifying the Gaussian approximation underlying the proposed bootstrap recycling procedure.

Residuals from the least squares fit are used to estimate the other unknowns in (3.2). The motivation for this comes from

$$\begin{aligned} r_{ij} &\equiv z_{ij} - x_j'\hat{\alpha}_i \approx z_{ij} - x_j'\alpha_i = \sigma_{ij}\epsilon_{ij} \equiv \sigma_i\phi_j\epsilon_{ij} \\ \text{so } r_{ij} &\approx \sigma_i\phi_j h_{ij} e_{ij} \quad \text{with} \quad h_{ij}^2 = Var(\epsilon_{ij}) \end{aligned} \tag{3.6}$$

and $e_{ij} = \epsilon_{ij}/h_{ij}$ has mean zero and unit variance. From (3.6), natural

conditional estimates of ϕ and σ are

$$\hat{\phi}_j^2 = \frac{1}{N}\sum_{i=1}^{N} w_{ij}(\sigma, h) r_{ij}^2 \quad \text{and} \quad \hat{\sigma}_i^2 = \frac{1}{T}\sum_{j=1}^{T} w_{ij}(\phi, h) r_{ij}^2 \tag{3.7}$$

where $w_{ij}(\sigma, h) = \sigma_i^{-2} h_{ij}^{-2}$ and $w_{ij}(\phi, h) = \phi_j^{-2} h_{ij}^{-2}$. $\hat{\phi}_j^2$ values are scaled so that $\sum_j \hat{\phi}_j^2 = T$. For any specified h, (3.7) can be iterated, starting with σ constant, to obtain converged values $\tilde{\phi}(h)$ and $\tilde{\sigma}(h)$. These are maximum likelihood estimates when e_{ij} is standard Gaussian. With $h_{ij} = 1$, the converged values in (3.7), denoted $\tilde{\phi}$ and $\tilde{\sigma}$, are used as estimates of ϕ and σ in model (3.1). This is important for specification of κ. The set of $\hat{\kappa}$-values are defined by $\hat{\kappa}_{ij} = \frac{\hat{z}_{ij}}{\tilde{\sigma}_i \tilde{\phi}_j}$ where $\hat{z}_{ij} = x_j' \hat{\alpha}_i$.

For estimation of Q, we restrict to piecewise constant approximation as a function of the κ variable. With $\kappa_{(0)} = -\infty$ and $\kappa_{(l)}$ the $\frac{l}{L} \times 100\%$'th percentile of the $\hat{\kappa}_{ij}$ values, let I_l be the interval $(\kappa_{(l-1)}, \kappa_{(l)}]$, for $l = 1, 2, ..., L$. Piecewise constant approximation means $Q(\cdot|\hat{\kappa}) = \hat{Q}(\cdot|l)$ for $\hat{\kappa} \in I_l$. Our experience is that Q is a smooth function of $\hat{\kappa}$ so that a modest value for L (in the 50 to 100 range) seems to be quite adequate. As Q is piecewise constant, its variance is also piecewise constant - $Var(Q(\eta|\hat{\kappa})) = h(\hat{\kappa})^2 = h_l^2$ for $\hat{\kappa} \in I_l$. This implies $h_{ij} = h_l$ for $\hat{\kappa}_{ij} \in I_l$. Similar to (3.7), a conditional estimate of h_l given σ and ϕ is

$$\hat{h}_l^2 = \frac{1}{|I_l|}\sum_{\hat{\kappa}_{ij} \in I_l} w_{ij}(\sigma, \phi) r_{ij}^2 \quad \text{with} \quad w_{ij}(\sigma, \phi) = \sigma_i^{-2}\phi_j^{-2} \tag{3.8}$$

normalized so that $\sum_l \hat{h}_l^2 = L$. Combining (3.7) and (3.8), provides an iteration for joint estimation of σ, ϕ and h. This defines $\hat{\sigma}$ and $\hat{\phi}$. The converged $\hat{\sigma}$ values are inflated by multiplication by $\frac{T}{T-K}$ where K is the number of columns of X. This is to ensure there is adjustment for the bias arising from fitting the α-coefficients at each voxel. Such adjustments are standard in most parametric model fitting settings - see (Kutner et al. 2013, Seber 2015) for its use in linear regression.

The converged values of $\hat{\sigma}$ and $\hat{\phi}$ are used to compute scaled residuals $\hat{\epsilon}_{ij} = r_{ij}/\hat{\sigma}_i\hat{\phi}_j$. The empirical distribution of these scaled residuals, $E_l = \{\hat{\epsilon}_{ij} \ ; \ \hat{\kappa}_{ij} \in I_l\}$, is used to evaluate $\hat{Q}(\cdot|l)$. Here we match order statistics of E_l to the corresponding quantiles of a standard normal distribution -

$\mathcal{N}_l = \{\hat{\eta}_{ij} \; ; \; \hat{\kappa}_{ij} \in I_l\}$. This is simply the standard normal quantile-quantile plot procedure – $c.f.$ (R Core Team 2021). The inverse map allows arbitrary quantiles of the standard normal to be mapped to quantiles of E_l.

For estimation of λ, the full set of normalized residuals, $\hat{\eta}$, are mapped to the imaging domain and using the 3-D FFT their 3-D periodogram is evaluated for each time-frame. Averaging these periodograms over time-frames, with weights $\hat{\phi}_j^{-2}$, produces the final estimate of the required power spectrum, $\hat{\lambda}$. Using the Weiner-Khinchine theorem (Brockwell & Davis 1991), the inverse 3-D FFT of the power spectrum provides the corresponding of the 3-D spatial auto-correlation function $\hat{\rho}$. This completes the specification of all unknowns in the image-domain bootstrapping model. Before investigating the reliability of the bootstrapping method, we first present some illustrations of the technique with real data. Model diagnostics are an essential part of any statistical modeling process, particularly if model-based bootstrapping is of interest. This aspect is highlighted in the illustrative examples.

3.3 Applications to Parametric Imaging

We present two dynamic PET imaging studies of cancer patients. One is from a series reported in (Spence et al. 1998) and involves brain tumor scanning with ^{18}F-labeled Fluorodeoxyglucose (FDG); the second comes from a more recent breast cancer imaging trial with ^{18}F-labeled Fluorothymidine (FLT) (Kostakoglu et al. 2015). The studies are chosen in part because they represent data with different imaging challenges. The brain FDG study is from an early generation PET scanner using direct FBP reconstruction. The scanner in the FLT study is more recent and uses an ML reconstruction technique. Raw projection data are not available for either study. Thus only image-domain bootstrapping is practical. In each case the bootstrap generated dataset, $\mathcal{B}_I$, is processed to map metabolic parameters and their associated standard errors. Before presenting the examples, we provide some background on the approach used for mapping voxel-level kinetic parameters. This material draws on (O'Sullivan 1993, O'Sullivan et al. 2014).

3.3.1 Non-Parametric Residue Mapping (NPRM) of Kinetics

The basic principle of most tracer imaging studies with PET is that the tracer's interaction with the local tissue is linear and time-invariant. While there are situations where this assumption is not valid, it is very reasonable for FDG and FLT. The arterial supply is the primary system for transport of tracer to tissue, so linearity and time-invariance implies that the true tissue concentration, $C(x,t)$, can be described by a convolution between the local arterial blood concentration supplied by the output of the left-ventricle (LV) of the heart, C_p, and the corresponding impulse-response, or so-called tissue residue function R. Thus

$$C(x,t) = \int_0^t R(x,t-s)C_p(x,s)ds \tag{3.9}$$

Typically arterial dispersion effects are below the resolution of the PET scanner and the arterial concentration can be well-described by a suitable shift of the LV signal – $C_p(x,s) = C_p(s-\Delta_x)$ where $C_p(t)$ is the LV blood concentration and Δ_x is a suitable delay. From basic principles of blood-tissue exchange (Meier & Zierler 1954), the residue is a monotone-decreasing non-negative function - a life-table for the travel-times of tracer atoms introduced to tissue at time zero (O'Sullivan et al. 2009). While most tissue in a typical volume of interest behaves in the above manner, some exceptions may need to be kept in mind. For example, there may areas between the (venous) injection site and the corresponding pathway to the LV where the arterial pattern is irrelevant. Similarly, if the bladder is in the field of view, its time-course will not follow the pattern in (3.9). It is appropriate to describe it in terms of the outflow for a whole-body blood-tissue exchange process (Meier & Zierler 1954).

There is a substantial literature on modeling techniques for PET time-course data. Most of this focuses on the analysis of region of interest data; see, for example, (Huang et al. 1986, Vicini & Bassingthwaighte 2014, Mankoff et al. 2006). But there are also a number of techniques for voxel-level analysis. Spectral techniques use a positive linear combination of exponentials to approximate the voxel-level residue (Cunningham & Jones 1993, Veronese et al. 2016, Wang et al. 2020). The NPRM approach models

voxel-level time-course data by a positive linear combination of basis vectors, $\{\mu_k, k = 1, ..., K\}$ – referred to a sub-TACs (TAC stands for time-activity curve). This is a version of the form used in equations (3.1,3.2) in which the α-coefficients are constrained to be non-negative. In the NPRM setting, the backwards elimination scheme in Section 3.2.3 is modified by replacing the initial cluster-mean vectors in X_L by elements based on non-parametric residue modeling of the cluster mean data – $i.e.$ $\tilde{\mu}_l$ is replaced by the approximation $\mu_l(t) = \int_0^t R_l(t-s)C_p(s-\Delta_l)ds$. In addition, the basis in NPRM is required to always include components corresponding to the time-courses for the arterial input function (AIF) and its cumulative integral. The latter is referred to as the Patlak basis element because an analysis that only used that term would be substantially equivalent to the Patlak approach to evaluation of tracer flux (Patlak & Blasberg 1985).

As the basis elements are represented in terms of residue functions, $\mu_k(t) = \int_0^t R_k(t-s)C_p(s-\Delta_k)ds$, the linear model representation of the PET data leads to the approximation of the voxel-level residue as a linear combination of the basis residues $\{R_k, k = 1, ..., K\}$, $i.e.$

$$z_{ij} \approx \sum_{k=1}^{K} \alpha_{ik}\mu_k(t_j) \quad \rightarrow \quad R(x_i, t) \approx \sum_k \alpha_{ik}R_k(t) \tag{3.10}$$

Here a very short duration (less than 5 seconds) spiked residue is used to represent the AIF and a constant residue is used for the Patlak term.

In the NPRM approach, decomposition of the voxel-level residue is used to create summaries variables for mapping tracer kinetics. Suppose T_E is the study duration and let T_B for $0 < T_B < T_E$ represent a realistic upper-bound for large-vessel travel-time – for human PET studies with FLT and FDG, a value T_B of around 5 to 10 seconds is reasonable physiologically. The residue over the observed time-frame of the study, $[0, T_E]$, is decomposed in terms of vascular (R_b), in-distribution (R_d) and extraction (R_e) components as

$$R(t, x) = R_b(t, x) + R_d(t, x) + R_e(t, x) \tag{3.11}$$

where

$$\begin{aligned} R_e(t,x) &= R(T_E,x) \equiv K_i(x) \\ R_b(t,x) &= \begin{cases} R(t,x) - R(T_B,x) & ,0 \le t \le T_B \\ 0 & ,\text{elsewhere} \end{cases} \\ R_d(t,x) &= R(t,x) - R_b(t,x) - R_e(t,x) \end{aligned}$$

The apparent rate of extraction of tracer atoms by the tissue is measured by $K_i(x)$. This is a measure of flux (see further discussion below). Given the residue decomposition, the vascular (large vessel) blood volume, $V_b(x)$, as well as the in-distribution flow, $K_d(x)$, and volume, $V_d(x)$, are recovered from R_b and R_d as

$$\begin{aligned} V_b(x) &= \int_0^{T_B} R_b(t,x)dt \\ K_d(x) &= R_d(0) \quad ; \quad V_d(x) = \int_0^{T_E} R_d(t,x)dt \end{aligned} \tag{3.12}$$

By the central volume theorem (Meier & Zierler 1954), the mean transit time (MTT) is defined as the ratio volume to flow – $V_d(x)/K_d(x)$. However this does not take account of variation in the time of arrival of the tracer to the local tissue. To address this we use a flow-weighted average of mean transit-times associated individual sub-TACs – $i.e.$ $\text{MTT}(x_i) = \sum_k w_{ik}\text{MTT}_k$ where $\text{MTT}_k = \Delta_k + V_{Dk}/K_{Dk}$ with K_{Dk} and V_{Dk} obtained from k'th component residue (R_k). Here the weights, which are normalized to sum to unity, are proportional to the flow contributions from the different component tissues represented at the i'th voxel, $i.e$ $w_{ik} \propto \alpha_{ik}K_{Dk}$ for $k = 1, 2, ...K$. Thus MTT is written as

$$\begin{aligned} \text{MTT}(x_i) &= \Delta_w(x_i) + V_D(x_i)/K_D(x_i) \\ &= \Delta_w(x_i) + \frac{\sum_{k=1}^K \alpha_{ik}V_{Dk}}{\sum_{k=1}^K \alpha_{ik}K_{Dk}} \end{aligned} \tag{3.13}$$

$\Delta_w(x_i) = \sum_k w_{ik}\Delta_k$. In the case that the individual delays are all the same, $\Delta_w(x_i)$ will constant across voxels.

While a non-parametric approach is used for specification of sub-TAC residues, it is useful to record what the above summary parameters correspond to in the 2-compartmental model of Huang and Sokoloff, see (Huang et al. 1986).

This model is very widely used in PET data analysis. In this model there are four kinetic constants - (k_1, k_2, k_3, k_4). The impulse response function ($a.k.a$ tissue residue) for the model is a mixture of exponentials

$$I_C(t) = k_1(1-\pi)e^{-t\lambda_1} + k_1\pi e^{-t\lambda_2} \tag{3.14}$$

where $\lambda_{1(2)} = \frac{1}{2}(k_2 + k_3 + k_4 \pm \sqrt{(k_2+k_3+k_4)^2 - 4k_2k_4})$ and $\pi = \frac{k_3+k_4-\lambda_2}{\lambda_1-\lambda_2}$. When the model is applied to PET time-course data, there is typically an adjustment for the fractional blood volume (f_b), which gives rise to a model representation of the tissue time-course (C_T) as

$$C_T(t) \approx f_b C_p(t) + (1-f_b)\int_0^t I_C(t-s)C_p(s)ds \tag{3.15}$$

Suppose we introduce a simple linear residue R_o defined over the interval $[0, T_B]$ by

$$R_o(t) = \begin{cases} 2\frac{f_b}{T_B}(\frac{T_B-t}{T_B}) & , \ 0 \le t \le T_B \\ 0 & , \text{ elsewhere} \end{cases}$$

Note $\int_0^{T_B} R_o(t)dt = f_b$. As $T_B \to 0$, R_o becomes very spiked at 0. For small T_B and the convolution of R_o with the AIF is approximately $f_b C_p(t)$. As a result, for sufficiently small T_B, the 2-compartmental model can be given a residue representation

$$\begin{aligned} C_T(t) &\approx f_b C_p(t) + (1-f_b)\int_0^t I_C(t-s)C_p(s)ds \\ &= \int_0^T R_C(t-s)C_p(s)ds \end{aligned} \tag{3.16}$$

with $R_C(t) = R_o(t) + (1-f_b)I_C(t)$. Decomposing R_C as described in equation (3.11) and evaluating the residue summary measures gives

$$\begin{aligned} K_i &= K_1(1-\pi)e^{-\lambda_1 T_E} + K_1\pi + O(\lambda_2) \\ V_b &= f_b + O(T_B) \\ K_d &= K_1 - K_i + O(T_B) \\ V_d &= \frac{K_1(1-\pi)(1-e^{-\lambda_1 T_E})}{\lambda_1} + O(\lambda_2) + O(T_B) \end{aligned} \tag{3.17}$$

where $K_1 = (1-f_b)k_1$ and $O(x)$ indicates that corresponding terms vanish as $x \to 0$. If $k_4 = 0$ then $\lambda_2 = 0$. Here as $T_B \to 0$ with T_E large (so $e^{-\lambda_1 T_E}$ is

negligible) the residue summaries for the 2-C model become

$$\begin{aligned} K_i &= K_1\pi = \frac{K_1k_3}{k_2+k_3} \\ V_b &= f_b \\ K_d &= K_1(1-\pi) = \frac{K_1k_2}{k_2+k_3} \\ V_d &= \frac{K_1}{k_2+k_3}(1-\pi) = \frac{K_1k_2}{(k_2+k_3)^2} \end{aligned} \tag{3.18}$$

When both k_3 and k_4 are zero, the 2-compartment model reduces to the 1-compartment Kety-Schmidt model (Kety & Schmidt 1945). Here the parameters become: $K_i = 0$ (no retention), $V_b = f_b$, $K_d = K_1$ and $V_d = \frac{K_1}{k_2}$. The latter two quantities are the familiar flow and distribution volume terms associated with the Kety-Schmidt approach to the quantitation of PET studies with ^{15}O-labeled water.

In the two applications, the basis functions used for the generation of bootstrap data are the same as those used for NPRM kinetic analysis of the original image data (z). Individual bootstrap realizations ($z^b \in \mathcal{B}_I$) are processed in the same way as the original data using the NPRM procedure. If an alternative kinetic or other analysis method was of interest, it would be applied to the original data and to the realizations in $\mathcal{B}_I$. In this way the bootstrapping technique could also be used to generate assessments of uncertainties for alternative approaches to mapping kinetics, $e.g.$ such as those reviewed in (Wang et al. 2020).

3.3.2 FDG Brain tumor Study

PET studies with FDG play a major role in the diagnosis and management of many cancers (Barrio et al. 2020*a*). (Spence et al. 1998) reported on a series of NIH-supported studies, conducted at the University of Washington (Seattle), evaluating the ability to measure the metabolic rate of glucose consumption in glioma patients, post-surgery. We use data from one of these cases. Details of the study protocol, which also included direct arterial blood sampling, are provided in (Spence et al. 1998). Briefly, imaging was conducted a 35-plane scanner using a 2-D acquisition plane-by-plane process and a direct (FBP) reconstruction methodology. The 4-D PET data is

an array with $N = 128 \times 128 \times 35$ voxels ($2.25 \times 2.25 \times 4.25mm^3$) and $T = 31$ time-frames extending over a 90-minute period. The time-frame sequence is: 1(1 min) pre-injection, 4(20 sec), 4(40 sec), 4(1 min), 4(3 min) and 8(5 min). Main bootstrapping technique to evaluate sampling variation in computed metabolic images.

Results of analysis are presented in Figure 3.1 and Figure 3.2 & 3.3. NPRM metabolic images and associated bootstrap estimates of voxel-level standard errors are in Figure 3.1. Note that while the full data set is analyzed to produce a full volume of metabolic information, Figure 3.1 only shows a single transverse slice in which the tumor is most apparent. The results demonstrate a pattern of altered FDG kinetics, particularly in FDG-based glucose flux (K_i) and extraction (K_i/K_1), in the tumor region. Standard errors demonstrate that variability is very much related to the scale of the metabolic variable. This pattern is likely a consequence of the overall pseudo-Poisson characteristic of PET data, so areas with high metabolic values (high flow, volume, etc.) also have greater absolute variance. We examine this more formally in Section 3.4.2. The typical percent error, measured by the standard deviation relative to the metabolic parameter value, is on the order of 10-20% for most metabolic variables, even for the nonlinear MTT and extraction (K_i/K_1) values. As described in (Spence et al. 1998), volumes of interest (VOIs) for tumor and normal grey matter were identified using co-registered MRI scans. For the present case, the tumor VOI consists of 759 voxels of which 133 are on the slice shown in Figure 3.1; the normal VOI has 1979 voxels but none of these are on the slice shown in Figure 3.1. Histograms of the bootstrap-estimated sampling distributions for the 95'th percentile of the metabolic parameters in the VOIs are shown in Figure 3.1. These histograms demonstrate the ability of the bootstrap analysis to support inferences for comparisons between complex imaging biomarkers (here the 95'th percentile statistic) for VOIs. The differences between tumor and normal grey matter VOIs are quite dramatic for flux, MTT and extraction. By standard bootstrap analysis (Efron & Tibshirani 1994) these differences are readily confirmed to be highly significant in statistical terms.

Residual diagnostics associated with the image-domain bootstrap are shown in Figure 3.2 & 3.3. A set of seven vectors is identified by the basis selec-

tion procedure. As described in 3.3.1, in the NPRM setting, two of these basis elements are constrained to correspond to the time-courses for the arterial input function (AIF) and its cumulative integral (Patlak element). The cluster mean data defining each of the five other basis vectors and their corresponding non-parametric residue model fits are shown in Figure 3.2(i) & 3.3(i). The fitted residues for these basis elements are in Figure 3.2(ii) & 3.3(ii). The fitted time-courses as used in the image domain model - see (3.2). Temporal boxplots of the fully standardized residuals, $(z_{ij} - \hat{\mu}_{ij})/\hat{\sigma}_{ij}$, are shown in Figure 3.2(iii) & 3.3(iii). These boxplots are highly symmetric. Estimates of optimized and initial temporal scaling factors, $\hat{\phi}_j$ and ϕ_j^0 (see section 3.2.3) are also displayed. Apart from the initial 3-4 time-frames we see that these are remarkably similar to each other. Boxplots of residuals scaled by temporal ($\hat{\phi}_j$) and spatial ($\hat{\sigma}_i$) factors and binned by values of $\hat{\kappa}$ ($= \hat{z}_{ij}/\tilde{\sigma}_i\tilde{\phi}_j$) are in Figure 3.2(iv) & 3.3(iv). These boxplots show little or no variation for different κ-bins. In particular, there is little indication of variation in the scale of these boxplots. This is confirmed by the estimate of h is practically constant. The distributions of the standardized residuals are shown in Figure 3.2(v) & 3.3(v). The overall distribution is substantially Gaussian in appearance. Perhaps the proportion of more extreme values is somewhat less than what one would expect for the Gaussian - this is apparent from the quantile plots. The substantially Gaussian structure agrees with results reported in (Mou et al. 2017) for PET data reconstructed by FBP techniques. Sample transverse and axial auto-correlations of the sub-ordinate residual process ($\hat{\eta}$) as a function of spatial distance are shown in Figure 3.2(vi) & 3.3(vi). This is evaluated by inversion of the 3-D periodogram, $i.e.$ via the Wiener–Khintchine theorem (Brockwell & Davis 1991). The axial pattern shows little plane-to-plane auto-correlation. This is consistent with the 2D nature of data acquisition. The transverse pattern shows longer range dependence in the long-axis of brain cross-section – perpendicular to the scanning bed. This is fully consistent with results from elliptical phantom simulations reported in the literature (Huang et al. 2020, Razifar et al. 2005).

3.3.3 FLT Breast tumor Study

Cellular DNA is replicated during cell division so that its concentration in rapidly proliferating tumor tissues can be expected to be higher than in normal tissue. PET FLT imaging has the potential to provide an approximate measure of DNA concentration and for this reason FLT imaging may be helpful for diagnosis and treatment planning with certain cancers. Our data is from a multi-center American College of Radiology Imaging Network clinical imaging trial (ACRIN 6688) which conducted dynamic PET-FLT imaging of breast tumors before and during neo-adjuvant chemotherapy. The goal was to see if PET-FLT imaging could give an early indication of the tumor response – trial results are reported in (Kostakoglu et al. 2015). The ACRIN data are part of an anonymized cancer imaging archive developed and maintained by the National Cancer Institute (https://www.cancerimagingarchive.net). The data considered here are from a patient studied at baseline (before chemotherapy). The study was conducted on a 74-plane scanner using a 3-D acquisition process and ML reconstruction. The 4-D PET data set consists of an imaging volume with $N = 168 \times 168 \times 74$ voxels ($2.97 \times 2.97 \times 2.01 mm^3$) and $T = 45$ time-frames of acquisition over one hour. The time-frame binning sequence was: 16(5 sec), 7(10 sec), 5(30 sec), 5(1 min), 5(3 min) and 7(5 min). Note that more than half of the temporal sampling is focused on the first 2.5 minutes of the 1-hour acquisition. This is in part because the kinetics of FLT (a small molecule) are faster than those of FDG. The left-ventricle of the heart was used to directly recover a blood time-course, which after approximate adjustment for metabolites provided an arterial input function, C_p, used for kinetic analysis.

Data were processed using the same methods as used for the brain study. $N_B = 500$ image-domain bootstrap replicates were used for the evaluation of sampling variation in computed metabolic images. Metabolic images and associated bootstrap estimates of their voxel-level standard errors are in Figure 3.1. Metabolic images shown are for a transverse slice through the tumor region (indicated by an arrow on the flux image). Volume of distribution(V_d), flow(K_d) and flux (K_i) show significant enhancement in the tumor region. In a compartmental modeling framework, all three parameters have been suggested as appropriate ways to quantify FLT time-

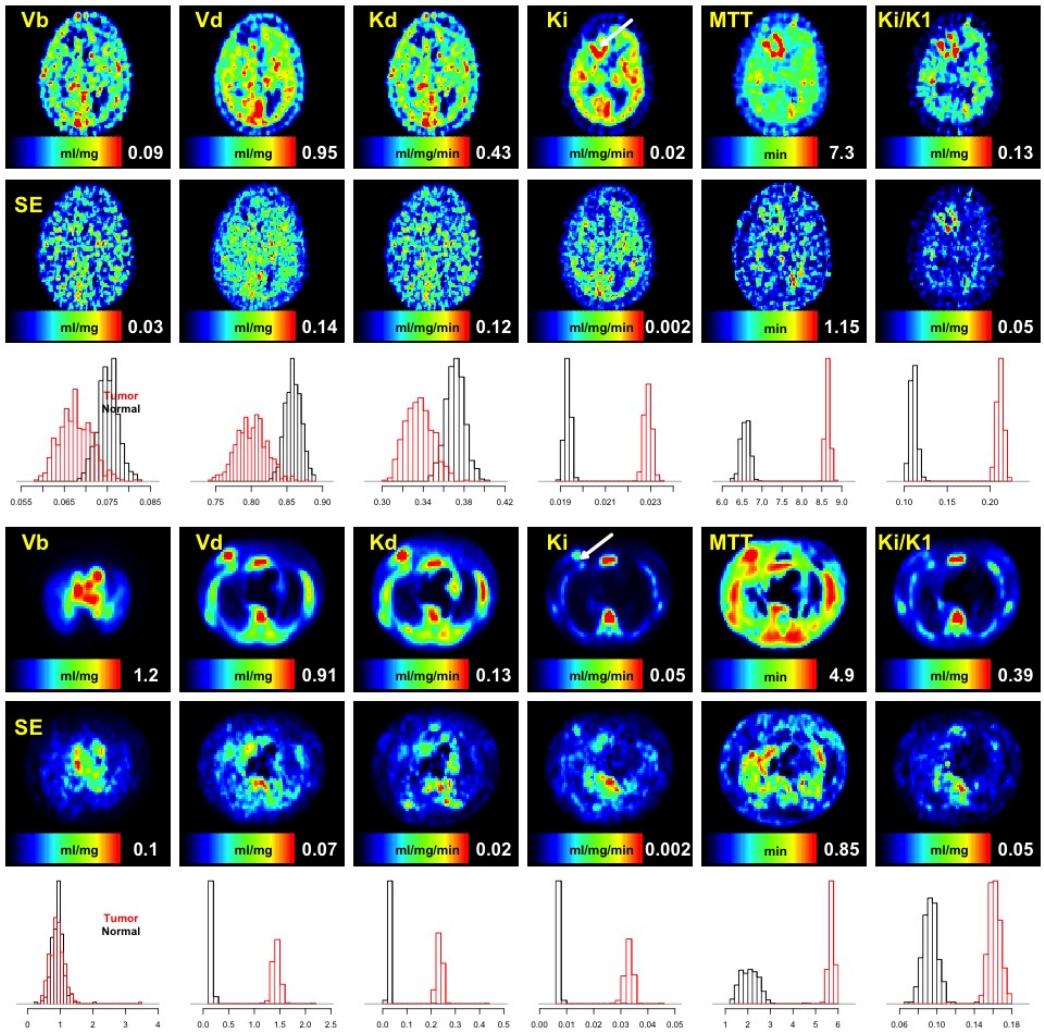


Figure 3.1: Metabolic Images with image-domain bootstrap assessment of standard errors: Rows 1-3 show the Brain tumor FDG data; 4-6 for the Breast tumor FLT data. The mapped parameters are shown on rows 1&4 – the location of tumor volume of interest (VOI) on the slice is indicated with an arrow. Columns correspond to different metabolic parameters (labeled in yellow) with color bars indicating units - see section 3.3.1 for definitions. Computed standard errors (SE) are on rows 2&5. Rows 3&6 show histograms of the bootstrap sampling distributions of the 95'th percentile of the metabolic parameter in the normal [black] and tumor [red] VOIs.

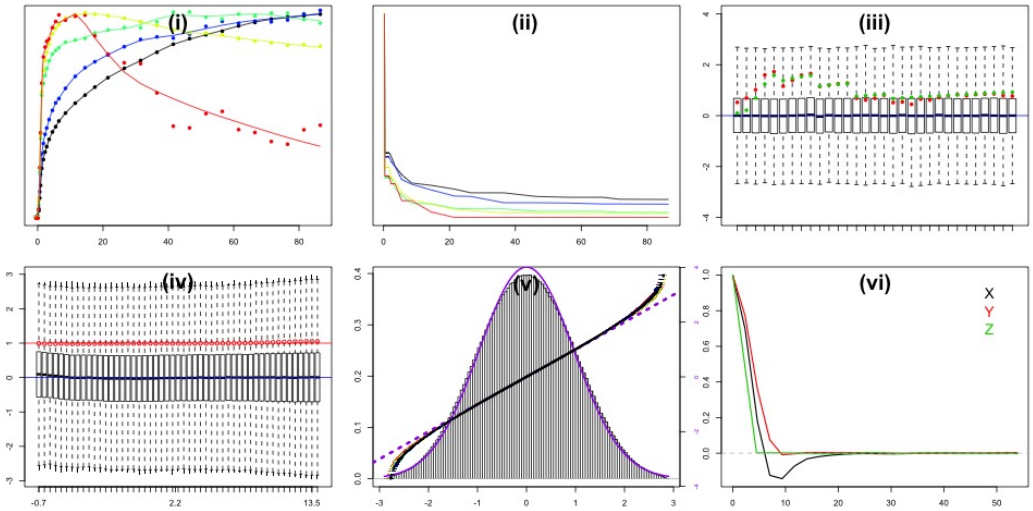


Figure 3.2: Diagnostics associated with the Image-Domain Bootstrapping Model (3.2) using the FDG-Brain data. Six plots, labeled (i) to (vi), are shown for each dataset: (i) raw sub-TACs (dots) and fitted models (lines) for the selected basis set - columns of X. (ii) Non-parametric residues corresponding to the fitted model - c.f. (3.10). (iii) Boxplots by time-frame of standardized residuals from the unconstrained least squares fit, $r_{ij}/\hat{\sigma}_i\hat{\phi}_j\hat{h}_{ij}$. The simple, $\hat{\phi}_j^0$ in (3.5), and optimized, $\hat{\phi}_j$, standard deviations are shown as green and red dots. (iv) Boxplots of scaled residuals, $\hat{\epsilon}_{ij} = r_{ij}/\hat{\sigma}_i\hat{\phi}_j$, for each κ-bin (each containing roughly 10000 data points). $\hat{h}_l$-values are shown as red points; the red line is for comparison with unity (zero skewness of bin data). (v) Histogram of the overall distribution of the standardized residuals and its relation to a Gaussian fit (purple curve). Super-imposed are points showing quantiles of standardized residuals from different κ-bins (colored from red to dark blue according to bin order) versus corresponding quantiles of the Gaussian (right y-axis). The quantile pattern for the overall histogram and the Gaussian fit are shown with dashed black and purple lines. (vi) Directional auto-correlation patterns of the normalized residuals, $\hat{\eta}$, as a function of distance in millimeters. X-Y are transverse with Y perpendicular to the scanning bed; Z is the axial direction.

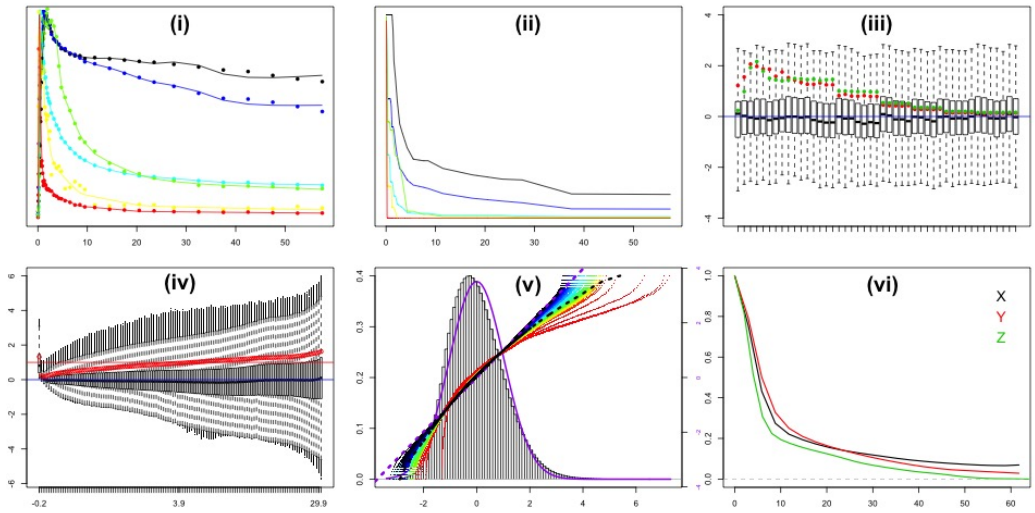


Figure 3.3: Diagnostics associated with the Image-Domain Bootstrapping Model (3.2) using the FLT-Breast data. Six plots, labeled (i) to (vi), are shown for each dataset: (i) raw sub-TACs (dots) and fitted models (lines) for the selected basis set - columns of X. (ii) Non-parametric residues corresponding to the fitted model - c.f. (3.10). (iii) Boxplots by time-frame of standardized residuals from the unconstrained least squares fit, $r_{ij}/\hat{\sigma}_i\hat{\phi}_j\hat{h}_{ij}$. The simple, $\hat{\phi}_j^0$ in (3.5), and optimized, $\hat{\phi}_j$, standard deviations are shown as green and red dots. (iv) Boxplots of scaled residuals, $\hat{\epsilon}_{ij} = r_{ij}/\hat{\sigma}_i\hat{\phi}_j$, for each κ-bin (each containing roughly 10000 data points). $\hat{h}_l$-values are shown as red points; the red line is for comparison with unity (zero skewness of bin data). (v) Histogram of the overall distribution of the standardized residuals and its relation to a Gaussian fit (purple curve). Super-imposed are points showing quantiles of standardized residuals from different κ-bins (colored from red to dark blue according to bin order) versus corresponding quantiles of the Gaussian (right y-axis). The quantile pattern for the overall histogram and the Gaussian fit are shown with dashed black and purple lines. (vi) Directional auto-correlation patterns of the normalized residuals, $\hat{\eta}$, as a function of distance in millimeters. X-Y are transverse with Y perpendicular to the scanning bed; Z is the axial direction.

course data (Kostakoglu et al. 2015). Standard errors again demonstrate a pseudo-Poisson characteristic — variability is higher in regions with higher values. The typical percent error, measured by the standard deviation relative to metabolic parameter value, is on the order of 10-20% for most of the metabolic variables displayed. It is again notable that the mean transit time (MTT) and extraction (K_i/K_1) appear quite stable as in the associated uncertainty measure. VOIs for tumor and contra-lateral normal breast were also accessed. The tumor region had 1280 voxels extending over 16 slices (3.2cm in axial extent); the normal VOI is not quite as large - 1054 voxels - but with a very similar shape. The bootstrap estimated histograms of the sampling distribution of the 95'th percentile of the metabolic parameters in the VOIs are shown in Figure 3.1. Similar to the FDG data, differences between tumor and normal VOIs are quite dramatic for all parameters, except for the vascular blood volume measure (V_b). These differences are highly significant when formally assessed via the bootstrap information.

Residual diagnostics for the analysis are shown in Figure 3.2 & 3.3. The presentation facilitates qualitative comparisons with the FDG brain results. Eight vectors are identified by the basis selection procedure. The cluster mean data defining the six non-AIF and Patlak basis vectors and their corresponding non-parametric residue model fits are again shown in Figure 3.2(i) & 3.3(i). Temporal boxplots of the fully standardized residuals are shown in Figure 3.2(iii) & 3.3(iii). These show more variability than the corresponding pattern for the FDG data. It is worth noting that the model (3.2) does not imply a common form for these distributions. Similar to the FDG data, the optimized and initial temporal scaling factors, $\hat{\phi}_j$ and ϕ_j^0 match each other quite closely, apart from the first few time-frames. Boxplots of residuals scaled by temporal ($\hat{\phi}_j$) and spatial ($\hat{\sigma}_i$) factors and binned by values of $\hat{\kappa}_{ij}$ ($= \hat{z}_{ij}/\tilde{\sigma}_i\tilde{\phi}_j$) are in Figure 3.2(iv) & 3.3(iv). These are quite different from the pattern for the FBP-reconstructed FDG data. Apart from the very first bin, the distributions show variation increasing with increasing values of $\hat{\kappa}$ - this is confirmed by $\hat{h}$ which is substantially linear as a function of the quantiles of $\hat{\kappa}$. The distribution of the standardized residuals, $(z_{ij} - \hat{\mu}_{ij})/\hat{\sigma}_{ij}$, show a marked skewness. The pattern deviates substantially from the Gaussian – Figure 3.2(v) & 3.3(v). Detailed evaluation of the distributions across κ-bins shows that as κ-increases, there is increasing confor-

mity to the Gaussian. As discussed in section 3.2, in a Gamma distribution κ is proportional to the shape parameter and as that parameter increases the Gamma distribution formally converges to a Gaussian. Thus the data are in line with (Mou et al. 2017) who showed that a Gamma-form was a good approximation for ML-reconstructed data. The directional spatial auto-correlation patterns of the scaled residuals are given in Figure 3.2(vi) & 3.3(vi). Here it can be seen that there is much less distinction between the auto-correlations in the X and Y directions. This may be due to the more circular nature of the source (see Figure 3.1). Axial auto-correlation is much more persistent than in the FDG data. This is consistent with the 3D nature of data acquisition and its reconstruction. Interestingly, the full-width-at-half-maximum (FWHM) of X-Y auto-correlations (5mm) are quite close to that seen in the FDG brain data. However the longer range persistence in auto-correlation is clearly more pronounced in the FLT case. Qualitatively the images for the FDG data in Figure 3.1 seem rougher than those for FLT. Thus the more persistent auto-correlation may in part be associated with the details of the reconstruction used. But of course, it would be inappropriate to draw any inference about the relative resolution properties of these scanners on the basis of the auto-correlation patterns in Figure 3.2(iv) & 3.3(iv) for the FDG and FLT data. Such comparisons would require data from similar objects being imaged in both instruments under similar conditions – ideally using a suitable physical phantom study (Scheuermann et al. 2013).

3.4 Assessment of Performance

The purpose here is to evaluate the performance of the novel image-domain bootstrapping technique for PET and make comparisons with the more computationally intensive, but fully non-parametric, projection-domain approach. Assessment of variance estimators is somewhat complicated because we do not have an analytic formula for the true target variance. Hence a number of replicate simulations (N_S) are needed to evaluate the true target variance with reasonable accuracy. Bootstrapping techniques involve simulation and the number of such simulations (N_B) also needs to be considered. Apart from the computation, in practice the storage require-

ments associated with retention of bootstrap samples may also be a factor. We will report studies in which both modest and large numbers of bootstraps are examined.

In mathematical terms, PET has the structure of a linear inverse problem. The raw list mode data is a realization of an inhomogeneous Poisson process in which the rate is linearly related to the target source. Our studies use a simplified representation of PET scanning. This enables us to conduct a more detailed set of studies. We assume that critical performance differences between image-domain and projection-domain bootstrapping methods for real PET scanners should be apparent in a simplified simulation setting, provided of course that the mathematical complexity of the simplification is substantially similar to PET. We report on experiments with 2-D and 1-D PET scanning models. The 2-D studies are focused on analytic (FBP) reconstruction only, but iterative ML and analytic reconstruction are considered in the 1-D case. Dynamic aspects of both 1-D and 2-D studies are based on results obtained for the FDG brain and FLT breast cancer data presented in section 3.3.

Table 3.1: Reliability of Bootstrap Estimates of voxel Standard Deviations for mapped Kinetics in 2-D. Means and maxima of voxel kinetic estimates, averaged over replicates, are shown as $\bar{\mu}_\bullet$ and $\bar{\mu}_\vee$. Mean of voxel standard deviations, averaged over replicates ($\bar{\sigma}_\bullet$) its standard error ($\bar{SE}_\bullet$) and the overall RMSE values, see (3.20), are reported as a percentage of the maximum ($\bar{\mu}_\vee$). Estimates $(\hat{a}, \hat{b}, \hat{c})$ correspond to (3.19).

	Brain FDG						Breast FLT					
Parameters	Vb	Vd	Kd	Ki	MTT	Ki/K1	Vb	Vd	Kd	Ki	MTT	Ki/K1
Mean ($\bar{\mu}_\bullet$)	0.04	0.50	0.23	0.01	4.19	0.02	0.22	0.23	0.04	0.01	4.58	0.12
Max ($\bar{\mu}_\vee$)	0.12	1.11	0.56	0.02	8.71	0.17	1.96	1.54	0.19	0.07	8.36	0.59
$\bar{\sigma}_\bullet$	20.00	11.17	14.59	5.47	10.41	7.22	2.61	3.81	11.14	1.52	22.73	12.52
$\bar{SE}_\bullet$	1.50	0.73	1.12	0.33	0.57	0.71	0.19	0.26	0.87	0.10	1.38	1.00
$\hat{a}$	1.11	1.08	1.08	1.16	1.14	1.12	1.04	1.08	1.12	1.07	1.20	1.18
$\hat{b}$	0.95	0.95	0.92	1.10	1.04	1.00	0.90	0.98	1.00	0.98	1.14	1.08
$\hat{c}$	0.97	0.97	0.94	1.12	1.06	1.04	0.91	0.99	1.03	0.99	1.16	1.11
$\text{RMSE}^y_\bullet$	6.17	2.38	4.33	1.50	2.89	3.69	0.69	1.00	4.14	0.35	8.43	5.13
$\text{RMSE}^z_\bullet$	7.10	2.95	5.29	1.41	2.79	4.04	0.91	1.11	4.35	0.40	8.04	5.09
$\text{RMSE}^{z*}_\bullet$	8.31	3.65	6.13	1.76	3.41	4.55	1.08	1.35	5.08	0.50	9.40	5.88

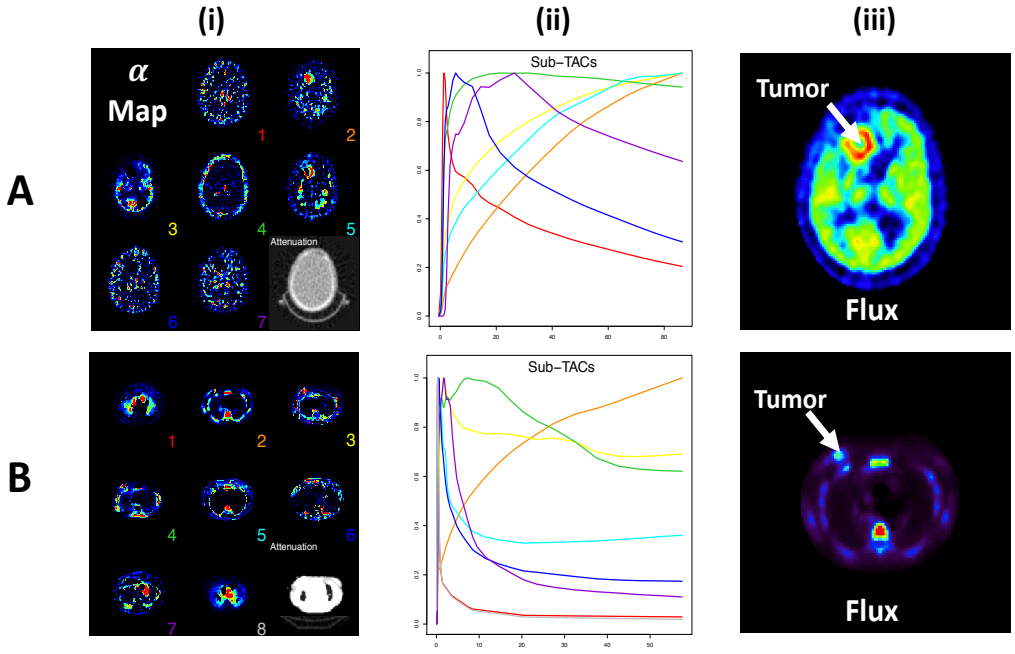


Figure 3.4: Source distribution, $\lambda_{xt} = \sum_{k=1} \alpha_k(x)\mu_k(t)$, for the 2-D simulation experiments. Rows correspond to the FDG-Brain data (A) and FLT-Breast data (B). $\alpha_k(x)$ patterns and attenuation in (i), time-courses for each component, $\mu_k(t)$ (normalized), are in (ii). Flux parameters are in (iii).

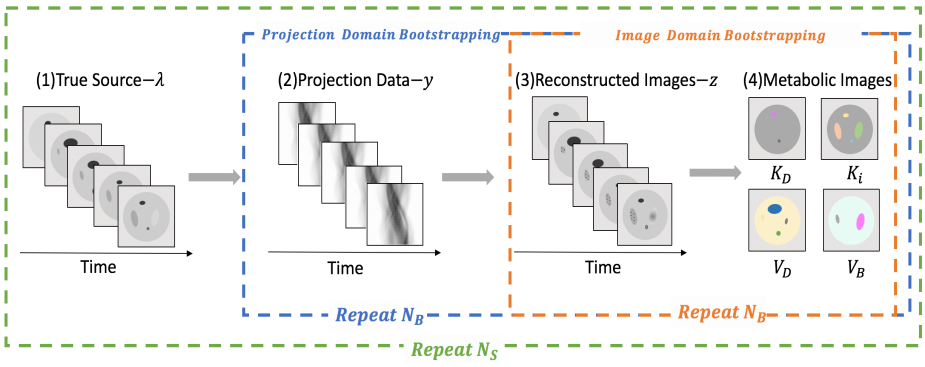


Figure 3.5: Dynamic image-domain source leads to a corresponding projection domain array. Simulated counts are reconstructed and computed metabolic images. Each replicate of the simulation has both non-parametric (projection-domain) and model-based (image-domain) bootstrapping.

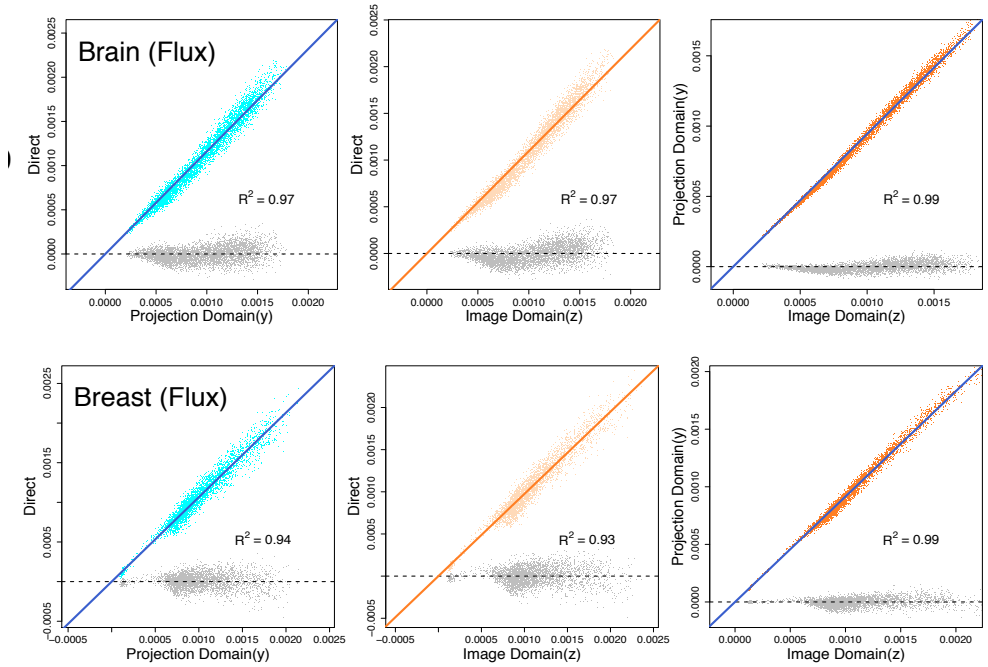


Figure 3.6: Voxel estimates of average standard deviations of flux. The true values are estimated by direct replication, these values are compared to image and projection domain bootstraps for a single replicate.

The 2-D setup focuses on central slice containing the tumor. The dynamic source for the selected slice, Figure 3.4 corresponds to the models fitted in NPRM mapping of kinetics — see (3.10). Temporal sampling and tissue attenuation are also matched to the real data. A simple scanning model involving Poisson sampling of a discretized (attenuated) parallel-beam Radon transform of the source is used (Kak et al. 2002, Natterer 2001). The imaging domain is the unit square, discretized to an array of dimension 128×128, and the projection domain is the region $[-\sqrt{2}, \sqrt{2}] \times [0, \pi]$, discretized to a 183×181 sinogram array of distances and angles. Note the π-periodicity of the parallel beam Radon transform restricts the angular extent of the projection domain. As shown in Figure 3.5, the discretized dynamic source is projected to produce the corresponding dynamic sinogram array of suitably attenuated rates. The scale of the rate array is adjusted by a factor corresponding to study dose, τ_R. This dose is specified so that the voxel-level noise in the reconstructed data matches the apparent voxel-level noise level of the real data. Independent Poisson count simulation from each element of the scaled sinogram array yields the synthetic projection-domain data (y). Each frame of the sinogram data is reconstructed analytically using a

standard filtered backpojection (FBP) procedure with the raw ramp-filter result smoothed by convolution with a Gaussian resolution filter. The resolution filter bandwidth is required to be common across all time frames and by grid-search its value is selected in order to minimize the average squared error difference between the estimated and true activity summed over frames. This choice of bandwidth is to ensure that the uptake image is objectively adapted to the study dose (O'Sullivan 1995). Simulated data are processed using the NPRM procedure in section 3.3, to produce a set of metabolic maps.

In addition data sets for the projection-domain (non-parametric), the image-domain and the approximate image-domain bootstraps are acquired. $N_B = 25$ bootstrap samples are used for the projection and image-domain bootstraps; a set of, $N_B^* = 10$, samples were used with the approximate image-domain method, with $\tilde{N}_B = 200$ samples used in recyclying - see Section 3.2.2.3. Note these numbers of bootstrap samples would be viewed as quite small relative to what might be used in standard statistical application (Efron & Tibshirani 1994), however, they are likely to be realistic for practical use in most clinical imaging settings. The bootstrap datasets were used to evaluate a set of voxel-by-voxel standard deviations in estimated metabolic parameters. These values are compared to the true values estimated by direct replication. This is indicated in Figure 3.6.

Quantitative comparisons between the estimated and true standard deviations were assessed on a voxel-by-voxel basis using a simple linear regression analysis and also in terms of an overall root mean square error (RMSE) measure. Regression analysis considered the relation between the true standard deviation, estimated by replication, with the corresponding values evaluated by the bootstrap methods. These regression analysis models are expressed as

$$\sigma_{ip} \approx a_p \, \sigma_{ip}^y \quad ; \quad \sigma_{ip} \approx b_p \, \sigma_{ip}^z \quad ; \quad \sigma_{ip} \approx c_p \, \sigma_{ip}^{z*} \tag{3.19}$$

for $i = 1, 2, ..., N$. Here σ_{ip} is the true standard deviation of the p'th metabolic parameter estimate for the i'th voxel; $\sigma_{ip}^y, \sigma_{ip}^z$ and $\sigma_{ip}^{z^*}$, are the values for the projection-domain, image-domain and recycled image-domain bootstraps. In all cases, the simple linear regression analysis models are found to de-

scribe the relation between the true and bootstrap estimated standard deviation very well. The model R^2 exceeds 0.9 for all metabolic parameters and for both FDG and FLT simulations – values for flux (K_i) are shown in Figure 3.6.

The regression parameters, (a, b, c), in (3.19) summarize the average bias in the bootstrap estimate. If the regression parameter is close to unity, it indicates that the bootstrap estimated standard deviations are well aligned with the true; a value less/greater than unity indicates over/under-estimation of standard deviation by the bootstrapping method. Table 3.1 reports the values of these regression coefficients estimated from the simulation data. There is little indication of significant bias with any of the bootstrapping methods - the non-parametric projection domain approach generally tends to under-estimate the true standard deviation by an average of 9-10% in both the FDG and FLT settings. In contrast the image-domain procedures tend to over-estimate the standard-deviation, typically by around 1-3%. RMSE evaluates the mean square deviation between the estimated and true standard deviation at each voxel, with these values then averaged over all voxels. If $\hat{\sigma}_{ips}$ is the standard deviation in the p'th metabolic parameter estimate at voxel i for the s'th replicate data for the bootstrap estimate, the RMSE is given by

$$\text{RMSE}^{\hat{\sigma}}_{p\bullet} = \sqrt{\frac{1}{NN_S}\sum_{i=1}^{N}\sum_{s=1}^{N_S}[\hat{\sigma}_{ips} - \sigma_{ip}]^2} \tag{3.20}$$

The RMSE values for projection-domain and image-domain methods are denoted $\text{RMSE}^{y}_{p\bullet}$, $\text{RMSE}^{z}_{p\bullet}$ and $\text{RMSE}^{z*}_{p\bullet}$. These values are reported in percentage terms in Table 3.1. There is little difference between the alternative bootstraps procedures with the image-domain technique out-performing the projection-domain method for some parameters (K_i, MTT, and K_i/K_1) but not for other parameters (V_b, V_d, and K_d). RMSE values for the approximate image-domain bootstrap are consistently the largest. However, it needs to be appreciated that in light of the typical standard error of the true standard deviation, the significance of any of these differences is small. Standard errors are reported as $\bar{\text{SE}}_{p\bullet}$ in Table 3.1. Note that the corresponding standard errors for averaged bootstrap estimates of standard deviations

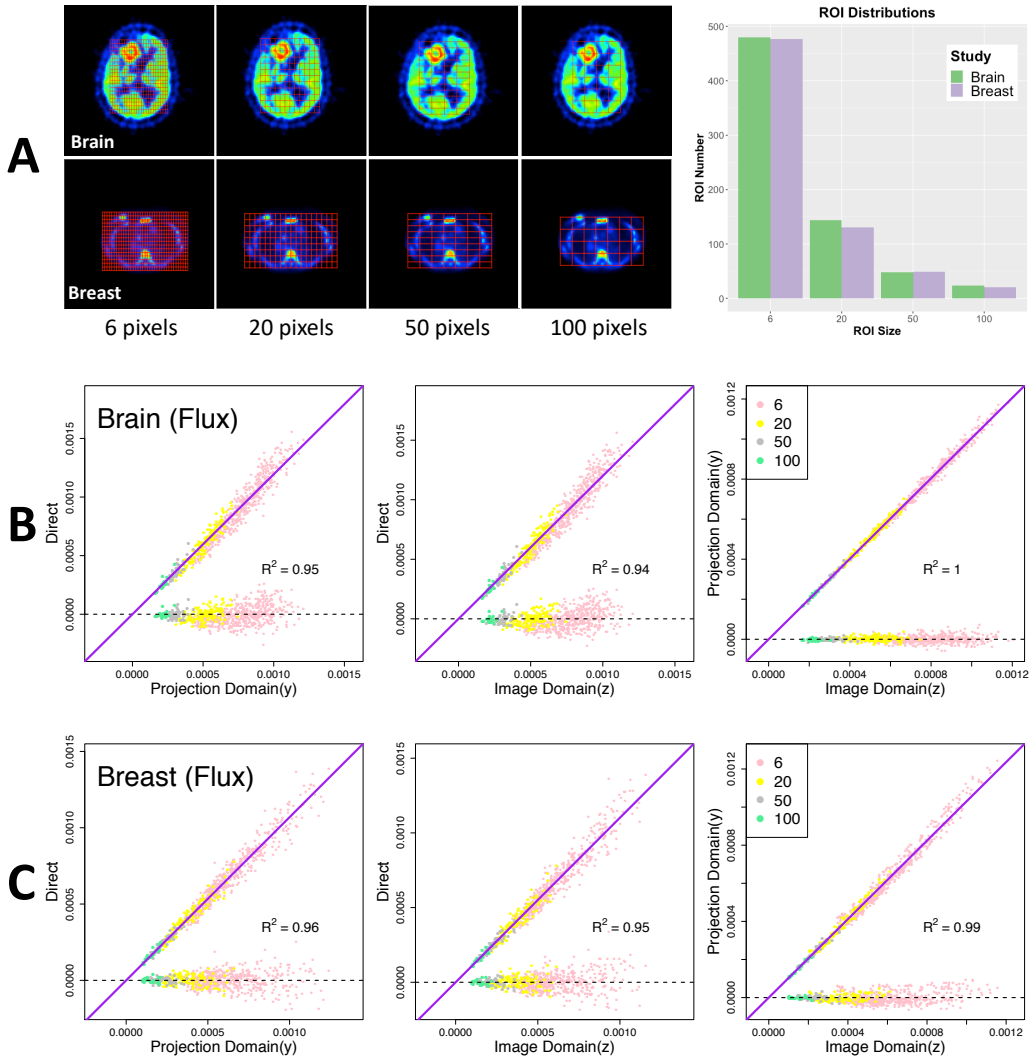


Figure 3.7: Schematic for 2-D investigation of Bootstrapping ROI averages. A total of 696 and 676 ROIs are defined for Brain and Breast, respectively. (A) Grids of rectangular ROIs and their size distributions. Estimates of average ROI standard deviations of flux are shown on rows B and C - colors correspond to different ROI sizes.

are very similar - these are not reported in the table. Further 2D studies with higher are lower count rates were also conducted and gave results very much in line with those reported in Table 3.1.

Bootstrapping ROI Averages

Table 3.2: Reliability of Bootstrap Estimates of Standard Deviations for ROI means of mapped Kinetics. Note approximately 700 ROIs are considered in each case, see Fig 3.7. Means and maxima of ROI-averaged kinetic parameters, averaged over replicates, are shown as $\bar{\mu}_\bullet$ and $\bar{\mu}_\vee$. Mean ROI standard deviation, averaged over replicates ($\bar{\sigma}_\bullet$), its standard error ($\bar{SE}_\bullet$) and the overall RMSE values, computed by ROI version of (3.20), are reported as a percentage of the maximum ($\bar{\mu}_\vee$). Estimates $(\hat{a}, \hat{b}, \hat{c})$ are based on the ROI version of (3.19).

	Brain FDG						Breast FLT					
Parameters	Vb	Vd	Kd	Ki	MTT	Ki/K1	Vb	Vd	Kd	Ki	MTT	Ki/K1
Mean ($\bar{\mu}_\bullet$)	0.04	0.60	0.26	0.01	4.56	0.04	0.27	0.26	0.04	0.01	4.24	0.14
Max ($\bar{\mu}_\vee$)	0.09	1.08	0.49	0.02	8.58	0.18	1.63	1.30	0.17	0.07	8.04	0.52
$\bar{\sigma}_\bullet$	19.93	8.97	12.04	4.21	6.47	5.54	1.82	2.54	7.00	0.85	11.58	7.24
$\bar{SE}_\bullet$	1.48	0.61	0.91	0.27	0.40	0.46	0.12	0.17	0.50	0.06	0.76	0.52
$\hat{a}$	1.18	1.14	1.14	1.22	1.22	1.18	1.27	1.18	1.23	1.10	1.24	1.23
$\hat{b}$	1.12	1.08	1.08	1.21	1.18	1.14	1.04	1.08	1.11	1.07	1.20	1.16
$\hat{c}$	0.73	0.82	0.70	0.77	0.98	0.53	0.71	0.63	0.58	0.57	0.87	0.55
$\text{RMSE}^y_\bullet$	5.55	1.80	3.25	1.12	1.62	2.25	0.38	0.54	1.92	0.17	3.36	2.27
$\text{RMSE}^z_\bullet$	5.99	2.08	3.47	1.16	1.77	2.32	0.54	0.64	2.23	0.19	3.51	2.44
$\text{RMSE}^{z*}_\bullet$	12.39	4.17	8.21	2.36	3.13	7.91	1.22	2.04	6.83	0.85	7.35	8.08

For this analysis a nested sequence of grids was used to construct a range of ROIs with different sizes and tissue heterogeneity characteristics. Figure 3.7 gives a schematic of the ROI generation scheme as well as summary information about ROI size distributions. Comparison between bootstrap estimates of standard deviations of ROI averages of flux (K_i) is also shown in Figure 3.7. There is no indication that the alignment of the bootstrap estimates with the true standard deviations varies by ROI size. Detailed assessments of the reliability of the bootstrap estimates is provided in Table 3.2. These are based on an ROI version of (3.19) and (3.20) - $i.e.$ the voxel indicator (i) is replaced by an indicator of the ROI. Similar to the

voxel case, bootstrap estimates perform very well. There is no evidence that these results are substantially impacted by the size-distribution or positioning of ROIs. The non-parametric and image-domain method (with $N_B = 25$ replicates) have very similar RMSE reliabilities both for FDG and FLT. Both bootstraps tend to under-estimate the true ROI mean standard deviation. However, the amount of bias is small - on the order of 10-14% across the different kinetic parameters. Recycling is found to lead to more unreliable values - largely due to a greater systematic over-estimation of the true ROI standard deviation - on the order of 20% for most parameters. But the overall indication from the 2-D experiments is that image-domain bootstrapping scheme is very well aligned with the non-parametric projection domain approach and provides a viable mechanism for assessments of uncertainties at both the voxel and ROI level.

3.4.1 1-D Experiments

These studies have a similar temporal structure to the 2-D simulations but a more simplified 1-dimensional Poisson deconvolution scanning model from (O'Sullivan & Roy Choudhury 2001) is used. The simplified structure allows a detailed investigation of bootstrapping when the input data used for kinetic analysis has been reconstructed by methods analogous to the direct FBP and iterative maximum likelihood (ML) procedures used in PET. The scanning model is defined as follows: we observe a discretized Poisson process whose intensity is of the form $\gamma_{xt} = a_x[\mathcal{R}\lambda]_{xt}$ for $x = 1, 2, .., N$ (even) and $t = 1, 2, ..., T$. Here $0 < a_x \leq 1$ is a known attenuation factor and the matrix $\mathcal{R}$ is given by $\mathcal{R} = I_T \otimes K_\beta$ where $K_\beta : R^N \rightarrow R^N$ and K_β has the form of a discrete convolution. Letting $\mathcal{F}$ be the discrete Fourier transform, for any vector $x \in R^N$, $[\mathcal{F}K_\beta x]_\nu = |\nu|^{-\beta}[\mathcal{F}x]_\nu \equiv \widehat{x}_\nu$ for $\nu = \pm 1, \pm 2, ..., N/2$. With $\beta > 0$, the action of K_β is to smooth the vector x. If y is a realization of a Poisson with mean $\tau\gamma$, then an unbiased estimate of the underlying source distribution λ is obtained by adjusting for the y-data by the attenuation factor and applying a least squares (LS) inversion procedure. This result is then smoothed to achieve consistent mean square error performance. As FBP is essentially equivalent to LS in the 2-D setting (O'Sullivan 1995), we refer to LS as FBP in our 1-D model.

Letting S_h be a smoothing matrix with bandwidth $h > 0$ the smoothed

estimate is

$$z = I_T \otimes S_h z^{(fbp)} \text{ with } z^{(fbp)} = \frac{1}{\tau} I_T \otimes [K'_\beta K_\beta]^{-1} K'_\beta (y/a) \tag{3.21}$$

where $(y/a)_{xt} = y_{xt}/a_x$.

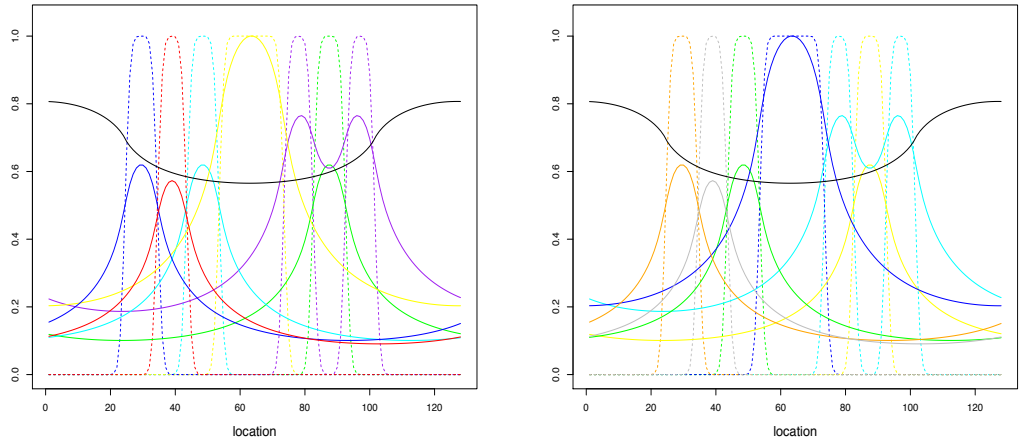


Figure 3.8: Scaled spatial patterns (α_j) for source distribution in 1-D experiments (dotted lines); projection domain patterns ($K_\beta \alpha_j$) are also shown (solid lines). Left - FDG studies; Right - FLT studies. Source sub-TACs (μ_j) are in Figure 3.4 A(ii) (FDG) and Figure 3.4 B(ii) (FLT). Colors of α_j's here match the colors of corresponding sub-TACs in Figure 3.8. The solid black line is the attenuation pattern.

If S_h has a discrete Fourier representation, $z^{(fbp)}$ and z are efficiently computed using the 1-D FFT. Adapting (Vardi et al. 1985), the EM algorithm can be used to evaluate a maximum likelihood (ML) estimate, $z^{(ml)}$, and a corresponding smoothed value $z^+ = S_h z^{(ml)}$. The ML estimator is asymptotically efficient, as $\tau \to \infty$, as indeed is the FBP estimator. In estimation terms, 1-D scanning model shares some of the essential complexity of PET. In PET, K_β is replaced by the line-integral Radon transform, $\mathcal{K}$. FBP estimation is known as filtered backprojection (FBP). Similar to $K'_\beta K_\beta$, the operation $\mathcal{K}'\mathcal{K}$ is Toeplitz (Natterer 2001). In d-dimensions, the eigenvalues of $\mathcal{K}'\mathcal{K}$ are proportional to $|\xi|^{-d/2}$; while the eigenvalues of $K'_\beta K_\beta$ are proportional to $|\nu|^{-2\beta}$. Studies reported in (Gu 2023) show that with a choice of $\beta = 1.35$, there is a good agreement between the bandwidth optimized mean square error (MSE) estimation characteristic as a function of dose for the 1-D Poisson deconvolution model, and the corresponding MSE

characteristic of 2-D PET reconstruction.

Table 3.3: Reliability of Bootstrap Estimates of voxel Standard Deviations for mapping Kinetics in 1-D based on FBP and ML reconstructed data. Means and maxima of voxel kinetic estimates, averaged over replicates, are shown as $\bar{\mu}_\bullet$ and $\bar{\mu}_\vee$. Mean of voxel standard deviations, averaged over replicates ($\bar{\sigma}_\bullet$), its standard error ($\bar{SE}_\bullet$) and the overall RMSE values, see (3.20), are reported as a percentage of the maximum ($\bar{\mu}_\vee$). Estimates $(\hat{a}, \hat{b}, \hat{c})$ correspond to (3.19).

		FBP						ML					
Tracer	Parameters	Vb	Vd	Kd	Ki	MTT	Ki/K1	Vb	Vd	Kd	Ki	MTT	Ki/K1
FDG	Mean ($\bar{\mu}_\bullet$)	0.05	0.49	0.26	0.01	3.03	0.02	0.05	0.49	0.26	0.01	3.06	0.02
	Max ($\bar{\mu}_\vee$)	0.26	0.95	1.07	0.02	4.36	0.07	0.26	0.95	1.07	0.02	4.36	0.07
	$\bar{\sigma}_\bullet$	4.68	7.11	4.38	2.57	14.16	7.56	3.68	6.79	3.63	2.39	12.04	6.66
	$\bar{SE}_\bullet$	0.20	0.22	0.18	0.09	0.41	0.28	0.15	0.21	0.14	0.09	0.37	0.22
	$\hat{a}$	1.06	1.16	1.07	1.03	1.19	1.12	1.09	1.17	1.11	1.04	1.18	1.15
	$\hat{b}$	1.12	1.20	1.13	1.04	1.22	1.16	1.06	1.20	1.10	1.04	1.22	1.15
	$\hat{c}$	1.16	1.23	1.16	1.07	1.25	1.19	1.09	1.23	1.13	1.07	1.26	1.18
	$\text{RMSE}^y_\bullet$	29.7	31.4	26.9	17.9	31.3	29.2	28.0	32.5	25.9	17.2	29.1	26.7
	$\text{RMSE}^z_\bullet$	33.1	34.3	30.6	23.7	33.7	32.9	34.2	35.9	30.9	24.7	34.6	31.4
	$\text{RMSE}^{z*}_\bullet$	41.9	42.3	39.5	34.2	42.2	42.3	44.3	44.5	40.5	36.0	42.9	41.6
FLT	Mean ($\bar{\mu}_\bullet$)	0.18	0.71	0.16	0.02	3.46	0.12	0.18	0.71	0.16	0.02	3.47	0.12
	Max ($\bar{\mu}_\vee$)	1.04	2.17	0.36	0.05	7.50	0.61	1.04	2.17	0.36	0.05	7.57	0.61
	$\bar{\sigma}_\bullet$	2.01	1.93	4.26	1.72	9.69	2.93	1.62	1.83	3.65	1.66	9.23	2.45
	$\bar{SE}_\bullet$	0.08	0.08	0.17	0.08	0.46	0.15	0.06	0.08	0.15	0.07	0.44	0.11
	$\hat{a}$	1.02	0.98	1.01	0.99	1.11	1.08	1.05	1.01	1.06	1.03	1.13	1.14
	$\hat{b}$	1.20	0.98	1.05	0.98	1.12	1.11	1.22	0.97	1.03	0.99	1.13	1.13
	$\hat{c}$	1.23	1.01	1.08	1.02	1.18	1.17	1.25	1.01	1.06	1.03	1.20	1.18
	$\text{RMSE}^y_\bullet$	25.4	31.6	27.2	37.8	44.4	56.0	22.2	30.6	24.9	33.7	44.2	50.2
	$\text{RMSE}^z_\bullet$	33.3	34.7	29.3	41.3	46.0	59.0	34.6	35.0	28.8	39.2	47.5	58.0
	$\text{RMSE}^{z*}_\bullet$	41.3	45.6	38.7	51.2	57.6	72.7	42.6	44.8	38.4	48.8	59.3	71.4

In the 1-D case simulations were conducted both for FDG and FLT using source distributions consisting of a mixture of six temporal components, $\lambda_{xt} = \sum_{j=1}^{6} \alpha_j(x)\mu_j(t)$. The number of voxels was set at $N = 128$. The temporal patterns are matched to those arising in the 2-D simulations. Spatial patterns are indicated in Figure 3.8, together with the transformed profiles, $K_\beta\alpha_j$'s, and the attenuation pattern. Reference dose-values τ_R were again

chosen so that the qualitative variability of simulated 1-D data matched that seen at the voxel-level in the real FDG and FLT data. Five dose levels, $\tau = \tau_R/5, \tau_R/2.5, \tau_R, 2.5\tau_R, 5\tau_R$ were examined with FDG and FLT. In the 1-D setting a more extensive bootstrapping process was used ($N_B, \tilde{N}_B = 200$ with $N_B^* = 10$) and the number of replicates was also increased ($N_S = 400$). Simulated data were reconstructed using FBP and iterative ML techniques. Raw frame-by-frame reconstructions were smoothed by convolution with a Gaussian kernel. Similar to the 2-D case, bandwidth was common across all frames, and its value was optimized according to the mean square deviation of the estimated total uptake from the true known source. Due to the implicit regularization associated with raw ML reconstruction (O'Sullivan 1995, O'Sullivan & Roy Choudhury 2001) bandwidths were separately optimized for the FBP and ML reconstructions. Results for the middle dose are presented in Table 3.3. Very similar results were found at other doses. Regression analysis again finds a strong alignment between the bootstrap generated standard deviations and the true values. Generally there is a tendency for the methods to underestimate the true standard deviation by on the order of 14% for FDG and 7% for FLT. The approximate image-domain bootstrap is 2-4% higher than the others. There is little or no difference between the pattern for FBP and ML reconstructed data. Raw RMSE values, computed by (3.20), are typically 16% smaller for ML reconstructed than FBP reconstructed data. However this is undoubtedly a reflection of the fact that the metabolic parameter standard deviations, summarized by $\bar{\sigma}_\bullet$ in Table 3.3, are on the order of 14% lower for data reconstructed by ML versus the FBP. In light of this, Table 3.3 reports RMSE values as a percent of the average true standard deviation. The adjusted RMSE values are very similar for FBP and ML. In the case of FDG RMSE values are 0.2% lower for FBP; they are 1.1% higher for FLT. In practical terms these differences are inconsequential. Results demonstrate the ability of the methodology to adapt to the characteristics of the ML data. Overall, the RMSE is 4.5% lower for the projection-domain bootstrap than the image-domain approach; the approximate method is 9.3% higher again. A similar calculation for the RMSE values reported in the 2-D simulation but expressed as a percentage of $\bar{\sigma}_\bullet$, gives values that are remarkably similar to this: The image-domain method is 2.8% higher than the projection-domain with the RMSE for the approximate method a further 6.3% higher again.

3.4.2 Statistical Interpretation of Simulation Data

Table 3.4 reports on a number of further analyses applied to all the simulation data generated in 2-D and 1-D experiments. These analyses are applied separately in 1-D and 2-D so the table gives the ability to see similarities across the various configurations explored and appreciate overall patterns. The focus is on two analyses, (i) the direct systematic relation between the projection-domain and image-domain bootstrapping methods, and (ii), the relation between relative uncertainty in voxel-level kinetic parameters and data reconstruction error. For the first analysis we conducted regression analyses, similar to (3.19), relating the voxel-level projection-domain bootstrap standard deviation to the values from the image-domain approaches, $i.e.$

$$\sigma^y_{ip} \approx \alpha_p \sigma^z_{ip} \quad ; \quad \sigma^y_{ip} \approx \beta_p \sigma^{z^*}_{ip} \quad \text{for} \quad i = 1, 2, ..., N \tag{3.22}$$

The estimates of the α and β coefficients are in Table 3.4. Across all the simulation settings we see a very similar pattern. Apart from blood volume (V_b), whose standard deviation by the image-domain methods are consistently lower than reported by the projection-domain bootstrap, there is remarkably close alignment between the methods.

The relation between voxel-level parameter standard deviation and reconstruction error was also examined. Our analysis is motivated by the approximation used in constructing the recycling process for the simplified image-domain bootstrap in (3.4). The covariance of unconstrained α-coefficients should be approximately $\sigma_i^2[X'WX]^{-1}$, where σ_i^2 is the average voxel-level measurement variance in (3.1) or (3.2) and W is the diagonal matrix with elements ϕ_j^{-2} for $j = 1, 2..., T$. The NPRM kinetic analysis procedure involves fitting the model (3.2) but subject to the constraint that the α-coefficients are non-negative. By (3.10), the true kinetic parameters, $\theta = (V_b\ ,\ V_d\ ,\ K_d\ ,\ K_i\ ,\ MTT\ ,\ K_i/K_1)$, are simple functions of the constrained α-coefficients. Assuming the unconstrained α-coefficients are sufficient for the constrained values, θ can also be regarded as a function of the unconstrained coefficients. Hence we can consider the the estimated kinetic parameters as functions of the unconstrained α-coefficients ($\hat{\alpha}$): $i.e.\ \hat{\theta} = g(\hat{\alpha})$ where $g : R^K \to R^P$ $(P = 6)$. By application of the delta method, $e.g.$ (Kutner et al. 2013, Rao 1973), the covariance of kinetic parameters can be ap-

Table 3.4: Analysis of Voxel-level Error Characteristics across all Simulations. The coefficients are for the models in (3.22) and (3.23). The R^2-values only reported for (3.23). Corresponding values for (3.22), are uniformly high (in excess of 90%)

		FDG						FLT					
		Vb	Vd	Kd	Ki	MTT	Ki/K1	Vb	Vd	Kd	Ki	MTT	Ki/K1
FBP (2D)	$\hat{\alpha}$	0.86	0.88	0.86	0.94	0.92	0.90	0.86	0.91	0.90	0.92	0.95	0.92
	$\hat{\beta}$	0.88	0.89	0.87	0.95	0.93	0.93	0.88	0.93	0.92	0.93	0.97	0.94
	$\hat{\gamma}_1$	0.58	0.63	0.65	0.59	0.55	0.48	0.79	0.63	0.59	0.63	0.90	0.75
	R^2	0.93	0.94	0.94	0.90	0.33	0.61	0.97	0.94	0.85	0.94	0.97	0.91
FBP (1D)	$\hat{\alpha}$	1.06	1.03	1.05	1.01	1.03	1.03	1.18	1.00	1.03	0.99	1.01	1.03
	$\hat{\beta}$	1.10	1.06	1.09	1.04	1.06	1.07	1.21	1.04	1.07	1.03	1.06	1.08
	$\hat{\gamma}_1$	0.73	0.65	0.70	0.85	0.65	0.47	0.77	0.92	0.86	0.85	1.11	0.56
	R^2	0.91	0.69	0.91	0.98	0.15	0.72	0.97	0.91	0.94	0.89	0.83	0.37
ML (1D)	$\hat{\alpha}$	0.97	1.02	0.99	1.00	1.03	1.00	1.16	0.96	0.97	0.96	1.00	0.99
	$\hat{\beta}$	1.01	1.05	1.02	1.03	1.07	1.03	1.19	1.00	1.00	1.00	1.05	1.04
	$\hat{\gamma}_1$	0.64	0.67	0.57	0.83	0.07	0.43	0.65	0.92	0.83	0.85	1.11	0.55
	R^2	0.89	0.55	0.83	0.98	0.00	0.73	0.90	0.92	0.92	0.88	0.81	0.40

proximated by $\ell'_\alpha V(\hat{\alpha})\ell_\alpha$, where ℓ_α is the $K \times P$ matrix whose columns are the gradients of the components of θ $w.r.t.$ the α-coefficients. But as discussed in section 3.2.3, $V(\hat{\alpha}) \approx \sigma_i^2[X'WX]^{-1}$, so we are lead to $V(\hat{\theta}) \approx \sigma_i^2 \ell'_\alpha [X'WX]^{-1}\ell'_\alpha$. In general, since the mapping g takes unconstrained α-coefficients and maps them to kinetic parameters, g may well be non-linear even for the components (V_b, V_d, K_d, K_i) that have a linear dependence on the constrained α-coefficients. Hence ℓ_α may depend on the local α-value. In spite of this, the analysis suggests a relation between the voxel-level parameter standard deviation and the standard deviation of the measurement. In the simulation setting, the square-root of the weighted mean square reconstruction error can be used as an assessment of measurement error: $\sigma_i^R = \sqrt{\sum_{j=1}^T w_j^0[z_{ij} - \lambda_{ij}]^2/T} \approx \sigma_i$. Motivated by these theoretical considerations, we examined the relation between the relative error in kinetic parameters and a scaled reconstruction error, by fitting regression models in the form

$$\log(\sigma_{ip}/\mu_{ip}) = \gamma_{0p} + \gamma_{1p}\log(\sigma_i^R/\mu_{ip}) + error \tag{3.23}$$

to each of the simulation datasets.

Table 3.4 [1] shows estimates of γ_{1p} as well as the quality of fit of the model measured by the R^2 statistic. The model fits are remarkably good (most in excess of 80%) particularly for (V_b, V_d, K_d, K_i). With MTT the model pattern is continues to be remarkably accurate for FLT; but not for FDG. On the other hand the model variance pattern for extraction (K_i/K_1) is still very reasonable for FDG but not for FLT. While these analyses give an understanding of the behaviour of voxel-level kinetic parameter variability, they also help to provide some underpinning for the basic theoretical heuristic for the approximation used to recycle the image-domain bootstrapping. Further studies were conducted in 1-D in order to evaluate the accuracy of the bootstrapping techniques as a function of the size of the imaging domain (Badawi et al. 2019*a*). Remarkably, our analysis finds that the dependence is very limited. Based on linear regression theory (Seber 2015), the primary factor impacting the RMSE of uncertainty estimation relative to the scale of the noise, $i.e.$ $\sqrt{var(\hat{\sigma})}/\sigma$, is the dimension of the model basis in relation to the number of data points (K/T). But in PET, dose constraints mean that reconstruction error will increase with temporal sampling. So the ability to manipulate relative RMSE performance merely by increased temporal sampling would be unrealistic.

3.5 Discussion

The work has presented a novel image-domain approach to bootstrapping PET data having a dynamic component. The method is based on a novel general linear model approximation of the dynamic source distribution in which the error is described in terms of a sub-ordinate Gaussian process that is assumed independent across time-frames and stationary in the imaging space. In addition the distribution of error is allowed to adapt to the local skewness of the data. Thus there is no requirement for the method to be modified depending on whether an analytic or iterative data reconstruction process is used. This removes a number of potentially limiting assumptions used in (Huang et al. 2020). The bootstrapping scheme in (Huang et al. 2020) also made essential use of the near-replicate nature of

[1] The logarithmic transform is used for variance stabilization in fitting.

re-binned time-frame data. But this is not required here. In essence, the generalized linear modeling of the dynamic PET data used here creates an approximate replicate residual process that provides information for data simulation. Conceptually this is similar to information provided by time-frame re-binning in (Huang et al. 2020).

Our methodology is illustrated by application to real examples involving the use of dynamic PET imaging for the purpose of mapping metabolic parameters of tissues in the field of view. The general linear modelling analysis technique enables us to create bootstrap replicate data sets for analysis. Application of the NPRM kinetic mapping technique to the bootstrap data provides voxel-level estimates of metabolic parameters and their associated uncertainties (SEs). Numerical studies motivated by these examples compare the image-domain bootstrapping approach to the more computationally demanding but fully non-parametric projection-domain approach (Haynor & Woods 1989). Image-domain bootstrapping is found to substantially match the RMSE performance characteristics of projection-domain bootstrapping.

The current analysis is implemented in (R Core Team 2021) - an open-source statistical programming platform. An R-package is currently under development and is expected to be available on the CRAN network (`https://cran.r-project.org`) in the near future. In comparison to projection-domain bootstrapping, in which each bootstrap replicate requires reconstruction of simulated list-mode data; computation of image-domain bootstrap replicates are negligible. But of course significant computation is required to setup the image-domain bootstrapping model. For the 3-D data sets analyzed in section 3.3, the computation of the image-domain model took 1-1.5 hours on a small desktop computer configured with a single 3.2 GHz Intel Core i7 processor and 16 GB 2667 MHz DDR4 memory. Based on our 2-D numerical studies, the computation of the image-domain bootstrapping model is less than what would be required for a single ML reconstruction of a list-mode time-course data set. In light of this, with iteratively reconstructed PET data - the norm in most PET scanners now - image-domain bootstrapping will always be faster than the projection-based approach; the difference between them becoming more extreme as temporal sampling or the number of bootstrap replicates required increases.

Of course as computing capabilities grow and it becomes standard to re-

tain list-mode data for dynamic PET studies, non-parametric projection-domain bootstrapping may become practical as well. Indeed, this would be an ideal circumstance because the theory underpinning the non-parametric approach is very well developed (Efron & Tibshirani 1994). However, current PET scanning technology is very far from that. In addition, current archives of well-curated cancer clinical trial PET imaging data combined with associated patient outcomes, $e.g.$ National Cancer Institute (https://www.cancerimagingarchive.net), do not to our knowledge include any list-mode information. Thus the analysis of image uncertainty using data from such archives can only be based on a suitable image-domain bootstrapping approach, as we have described here.

For situations where retention of extensive bootstrap samples is prohibitive, we have proposed a novel recycling process as an approximate image-domain bootstrapping approach. While the RMSE performance of this approximation is not as good as a full bootstrap, the results are still quite reasonable. Importantly our studies indicate that the performance of the image-domain simulation techniques are not impacted by whether or not the reconstruction methodology is analytic (FBP) or iterative (ML).

It would be interesting to use the methods here to examine multiple studies with similar anatomy on the same scanner in order to develop a practical scanner-specific understanding of the study-to-study stability of the image-domain model estimates. If list-mode data were available, it would also be possible to use the projection-domain bootstrap to gain some insight into this. Specifically such a bootstrap could be used to create replicate projection-domain scanning data that could be used to estimate image-domain model parameters. The collection of model parameters obtained across bootstrap replicates would then provide a direct assessment of their sampling characteristics.

There are a number of other medical imaging modalities where subject-specific assessment of uncertainty in quantitated imaging measurements are not currently available and the techniques here might be useful. For example, dynamic imaging with MR (DCE,DSC) or CT are routine in the clinical management of cancer and stroke and the structure of datasets is substantially similar to dynamic PET. This will be a focus for future work.

Chapter 4

Mapping ^{18}F-FDG Kinetics together with Patient-Specific Bootstrap Assessment of Uncertainties: An Illustration with data from a Long-Axial FOV PET/CT Scanner

Abstract

Purpose: Examine a non-parametric approach to mapping kinetic parameters and their uncertainties with data from the emerging generation of dynamic whole-body PET/CT scanners. **Methods:** Dynamic PET ^{18}F-FDG data from a set of twenty-four cancer patients studied on a long-axial field-of-view (LAFOV) Biograph Vision Quadra PET/CT scanner at Bern Hospital were considered. Kinetics were mapped using a non-parametric residue modelling (NPRM) technique.Uncertainties were evaluated using an image-based bootstrapping methodology. Kinetics and bootstrap-derived uncertainties are reported for voxels, maximum intensity projections and volumes of interest (VOIs) corresponding to several key organs and tumor lesions. Comparisons between NPRM and standard 2C modelling of VOI kinetics are

carefully examied. **Results:** NPRM generated kinetic maps were of good quality, well-aligned with the vascular and metabolic ^{18}F-FDG patterns, reasonable for the range of VOIs considered. On a single 3.2 GHz processor, specification of the bootstrapping model took 140 minutes; individual bootstrap replicates required 80 minutes each. VOI time-course data were much more accurately represented, particularly in the early time-course, by NPRM than by 2C modelling constructs - improvements in fit were highly significant, statistically. While ^{18}F-FDG flux values evaluated by NPRM and 2C were generally similar, significant deviations between vascular blood and distribution volumes estimates were found. The bootstrap enables assessment of quite complex summaries of mapped kinetics. This is illustrated with maximum intensity maps of kinetics and their uncertainties. **Conclusion:** NPRM kinetic mapping combined with image-domain bootstrapping is practical with large whole-body dynamic FDG data sets. The information provided by bootstrapping could support more sophisticated use of PET biomarkers used in clinical decision-making for the individual patient.

4.1 Introduction

High resolution dynamic whole body positron emission tomography (PET) scanning enhances the opportunities for mapping metabolic characteristics of tissue, particularly in the context of cancer. The current focus has been on dynamic PET studies with ^{18}F-FDG (^{18}F-fluorodeoxyglucose), using the well-established Huang-Sokoloff two compartment (2C) modelling framework (Feng et al. 2021, Sari et al. 2022*b*, Wang et al. 2021*a*). While 2C modelling has had widespread application in PET, far beyond the brain setting in which it was developed, the biochemical understanding of the transporters involved in metabolism of ^{18}F-FDG and indeed their distribution across normal and cancerous tissues has evolved in the years since the Huang-Sokoloff construct was proposed (Spence et al. 1998, Muzi et al. 2006, Barrio et al. 2020*a*, Gu & Wu 2023). The temporal and spatial resolution of emerging scanners has transformed the ability to objectively assess the accuracy of the 2C framework to represent ^{18}F-FDG time-course data across the diverse tissues encountered in the human body. In this context, the assessment of ^{18}F-FDG kinetics based on more flexible nonparametric analysis approaches

(Cunningham & Jones 1993, O'Sullivan 1993) may be necessary. The most recent implementation of the non-parametric voxel level analysis scheme in (O'Sullivan 1993) is particularly efficient - largely due to an extensive reliance on quadratic programming techniques - and its non-parametric aspect gives an ability to apply an image-domain bootstrapping process for evaluation of statistical uncertainties in derived kinetic maps and associated biomarkers (O'Sullivan et al. 2021, Gu et al. 2021*b*). Uncertainties in diagnostic information recovered from PET scans could augment decision making about individual patients that are based on complex non-linear radiomic metrics derived from a kinetic map.

The volume of data produced by a dynamic PET-FDG study on a state-of-the-art long-axial field of view (LAFOV) scanner is a practical computational challenge for voxel-level analysis of kinetics. The bootstrap uncertainty assessment requires that comprehensive voxel-level analyses be applied to multiple simulated data sets, each created to match the full character and extent of the original data. This significantly adds to the computational challenge involved.

The work here uses a series of dynamic ^{18}F-FDG data acquired on the LAFOV scanner (Sari et al. 2022*b*) to investigate the approach. Apart from the demonstration of the practical feasibility of kinetic mapping with uncertainty evaluation, the analysis allows regional comparisons between non-parametric and 2C modelling results both in terms of derived kinetics and in terms of the accuracy of data representation.

4.2 Materials and Methods

4.2.1 Patient Scans and Volumes of Interest (VOIs)

The data considered arise from a set of twenty-four patients with different types of cancer who participated in an institutionally approved ^{18}F-FDG PET/CT study at Bern University Hospital (KEK 2019–02,193). Details of the study are reported in (Sari et al. 2022*b*). In summary, PET scanning was conducted on a Biograph Vision Quadra device - a scanner with 106 cm axial FOV and nominal in-plane resolution of 3.3 mm full-width at half-maximum (FWHM) (Prenosil et al. 2022). Data were acquired in list-mode

starting 15 s before the intravenous bolus injection of ^{18}F-FDG (with activity of approximately 3 MBq per kg of patient weight) to the left or right arm; followed by flushing with 50 mL saline solution. The first 20 seconds are empty frames until the tracer starts to arrive to the body. This explains why the first few frames have 10 second duration - see (Sari et al. 2022*b*). The plasma glucose level was measured for each patient. Emission data were acquired for 65 min and binned into 62 contiguous time-frames with durations: $2 \times 10s, 30 \times 2s, 4 \times 10s, 8 \times 30s, 4 \times 60s, 5 \times 120s,$ and $9 \times 300s$. Images were reconstructed with a voxel size of $1.65 \times 1.65 \times 1.65\ mm^3$ using the full acceptance angle of the scanner but reconstructed using the high sensitivity mode with limited acceptance angle (MRD85). The PSF-TOF iterative reconstruction with 4 iterations 5 subsets and a 2 mm FWHM Gaussian filter is used (Sari et al. 2022*b*). Standard uptake value (SUV) images were generated by normalizing late-time images (55–65 min, p.i.) to body weight and injected dose. Low-dose CT scans (voltage: 120 kV, tube current 25 mA, CareDose4D, CarekV) were acquired as part of the examinations. The CT images were reconstructed with a voxel size of $1.52 \times 1.52 \times 1.65\ mm^3$.

Automated segmentation algorithms based on CT and PET were used to define VOIs corresponding to a number of tissue structures including grey and white matter in the brain, liver, lungs, kidneys, spleen, and bones. A further set of 49 VOIs corresponding to tumor tissue were identified by an experienced nuclear medicine physician. In (Sari et al. 2022*b*) both the ascending aorta and descending aorta were considered and gave very comparable results. Finally, a VOI placed in the descending aorta was used to define the whole blood arterial input function (AIF) for kinetic analyses.

4.2.2 Parametric Imaging Techniques

4.2.2.1 Tissue Residue

Following Meier-Zierler (Meier & Zierler 1954), the analysis assumes the PET measured time-course for a tissue region is represented as a convolution between the local arterial input function (AIF), C_p, and the regional tissue residue function, R. Kinetic parameters are defined in terms of the residue - see Figure 4.1. The material is developed in detail in (O'Sullivan et al. 2009, 2014, 2021).

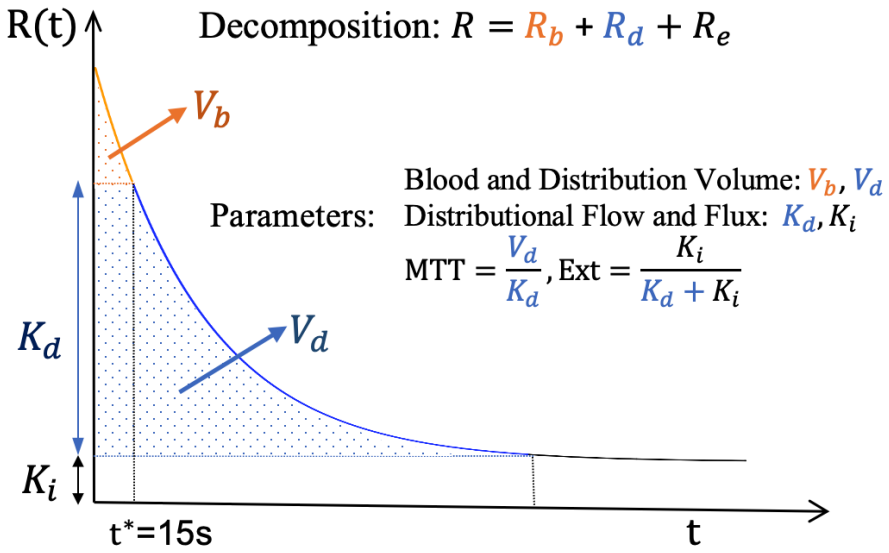


Figure 4.1: Meier-Zierler tissue residue (R) and a decomposition into vascular (R_b), based on consideration of atoms with travel-times less than 15 seconds in the tissue), in-distribution (R_d) and extracted (R_e) components. These are used to defineassociated metabolic parameters indicated.

4.2.2.2 Summary Kinetic Parameters

Our methodology uses the Meier-Zierler tissue residue function form to define the summary kinetic variables (V_b, V_d, K_d, K_i). Large vessel vascular blood and distribution volumes (V_b and V_d) are evaluated as areas under the tissue residue. The apparent rate of retention or flux (K_i) of the tracer, measurable by the PET, is height of this residue at the end of the acquisition period. Also the mean transit time (MTT) of the tracer in tissue and extraction fraction (Ext) are defined as ratios of amplitude and integral measurements.

A variety of approaches might be used to approximate the residue: A nonparametric (NP) method used here. Patlak analysis uses a constant residue (Patlak et al. 1983). Compartmental model forms, e.g. one compartment (1C) Kety-Schmidt (Kety & Schmidt 1945) model for water the two compartment (2C) Huang-Sokoloff (Phelps et al. 1979) model for ^{18}F-FDG in brain, represent residues by positive linear combination of exponentials.

In the 6-parameter 2C model there is additive adjustment for arterial signal. By adding a very sharp residue element to the two exponential form, a Meier-Zierler residue is also available for this model. This allows residue

defined metabolic parameters for the extended compartmental model to be evaluated via the decomposition shown in Figure 4.1, (O'Sullivan et al. 2014). In the case of the 2-compartmental model, relation between these variables and underlying compartmental model parameters $(f_b, K_1, k_2, k_3, k_4)$ is described in (O'Sullivan et al. 2009) - Tables 1-3 of (O'Sullivan et al. 2009). Further discussion of this is provided in (O'Sullivan et al. 2014, 2021). Note that the K_1 parameter in the 2C model is often referred to as a flow. But this flow is focused on transport of FDG atoms across the capillary and cellular membranes on route to the cellular space. In contrast, by choice of t^* the flow variable - Blood Flow (BF) here is focuses on flow within the vasculature supply network. As such the BF, a simple scale of blood volume parameter (V_b), is more comparable to the flow that would normally be ideally assessed using a PET-H_2O study. Note that in Figure 4.1, the time scale $t^* = 15s$ is used to identify tracer atoms whose transit time duration of stay is considered to be in vascular transport, i.e. negligible crossing of capillary membranes and incorporation into a cellular environment. Physiologically this might be considered reasonable given that mean cerebral vascular transit time in the brain (a very well studied case) is typically on the order of 6 seconds. From equation 3.18, as t^* in Figure 4.1 and k_4 tends to zero and the duration for the dynamic scan (T_e) increases, we have

$$V_b = f_b \; ; \; V_d = (1 - f_b)\frac{K_1}{k_2 + k_3} \; ; \; K_d = (1 - f_b)\frac{K_1 k_2}{k_2 + k_3} \; ; \; K_i = (1 - f_b)\frac{K_1 k_3}{k_2 + k_3} \tag{4.1}$$

4.2.2.3 Compartmental Model Kinetic Analysis

The well-established 2-compartmental Sokoloff-Huang model for FDG, including delay and fraction blood volume, has 4 rate constant (K_1, k_2, k_3, k_4), a delay (Δ) and a fractional blood volume term f_b. As discussed in (Phelps et al. 1979) the sum of ^{18}F activity in the extra-vascular tissue compartments of the 2C model (C_M) is a convolution between local arterial blood signal, and a bi-exponential form $i.e.$

$$C_M(t|K_1, k_2, k_3, k_4) = R_M \otimes C_p(t) \;\; \text{with} \;\; R_M(t) = K_1(1 - \pi)e^{-t\phi_1} + K_1\pi e^{-t\phi_2} \tag{4.2}$$

with $\phi_{1(2)} = (1/2)\left((k_2+k_3+k_4) \pm \sqrt{(k_2+k_3+k_4)^2 - 4k_2k_4}\right)$ and $\pi = (k_3+k_4-\phi_2)/(\phi_1-\phi_2)$. Note $0 < \phi_2 < \phi_1$, so the second exponential in R_M represents the slower component of the kinetics. Following the development in Chapter 3, the resolution of a discretely sampled C_p function is limited, so it is possible to represented it, to any computationally meaningful numerical precision, as the convolution between C_p and a sharp triangular residue of sufficiently short duration (O'Sullivan et al. 2021)

$$R_\delta(t) = \begin{cases} \frac{2}{\delta}(1-t/d) & ; \ 0 \le t \le \delta \\ 0 & ; \ \text{otherwise} \end{cases} \tag{4.3}$$

In formal terms, the sharp residue, R_δ, behaves as a finite resolution analogue of Dirac's delta-function. With this, the 6-parameter, $\theta = (\Delta,\ f_b\ , K_1\ , k_2\ ,\ k_3\ ,\ k_4)$, compartment model prediction of the tissue time-course activity ($C_T(t|\theta)$) is equivalently expressed in terms of a Meier-Zierler tissue residue function.

$$C_T(t|\theta) = f_b C_p(t-\Delta) + (1-f_b) C_M(t-\Delta|K_1,k_2,k_3,k_4) \equiv \int_0^t R_C(t-s) C_p(s-\Delta) ds \tag{4.4}$$

where $R_C(t) = \alpha_0 R_\delta(t) + \alpha_1 e^{-t\phi_1} + \alpha_2 e^{-t\phi_2}$ with $\delta < 1$ second and $\alpha_0 = f_b$, $\alpha_1 = (1-f_b)K_1(1-\pi)$ and $\alpha_2 = (1-f_b)K_1\pi$.

The Broyden-Fletcher-Goldfarb-Shanno algorithm as implemented in the *optim* function in R (R Core Team 2021) is used for optimization of the 2C model. For fixed delay, the numerical optimimization. is focused on the two intrinsically non-linear rate parameters (ϕ_2, ϕ_1), defining the bi-exponential impulse-response of the 2C - see equation (4.2). Let $\{z(t_j), j = 1, ..., J\}$ be the data time-course. Using the parameterization in equation (4.4) and Δ fixed, the objective function, $g(\cdot,\cdot|\Delta)$, for model optimization of the rates is

$$g(\phi_1,\phi_2|\Delta) = \text{Min}_{\{\alpha_0\ge 0,\alpha_1\ge 0,\alpha_2\ge 0\}} \left\{ \sum_{j=1}^{J} w_j [z(t_j) - C_T(t_j|(\Delta,\alpha_0,\alpha_1,\alpha_2,\phi_1,\phi_2)]^2 \right\} \tag{4.5}$$

where the weight, w_j, is proportional to the product of frame duration and the decay correction factor used to convert raw counts to decay-corrected tracer activity. The evaluation of g for any (ϕ_1, ϕ_2), uses quadratic programming for determination of $(\alpha_0, \alpha_1, \alpha_2)$. This is similar to the method used

for determination of the α-coefficients in the NP model in equation (1).

Although $g(\phi_1, \phi_2|\Delta)$ is not guaranteed to be convex in (ϕ_1, ϕ_2), it is infinitely differentiable. In our experience it is also typically quasi-convex. As such, it is a very good candidate for application of the Broyden-Fletcher-Goldfarb-Shanno algorithm. Figure 4.7 demonstrates the well-behaved nature of the objective function and the reliability of the Broyden-Fletcher-Goldfarb-Shanno algorithm for the 2C modelling results presented in Figure 4.3 of the paper and also for a randomly chosen voxel in each of the VOIs in that data set. This supports the reliability of choice of optimizer used.

4.2.2.4 Non-parametric Residue Mapping (NPRM) of Kinetics

This method approximates the voxel-level residue by positive linear sum of basis elements that have been selected by a cross-validation guided analysis of a comprehensive collection of time-courses produced by segmentation of all the available dataset in the study (O'Sullivan et al. 2014, 2021). Individual basis elements are of the form $\mu_k(t) = \int_0^t R_k(s)C_p(s - \Delta_k)ds$ for $k = 1, ..., K$. Here C_p is the arterial input function (AIF), R_k is the basis element residue and Δ_k is its associated delay factor. Note cross-validation is used to select the number (K) (O'Sullivan et al. 2021). Given the basis set, PET-measured voxel-level time-course data over the available set of J time-frames, $\{z(t_j), j = 1, 2, ..., J\}$, is expressed as

$$z(t_j) = \alpha_1\mu_1(t_j - \delta) + ... + \alpha_K\mu_K(t_j - \delta) + \epsilon(t_j) \tag{4.6}$$

Here δ and $(\alpha_1, \alpha_2, ..., \alpha_K)$ are the unknown voxel-level delay and basis amplitude parameters and $\epsilon(t)$ represents (random) model error. A weighted least squares criterion, with weights proportional to the product of frame duration and the decay correction factor used to convert raw counts to decay-corrected tracer activity, is used for optimization of the unknown parameters. For any delay, the optimal set of α-coefficients is found by quadratic programming. A crude grid-search is used to optimize delay (O'Sullivan et al. 2021).

4.2.2.5 Bootstrap Assessment of Uncertainty

Model residuals across (N) voxels and (J) time-frames, $\{z_i(t_j) - \hat{z}_i(t_j); i = 1, ..., N; j = 1, ..., J\}$, are used to construct an image-domain data generation process (DGP) for bootstrapping. The DGP generates data according to

$$z^*(t_j) = \hat{z}(t_j) + \epsilon^*(t_j) \tag{4.7}$$

where $\hat{z}(t_j) = \hat{\alpha}_1\mu_1(t_j - \hat{\delta}) + ... + \hat{\alpha}_K\mu_K(t_j - \hat{\delta})$ and the simulated error process, ϵ^*, mimics the stochastic character of analysis residuals. Analysis of bootstrapped data sets arising from the DGP leads to a set of bootstrapped kinetic parameter values at each voxel. The standard deviation of these values estimates the voxel-level standard error (SE) of the kinetic parameter. Similarly, the SEs for more complex quantities such as the maximum intensity projection (MIP) for a kinetic map is created as the standard deviation of the bootstrapped MIPs of the kinetic parameter - an example is shown in Figure 4.2. Numerical studies in (O'Sullivan et al. 2021, Gu et al. 2021*b*) have shown that image-domain DGP bootstrapping matches the accuracy of the much more computationally intensive list-mode bootstrapping approach of Haynor and Woods (Haynor & Woods 1989). The number of bootstrap simulations impacts the accuracy of SEs it produces (Efron & Tibshirani 1994), this is discussed in 4.4.

4.2.2.6 Analysis of Fitting VOI Time-Course Data

Suppose the time course is $\{z(t_j), j = 1, ..., J\}$ and the model predicted time-course for a given set of model parameters, θ, is denoted $\{m(t_j|\theta), j = 1, ..., J\}$. As a function of θ, weighted residual sum of squares is defined as

$$WRSS(\theta) = \sum_{j=1}^{J} w_j[z(t_j) - m(t_j|\theta)]^2 \tag{4.8}$$

$\hat{\theta}$ is the optimized parameter vector and the corresponding model-predicted time-course is demoted $\hat{z}(t_j) = \{m(t_j|\hat{\theta})$ for $j = 1, ..., J\}$. The tissue residue function associated with the model, $m(\cdot|\hat{\theta})$, is used to recover a corresponding set of kinetic parameters, $(\hat{V}_b, \hat{V}_d, \hat{K}_d, \hat{K}_i, \widehat{\text{MTT}}, \widehat{\text{Ext}})$ - c.f. Figure 4.1,.

The mean time-course for a VOI is the average of the time-courses for all

voxels in that VOI, $i.e.$

$$z(t) = \frac{1}{\#\text{VOI}} \sum_{i \in VOI} z_i(t) \tag{4.9}$$

where #VOI denotes the number of voxels in the VOI. Analysis of the VOI time-course using a non-parametric (NP) or two-compartment (2C) involves minimization of the weighted residual sum of squares difference between the VOI time-course are either the NP or 2C model. The resulting model predicted time-courses are referred to as VOI-NP and VOI-2C, respectively - see Figure 4.3 and Tables 4.1 and 4.2. When a voxel-level times-course, $\{z_i(t_j), j = 1, ..., J\}$, is analyzed, the resulting model-predicted time-course is denoted $\{\hat{z}_i(t_j), j = 1, ..., J\}$. Averaging these voxel-level predictions over the VOI provides an alternative fit to the VOI time-course

$$\hat{z}(t) = \frac{1}{\#\text{VOI}} \sum_{i \in VOI} \hat{z}_i(t) \tag{4.10}$$

Voxel-NP and Voxel-2C in Figure 4.3 and Tables 4.1 and 4.2. The additional flexibility in voxel-wise fitting would generally lead to improved fitting of the overall VOI. However, a cruder grid-search procedure is used for optimisation of delay at the voxel-level and this may occasionally lead to VOI data being better fit by analysis of the VOI time-course.

4.2.3 Statistical Analysis

NPRM kinetic analysis with 25 bootstrapped simulations was evaluated for each of the studies in the series. Results were examined in four separate ways.

4.2.3.1 Representation of VOI Time-Course Data

VOI-mean time-course data were compared to the corresponding VOI-mean of the fitted (NPRM) voxel-level time-courses - $\hat{z}(t_i)$ in equation (4.7). Mean VOI time-course data were also analyzed using the non-parametric model as well as with the Huang-Sokoloff two-compartment (2C) including a fractional blood volume and delay of the AIF. To facilitate fitting, a wide range of delays - ± 5 minutes - were allowed in the NPRM and 2C analysis of the VOI time course data. The Broyden-Fletcher-Goldfarb-Shanno algorithm as

implemented in the *optim* function in R (R Core Team 2021) is used for optimization of the 2C model.

Results of alternative analyses for a sample case are presented graphically. Formal comparisons are focused on the weighted residual sums of squares (WRSS) misfit achieved with alternative analyses. The mean relative difference between alternative representations of VOI time-course data and associated standard deviation is evaluated for each VOI type. For a given VOI type, the scale of WRSS values vary with dose. As a result comparisons between alternative fits of VOI time course are based on the percent relative deviations in the WRSS criterion. For a particular VOI type, the percent relative differences VOI-NP vs Voxel-NP and VOI-2C vs Voxel-NP on the k'th VOI data set are calculated as follows

$$D1_k = \text{VOI-NP vs Voxel-NP} = (\frac{\text{WRSS}_{\text{VOI-NP}}}{\text{WRSS}_{\text{Voxel-NP}}} - 1) \times 100\% \quad (4.11)$$

$$D2_k = \text{VOI-2C vs Voxel-NP} \quad = (\frac{\text{WRSS}_{\text{VOI-2C}}}{\text{WRSS}_{\text{Voxel-NP}}} - 1) \times 100\% \quad (4.12)$$

For $k = 1, ..., n_K$. Here n_K is the number of VOIs (typically 24) of the given type. There is substantial variation in relative deviation values. Statistical inference is based on the mean deviations and associated standard deviation.

4.2.3.2 VOI Kinetics

Means and standard deviations of VOI-averaged NPRM kinetics are reported for each VOI type. Quantitative statistical analysis is based on direct paired comparison between values produced by alternative methods. Kinetics based on non-parametric and 2C analysis of VOI mean time-course data are similarly summarized in Table 4.2. Given the non-Gaussian character of the paired differences, deviations between alternative VOI kinetic values are summarized and their statistical significance evaluated using the paired Wilcox test.

4.2.3.3 DGP Model

The bootstrap DGP is expressed in more detail as

$$z_i^*(t_j) = \hat{z}_i(t_j) + \hat{\sigma}_e \hat{\psi}_i \hat{\phi}_j \epsilon_i^*(t_j) \tag{4.13}$$

where the random errors, $\epsilon_i^*(t)$, have unit standard deviation and $\hat{\sigma}_e$ is an overall noise scale of the model error. In equation (4.13), the factors $\hat{\psi}_i$ and $\hat{\phi}_j$ are scale-free quantities representing the relative uncertainty across voxels (i) and time-frames (j). The random errors, $\epsilon_i^*(t_j)$ are produced using quantile-based transformation of a stationary Gaussian process. The stationary Gaussian process is independent across time-frames (j) with common spatial auto-covariance whose associated 3-D spectral density is estimated from analysis of transformed model residuals. As the PET-measured activity scales with dose, the DGP error scale ($\hat{\sigma}_e$) should also scale with dose - this is examined graphically. The overall axial pattern variation is described by the spatial scale factor $\hat{\psi}_i$. In a uniform cylindrical phantom this has a familiar U-shaped pattern related to scanner sensitivity - e.g. (O'Sullivan et al. 2021). With a patient in the scanner, the distribution of activity and attenuation is far from uniform. Physiologic patient motions, such as breathing, may also impact axial variation. Skewness is a key feature of iteratively reconstructed PET data. A histogram of scaled resdiuals shows how the DGP captures this aspect. After adjustment for spatial scale-factors, the 3-D power spectrum of the normalized residual process provides insight into the effective resolution of the scanning. Co-ordinate-wise auto-correlation functions (ACF) associated with the spectrum, give insight into the actual resolution of the scanner. Again, physiologic movements may well lead to the actual resolution deviating from what might be predicted based on static phantom measurements.

4.2.3.4 Log-Linear Modelling of VOI SEs

A standard multivariate linear regression model in which N-dimensional data y is expressed as a linear combination of columns of an $N \times K$ dimensional matrix X subject to weighted errors can be expressed as

$$y = X\theta + w^{-1/2}\epsilon \tag{4.14}$$

where the errors are independent with mean zero and constant variance (σ^2). The weighted least squares estimates of the unknown coefficients θ, are given by $\hat{\theta} = [X'WX]^{-1}X'Wy$ and the variance-covariance matrix of these coefficients is $\sigma^2[X'WX]^{-1}$. A derived parameter, such as $c'\theta$ - a linear combination of θ, is estimated by $c'\hat{\theta}$ and its standard error is estimated by $\hat{\sigma}\sqrt{c'[X'WX]^{-1}c}$, where $\hat{\sigma}^2$ is the weighted residual sum of squares (WRSS) difference between the data and the weighted least squares model fit $\hat{y}$ - WRSS $= \frac{1}{N}\sum_i w_i[y_i - \hat{y}_i]^2$. Thus

$$\log(\text{SE}) = .5\log(\text{WRSS}) + .5\log(c'[X'WX]^{-1}c) \tag{4.15}$$

While NP-voxel fitting of PET VOI data is more complex than the standard multivariate linear model, analogy with the linear model motivates an approach to empirical modelling of the bootstrap-estimated standard errors for VOI kinetics. Standard errors for VOI kinetics are represented by the dataset $\{\text{SE}_{rjp}$ for $r = 1, ..., n_j; j = 1, ..., 9$ and $p = 1, ..., P\}$. Here p represents a parameter -*i.e.* on of $(V_b, V_d, K_d, K_i, \text{MTT}, \text{Ext})$, j is the VOI type - (GM, WM, Lung, Liver, Spleen, Kidney, Bladder, Bones, Tumor) and r is an instance for the VOI type - mostly $n_j = 24$ but for Tumor VOIs there are more instances when than one lesion VOI is acquired within a given patient. In modelling the VOI SE the kinetic profile for the VOI is summarised using the variables: $(K_1 = K_d + K_i, K_i, \frac{V_b}{V_b+V_d}, \text{Ext} = \frac{K_i}{K_1})$. Our log-linear model expresses the logarithm of the SE as a linear combination of these variables on a logarithmic scale.

$$\begin{aligned}\log(\text{SE}_{rjp}) \approx\ & \alpha_j + \beta_{1p}\log(\text{WRSS}^{rj}) + \beta_{2p}\log(K_1^{rj}) + \beta_{3p}\log(K_i^{rj}) \\ & + \beta_{4p}\log(\frac{{V_b}^{rj}}{{V_b}^{rj} + {V_d}^{rj}})) + \beta_{5p}\log(\text{Ext}^{rj})\end{aligned} \tag{4.16}$$

Here the β_1 captures the impact of VOI the kinetic analysis modelling error - WRSS^{rj}; $\beta_{2p} - \beta_{5p}$ model the effect of the VOI kinetic profile of the SE for each of kinetic parameters (p). Overall adjustment for each VOI type is captured by α_j. The fitted log-linear model produces predictions, $\widehat{\text{SE}}_{rjp}$. These predictions are compared to the measured values SE$_{rjp}$, both directly and also on a logarithmic scale. The quality of the predictions are summarized

by correlation values.

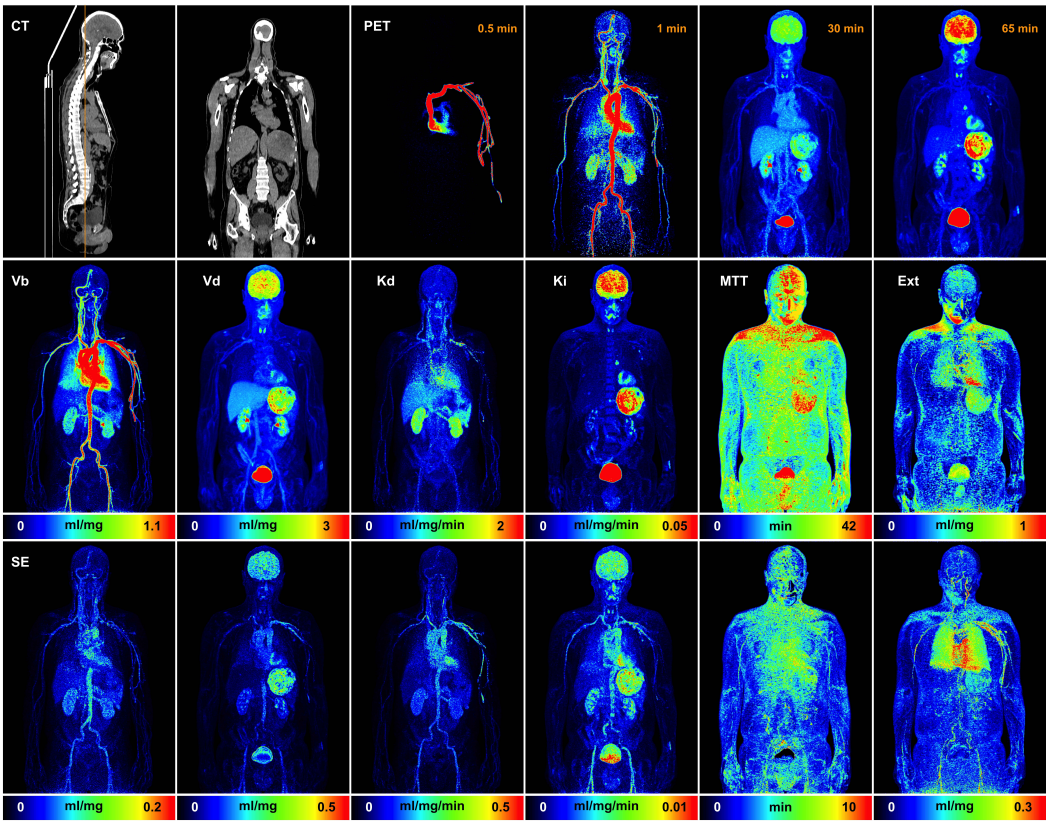


Figure 4.2: MIP maps of NPRM kinetic parameters including associated SEs. SEs are based on the standard deviation of MIP results for each of 25 bootstrap replications. Top-row: CT images for a selected cross-sections through the volume and PET MIP maps at indicted times.

4.3 Results

4.3.1 Illustration

Sample kinetic maximum intensity projection (MIP) maps with associated SEs obtained using the NPRM technique and bootstrapping are shown in Figure 4.2, a video of rotation MIP maps is provided at (https://doi.org/10.2967/jnumed.123.266686). Note the data set is the same as that used in (Sari et al. 2022*b*). The results are of high quality, well aligned with the vascular and metabolic ^{18}F-FDG patterns expected for key organ structures like the brain, liver, kidneys, spleen etc - c.f. (Sari et al. 2022*b*). It is clear that the uncertainties of V_b, V_d, K_d and K_i are generally higher for regions

with larger magnitudes for the kinetic variable. This is perhaps related to the fact that these parameters, which linear functions of the fitted voxel-level residue, ultimately scale with the magnitude of the time-course data. MTT and Ext deviate somewhat from this pattern. This is likely to be related to the fact that both MTT and Ext are defined in terms of ratios of the V_d, K_d and K_i variables and as a result do not necessarily scale with the voxel time-course. The large blood vessels are seen to impact the structure of the MIP uncertainty for several parameters. The algorithms developed allowed kinetic mapping, including the bootstrapping process to be achieved in a timely fashion. On a single 3.2 GHz processor the compute-time for the NPRM kinetic analysis including definition of the DGP was 140 mins; each bootstrap replicate took 80 mins.

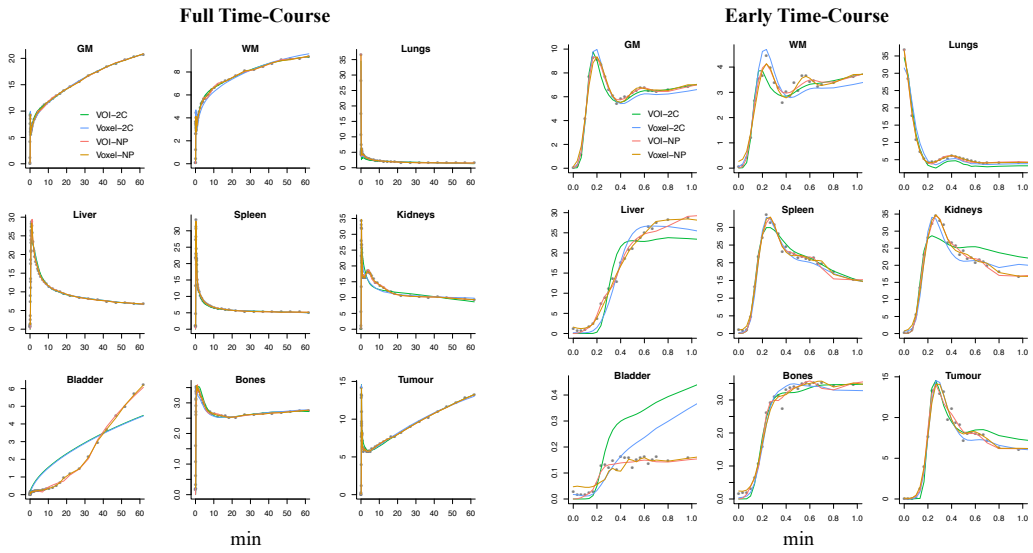


Figure 4.3: Results of four fitting procedures to the VOI time-course data in Figure 4.2. Data are points, line-colors correspond to methods used [top-left]. Full time course on the left; first minute on the right.

4.3.2 Representation of VOI Time-Course Data

The full time-course as well as the time-course over the first minute of data acquisition are shown in Figure 4.3. Average VOI time-course data are fit directly using the NP and 2C models; averages of voxel-level fits are also provided. This gives a reference to the results reported in (Sari et al. 2022*b*). Although the 2C fitting of some VOIs are reasonable, *e.g.* grey and white

Table 4.1: VOI time-course fitting across all 24 studies. Mean and standard deviations of the WRSS deviations between the VOI time-course and the VOI average of voxel-wise (Voxel-NP) and direct NP (VOI-NP) and 2C (VOI-2C) fits of the VOI time-course are shown. Last two columns summarize mean and standard deviation of percent deviations between WRSS values of Voxel-NP and VOI-NP fits, and between Voxel-NP and VOI-2C values.

Region(VOI)	Size ($\times 10^3$ voxels) $1\ voxel = 1.65 \times 1.65 \times 1.65 mm^3$	Voxel-NP	VOI-NP	VOI-2C	Voxel-NP *vs* VOI-NP	Voxel-NP *vs* VOI-2C
GM	122.5±23.3	0.02±0.06	0.04±0.14	0.09±0.26	35± 50	161± 216
WM	18.8±7.0	0.02±0.04	0.02±0.02	0.06±0.20	25± 32	141± 117
Lung	434.5±124.2	0.06±0.27	0.08±0.69	0.10±0.29	70± 76	448± 690
Liver	233.0±66.1	0.08±0.08	0.07±0.08	0.55±0.30	46± 39	865± 453
Spleen	42.8±48.5	0.10±0.11	0.11±0.16	0.13±0.09	69± 40	64± 87
Kidney	40.5±10.7	0.27±0.26	0.35±0.56	1.83±1.29	83± 45	880± 576
Bladder	234.9±81.6	0.04±0.10	0.07±0.77	3.25±3.04	887±783	18266±14809
Bones	306.2±82.7	0.002±0.003	0.002±0.003	0.007±0.01	35± 23	327± 206
Tumour	2.5±7.4	0.21±0.25	0.23±0.51	0.67±3.77	28± 31	231± 250

matter, there are clearly some VOIs where 2C modelling is substantially inferior -e.g. kidney, liver, bone and bladder. The data fit achieved by the VOI averaging of the voxel-level NP fit is quite good, overall and especially over the first 1-minute of acquisition. But it is important to appreciate that almost half the total number of frames occur in the first 80 seconds. For this example, over the first minute differences between the VOI average of the voxel-wise 2C fits and the fit of the 2C model to the mean of the VOI time-course data are quite pronounced. In contrast, differences between the corresponding NP fits are much smaller.

Quantitative summaries of the NP fitting of VOI time-course data and comparisons with direct analysis of the mean VOI time-course data using NP and 2C analysis are presented in Table 4.1. While WRSS fit values for VOIs are similar based on the VOI average of voxel-level NP fits or by direct fitting of the VOI time-course data, there is a marked increase in WRSS fits when the VOI time-course is approximated using the best fitting 2C model. VOI time-course fitting by the NP model is consistently improved by averaging voxel-level NP fits, the percent improvement is a modest 50%. VOI

time-course fitting by the 2C model is substantially worse than NP fitting. The mean percent improvement here is almost 390%.

Table 4.2: VOI Kinetics (mean± standard deviation) recovered using different methodologies. VOI averaged voxel kinetics are in the top panel; kinetics obtained by analysis of the VOI time-course using the NP model and 2C model are shown in the middle (VOI-NP) and bottom (VOI-2C) panel. Significance of deviations from Voxel-NP values, evaluated by the paired Wilcoxon test, are indicated by $*, **$ and $***$ for p-values less than 0.05, 0.01 and 0.001, respectively.

Method	Region(VOI)	V_b mL/g	V_d mL/g	K_d $mL/min/g$	K_i $mL/min/100g$	MTT min	Ext %
Voxel-NP	GM	0.05±0.01	0.88±0.26	0.16±0.03	3.01±0.81	5.80±1.64	18.38±5.18
	WM	0.03±0.01	0.64±0.27	0.10±0.03	1.09±0.33	6.61±2.04	12.30±4.12
	Lung	0.18±0.04	0.09±0.03	0.03±0.01	0.07±0.04	3.17±0.77	3.17±1.82
	Liver	0.09±0.04	0.86±0.08	0.54±0.11	0.23±0.08	1.77±0.41	0.57±0.38
	Spleen	0.21±0.09	0.42±0.09	0.41±0.14	0.23±0.16	1.39±0.54	1.14±2.09
	Kidney	0.25±0.07	1.20±0.34	0.49±0.11	0.42±0.25	2.62±0.60	1.22±0.97
	Bladder	0.00±0.01	0.54±0.32	0.04±0.03	1.46±1.13	6.73±2.85	19.11±11.36
	Bones	0.03±0.02	0.22±0.07	0.08±0.02	0.27±0.08	3.54±0.79	4.66±1.32
	Tumour	0.08±0.05	0.65±0.38	0.19±0.08	2.33±1.59	3.62±1.57	12.93±6.44
VOI-NP	GM	0.04±0.01***	0.58±0.16***	0.13±0.03***	3.25±0.89***	4.53±1.19***	20.13±5.42
	WM	0.02±0.01***	0.58±0.31**	0.09±0.03	1.10±0.38	5.99±2.25**	10.96±4.37
	Lung	0.17±0.04**	0.08±0.03*	0.03±0.02	0.08±0.04**	2.43±0.65***	2.66±1.48
	Liver	0.05±0.04***	0.83±0.07*	0.53±0.13	0.28±0.08***	1.64±0.39***	0.57±0.24
	Spleen	0.18±0.09**	0.39±0.11*	0.46±0.17*	0.29±0.19***	0.91±0.22***	0.86±1.38*
	Kidney	0.23±0.08	1.19±0.37	0.51±0.15	0.30±0.26*	2.46±0.82	0.62±0.51***
	Bladder	0.00±0.01***	0.44±0.29**	0.03±0.03***	1.61±1.21**	13.85±11.15***	33.87±26.48***
	Bones	0.01±0.01***	0.17±0.08***	0.08±0.03	0.29±0.07***	2.24±0.50***	3.80±0.90**
	Tumour	0.07±0.04***	0.45±0.34***	0.18±0.09*	2.48±1.62***	2.62±1.59***	13.27±7.68
VOI-2C	GM	0.03±0.01***	0.56±0.23	0.09±0.02***	3.12±0.87**	5.91±1.71*	26.41±6.41***
	WM	0.02±0.01***	0.55±0.16	0.05±0.01***	1.13±0.32	11.00±3.23***	18.65±4.48***
	Lung	0.15±0.04***	0.09±0.03*	0.04±0.01**	0.07±0.04*	1.18±1.44***	1.70±0.83***
	Liver	0.02±0.01***	0.88±0.09***	0.53±0.13	0.23±0.08***	1.68±0.33	0.45±0.21***
	Spleen	0.11±0.05***	0.49±0.12***	0.61±0.18***	0.21±0.21***	0.73±0.32***	0.69±1.97***
	Kidney	0.15±0.05***	1.25±0.36*	0.42±0.11**	0.21±0.22*	2.81±1.18*	0.52±0.54
	Bladder	0.00±0.00	0.05±0.10***	0.01±0.02***	1.63±0.95	1.66±5.36***	86.89±29.33***
	Bones	0.00±0.00***	0.20±0.06**	0.08±0.03	0.26±0.07***	2.65±0.65***	3.53±0.94*
	Tumour	0.05±0.05***	0.34±0.19	0.17±0.10	2.38±1.50*	1.80±1.26**	16.83±18.38

4.3.3 VOI Kinetics

VOI kinetics are reported in Table 4.2. Statistically significant deviations between the kinetics recovered by alternative methods are largely linked to early time-course parameters - c.f. Figure 4.1 - particularly blood volume. Deviations between voxel-averaged parameters and values recovered from NP and 2C analysis of the VOI time-course are much smaller for NP than with 2C. But it is noteworthy that for most VOIs flux values (K_i) are quite similar in magnitude across all three analyses. This might be because flux is a late time-course parameter- c.f. Figure 4.1 - and alternative methods fit the late time-course quite similarly - c.f. Figure 4.3.

4.3.4 DGP Model

Figure 4.4 shows an expected linear relation between the scale of the DGP and study dose - the linear correlation of 0.68 and is highly significant. The axially averaged spatial scale of the DGP increases towards the top and bottom of the patient in the FOV. As expected the increased scale is not just a function of the nominal sensitivity but is clearly impacted by patient-specific factors including the varying uptake, attenuation and perhaps any impacts of small patient movements. The skewed nature of random fluctuations in the DGP model, which vary based on the data coefficient of variation, are fully consistent with patterns for iteratively reconstructed PET data - c.f. (Mou et al. 2017, O'Sullivan et al. 2021).

As reviewed in (Gu et al. 2021*a*) error characteristics of reconstructed PET data have been shown to have a skewness pattern that tends to vary depending on the data coefficient of variation (COV). (Mou et al. 2017) used a Gamma-distribution to describe this type of behaviour. In the bootstrap DGP, the error distributions are varied according to the inverse of a COV measurement ($\hat{\kappa}_{ij}$). For a given voxel (i) and time-frame (j), the COV measure is defined as, $\hat{\kappa}_{ij} = \frac{\hat{z}_i(t_j)}{\hat{\psi}_i\hat{\phi}_j}$, the data expected value divided by the data standard deviation. The value of $\hat{\kappa}_{ij}$ determines the distribution for the simulated error value by a quantile transform. The transform converts the Gaussian variable, η^*_{ij}, produced as part of the simulation of the underlying stationary Gaussian process, $\{\eta^*_{ij}, i = 1, ..., N, j = 1, ..., J\}$, using a normal quantile function that will produce a value, $\epsilon^*_i(t_j)$, whose distribution

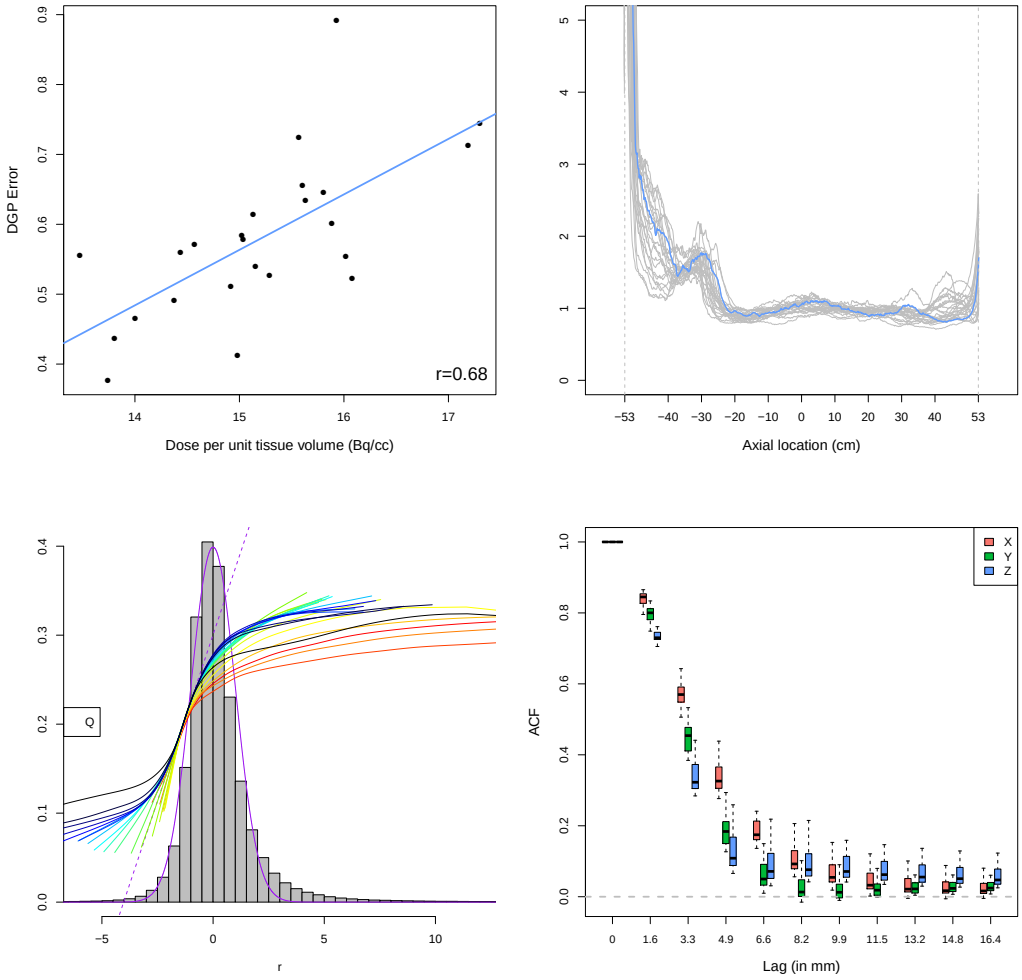


Figure 4.4: Elements of Bootstrap DGP - equation (4.7). (a) DGP scale, $\hat{\sigma}_e$, versus injected dose per unit tissue voxel, (b) Axially averaged scale, (c) The histogram is the overall residual distribution - pooling residuals regardless of $\hat{\kappa}$ values. The y-axis is in density units. The solid purple line is a standard Gaussian to this histogram. The linear quantile for the standard Gaussian is shown with the dashed purple line. Normal quantile functions (coloured lines) for used in the bootstrap DGP to map simulated Gaussian process variables, η^*_{ij} to the values ϵ^*_{ij} in equation (4.13). Different solid coloured lines (NIH colors from black to red) correspond to quantile transforms over different ranges for the COV measure $\hat{\kappa}$ - black for lowest $\hat{\kappa}$ and red for the largest $\hat{\kappa}$ range. The higher $\hat{\kappa}$ range have quantiles that are linear (Gaussian) on the left and quite flat on the right - this corresponds to a right-skewed error distribution pattern; lower $\hat{\kappa}$ values are more heavy-tailed than a standard Gaussian on the left and right. (d) Boxplot of directional (x-perpendicualar to scan table,z-axial) Spatial Correlation Patterns (ACF) across all studies.

matches the observed characteristics associated with residuals corresponding to COV values like $\hat{\kappa}_{ij}$. If the quantile transform is linear, the simulated data will also be Gaussian. Non-linearity in quantile transforms generates distributions can be highly non-Gaussian in form. In particular, skewness patterns in distributions associated with iteratively reconstructed data in low-count regions $e.g.$ short time-frames or areas with low detector sensitivity, are readily accommodated with this approach. Figure 4.4 shows a collections of quantile functions used in a DGP.

If the scanner data is viewed as the result of a convolution between an effective Gaussian resolution kernel and the underlying true image-domain signal. The Wiener-Khinchine theorem would predict the output ACF for an input white noise signal would have a Gaussian form with full-width at half-maximum (FWHM) equal to $\sqrt{2}$ times the FWHM of the effective resolution kernel. Thus the ACF FWHM divided by $\sqrt{2}$ is an overall measure of the effective FWHM resolution of the scanner. This calculation applied to the ACFs of the DGPs from patient data gives median x-,y-,z- direction resolutions of 5.32mm,4.35mm, and 3.67mm. The co-ordinate-wise ACF shows greater spatial persistence in the x (perpendicular to scanning bed) and z (axially) directions - c.f. Figure 4.5. These values are in reasonable agreement with the values reported in (Prenosil et al. 2022) based on measurement of a static phantom. The physiologic movements and activity variation in variation in a human study would may well lead to the actual resolution deviating from what might be predicted based on static phantom measurements.

4.3.5 SEs of VOI Kinetics

Standard errors of VOI kinetics (voxel-NP) are well approximated using a log-linear model that accounts for the VOI type, the VOI mean kinetics and the residual weighted RMSE of the voxel-NP fit of the VOI time-course - Figure 4.6. The overall correlation between the bootstrap-measured SE and the SE values predicted by log-linear modelling is 0.96 and are also seen to be quite high for individual kinetic parameters. In theory, uncertainty in parameters recovered by kinetic model fitting should be proportional to the scale of the residual model error but it may also be a function of the rele-

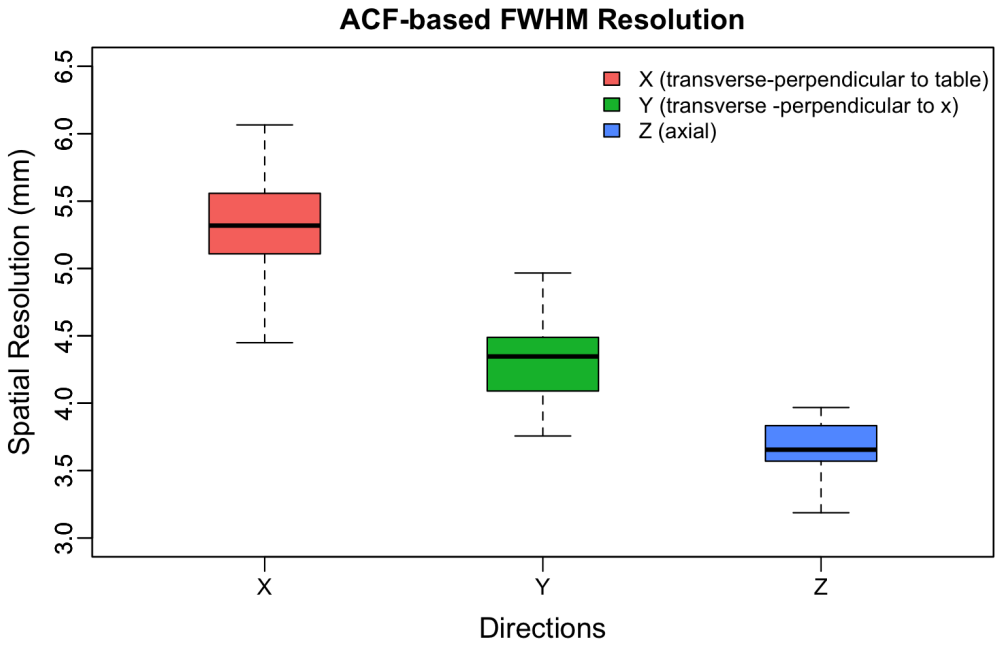


Figure 4.5: ACF-based measure of Scanner FWHM Resolution. Note this measure takes account of patient specific factors - activity distribution, positioning and movements associated with breathing etc - which may impact the 3-D resolution of data.

vant sensitivity matrix for the model. We examine the relation between the bootstrap assessment of VOI-mean kinetic standard errors (SE) and suitable explanatory factors including the WRSS fit of the VOI and the VOI-mean kinetic values. For each kinetic parameter linear regression analysis on a logarithmic SE scale is applied. Adjustment of this regression analysis based on the VOI-type and the kinetics are explored. Regression predictions of SEs are compared to the true, graphically and correlation values summarized.

4.4 Discussion

This work demonstrates the practicality of using image-domain bootstrapping for construction of patient-specific uncertainty assessment in kinetics variables for voxel, VOI and more complex derived quantities such as MIPs, from a whole-body dynamic PET-FDG study. This development creates a opportunity to incorporate uncertainty about a PET-guided kinetic biomarker that might be used to guide a clinical decisions for a patient. This could be particularly helpful in case where the biomarker value is close to a boundary

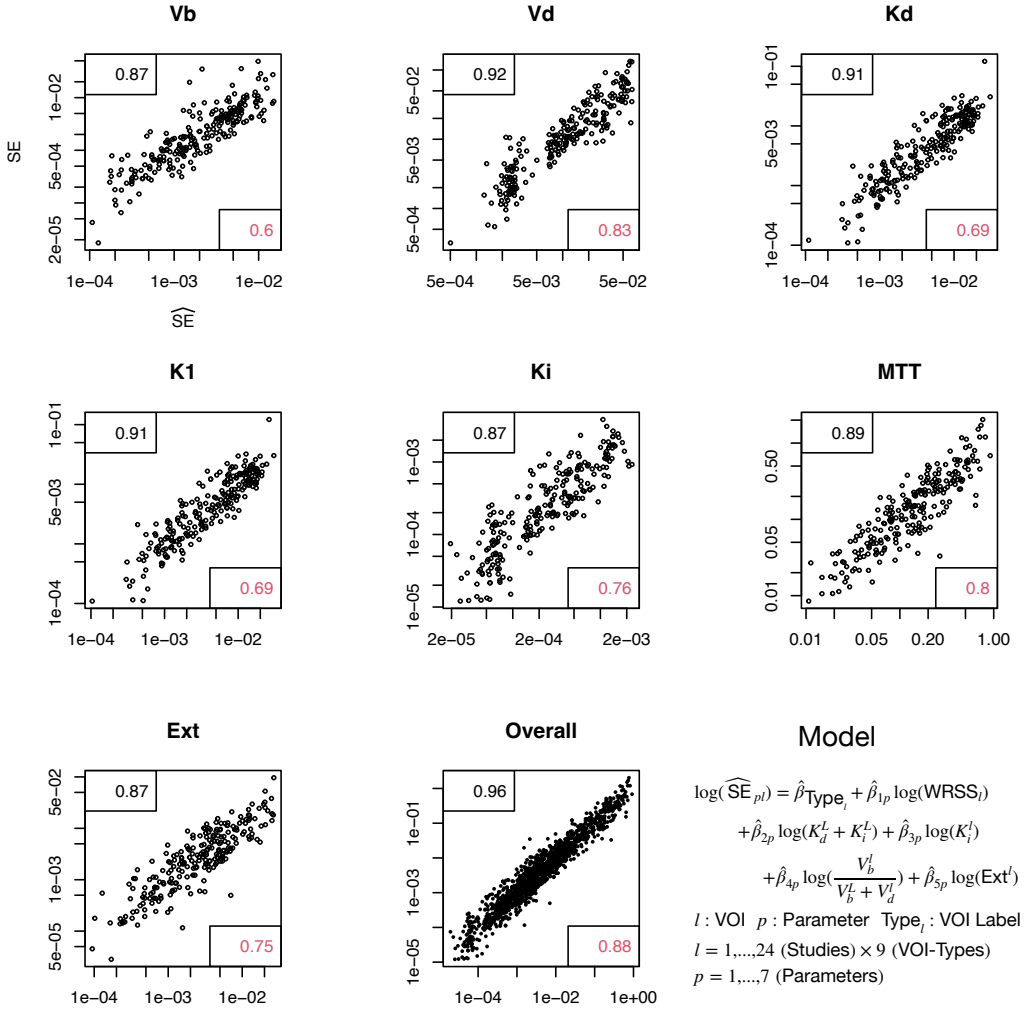


Figure 4.6: Prediction of VOI kinetic standard errors (SE - vertical axes) via a log-linear model prediction ($\widehat{SE}$ - horizontal axes) - formula indicated. Correlations in black are for logarithmic SE values; red for the raw scale.

between alternative treatment options.

Bootstrap reliability depends both on number of bootstrap simulations (N_B) used and on the accuracy of the representation of the data used in the DGP used (Efron & Tibshirani 1994). Computational resources dictate the choice of N_B. The results here are based on just $N_B = 25$ but for the data in Figure 4.2, a four fold increase in the number of bootstrap simulations leads to little difference in resulting voxel-level bootstrap standard errors. This is demonstrated in Figure 4.8. From (Efron & Tibshirani 1994), error in bootstrap is viewed as a sum of the DGP error and the sampling error

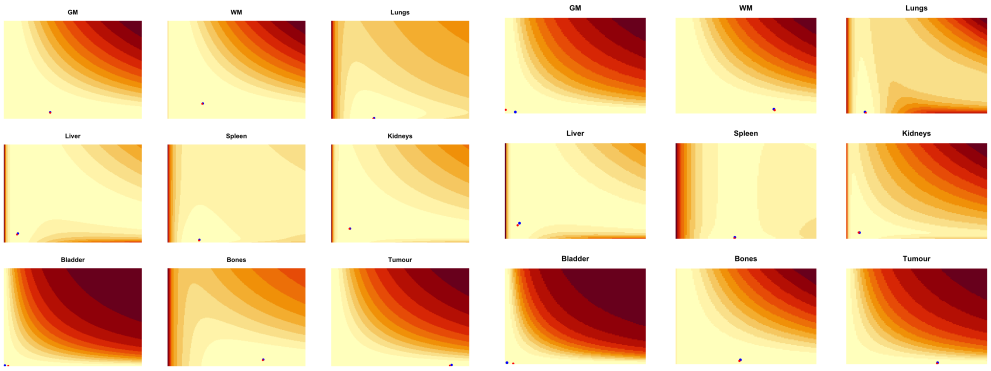


Figure 4.7: Contoured images of the reduced objective function in 2C-VOI analysis, $g(\phi_2, \phi_1|\Delta)$ in equation(4.5) with Δ fixed at the optimal value, over a fine grid of values for (ϕ_2, ϕ_1). Darker colors correspond to large values for the objective function. The minimum value of the objective function over the grid is the red point; the value determined by the Broyden-Fletcher-Goldfarb-Shanno algorithm is in blue. Two panels of results for 9 VOIs are shown. The left set is for the VOI data in Figure 4.3; the right set is for a time-course corresponding to a randomly selected voxel in each VOI. Note the colors in each image ranges from the minimum (bright yellow) to a maximum (dark red). In all cases the value of the objective function at the blue point is no bigger than its value at the red point, demonstrating the reliability of the algorithm.

associated with the number of simulations used - N_B. As sampling error behaves as $\frac{1}{\sqrt{N_B}}$ so a 4-fold increase in N_B would cut this component of the error in half.

Figure 4.3 and Table 4.1 clearly demonstrate benefit of using a non-parametric (NP) methodology in the DGP. Relative to the well-established 2C ^{18}F-FDG model, substantial and highly significant improvements in data representation are achieved using the NP approach. These benefits are mostly associated with the ability of the NP technique to capture the highly resolved early time-course pattern of data from the current generation of PET scanners. The generally more modest deviations between NP and 2C fits beyond the very early time-period, say after 1 minute, suggests that the deficiencies in the 2C model may primarily relate to the lack of sophistication in the representation of the vascular components of blood-tissue exchange (Li et al. 1997). The high temporal resolution of the scans here as well as the use of a bolus injection, contributes to the ability to scrutinize the 2C model ways that have likely not been possible in the past. The VOIs here are

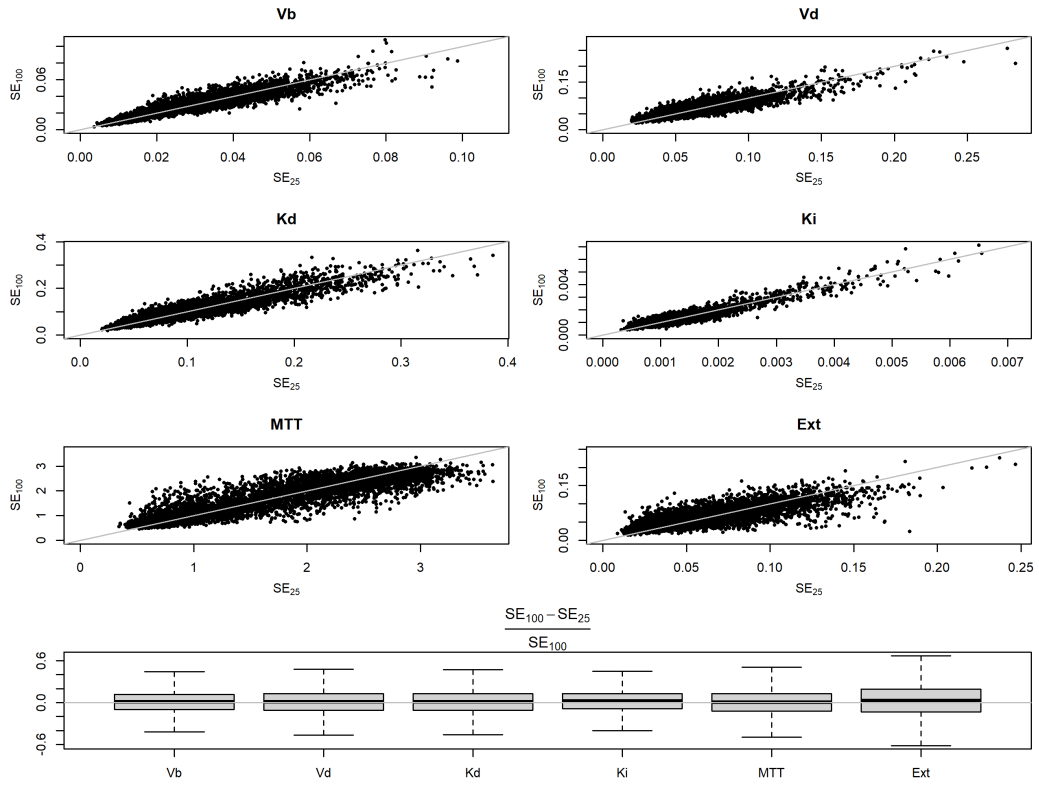


Figure 4.8: Comparison of bootstrap generated voxel-level SEs based on 25 and 100 bootstrap samples - SE_{25} and SE_{100}. Points correspond to 5000 voxels randomly sampled from each VOI. The boxplot shows the relative deviations between SE_{25} and SE_{100}. The mean absolute deviation is on the order of 10% for all parameters.

large and heterogeneous - far from the assumption of homogenous well-mixed compartments which underly the 2C model. But it is notable that (O'Sullivan et al. 2009) reported significant discrepancies between 2C and NP representation of dynamic ^{18}F-FDG brain data in normal subjects using much smaller and highly homogeneous VOIs. Similar to what is reported in Table 4.2 for grey matter and white matter, the discrepancies primarily impact the accuracy of the initial phase of the ^{18}F-FDG tissue residue - blood volume especially - but have must less impact on several other variables including flux and distribution volume. But statistically significant differences between voxel-NP and VOI-2C parameters does not imply that parameters are unrelated. For example, Figure 4.9 shows pairwise plots and summary correlations for the ^{18}F-FDG metabolic rate MR_{FDG} - flux scaled

by the plasma glucose see equation (4.4). The strong linear dependence in this figure, emphasises the importance of differentiating statistical and practical significance. Calculated flux values based on NP or 2C analysis would likely yield similarly effective diagnostic values. Indeed it is well appreciated that even simpler assessments of ^{18}F-FDG flux by Patlak and SUV are also highly effective too (Barrio et al. 2020*a*).

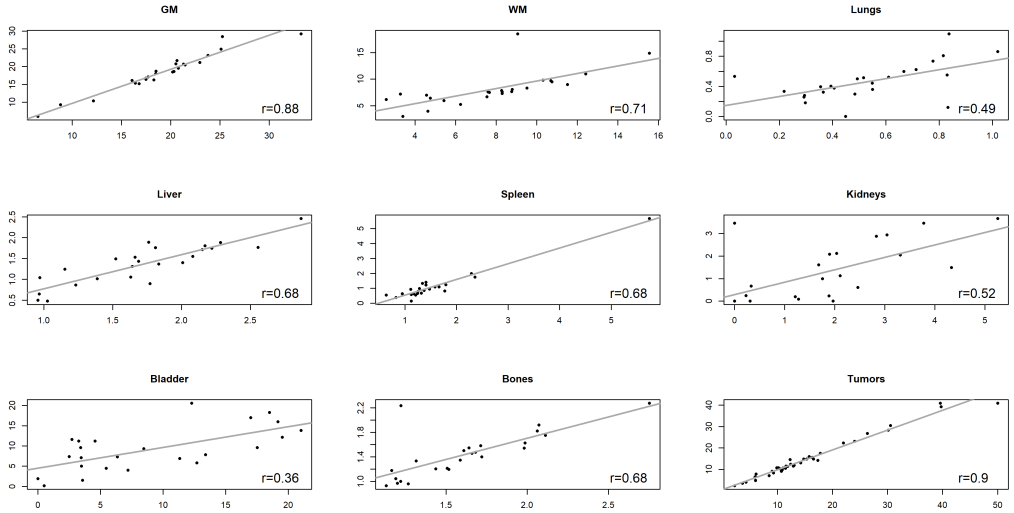


Figure 4.9: Pairwise plots for each VOI type of the relation between ^{18}F-FDG flux values (MR_{FDG}) computed using the NP-voxel (vertical-axis) and 2C (horizontal) analysis. Correlation (indicated by: $r = **$) values and best fitting linear regression (solid line) are shown.

The NP technique here uses a linear basis but the structure and number of elements involved is are adapted to the full 4-D dynamic data, and guided by cross-validation to prevent overfitting (O'Sullivan et al. 2021). The accuracy and stability of a kinetic mapping procedure is best evaluated numerically. Some work of this type is reported in Studies in (Gu et al. 2021*a*), based on a 2-minute constant infusion injection of ^{18}F-FDG and a temporal sampling protocol in which the shortest time-frames were 20 seconds in duration, provide mean square error (MSE) performance characteristics of NPRM and 2C kinetic mapping of PET-FDG data as a function of study dose and also as function of whether the underlying ground-truth is governed by a compartmental model or not. In this study the accuracy of flux is largely unaffected by whether a 2C or NPRM mapping technique is used. Across other kinetic variables, when the ground truth is not-compartmental, the

NPRM approach is much better. Remarkably, when the ground truth is a 2C model, the NPRM continues to outperform the 2C approach especially for variables like V_b and V_d. Further study of the mean square performance would clearly be useful, particularly in the settings where the ground truth, study protocol and scanning methods are similar to those encountered with current generation of whole body PET-FDG studies.

VOI values of three variables - ^{18}F-FDG metabolic rate (MR_{FDG}), distribution volume (DV) and vascular blood flow (BF) - are compared with literature reports. Each variable is directly obtained by simple scaling of our summary kinetic values - K_i, V_d and V_b.

$$\text{MR}_{\text{FDG}} = \mu_{glc} K_i \ : \ DV = V_d \ : \ \text{BF} = \frac{V_b}{t^*/2} \tag{4.17}$$

Here μ_{glc} is the plasma glucose concentration and t^* is the value used to define the vascular component in the decomposition of the Meier-Zierler residue in Figure 4.1. In a cancer setting, MR_{FDG} is by far the most clinically important of these variables. Note we do not try to use ^{18}F-FDG as a means to evaluate the glucose metabolic rate, MR_{Glc}, as described in Phelps et al (Phelps et al. 1979). The recent article (Barrio et al. 2020*a*) expresses considerable doubt on the ability to do this in the context of cancer applications. Consideration of the BF variable is motivated by interest in deriving potentially useful additional diagnostic information related to tissue vascularity from on ^{18}F-FDG - see (Feng et al. 2021, Pouzot et al. 2013), for example. There is no intention of questioning PET ^{15}O-H_2O as the gold-standard for blood flow determination. Our BF formula is an application of the central volume theorem (Meier & Zierler 1954) based on an assumed mean transit time of tracer atoms in the vasculature of $t^*/2$ - here 7.5 seconds.

Table 4.3 compares the VOI-averages of three variables to literature reports c.f. (Huang et al. 1983, Liu et al. 2021*b*, Sari et al. 2022*b*, Dias et al. 2022, Matsunaga et al. 2017, Lauritsen et al. 2020, Oguro et al. 1993, Slimani et al. 2008, Lauritsen et al. 2020, Kahn et al. 1994, HS 2000, Materne et al. 2000, HS 2000, Schuster et al. 1995, Kudomi et al. 2008, Piert et al. 2002). For MR_{FDG} and DV values are seen to be very much in the range reported using 2C analysis and Patlak analysis (Dias et al. 2022). Blood flow values

are compared to reports based on PET ^{15}O-H_2O and dynamic susceptibility contrast $(DSC) - MR$ techniques. The results for the NPRM approach are remarkably similar to those in the literature, particularly given that study group here is older and unhealthy (Wu et al. 2016). Further examination of the BF variable could be merited. Viability of conducting PET ^{15}O-H_2O on this scanner is demonstrated in (Knuuti et al. 2023)

While our focus has been on parameters that have traditionally been used to quantify PET-FDG dynamics, the NP technique gives a possibility to also evaluate a summary of the arrival pattern of ^{18}F-FDG at the voxel level as an additional parameter. A sample amplitude-weighted average of voxel-level basis element delays - c.f. equation (4.6) - is shown in Figure 4.10. The result shows early arrival of signal to the lung and much more delayed arrival to the bladder and more peripheral regions - c,f, Table 4.1 in equation (4.6). This result motivates more detailed consideration of the ^{18}F-FDG arrival pattern as a further summary of the full information yielded by this scanning technology.

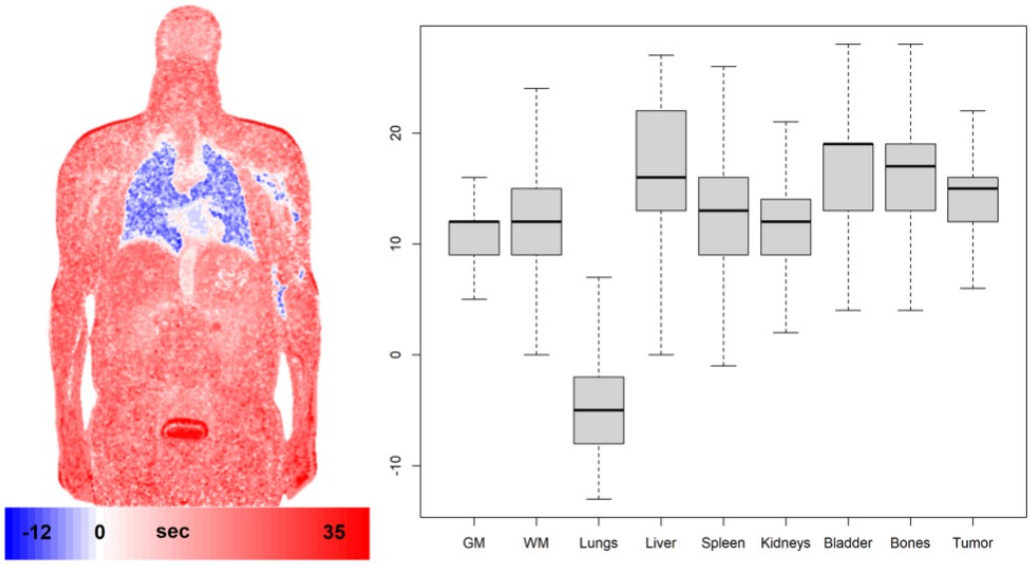


Figure 4.10: Voxel mapping of arrival of ^{18}F-FDG signal. Mapped values are the amplitude-weighted delay values, $\{\delta + \Delta_k, k = 1, 2, ..., K\}$ in equation 4.6. Data are centered so that the mean delay in the LV is zero. Left: Image of coronal scan corresponding to the CT slice in Figure 4.2. The boxplot on the right shows the distribution of mapped delay values by VOI.

Table 4.3: Comparison with Literature Values for MR_{FDG}, DV and Blood Flow in Different Tissues. c.f. equation (4.4).

Parameter	Method	GM	WM	Lung	Liver	Spleen	Kidney	Bones
MR_{FDG} μmol/100g/min	Voxel-NP	18.54±6.81	6.66±2.44	0.42±0.31	1.40±0.53	1.40±0.94	2.52±1.51	1.63±0.63
	VOI-2C	18.98±7.18	6.83±2.26	0.43±0.32	1.38±0.47	1.08±1.24	1.19±1.43	1.58±0.55
	Literature	20.26±6.14	7.17±2.09	0.47±0.35	1.39±0.89	1.39±0.83	1.98±2.20	1.72±0.63
		22.22±2.71	7.60±1.58	0.60±0.42	5.22±2.67	9.40±4.57	9.15±6.44	1.34±0.46
		17.46 [11.68–27.61]	6.03 [4.02–9.53]	0.35 [0.03–1.74]	2.02 [0.74–4.35]	2.45 [1.18–15.30]	3.81 [0.08–7.95]	3.69 [1.08–9.09]
DV mL/g	Voxel-NP	0.88±0.26	0.64±0.27	0.09±0.03	0.86±0.08	0.42±0.09	1.20±0.34	0.22±0.07
	VOI-2C	0.56±0.23	0.55±0.16	0.09±0.03	0.88±0.09	0.49±0.12	1.25±0.36	0.20±0.06
	Literature	0.62±0.56	0.67±0.22	0.26±0.06	0.98±0.15	0.63±0.14	1.44±0.55	0.23±0.10
		0.81 [0.14–1.41]	0.46 [0.15–0.87]	0.15 [0.02–0.28]	0.84 [0.44–1.26]	0.58 [0.10–1.12]	0.96 [0.33–1.41]	0.31 [0.04–0.51]
Blood Flow mL/min/g	Voxel-NP	0.43±0.11	0.24±0.08	1.41±0.32	0.73±0.34	1.70±0.74	1.99±0.58	0.22±0.12
	VOI-2C	0.26±0.04	0.13±0.04	1.16±0.34	0.14±0.07	0.85±0.42	1.22±0.38	0.03±0.02
	Literature	0.59±0.11	0.20±0.04	1.40±0.30	1.11±0.34	1.92±0.76	1.74±0.44	0.18±0.03
		0.41±0.11	0.22±0.04	1.21±0.32	1.78±0.56	1.68±0.12	1.57±0.60	0.18±0.05

Chapter 5

Shortened Dynamic Imaging Protocols for ^{18}F-FDG PET Scans

Abstract

Positron emission tomography-FDG scanning, a technique that has become an integral tool in the management of various types of cancers, is gaining more attention in recent years. This is largely due to the significant improvements in the spatial and temporal resolution of PET scanners, which have substantially increased the interest in mapping kinetic parameters from shorter scans. Several protocols have been put forward in an attempt to generate K_i at both the voxel level and ROI level. The main challenge, however, is the absence of imaging data immediately after the tracer injection, which limits the ability to recover information from the early phase. In order to address this challenge, three different approaches have been evaluated for the feasibility of this protocol. Utilizing the non-parametric residue mapping (NPRM), along with machine learning adjustments, we are able to produce K_i image. This image is created using either 15 or 30 minutes of data collected immediately after the administration. This process is carefully evaluated within the context of a series of breast tumor studies with dynamic FDG PET scans. Two methods have been evaluated in the region of interest (ROI) domain: the Population Residue basis and the Exponential extension of the non-parametric Residue. Both of these methods have undergone thorough examination at the ROI level to ensure

accuracy and reliability. The raw correlation of Flow between the Residue extension method with the first 15 minutes of data and the full data set with NPRM is found to be 0.81. Impressively, the overall correlations for flux are generally found to be around 0.9 when combined with Machine learning correction. The high correlation values may suggest that the short scan is a feasible method, given that the early kinetics Flow can be readily obtained. Furthermore, it implies that the K_i value from the full scan can be accurately estimated, providing valuable insights for further studies and applications.

5.1 Introduction

Positron emission tomography (PET) scanning with the radiotracer ^{18}F-FDG is an established and commonly used medical imaging tool in the diagnosis and management of several types of cancers. Typically, a standard whole-body clinical PET-FDG scan, which involves imaging approximately 60-90 minutes post-injection of the radiotracer (Delbeke et al. 2006, Dunnwald et al. 2011, Pantel et al. 2022*a*, Spence et al. 2002). The standard uptake value (SUV), a semi-quantitative measure that is derived from a single imaging acquisition time, is frequently employed in the clinical setting. SUVs are sufficient for many diagnostic applications in clinical practice, including tumor grading (Bansal et al. 2011). A standard dynamic acquisition protocol requires more than 60 minutes of acquisition after tracer injection. This longer scanning protocol limit the patient throughput and comfort. In the realm of research, dynamic scans with multiple time frames are used for more advanced diagnosis, response assessment, therapy management, and tracer development. These techniques allow a more comprehensive understanding of tumor behavior and metabolism, and they have significant potential to enhance clinical decision-making and patient outcomes (Tomasi et al. 2012, Wijngaarden et al. 2023). Net influx rate K_i , which is a fully quantitative parameter that can be derived from dynamic scans, was found to outperform SUV in terms of lesion detectability (Wu et al. 2024*b*). Moreover, the prediction of the outcome was also more accurate when using the net influx rate K_i compared to SUV. (Dunnwald et al. 2011).

The next generation of PET total-body scanners, which will have full cov-

erage of blood pools (Badawi et al. 2019*b*), offer a unique potential for dynamic acquisitions. These could yield more detailed information about FDG delivery and metabolism. They may also have the potential to refine the acquisition of clinical scan data, enabling the extraction of useful kinetic information and optimizing the amount of tracer administration. One of the primary benefits of these advancements is the potential for dosimetry, which can reduce the amount of radiation patients are exposed to. This is particularly beneficial for populations that are sensitive to radiation, thereby improving patient safety during diagnostic procedures (Chen et al. 2024). Image noise level in PET imaging is often characterized by the Signal-to-noise ratio (SNR). The SNR in a reconstructed image can be approximated as $SNR \approx k\sqrt{S \times A \times T}$, where k is a constant, S is the effective sensitivity of scanner, A is the administered activity and T stands for the acquisition time (Cherry et al. 2017, Tan et al. 2020, Alberts et al. 2021). With the much increased sensitivity in Long axial field of view scanner, the lower dose administration, shorter acquisition time, improved image quality and better lesion detectability becomes clinically feasible (Alberts et al. 2021, Chen et al. 2023*b*, Cherry et al. 2017, Tan et al. 2020, Chen et al. 2024). Fused with the prior anatomical information, the use of multimodal artificial intelligence techniques has shown promising results in improving the quality of PET images. A mere 60 seconds of scanning data could potentially produce images of quality comparable to that of the full 10-minute data (Zhang et al. 2024). In terms of optimizing the scanning process for clinical diagnosis, a 1-minute scan with a full dose and a 2-minute scan with a half dose have been identified as the ideal protocol when employing the new Bayesian penalized-likelihood iterative PET reconstruction technique (HYPER iterative). A 2-minute scan with a full dose and a 3-minute scan with a half dose are recommended for the ordered subset expectation maximization (OSEM) reconstruction (Hu et al. 2023). Due to the artificial intelligence techniques and new algorithms being developed in conjunction with the high-performance capabilities of the Long Axial Field of View (LAFOV) scanner, the improvements could be dramatic. Similar types of research have also been conducted on a digital Biograph Vision PET/CT system (Siemens Healthcare; Erlangen, Germany), an axial field of view 26.3cm scanner. Under this system, the clinical standard scan was acquired approximately after 15 minutes. Using an approximate threefold reduction

of the time, all defined regions were correctly classified and no changes in staging were observed (Weber et al. 2021).

Numerous studies have established that the information derived from early dynamic (ED) PET data could be beneficial in various medical applications. This has been particularly noted in the analysis of FDG uptake in the initial 10-minute imaging phase. The significant increase in FDG uptake observed in clear cell carcinoma compared to non-clear cell carcinoma in renal cell carcinoma (Nakajima et al. 2015). The maximal standardized uptake value (SUVmax) and the mean standardized uptake value (SUVmean) were notably higher in tumor tissue compared to non-tumor tissue in the first 4-minute data. This finding effectively highlights the detection of hyperperfusion in hepatocellular carcinoma(HCC) (Schierz et al. 2013). Blood flow(BF) can be estimated from the first-pass of ^{18}F-FDG data as suggested by multiple studies (Mullani & Gould 1983, Mullani et al. 2008, Zhang et al. 2023) Blood flow estimated from the first 2 min data has been found to have a high correlation coefficient (r=0.86) relative to ^{15}O-water BF (Mullani et al. 2008), similar findings have been observed in LAFOV scanner in multiple organ studies, as presented in table 4.4. Several parameters can be calculated from first-pass data. e.g. BF, time to peak(TTP), hepatic perfusion index (HPI) can be derived. (Zhang et al. 2023) shows higher HPI in liver cirrhosis compared to non-liver cirrhosis patients. Utilising kinetic analysis with traditional compartmental model, early kinetics like K1, k2, V_b and delay time can be estimated. Combining with SUV can differentiate benign from malignant pulmonary lesions and squamous cell carcinoma from adenocarcinoma. SUVmax and K1 were also found to correlate with Ki-67 (Meng et al. 2023). K1 and V_b have been found to have a high correlation coefficient of more than 0.95 between a 90-second early dynamic scan using a one-compartmental model and 1-hour data using an irreversible two-compartmental model on the total body scanner uEXPLORER (Feng et al. 2021).

The concept of generating K_i images directly from SUV images using the sophisticated methods of deep learning has been proposed. The K_i is often seen as a more accurate parameter than the SUV in measuring metabolic information. The primary goal of this approach is to reduce the acquisition time, eliminate the dependence on the input function and improve the SNR

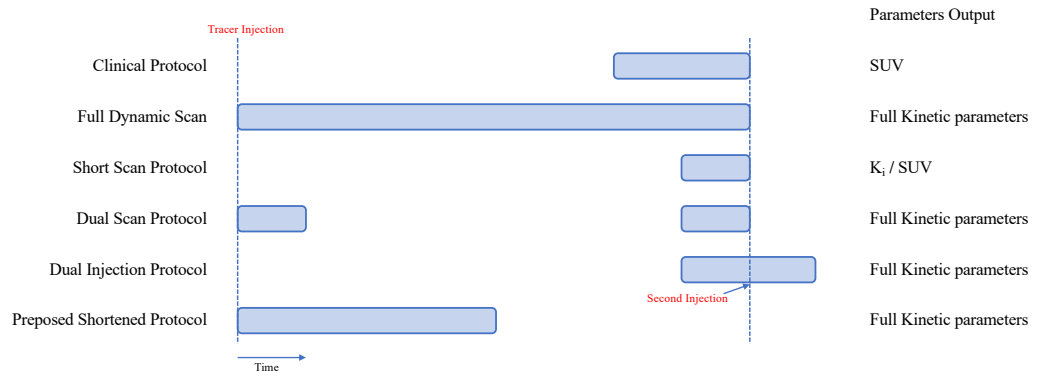


Figure 5.1: Schematic representation of an overview of short-duration dynamic FDG PET scanning protocols.

(Wang et al. 2022*c*, Huang et al. 2022, Li et al. 2022*c*)Comprehensive study was conducted involving 200 patients. The study utilized a 3D U-Net convolutional neural network (CNN) where data spanning 50-60 minutes were acquired and used as the static SUV image. This image was then employed to predict the K_i image which had been generated using 20-60 minute data with the Patlak analysis. The predicted images were then compared to reference parametric K_i images. The structural similarity index measure (SSIM) between the predicted images and the reference ones was found to be above 0.9 for all the test patients. The median SSIM exceeded 0.94 at six different sites. These sites included the brain, neck, lung, abdomen, pelvis, and leg (Huang et al. 2022). Another study was carried out with 203 participants. In this case, a 50-60 minute static image was used to predict a 10-50 minute K_i image. This was accomplished by using an improved 3D cycle generative adversarial network (cycleGAN). In each of the training, validation, and testing groups, a similar proportion of malignant, benign, and healthy control subjects were included. The synthesized K_i images were found to have a significant correlation (Pearson correlation coefficient of 0.93) with the Patlak K_i images, while the SSIM exceeding 0.89 (Wang et al. 2022*c*). In a separate study, a convolutional encoder-decoder CNN network was used to predict the Patlak K_i using data collected between 40 to 65 minutes.This study involved 20 patients and covered 11 lesions. The results were quite promising, with a high SSIM of 0.98 and a high correlation (R^2=0.8382) (Li et al. 2022*c*).

Patlak analysis to generating K_i requires a data collection span of approximately 40 to 50 minutes, according to recent studies (Huang et al. 2022, Wang et al. 2022*c*). This is a significant amount of time compared to the semi-quantitative approach. Further research has been conducted on the Siemens Biograph Vision Quadra PET/CT system to shorten the duration of the study that can produce Patlak generated K_i. The research involved a cohort of 12 patients with lung malignancy. By using an scaled population-averaged input function, the scan time could be reduced to 20 or 30 minutes. Importantly, this reduced scan time did not significantly impact the accuracy of the results, with a bias of less than 7.38 (van Sluis et al. 2022). A study found that a 20-minute dynamic scan using Population Based Input Function (PBIF) and a Non-Local Means (NLM) filter could still maintain acceptable quality. The results were promising; even a shorter 16-minute scan was found to be sufficiently effective in detecting all lesions (Wu et al. 2022*c*).Patlak K_i can also be calculated as short as 10 minutes through a dual-time-point protocol, the first scan 20 to 25 minutes and the second between 80 to 85 or 85 to 90 minutes. A substantial correlation was noticed between the conventional K_i and the dual-time-point K_i. This correspondence was measured by R^2 values of 0.994, 0.980, 0.971, and 0.925 for various regions such as the nodule, tumor, cerebellum, and bone marrow (Wu et al. 2021).

The dual-time-window (DTW) protocol has been proposed as a promising method for enhancing the efficiency of dynamic imaging protocols. This protocol involves a single injection followed by dual scans, a short dynamic scan that is performed immediately after the injection to capture early information, and a second scan is then conducted at a later stage to gather metabolism information. In this approach, a 5-minute dynamic PET scan is conducted immediately after the injection. This scan is then followed by a 3-minute per bed static PET scan at 60 minutes post-injection. This gives a bias of less than 10% in both simulation and patient studies in 2C parameters. The study focused on 15 liver lesions from 9 patients, the early frame sampling revealed that maintaining a rate of 10 seconds per frame minimized the bias and standard deviation in the kinetic parameters (Samimi et al. 2020). In the 21 patient studies, high correlations were observed between MR_{FDG} generated from 75-minute dynamic data and a

two short dynamic scan protocol utilizing data from two time frames (0-6 and 60-75 minutes) (Wang et al. 2022*b*). Further studies were conducted using 5-minute dynamic data supplemented with 1-minute static data at 60 minutes post-injection. The results showed that K1,k2, k3, and V_b values were high correlated between the protocols (Wang et al. 2023*a*). Additional research was done on 28 patient scans performed on a uEXPLORER PET/CT. The results showed that K_i and K1 derived from the DTW protocol showed overall good consistency with the reference from the 60-minute dynamic scan with a 10-minute early scan and a 5-minute late scan. High correlations were observed in the cerebral cortex, muscle, and tumor lesion respectively (K_i: 0.971, 0.990, and 0.990; K1: 0.820, 0.940, and 0.975) (Wang et al. 2022*e*). Interestingly, similar research indicates that the total scan time could potentially be reduced to 10 minutes (0-4 and 54-60 minutes), with results that are comparable to the full scan times (Wu et al. 2022*d*). However, the DTW protocol has some limitations. It requires additional image registration, which could potentially introduce image artifacts. A second CT may be required in the second scan for accurate image registration and attenuation correction. The impact of these potential issues was not modeled in the study mentioned above. As a result, another protocol considered as a dual injection protocol that includes a single scan with the help of a dual injection scheme is being studied, and it shows promising results (Wu et al. 2022*d*). The full dynamic scanning protocol typically requires an acquisition time of more than 60 minutes. Whether the total scanning time can be reduced while still generating reliable kinetic parameters has been examined. This was done in three injected dose groups: full activity (3.7 MBq/kg), half activity (1.85 MBq/kg), and ultra-low activity (0.37 MBq/kg) of ^{18}F-FDG. Significant correlations in tumor kinetic metrics were identified between the 30/45 minute group and the group with 60-minute scanning time (Liu et al. 2023*b*).

The concepts of machine learning and deep learning were proposed several decades ago and have extensive applications in PET. Deep learning, in particular, has been employed for a multitude of tasks in the field of medical imaging. These tasks include noise reduction, image segmentation, image generation, and image reconstruction etc. (Wang et al. 2021*c*, Huang et al. 2022, Wang et al. 2022*c*, Li et al. 2022*c*, Liang et al. 2023, Lu et al. 2019,

Guo et al. 2019, Häggström et al. 2019, Cui et al. 2019, Reader et al. 2020, Zaidi & El Naqa 2021, Apostolopoulos et al. 2022, Niyas et al. 2021, Gong et al. 2021, Zaker et al. 2022). This technique can also be applied to predict K_i, while simultaneously preserving early information (Wu et al. 2019). This predictive ability of deep learning could significantly enhance the accuracy and efficiency. To examine this, we undertook a study to evaluate the value of the kinetic information that could potentially be retrieved from short dynamic scans, acquired immediately after the FDG tracer injection.

5.2 Materials and Methods

5.2.1 Materials

This study considers two data sets: brain tumor patients and breast tumor patients. Both groups underwent dynamic scanning for 60-90 minutes.

5.2.1.1 FDG Brain tumor Study

Data from a brain tumor study conducted at the University of Washington, as reported by (Spence et al. 1998, 2002), were used. The study included thirty-three patients, aged between 30 and 65, who were diagnosed with supratentorial malignant Glioma. Patients had dynamic PET-FDG scans within two weeks before and/or 1-3 weeks after radiation treatment (RT). A total of forty-eight scans are available in this study. The General Electric Advance whole body positron emission tomograph was used, which provides 35 image planes of data over a 15 cm axial field of view. It includes 18 rings of Bismuth germanium oxide (BGO) detectors with 672 crystals per ring. The system's sensitivity in two-dimensional mode is 135 kcps/mCi/ml, with a limiting transaxial resolution of 4.1 mm, a slice thickness of 4 mm, and a direct (FBP) reconstruction methodology.

The typical scan duration was 90 minutes, with some patients' scans lasting 70 minutes or less. Patients were typically injected with 7–10 mCi of FDG in 10 ml of normal saline over 2 minutes. All studies included frequent arterial sampling, similar to the dynamic image acquisition. The 1-ml blood samples were centrifuged, with 0.5 ml of plasma pipetted and counted for total plasma radioactivity using a Cobra multichannel gamma counter (Packard

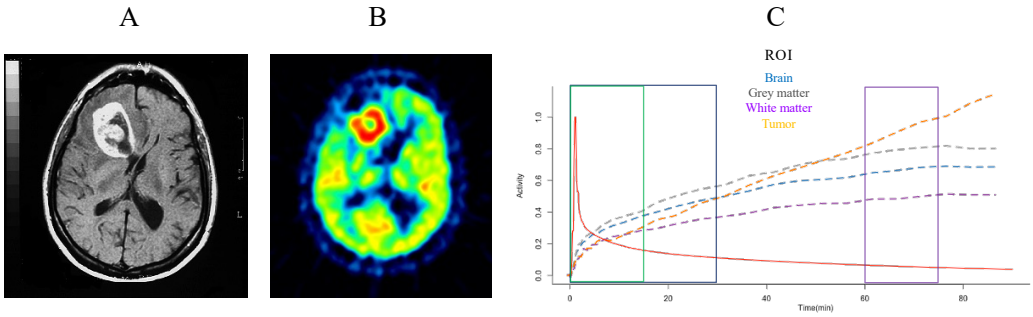


Figure 5.2: Diagram of resampled PET-FDG scan data in brain tumour series. First 15 minutes(green), 0-30 minutes(navy) and clinical setting 60-75 minutes(purple). A similar resampling approach was used for the breast series.

Corp., Chicago, IL). The 4-D PET data comprises an array with $N = 128 \times 128 \times 35$ voxels and $T = 31$ time-frames extending over a 90-minute period. The time-frame sequence is: 1×1 min (pre-injection), 4×20 s, 4×40 s, 4×1 min, 4×3 min, and 14×5 min. Time-course data for grey matter, white matter, and brain tumor regions were available for analysis.

5.2.1.2 FDG Breast tumor Study

Fifty-three female patients, aged between 32-76, with primary Locally Advanced Breast Cancer (LABC), underwent dynamic FDG PET scans before and at the midpoint of neoadjuvant chemotherapy (Mankoff et al. 2003, Dunnwald et al. 2008, 2011). Doses ranging from 218 to 396 MBq were administered over 2 minutes in a volume of 7-10 mL using a constant infusion pump. Dynamic imaging was then conducted for 60 minutes post-infusion. Data was collected on a GE-Advance scanner following the same procedure as the brain dataset. Corrections for attenuation, scatter, deadtime, and random events were made using a plane-by-plane FBP reconstruction algorithm. The 4-D PET data comprises an array with $N = 128 \times 128 \times 35$ voxels and $T = 25$ time-frames that extend over a 60-minute period. The time-frame sequence is as follows: 1×1 min (pre-injection), 4×20 s, 4×40 s, 4×1 min, 4×3 min, and 8×5 min. Arterial input functions were recovered from the left ventricle (LV) of the heart (O'Sullivan et al. 2017). Time-course data for tumor regions and contralateral normal regions were available for analysis.

5.2.2 Kinetic Analysis

The total tissue concentration, $C_T(t)$ is expressed as a convolution between the tissue response(Residue) and the arterial input function, $c.f.$ Meier and Zierler (Meier & Zierler 1954).

$$C_T(t) = K \int_0^t R(t-s) C_P(s) ds = R \otimes C_P(t) \tag{5.1}$$

where $C_T(t)$ is the concentration of radiolabeled tracer in a tissue region, measured as activity per unit volume (KBq/cm^3). $C_P(t)$ is the time-course of the tracer the arterial blood as activity per millilitre(ml) of blood. And R the tissue residue can be regarded as a life-table for tracer atoms in a tissue region. Where Residue can be calculated based on TAC and plasma data $C_P(t)$. Decomposition of the residue (Figure 4.1) can be used to define a set of metabolic variables. Vascular flow and volume (K_b,V_b), distribution flow and volume (K_d,V_d), flux (K_i), overall flow (K_1) and extraction (E=K_i/K_1). These variables represent metabolic features of residue. An example of the inputs and outputs when using the NPRM is shown in Figure 5.3. Our initial focus is on mapping the flux (K_i) based on the short scan data. More details about the non-parametric residue mapping approach used to recover voxel-level kinetics are presented in sections 3.3.1 and 4.2.2.

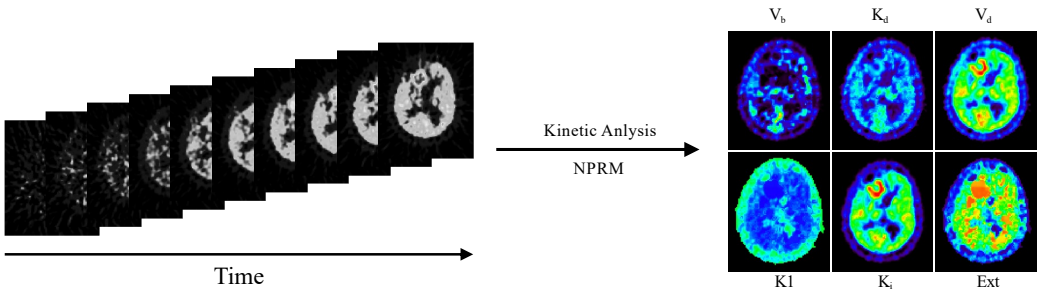


Figure 5.3: Diagram of the use of NPRM to convert 4D dynamic PET data into a set of 3D metabolic images.

5.2.3 Machine Learning Methods

Data from the full-time course were resampled to simulate series that might result from shorter imaging sessions. We considered series corresponding

to the first 15 minutes, first 30 minutes and 60-75 minutes. A diagram of these series is shown in Figure 5.2. By re-sampling the dynamic scanning data we were able to study the ability to evaluate/predict late FDG retention from early dynamic scans information. Data from each potential acquisition were evaluated using the NPRM in order to recover estimates of the kinetic parameters. The Patlak method was used to derived a flux estimates from 45-60 and 60-75 minute data.

Machine learning methods can be applied to Voxel-level and ROI data in the Metabolic Parameter Domain. Several techniques including Multiple Linear Regression, Generalized Additive Models, Random Forests and Neural Networks were applied (Wu et al. 2019). The results are found to be quite promising. The Generalized Linear Model (GLM) is a flexible extension of ordinary linear regression. GLM expands upon linear regression by using a link function to connect the linear model to the response variable.

$$g(E(Y)) = \beta_0 + \sum_{1}^{M} \beta_m x_m \tag{5.2}$$

The Generalized Linear Model (GLM) was formulated to unify various statistical models (Nelder & Wedderburn 1972). In Chapter 3, we discuss the Model-based Image Domain Bootstrap, which uses a data generation process (DGP) based on a GLM representation for the 4-D PET data. This model accommodates non-Gaussian errors and does not assume constant scale factors σ_{ij} (Seber 2015). Generalized Additive Models (GAM) are an extension of GLM. Unlike GLM, the linear predictor in GAM is the sum of smoothing functions applied to the predictor variables. Statistically, a GAM is a model in which the linear response variable linearly depends on unknown smooth functions of the predictor variables. GAMs offer several advantages, including flexibility, interpretability, non-linearity, regularization, and visualization. these features could enhance data interpretation and improve prediction accuracy.

$$g(E(Y)) = \beta_0 + \sum_{1}^{M} f_m(x_m) \tag{5.3}$$

Note if we take $f_m(x_m) = \beta_m x_m$, the formula will become equation 5.2.

However, overfitting can be a problem with GAMs. To reduce this, cross-validation can be used. Specifically, in this chapter, we've used the Leave-One-Out Cross-Validation (LOOCV) method to overcome overfitting.

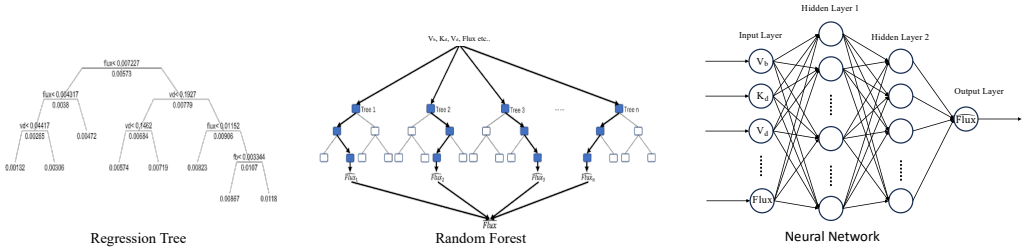


Figure 5.4: The diagram includes models such as regression trees, random forests, and neural networks.

5.2.4 Population Residue Basis

The analysis procedure in this section is used to develop a population of full-time course residues for mapping FDG kinetics. In this analysis each residue is defined in terms of a set of coefficients for a fixed set of basis residues so a residue function, R, is associated with a finite set of vector $B_k(t)$ of non-negative parameters α

$$R(t) = \sum_{k=1}^{K} \alpha_k B_k(t) \tag{5.4}$$

Assuming each data can contribute m basis residues. A population of N data sets yields a set of residue $\{R_{nm}, nm = 1, 2, ..., Nm\}$ Clustering partitions the entire set of R_{nm}, into L clusters with self-similar characteristics, where $k < L < Nm$. The mean within each cluster be denoted $B_l(t)$ for $l = 1, 2, ..., L$.

$$B_l(t) = \sum_{j=1}^{J} \theta_j B_j(t) \tag{5.5}$$

Let a subset of $B_l(t)$ be the final residue basis $B_j(t)$ and constrained to be unity at time zero. The coefficient θ_j are constrained to be non-negative.

$$WRSS(J) = \sum_t w_t [B_l(t) - \sum_{j=1}^{J} \theta_j B_j(t)]^2 \tag{5.6}$$

where $WRSS(J)$ is the weighted residual sum of squares when J basis residues has been selected. A cross-validated backwards elimination scheme is applied to estimate the number of J. The elimination starts with $J = L$, where L is a large number of clusters obtained in the previous step. A sequence indexed by J for $J = L, L-1, L-2, ..., 2$ to eliminate the most basis element in $B_l(t)$.

$$GCV = \frac{WRSS}{DFE^2} \tag{5.7}$$

where DFE is the effective degrees of freedom for error. Simplistic models often have a large degrees of freedom for error and may not fit the data well. Conversely, complex models may fit the data accurately but often result in a small margin for error. In both of these extremes, the prediction error and the Generalized Cross-Validation (GCV) statistic can be high. Usually, the model with the lowest GCV value also has the smallest prediction error (Wahba 1990, O'Sullivan 1993, 2005).

The residue basis $B_j(t)$ are further constrained to contain two fixed elements: a pure vascular term, R_1, and a pure retention term, R_P. For obvious reasons the latter is referred to as the Patlak residue. Thus the final residue basis set $B_k(t)$ has been constructed as described in equation 5.4.

Assuming the full length arterial input function C_P are available for each patient scan in shorter dynamic scanning protocol. The $\mu_K(t)$ in equation 4.6 could be generated $\mu_k(t) = \int_0^t B_k(t-s)C_p(s)ds$. The optimal set of α-coefficients can be found using quadratic programming when the duration of concentration $C_T(t)$ is shortened. The $R(t)$ for shortened protocol can still be obtained to generate a set of metabolic variables using residue decomposition (Figure 4.1).

5.2.5 Exponential Extension of Non-parametric Residue

The residue function can be viewed as the life table for the transit time of radiotracer atoms (O'Sullivan et al. 2014, Hawe 2016). In a compartmental

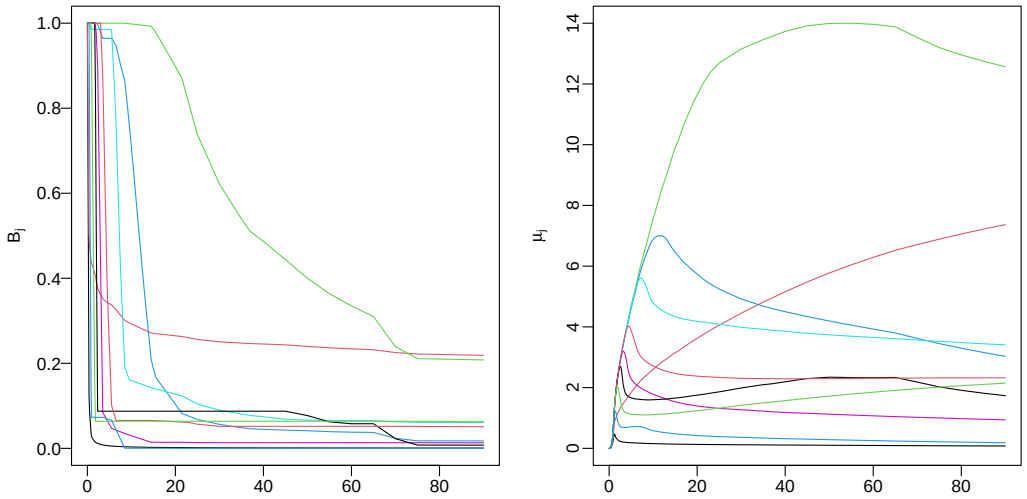


Figure 5.5: Population residue basis $B_j(t)$ and a sample basis elements $\mu_j(t)$ in a brain tumor study.

model, the residue functions are one or a combination of several exponential curves. In contrast, the NPRM presents the residue in a simple piecewise constant form, as shown in Table 2.3. The benefit of presenting the residue in a piecewise constant form is that it only assumes a non increasing pattern.

When $R(t)$ is calculated in a shortened protocol study, the duration of residue is also determined by the scan duration Ts. In kinetic analysis, both the distribution volume (V_d) and retention (K_i) are significantly influenced by Ts. To obtain the complete residue in a shortened protocol, the residue can be exponentially extended by using the proportionality of the data in $[t^*, Ts]$ to determine the γ.

$$R(t) = \begin{cases} piecewise\ constant & , \quad 0 < t \leq t^* \\ R(t^*) + e^{-\gamma(t-t^*)} & , \quad t^* < t \leq T \end{cases} \tag{5.8}$$

where t^* represents a certain time point and T denotes the length of a typical dynamic scan.

5.3 Results

Full image data were resampled to simulate the series that might result from shorter duration imaging sessions. Series corresponding to the first 15 minutes only and 0-30 minutes for breast data. Figure 5.6 shows the result of the analysis of data from one breast cancer subject. We used Neu-

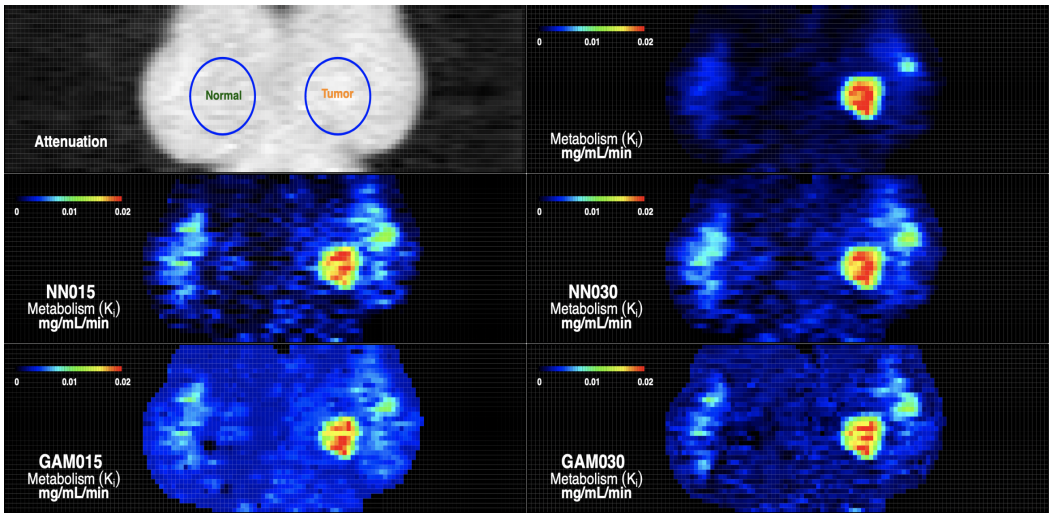


Figure 5.6: Row 1: Attenuation and voxel-level mapping of K_i acquired from the full dynamic data. Rows 2 & 3: Predicted voxel-level metabolic parameter K_i using metabolic information generated from shorter dynamic scans, with acquisition times of 15 and 30 minutes respectively. A neural network and Generalized Additive Model (GAM) are used in the image generation of a breast tumor study.

ral network and Generalized additive model to train the model with flux required from full dynamic scan as response variable and several kinetic parameters recovered from shorter duration scans, corresponding to first 15 minutes and first 30 minutes. And use separate patient's dynamic PET data for validation. Lower four images give the estimated flux image. The tumor region can be easily identified on these images and 30 minutes early scan can also shows the tumor characteristics which could has prognostic value in treatment planning. Results for the brain tumor data are less good but a more refined implementation that incorporates information about the specific range of tissues involved and different types of tumor may enhance performance (Wu et al. 2019).

Results for section 5.2.4 are reported in Figure 5.7 & 5.8. The distributions

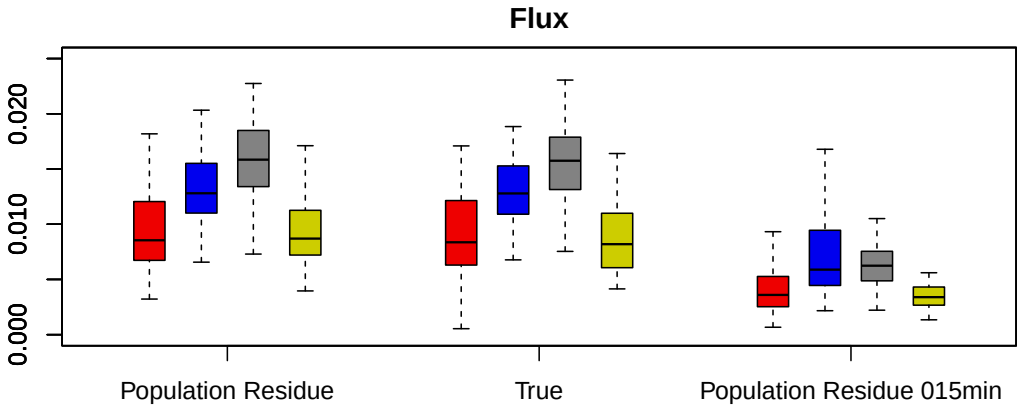


Figure 5.7: The boxplot shows the distribution of Flux recovered from a full scan using NPRM, the application of population residue, and the use of population residue with a short acquisition time of 15 minutes. The colors refer to different regions: red for tumor, blue for the whole brain, grey for grey matter, and yellow for white matter.

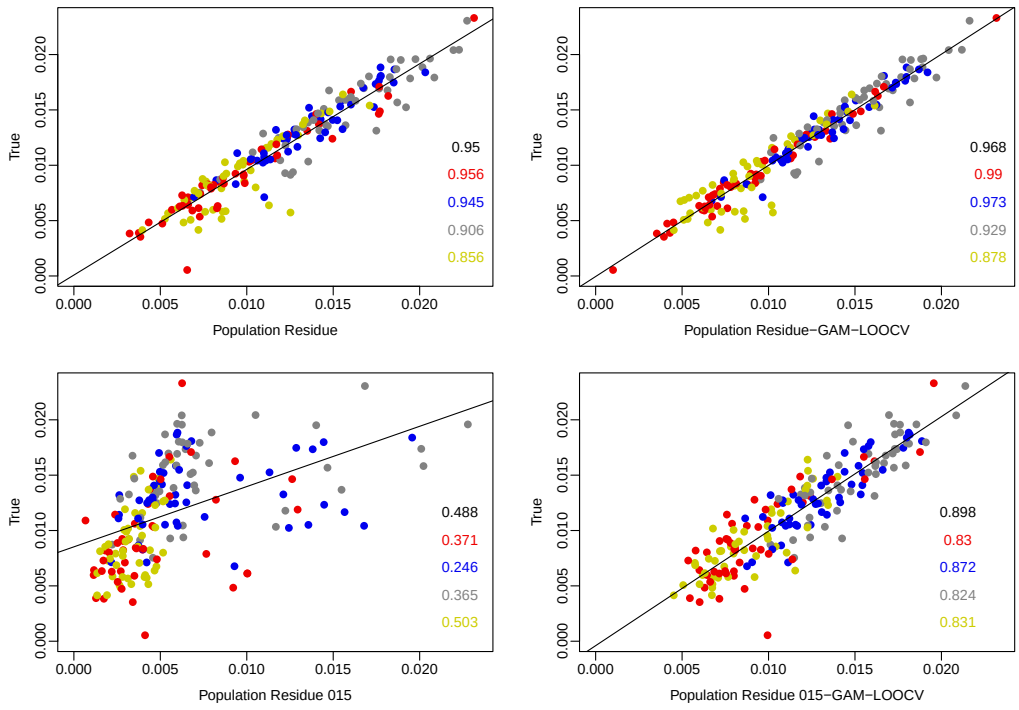


Figure 5.8: The comparison of flux values at the regional level. Left column: direct comparison of flux recovered from different methods. Right column: prediction of Flux as described in Section 5.2.4, using GAM and LOOCV. The colors refer to different regions: red for the tumor, blue for the whole brain, grey for grey matter, and yellow for white matter. The correlations shown in black represent overall correlations, the others correspond to their respective colors.

of ROI-level Flux values, obtained from a full scan using NPRM and the population residue for brain studies, are shown in Figure 5.7. The distributions of the population residue and true values appear visually comparable. Figure 5.8 presents pairwise plots and correlations for the overall and each region corresponding to Figure 5.7. A weaker correlation can be observed when comparing the true flux directly with the prediction from the first 15 minutes of data using population residue. The results of using GAM and LOOCV are also displayed. Although there is some variation across different regions, the correlations are above 0.8 for each region. The raw correlation of Flow is generally better than the Flux, as early information is obtained in a short scan session. The correlations for flux, calculated using population residue methods from full data and data from the first 15 minutes, are 0.72 and 0.71 respectively. With the correction, the correlation could generally exceed 0.85.

Results for section 5.2.5 are reported in Figure 5.9 & 5.10 The distributions of Flow and Flux values, obtained from a full scan using NPRM and the Exponential Extension of Non-parametric Residue, with short acquisition times of 15 and 30 minutes 5.9. The methods of Exponential Extension of a Non-parametric Residue with acquisition times of 15 and 30 minutes are referred to as RE015 and RE030 respectively. The distributions for each method are visually comparable, with clear differences between grey matter and white matter. Figure 5.10 presents pairwise plots and correlations for the overall and each region, corresponding to Figure 5.9. There is a strong correlation observed when comparing the true flux directly with the prediction from the first 15 or 30 minutes of data using Residue extension, with correlations generally above 0.7.The results of using GAM and LOOCV are also presented. The raw correlation of Flow between the true and RE015 or RE030 values are 0.81 and 0.84, respectively. These high values may indicate that the short scan is feasible, as the early kinetics Flow can be readily obtained. The overall correlations for flux between the true and RE015 or RE030 values, with GAM and LOOCV, are 0.877 and 0.905. Root mean square errors (RMSE) for Flux estimates across different regions and methods compare to true, the flux values calculated from full data using NPRM are summarized in Table 5.1.

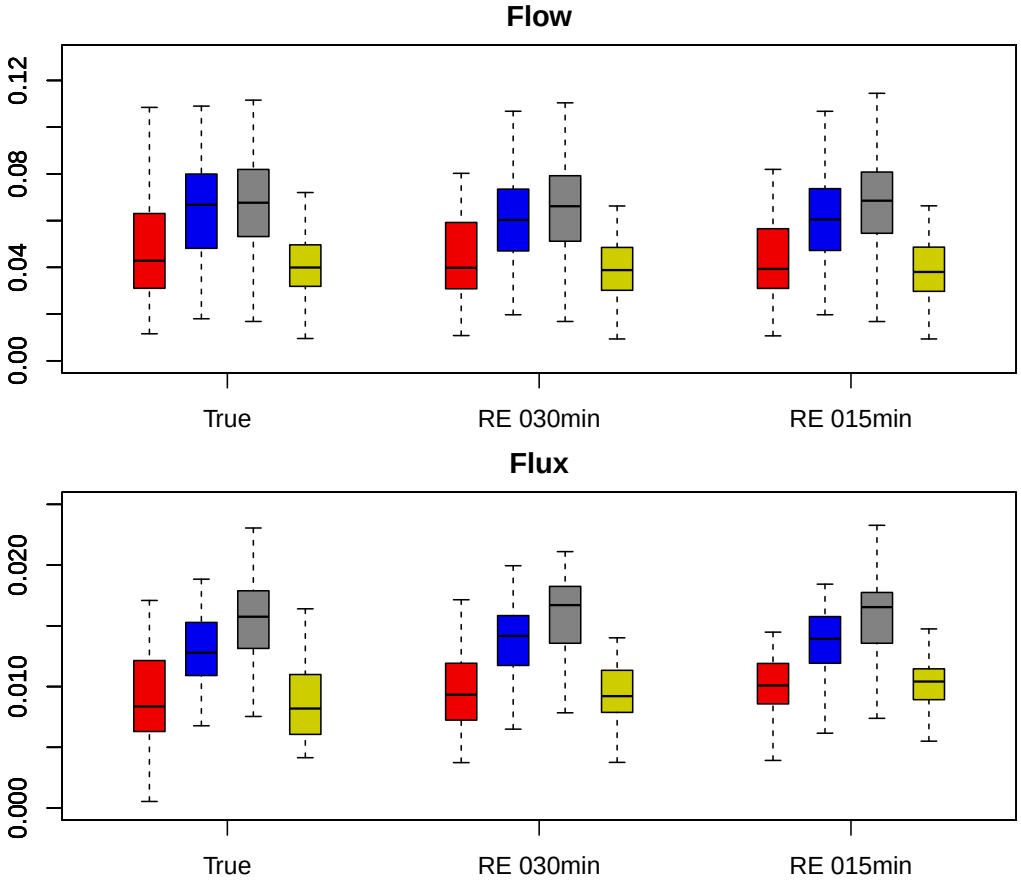


Figure 5.9: The boxplot shows the distribution of Flow and Flux recovered from a full scan using NPRM, and the use of residue extension with short acquisition times of 15 and 30 minutes. The colors refer to different regions: red for tumors, blue for the whole brain, grey for grey matter, and yellow for white matter.

5.4 Discussion

This work presents a shorter scanning protocol using NPRM and machine learning to recover flux comparable to that from full dynamic PET data. There is substantial agreement between the flux values recovered from the most alternative protocols. However, voxel level results are mixed, with better performance in breast cancer settings. Adjusting shortened voxel level data with machine learning produces a flux image quite comparable to that from full dynamic scanning. Overall, the results from this series are promising and merit further, more detailed evaluation. However, results for the brain tumor data are less satisfactory (Wu et al. 2019). More in-depth research has been conducted at the ROI level for the brain series. While the

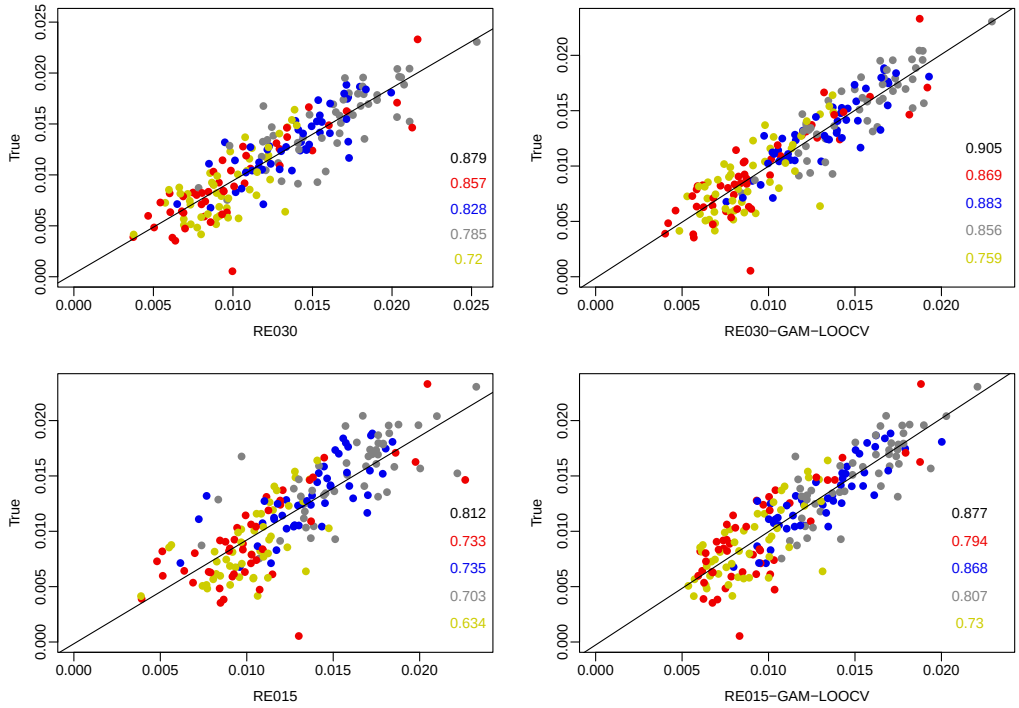


Figure 5.10: The comparison of flux values at the regional level. Left column: direct comparison of flux recovered from different methods. Right column: prediction of Flux as described in Section 5.2.5, using GAM and LOOCV. The colors refer to different regions: red for the tumor, blue for the whole brain, grey for grey matter, and yellow for white matter. The correlations shown in black represent overall correlations, the others correspond to their respective colors.

Table 5.1: RMSE for Flux estimates across different regions and methods compare to true.

	Overall	Tumor	Brain	Grey Matter	White Matter
PR	0.147	0.136	0.107	0.166	0.172
PR*	0.111	0.059	0.072	0.130	0.153
PR015	0.730	0.641	0.745	0.889	0.611
PR015*	0.194	0.237	0.154	0.200	0.178
RE030	0.228	0.235	0.189	0.251	0.233
RE030*	0.188	0.209	0.147	0.182	0.208
RE015	0.276	0.321	0.224	0.269	0.281
RE015*	0.213	0.257	0.156	0.207	0.218

* represents for predictions using GAM with LOOCV

PR = Population Residue

RE = Residue Extension

short scanning protocol, which acquires data immediately after the tracer injection, provides an opportunity to assess tissue perfusion (K1) characteristics, this series does not find that such information compensates for the decreased reliability of the FDG flux value. The parameters derived from the methods described in sections 5.2.4 and 5.2.5 suggest the feasibility of the proposed protocol, as demonstrated in Figures 5.8 and 5.10.

The non-parametric form provides more accurate estimates than a single or a combination of the exponential form when constructing Residue to produce kinetic parameters, as shown in Table 4.1. While the exponential form has been extensively used in compartmental modeling and model-based input function, as cited in (Kety & Schmidt 1948, Huang et al. 1980, Gunn et al. 2001, Feng et al. 1993). When the Arterial Input Function (AIF) is shortened or missing, the exponential curve can also be used to complete the data (Wu et al. 2022*d*). This is particularly useful when the complexity of the Residue decreases, especially when the tracer stabilizes in the late phase or after steady-state conditions between reversible tissue and plasma compartments are reached. In Non-Parametric Residue Modelling (NPRM), the Residue basis must be constructed individually for each study. Similar to the use of a Population-Based Input Function (PBIF), if a group of patients shares certain similarities, a Population Residue basis could also be generated to reduce computational requirements and the compution time. Figure 5.8 shows a direct comparison, illustrating that the flux using the Population Residue basis is quite comparable to the NPRM.

In general, this study suggest that the utilization of a shorter dynamic imaging protocol, when combined with the application of machine learning adjustments, has the potential to effectively extract kinetic information from Positron Emission Tomography (PET) imaging studies. However, it's important to note that a more thorough evaluation is necessary to fully confirm these findings. In addition, the development of scanner technology itself could also play a significant role in making this approach more clinically viable. Improvements in scanner sensitivity and enhanced temporal resolution may have the capacity to further optimize this method. The accuracy of the generated kinetic parameters could be significantly improved.

Chapter 6

Discussion and Conclusions

6.1 Discussion

Chapter 2 reviews the dynamic PET quantitation process, as shown in Figure 2.3. Kinetic modelling, including parametric and non-parametric approaches, is summarized in Table 2.3. Parametric models, such as the compartmental model, Patlak plot, and spectral analysis, generally rely on necessary assumptions. These assumptions can be challenging to justify for heterogeneous tissue regions, especially in LAFOV studies. Non-parametric methods like methods like B-spline and piece-wise linear approximation, which don't require assumptions, are more flexible and offer significant advantages. The feasibility, challenges, and potential of these methods are also discussed and summarized in Table 2.2. Their further developments for emerging total-body PET imaging are also reviewed (Zhang et al. 2020*b*, Viswanath et al. 2021, Sari et al. 2022*b*, Wu et al. 2024*a*). PET quantitation involves the use of an input function, which could be derived from arterial blood samples, image-derived input function (IDIF), population-based Input Function (PBIF), or a model-based input function. A brief introduction and their applications are reviewed. A summarized flowchart of IDIF, PBIF, and the population-based projection model (PBPM) is provided in Figure 2.5.

A list of reported dynamic total-body PET study cohorts, along with specific details, is provided in Table 2.1. While most scans were conducted exclusively with fluorine-18 labeled fluorodeoxyglucose (^{18}F-FDG), other

radiotracers of interest, such as ^{68}Ga-FAPI-04 (Chen et al. 2022*a*, 2023*a*, Liu et al. 2023*a*), ^{15}O-H_2O (Andersen et al. 2022), ^{89}Zr-Df-Crefmirlimab (Omidvari et al. 2023, 2022), ^{18}F-Fluciclovine (Abdelhafez et al. 2022), and [^{11}C]methionine (Li et al. 2023), have also been used. Different institutions have applied a range of scanning and reconstruction protocols, but the image voxels are generally on the order of ten million, and a denser sequence is commonly performed at the early time. Although these dynamic datasets may not be identical, the data analysis will face similar problems, which are also discussed in detail. In addition to the quantitative procedures addressed in Chapter 2, basic challenges such as motion, spillover, and partial volume can limit the reliability of estimated kinetics during the pre-processing stage. Patient movement, respiration motion, and cardiac motion are unavoidable during the PET acquisition, particularly for dynamic scanning with longer durations. Hence, a shorter dynamic scanning protocol was proposed in Chapter 5. Numerous motion correction methods have been examined, most of which rely on image registration algorithms or hardware motion tracking using an external device (Bertoldo et al. 2014). To the best of our knowledge, there's no universal solution for all organs, even though it's well-studied in brain images. However, we appreciate that some researchers have investigated this in total-body studies (Sun et al. 2022). Denoising is another way often used to ensure accurate results. Typically, a selected filter, such as Gaussian or non-local mean, is applied to lower the noise in PET images before the formal quantitation (Dutta et al. 2013).

While the emergence of total-body PET scanners brings several benefits, concerns about the adoption of dynamic studies in clinical practice remain and even more serious. For example, more static scans can be completed in a specific time interval (e.g., 1h) as they can be acquired faster on uEXPLORER (Hu et al. 2021). It could be argued that the cost of dynamic studies would be substantially higher. Therefore, some protocol designs, like the dual-injection scheme (Wu et al. 2022*d*), have been explored to reduce dynamic scanning time. There is a more comprehensive review in Chapter 5. Simultaneously, parameter estimation procedures including non-invasive input functions and improved kinetic models, are developed to make dynamic imaging more feasible and valuable in routine use (Kotasidis et al.

2014). Regardless of these challenges, the additional information recovered from dynamic PET scans has proven useful in predicting therapy response or survival (Mankoff et al. 2002, Dunnwald et al. 2011), which is valuable in precision medicine to improve individualized treatment by maximizing therapeutic effect and minimizing toxicity (Mankoff et al. 2019). From these perspectives, the role of dynamic PET imaging may not change in the short term, but we are confident in its bright future in clinics. In the past few years, more than 20 groups from nuclear medicine, physics, biomedical engineering, and statistics have been involved in total-body PET data acquisition and analysis. The early adopters have generously shared their insights into this new technology. Hicks provided an installation guide, including many aspects like financing, space, and power, for total-body PET/CT beginners (Hicks 2023). Vandenberghe et al. proposed a few design options to reduce the cost for total-body PET (Vandenberghe et al. 2023). The Bern group shared their experience obtained from 7,000 patient studies on Quadra (Alberts et al. 2023). An expert consensus was also proposed for the oncological use of uEXPLORER with ^{18}F-FDG based on the experience of imaging 40,000 cases (Yu et al. 2023). These reports greatly improve our understanding of the clinical use of advanced total-body systems.

Chapter 3 presents an image-domain bootstrapping strategy for dynamic PET data, inspired by (Huang et al. 2020). The model is applicable when the PET measurement has a complex temporal structure. It uses a parametric Gamma-model form for the marginal distributions of voxel-level data, and a parametric spatial auto-regressive (SAR) form for covariance patterns. The method employs the empirical distribution of rescaled data and a non-parametric approach for analyzing the spatial correlation structure. A straightforward recycling procedure is proposed to minimize computational demand and storage needs.

Illustrative examples are drawn from dynamic studies with PET-FDG and PET-FLT in brain and breast-cancer patients. These studies use a filtered-backprojection (FBP) reconstruction method and an iterative maximum likelihood (ML) approach. Numerical simulation studies with 2-D and 1-D simulations were conducted. Temporal sampling and tissue attenuation were matched to the real data. The RMSE performance of the model-based image-domain bootstrapping aligns with the performance of the well-

established projection-domain approach, regardless of the reconstruction method used. The model's utility in providing voxel-level and regional summaries, including maximum and coefficient of variation, has been demonstrated in the metabolic parameters domain.

Chapter 4 focuses on the non-parametric approach to mapping kinetic parameters and assessing their uncertainties with data from a long-axial field-of-view (LAFOV) Biograph Vision Quadra PET/CT scanner are evaluated using the model-based image-domain bootstrapping methodology. The construction of patient-specific uncertainties through image-domain bootstrapping and kinetics is reported for voxels, maximum intensity projections, and volumes of interest (VOIs). These correspond to several key organs and tumor lesions. Uncertainty measurements could be particularly beneficial when the biomarker value is close to a boundary between alternative treatment options. Sample kinetic maximum intensity projection (MIP) maps, along with their associated standard errors (SEs) obtained using the NPRM technique and image-domain bootstrap, are illustrated in Figure 4.2.

Figure 4.3 and Table 4.1 highlight the advantages of using the NPRM method. Compared to the well-established 2C model, significant improvements in data representation are achieved with the NP approach. These benefits are primarily associated with the NP technique's ability to capture the highly resolved early time-course pattern. The mean and standard deviations of the weighted residuals sum of squares (WRSS) deviations between the 2C and NP models are shown in Table 4.1. VOI time-course fitting by the 2C model is substantially inferior to that of the NP model, with a mean percent improvement of almost 390%. The full time-course and the time-course over the first minute of data are displayed in Figure 4.3. While the 2-compartment model fitting of some VOIs, such as grey and white matter, is reasonable, it is clearly inferior for certain VOIs like the kidney, liver, bone, and bladder. Table 4.3 compares the VOI averages of three variables to literature reports. MR_{FDG} and DV values align with those reported using the 2-compartment analysis and Patlak analysis (Dias et al. 2022). Blood flow values are compared to reports based on PET ^{15}O-H_2O and dynamic susceptibility contrast (DSC)-MR techniques. The results for the NPRM approach align remarkably with those in the literature. Further examination of the blood flow (BF) could be justified. The viability of conducting PET ^{15}O-H_2O

on this scanner is demonstrated in (Knuuti et al. 2023).

Chapter 5 provides an in-depth introduction to various protocols that have been proposed with the primary objective of generating K_i both at the voxel level and the region of interest (ROI) level. One of the main challenges associated with the previously proposed short duration dynamic scanning protocols lies in the absence of imaging data immediately after the tracer injection. This lack of immediate data necessitates a separate scan, which might require additional image registration. This limitation impedes the ability to recover critical information from the early phase of the scan, thereby potentially affecting the accuracy of the recovered parameters. We have adopted the use of the NPRM, supplemented with machine learning adjustments. This allows us to generate K_i images and make ROI predictions, improving the accuracy and reliability of analysis. The analysis utilizes either a 15-minute or 30-minute data, collected immediately post-injection. We have thoroughly examined this approach through a series of studies on breast and brain tumor patients. In addition, we have evaluated two other methods within the region of interest (ROI) domain: the Population Residue basis and the Exponential extension of the non-parametric Residue. Both of these methods have been thoroughly assessed at the ROI level. Figures 5.8 and 5.10 present a direct comparison, clearly demonstrating that the flux derived from these methods is quite comparable to the K_i obtained from a full scan. The raw correlation of Flow is found to be 0.81 using a 15-minute data. The potential of these methods and protocols to effectively extract kinetic information from PET imaging studies is highly promising.

6.2 Conclusions

Overall, this thesis presents a comprehensive study of the non-parametric residue mapping approach with an aim to enhance the accuracy of quantitation in dynamic whole-body PET imaging. This approach forms the cornerstone of the research, paving the way for reliable kinetic analysis on a large-scale dataset, which was a significant challenge in whole-body imaging with finer resolution. Image-domain bootstrap has been developed with the intention to generate reliable uncertainty estimates, which are crucial for the accurate interpretation of data and subsequent treatment decisions.

The robustness of this technique greatly contributes to the reliability and generalizability of the results derived from the kinetic analysis. A short-duration dynamic scanning protocol has been proposed. This simple protocol has been designed to specifically enhance the quantitation of a shortened dataset. This method has the potential to significantly minimize the time required for data acquisition without compromising the accuracy of results. These techniques could significantly contribute to the accuracy of diagnosis and consequently, impact the effectiveness of treatment decisions.

Appendix A

List of Publications and Presentations by the Author

A.1 Peer Reviewed Journals

1. Q Wu, F Gu, L O'Suilleabhain, H Sari, S Xue, K Shi, A Rominger, F O'Sullivan. "Mapping FDG Kinetics together with Patient-Specific Bootstrap Assessment of Uncertainties: An Illustration with data from a Long-Axial FOV PET/CT Scanner". *Journal of Nuclear Medicine*, 65:971-979, 2024. URL: https://doi.org/10.2967/jnumed.123.266686

2. F Gu, Q Wu. "Quantitation of dynamic total-body PET imaging: recent developments and future perspectives". *European Journal of Nuclear Medicine and Molecular Imaging*, 50:3538-3557, 2023. URL: https://doi.org/10.1007/s00259-023-06299-w

3. F O' Sullivan, F Gu, Q Wu and L D O'Suilleabhain. "A Generalized Linear modeling approach to bootstrapping multi-frame PET image data". *Medical Image Analysis*, 72:102-132, 2021. URL: https://doi.org/10.1016/j.media.2021.102132

4. F Gu, F O' Sullivan and Q Wu. "Bootstrap averaging enhances the mean square error of kinetic maps recovered from PET data". *Manucript*.

During the Internship in United Imaging Healthcare

5. Z Huang, Y Wu, F Fu, N Meng, F Gu, Q Wu, Y Zhou, Y Yang, X Liu, H Zheng, D Liang, M Wang and Z Hu, "Parametric image generation with the uEXPLORER total-body PET/CT system through deep learning". *European Journal of Nuclear Medicine and Molecular Imaging*, 49:2482-2492, 2022. URL: https://doi.org/10.1007/s00259-022-05731-x

6. Y Wu, T Feng, Y Shen, F Fu, N Meng, X Li, T Xu, T Sun, F Gu, Q Wu, Y Zhou, H Han, Y Bai and M Wang, "Total-body parametric imaging using the Patlak model: feasibility of reduced scan time". *Medical Physics*, 2022. URL: https://doi.org/10.1002/mp.15647

A.2 Conference Publications

1. Q Wu, F O' Sullivan, M Muzi and D A Mankoff. "An exploration of the prognostic utility of shortened dynamic imaging protocols for PET-FDG scans". *IEEE Nuclear Science Symposium and Medical Imaging (NSS& MIC) Records 2019*. URL: https://doi.org/10.1109/NSS/MIC42101.2019.9059874

2. F Gu, Q Wu, F O' Sullivan, J Huang, M Muzi and D A Mankoff. "An illustration of the use of model-based bootstrapping for evaluation of uncertainty in kinetic information derived from dynamic PET". *IEEE NSS& MIC Records 2019*. URL: https://doi.org/10.1109/NSS/MIC42101.2019.9059736

3. F Gu, Q Wu and F O' Sullivan. "Image-domain bootstrapping of PET time-course data for assessment of uncertainty in complex regional summaries of mapped kinetics". *IEEE NSS& MIC Records 2021*. URL: https://doi.org/10.1109/NSS/MIC44867.2021.9875531

4. F O' Sullivan, Q Wu, F Gu, K Shi, L O'Suilleabhain, S Xue and A Rominger. "Mapping FDG Tracer Kinetics and their Uncertainties via the Bootstrap using data from a Long-Axial FOV PET/CT Scanner". *Journal of Nuclear Medicine*, 63(3220), 2022. URL: https://jnm.snmjournals.org/content/63/supplement_2/3220

During the Internship in United Imaging Healthcare

5. Q Wu, F Gu, Y Wu, Z Zhu, Y Bai, Q Ge, F Fu, Y Zhou and M Wang.

"Assessment of Compartmental Models and delay estimation schemes for dynamic Total-body PET imaging using uEXPLORER". *Journal of Nuclear Medicine*, 63(3186), 2022. URL: https://jnm.snmjournals.org/content/63/supplement_2/3186

6. Q Wu, F Gu, Y Gu, Y Liu, F Shi, T Xu, Y Zhou and H Shi. "Impact of equilibration time (t*) on Patlak quantitation in dynamic total-Body imaging using the uEXPLORER PET scanner". *Journal of Nuclear Medicine*, 63(3184), 2022. URL: https://jnm.snmjournals.org/content/63/supplement_2/3184

7. F Gu, Q Wu, J Wu, D Hu, S Cao, Y Zhou and H Shi. "Feasibility of standard and generalized Patlak Models for dynamic imaging of multiple organs using the uEXPLORER PET scanner". *Journal of Nuclear Medicine*, 63(3185), 2022. URL: https://jnm.snmjournals.org/content/63/supplement_2/3185

8. F Gu, Q Wu, Y Wu, Y Bai, Y Li, J Wang, F Fu, Y Zhou and M Wang. "Impact of fit time interval on Patlak quantitation in dynamic total-body Imaging using the uEXPLORER PET scanner". *Journal of Nuclear Medicine*, 63(3190), 2022. URL: https://jnm.snmjournals.org/content/63/supplement_2/3190

9. Y Wu, Y Bai, F Gu, W Wei, Q Wu, X Yu, Y Zhou and M Wang. "Assessment of local and global input functions for total body [18F]-FDG Patlak imaging using uEXPLORER PET scanner". *Journal of Nuclear Medicine*, 63(3189), 2022. URL: https://jnm.snmjournals.org/content/63/supplement_2/3189

A.3 Conference Presentations

1. Q Wu, F O'Sullivan, M Muzi. "An exploration of the prognostic utility of Shortened Dynamic Imaging Protocols for PET-FDG Scans in Brain-Tumor Patients". *World Molecular Imaging Congress (WMIC)*, Montreal, Canada, 4-7 Sep. 2019. [Poster Presentation]

2. Q Wu, F O'Sullivan, M Muzi and D A Mankoff. "An exploration of the prognostic utility of Shortened Dynamic Imaging Protocols for PET-

FDG Scans", *IEEE NSS& MIC*, Manchester, UK, 26 Oct-2 Nov. 2019. [Poster Presentation]

3. F Gu, Q Wu, F O'Sullivan, J Huang, M Muzi and D A Mankoff. "Use of the Model-Based Bootstrap for Practical Evaluation of Uncertainty in Kinetic Information Derived from Dynamic PET Studies", *IEEE NSS& MIC*, Manchester, UK, 26 Oct-2 Nov. 2019. [Poster Presentation]

4. Q Wu, F O'Sullivan, M Muzi and D. A. Mankoff. "An exploration of the use of statistical machine learning techniques to create short duration dynamic PET-FDG imaging protocols for a clinical setting". *Joint Statistical Meeting (JSM)*, Virtual, Philadelphia, USA, 1 Aug-6 Aug. 2020. [Poster Presentation]

5. F Gu, F O'Sullivan, Q Wu, M Muzi and D. A. Mankoff. "A Statistical Evaluation of Alternative Techniques for Kinetic Analysis of Multiple Injection Dynamic PET Scans". *Joint Statistical Meeting (JSM)*, Virtual, Philadelphia, USA, 1 Aug-6 Aug. 2020. [Oral Presentation]

6. F Gu, Q Wu and F O' Sullivan. "Image-domain bootstrapping of PET time-course data for assessment of uncertainty in complex regional summaries of mapped kinetics". *IEEE NSS& MIC*, Virtual, Yokohama, Japan, 16-23 Oct. 2021. [Oral Presentation]

7. F O'Sullivan, Q Wu, F Gu, K Shi, L D O'Suilleabhain, S Xue and A Rominger, "Mapping FDG Tracer Kinetics and their Uncertainties via the Bootstrap using data from a Long-Axial FOV PET/CT Scanner". *Society of Nuclear Medicine & Molecular Imaging Annual Meeting (SNMMI)*, Virtual,11-14 Jun. 2022. [Poster Presentation]

During the Internship in United Imaging Healthcare

8. Q Wu, F Gu, Y Gu, Y Liu, F Shi, T Xu, Y Zhou, H Shi. "Impact of Equilibration Time (t*) on Patlak Quantitation in Dynamic Total-Body Imaging using the uEXPLORER PET Scanner". *Society of Nuclear Medicine & Molecular Imaging Annual Meeting (SNMMI)*, Virtual,11-14 Jun. 2022. [Poster Presentation]

9. Q Wu, F Gu, Y Wu, Z Zhu, Y Li, J Wang, F Fu, Y Zhou, M Wang. "Assessment of Compartmental models and delay estimation schemes for dynamic Total-body PET imaging using uEXPLORER". *Society of Nu-*

clear Medicine & Molecular Imaging Annual Meeting (SNMMI), Virtual,11-14 Jun. 2022. [Poster Presentation]

10. F Gu, Q Wu, J Wu, D Hu, T Xu, S Cao, Y Zhou, H Shi. "Feasibility of standard and generalized Patlak Models for dynamic imaging of multiple organs using the uEXPLORER PET scanner". *Society of Nuclear Medicine & Molecular Imaging Annual Meeting (SNMMI)*, Virtual,11-14 Jun. 2022. [Poster Presentation]

11. F Gu, Q Wu, Y Wu, Y Bai, Y Li, J Wang, F Fu, Y Zhou, M Wang. "Impact of Fit Time Interval on Patlak Quantitation in Dynamic Total-Body Imaging using the uEXPLORER PET Scanner". *Society of Nuclear Medicine & Molecular Imaging Annual Meeting (SNMMI)*, Virtual,11-14 Jun. 2022. [Poster Presentation]

12. Y Wu, Y Bai, F Gu, W Wei, Q Wu, X Yu, Y Zhou, M Wang. "Assessment of local and global input functions for total body [18F]-FDG Patlak imaging using uEXPLORER PET scanner". *Society of Nuclear Medicine & Molecular Imaging Annual Meeting (SNMMI)*, Virtual,11-14 Jun. 2022. [Poster Presentation]

Bibliography

Abdelhafez, Y., Azghadi, S., Spencer, B., Evans, C., Valicenti, R., Parikh, M., Verma, R., Dall'Era, M., Foster, C., Hagge, R., Sen, F., Cherry, S., Badawi, R. & Nardo, L. (2022), 'Detection rates from 18f-fluciclovine total-body pet/ct in prostate cancer patients with biochemical recurrence', *Journal of Nuclear Medicine* **63**(supplement 2), 3042–3042.

Ahn, J., Seo, K., Lee, J. & Lee, D. (2000), Factor analysis for the quantification of renal cortical blood flow using o-15 water dynamic pet, *in* '2000 IEEE Nuclear Science Symposium. Conference Record (Cat. No. 00CH37149)', Vol. 3, IEEE, pp. 18–153.

Alavi, A., Saboury, B., Nardo, L., Zhang, V., Wang, M., Li, H., Raynor, W. Y., Werner, T. J., Høilund-Carlsen, P. F. & Revheim, M.-E. (2022), 'Potential and most relevant applications of total body pet/ct imaging', *Clinical nuclear medicine* **47**(1), 43–55.

Alberts, I., Hünermund, J., Prenosil, G., Mingels, C., Bohn, K. P., Viscione, M., Sari, H., Vollnberg, B., Shi, K. & Afshar-Oromieh, A. (2021), 'Clinical performance of long axial field of view pet/ct: a head-to-head intra-individual comparison of the biograph vision quadra with the biograph vision pet/ct', *Eur J Nucl Med Mol Imaging* pp. 1–10.

Alberts, I., Sari, H., Mingels, C., Afshar-Oromieh, A., Pyka, T., Shi, K. & Rominger, A. (2023), 'Long-axial field-of-view pet/ct: perspectives and review of a revolutionary development in nuclear medicine based on clinical experience in over 7000 patients', *Cancer Imaging* **23**(1), 1–15.

Alpert, N., Chesler, D., Correia, J., Ackerman, R., Chang, J., Finklestein, S., Davis, S., Brownell, G. & Taveras, J. (1982), 'Estimation of the local

statistical noise in emission computed tomography', *IEEE transactions on medical imaging* **1**(2), 142–146.

Andersen, T. L., Andersen, F. L., Larsson, H. B., Haddock, B., Shah, V., Fischer, B. M., Højgaard, L., Law, I. & Ulrich, L. (2022), Quantitative image derived input function from long axial field of view scanners, *in* 'PSMR-TBP 9thConferenceon PET/MR and SPECT/MR & Total-body PET workshop', p. 9.

Apostolopoulos, I. D., Papathanasiou, N. D., Apostolopoulos, D. J. & Panayiotakis, G. S. (2022), 'Applications of generative adversarial networks (gans) in positron emission tomography (pet) imaging: A review', *European Journal of Nuclear Medicine and Molecular Imaging* pp. 1–23.

Asselin, M.-C., Montgomery, A. J., Grasby, P. M. & Hume, S. P. (2007), 'Quantification of pet studies with the very high-affinity dopamine d2/d3 receptor ligand [11c] flb 457: re-evaluation of the validity of using a cerebellar reference region', *Journal of Cerebral Blood Flow & Metabolism* **27**(2), 378–392.

Badawi, R. D., Shi, H., Hu, P., Chen, S., Xu, T., Price, P. M., Ding, Y., Spencer, B. A., Nardo, L. & Liu, W. (2019*a*), 'First human imaging studies with the explorer total-body pet scanner', *Journal of Nuclear Medicine* **60**(3), 299–303.

Badawi, R. D., Shi, H., Hu, P., Chen, S., Xu, T., Price, P. M., Ding, Y., Spencer, B. A., Nardo, L., Liu, W. & et al. (2019*b*), 'First human imaging studies with the explorer total-body pet scanner*', *Journal of Nuclear Medicine* **60**(3), 299–303.

Bansal, A., Z., T. & R., T. (2011), *PET Imaging of Gliomas*, InTech.

Bardet, J.-M., Doukhan, P., Lang, G. & Ragache, N. (2008), 'Dependent lindeberg central limit theorem and some applications', *ESAIM: Probability and Statistics* **12**, 154–172.

Barrett, H. H., Wilson, D. W. & Tsui, B. M. (1994), 'Noise properties of the EM algorithm. I. Theory', *Physics in medicine and biology* **39**(5), 833–846.

Barrio, J., Huang, S., Satyamurthy, N., Scafoglio, C. R., Yu, A., Alavi, A. &

Krohn, K. (2020*a*), 'Does 2-fdg pet accurately reflect quantitative in vivo glucose utilization?', *The Journal of Nuclear Medicine* **61**, 931 – 937.

Barrio, J. R., Huang, S.-C., Satyamurthy, N., Scafoglio, C. S., Amy, S. Y., Alavi, A. & Krohn, K. A. (2020*b*), 'Does 2-fdg pet accurately reflect quantitative in vivo glucose utilization?', *Journal of Nuclear Medicine* **61**(6), 931–937.

Berezhkovskiy, L. M., Zhang, X. & Cheong, J. (2011), 'A convenient method to measure blood–plasma concentration ratio using routine plasma collection in in vivo pharmacokinetic studies', *Journal of pharmaceutical sciences* **100**(12), 5293–5298.

Bertoldo, A., Rizzo, G. & Veronese, M. (2014), 'Deriving physiological information from pet images: from suv to compartmental modelling', *Clinical and Translational Imaging* **2**(3), 239–251.

Bober, R. (2021), 'Decay correction for quantitative myocardial pet perfusion in established pet scanners: a potentially overlooked source of errors', *Journal of Nuclear Medicine Technology* **49**(4), 344–349.

Box, G. E. (1976), 'Science and statistics', *Journal of the American Statistical Association* **71**(356), 791–799.

Brockwell, P. J. & Davis, R. A. (1991), *Time Series: Theory and Methods*, Springer, New York, NY, USA.

Buvat, I. (2002), 'A non-parametric bootstrap approach for analysing the statistical properties of SPECT and PET images', *Physics in medicine and biology* **47**(10), 1761–1775.

Caobelli, F., Seibel, S., Krieger, K., Bregenzer, C., Viscione, M., Silva Mendes, A. F., Sari, H., Mercolli, L., Afshar-Oromieh, A. & Rominger, A. (2023), 'First-time rest-stress dynamic whole-body 82rb-pet imaging using a long axial field-of-view pet/ct scanner', *European journal of nuclear medicine and molecular imaging* pp. 1–3.

Carson, R. E. & Lange, K. (1985), 'Comment: the em parametric image reconstruction algorithm', *Journal of the American Statistical Association* **80**(389), 20–22.

Carson, R. E., Yan, Y., Daube-Witherspoon, M. E., Freedman, N., Bacharach,

S. L. & Herscovitch, P. (1993), 'An approximation formula for the variance of PET region-of-interest values', *IEEE transactions on medical imaging* **12**(2), 240–250.

Chen, B. C., Huang, S.-C., Germano, G., Kuhle, W., Hawkins, R. A., Buxton, D., Brunken, R. C., Schelbert, H. R. & Phelps, M. E. (1991), 'Noninvasive quantification of hepatic arterial blood flow with nitrogen-13-ammonia and dynamic positron emission tomography', *Journal of Nuclear Medicine* **32**(12), 2199–2206.

Chen, K., Bandy, D., Reiman, E., Huang, S.-C., Lawson, M., Feng, D., Yun, L.-s. & Palant, A. (1998), 'Noninvasive quantification of the cerebral metabolic rate for glucose using positron emission tomography, 18f-fluoro-2-deoxyglucose, the patlak method, and an image-derived input function', *Journal of Cerebral Blood Flow & Metabolism* **18**(7), 716–723.

Chen, K., Reiman, E., Lawson, M., Feng, D. & Huang, S.-C. (1995), 'Decay correction methods in dynamic pet studies', *IEEE Transactions on nuclear science* **42**(6), 2173–2179.

Chen, R., Sun, T., Huang, G., Zhou, Y. & Liu, J. (2024), 'Current progress and future perspectives in total-body positron emission tomography/computed tomography. part ii: Clinical applications', *iRADIOLOGY* .

Chen, R., Yang, X., Ng, Y. L., Yu, X., Huo, Y., Xiao, X., Zhang, C., Chen, Y., Zheng, C. & Li, L. (2023*a*), 'First total-body kinetic modeling and parametric imaging of dynamic 68ga-fapi-04 pet in pancreatic and gastric cancer', *Journal of Nuclear Medicine* .

Chen, R., Yang, X., Yu, X., Zhou, X., Ng, Y. L., Zhao, H., Li, L., Huang, G., Zhou, Y. & Liu, J. (2022*a*), 'Tumor-to-blood ratio for assessment of fibroblast activation protein receptor density in pancreatic cancer using [68ga]ga-fapi-04', *European Journal of Nuclear Medicine and Molecular Imaging* **50**(3), 929–936.

Chen, S. & Feng, D. (2004), 'Noninvasive quantification of the differential portal and arterial contribution to the liver blood supply from pet measurements using the/sup 11/c-acetate kinetic model', *IEEE transactions on biomedical engineering* **51**(9), 1579–1585.

Chen, X., Hu, P., Yu, H., Tan, H., He, Y., Cao, S., Zhou, Y. & Shi, H. (2023*b*), 'Head-to-head intra-individual comparison of total-body 2-[18f]fdg pet/ct and digital pet/ct in patients with malignant tumor: how sensitive could it be?', *European Radiology* **33**(11), 7890–7898.

Chen, X., Zhang, S., Zhang, J., Chen, L., Wang, R. & Zhou, Y. (2021*a*), 'Noninvasive quantification of nonhuman primate dynamic 18f-fdg pet imaging', *Physics in Medicine & Biology* **66**(6), 064005.

Chen, Y., Goldsmith, J. & Ogden, R. T. (2019), 'Functional data analysis of dynamic pet data', *Journal of the American Statistical Association* **114**(526), 595–609.

Chen, Y., Li, L., Yu, X., Wang, J., Wang, Y., Huang, G. & Liu, J. (2021*b*), 'Is dynamic total-body pet imaging feasible in the clinical daily practice?'.

Chen, Z., Cheng, Z., Duan, Y., Zhang, Q., Zhang, N., Gu, F., Wang, Y., Zhou, Y., Wang, H., Liang, D., Zheng, H. & Hu, Z. (2022*b*), 'Accurate total-body ki parametric imaging with shortened dynamic 18f-FDG PET scan durations via effective data processing', *Medical Physics* .

Cheng, Z., Wen, J., Huang, G. & Yan, J. (2021), 'Applications of artificial intelligence in nuclear medicine image generation', *Quantitative Imaging in Medicine and Surgery* **11**(6), 2792.

Cherry, S. R., Jones, T., Karp, J. S., Qi, J., Moses, W. W. & Badawi, R. D. (2017), 'Total-body pet: Maximizing sensitivity to create new opportunities for clinical research and patient care', *Journal of Nuclear Medicine* **59**(1), 3–12.

Choi, Y., Hawkins, R. A., Huang, S.-C., Brunken, R. C., Hoh, C. K., Messa, C., Nitzsche, E. U., Phelps, M. E. & Schelbert, H. R. (1994), 'Evaluation of the effect of glucose ingestion and kinetic model configurations of fdg in the normal liver', *Journal of Nuclear Medicine* **35**(5), 818–823.

Choi, Y., Hawkins, R. A., Huang, S.-C., Gambhir, S. S., Brunken, R. C., Phelps, M. E. & Schelbert, H. R. (1991), 'Parametric images of myocardial metabolic rate of glucose generated from dynamic cardiac pet and 2-[18f] fluoro-2-deoxy-d-glucose studies.', *Journal of nuclear medicine: official publication, Society of Nuclear Medicine* **32**(4), 733–738.

Coello, C., Fisk, M., Mohan, D., Wilson, F. J., Brown, A. P., Polkey, M. I., Wilkinson, I., Tal-Singer, R., Murphy, P. S. & Cheriyan, J. (2017), 'Quantitative analysis of dynamic 18 f-fdg pet/ct for measurement of lung inflammation', *EJNMMI research* **7**(1), 1–12.

Cui, J., Gong, K., Guo, N., Wu, C., Meng, X., Kim, K., Zheng, K., Wu, Z., Fu, L. & Xu, B. (2019), 'Pet image denoising using unsupervised deep learning', *European journal of nuclear medicine and molecular imaging* **46**(13), 2780–2789.

Cunningham, V. J. & Jones, T. (1993), 'Spectral analysis of dynamic pet studies', *Journal of Cerebral Blood Flow & Metabolism* **13**(1), 15–23.

Dahlbom, M. (2001), Estimation of image noise in pet using the bootstrap method, *in* '2001 IEEE Nuclear Science Symposium Conference Record (Cat. No. 01CH37310)', Vol. 4, IEEE, pp. 2075–2079.

Dai, B., Daube-Witherspoon, M. E., McDonald, S., Werner, M. E., Parma, M. J., Geagan, M. J., Viswanath, V. & Karp, J. S. (2023), 'Performance evaluation of the pennpet explorer with expanded axial coverage', *Physics in Medicine & Biology* **68**(9), 095007.

Delbeke, D., Coleman, R., Guiberteau, M., Brown, M., Royal, H., Siegel, B., Townsend, D., Berland, L., Parker, J., Hubner, K., Stabin, M., Zubal, G., Kachelriess, M., Cronin, V. & Holbrook, S. (2006), 'Procedure guideline for tumor imaging with 18f-fdg pet/ct 1.0', *Journal of Nuclear Medicine* **47**(5), 885–895.

Dias, A. H., Pedersen, M. F., Danielsen, H., Munk, O. L. & Gormsen, L. C. (2021), 'Clinical feasibility and impact of fully automated multiparametric pet imaging using direct patlak reconstruction: evaluation of 103 dynamic whole-body 18f-fdg pet/ct scans', *European Journal of Nuclear Medicine and Molecular Imaging* **48**(3), 837–850.

Dias, A., Hansen, A., Munk, O. & Gormsen, L. (2022), 'Normal values for (18)f-fdg uptake in organs and tissues measured by dynamic whole body multiparametric fdg pet in 126 patients', *EJNMMI Res* **12**(1), 15.

Dimitrakopoulou-Strauss, A., Pan, L. & Sachpekidis, C. (2021), 'Kinetic modeling and parametric imaging with dynamic pet for oncological applications: general considerations, current clinical applications, and future

perspectives', *European Journal of Nuclear Medicine and Molecular Imaging* **48**(1), 21–39.

Dunnwald, L. K., Doot, R. K., Specht, J. M., Gralow, J. R., Ellis, G. K., Livingston, R. B., Linden, H. M., Gadi, V. K., Kurland, B. F. & Schubert, E. K. (2011), 'Pet tumor metabolism in locally advanced breast cancer patients undergoing neoadjuvant chemotherapy: value of static versus kinetic measures of fluorodeoxyglucose uptake', *Clinical Cancer Research* **17**(8), 2400–2409.

Dunnwald, L. K., Gralow, J. R., Ellis, G. K., Livingston, R. B., Linden, H. M., Specht, J. M., Doot, R. K., Lawton, T. J., Barlow, W. E. & Kurland, B. F. (2008), 'Tumor metabolism and blood flow changes by positron emission tomography: relation to survival in patients treated with neoadjuvant chemotherapy for locally advanced breast cancer', *Journal of Clinical Oncology* **26**(27), 4449.

Dutta, J., Leahy, R. M. & Li, Q. (2013), 'Non-local means denoising of dynamic pet images', *PloS one* **8**(12), e81390.

Efron, B. & Tibshirani, R. J. (1994), *An introduction to the bootstrap*, CRC press.

Feng, D. D., Chen, K. & Wen, L. (2020), 'Noninvasive input function acquisition and simultaneous estimations with physiological parameters for pet quantification: a brief review', *IEEE Transactions on Radiation and Plasma Medical Sciences* **4**(6), 676–683.

Feng, D., Huang, S.-C. & Wang, X. (1993), 'Models for computer simulation studies of input functions for tracer kinetic modeling with positron emission tomography', *International journal of bio-medical computing* **32**(2), 95–110.

Feng, D., Wong, K.-P., Wu, C.-M. & Siu, W.-C. (1997), 'A technique for extracting physiological parameters and the required input function simultaneously from pet image measurements: Theory and simulation study', *IEEE transactions on information technology in biomedicine* **1**(4), 243–254.

Feng, T., Tsui, B. M., Li, X., Vranesic, M., Lodge, M. A., Gulaldi, N. C. & Szabo, Z. (2015), 'Image-derived and arterial blood sampled input func-

tions for quantitative pet imaging of the angiotensin ii subtype 1 receptor in the kidney', *Medical physics* **42**(11), 6736–6744.

Feng, T., Zhao, Y., Shi, H., Li, H., Zhang, X., Wang, G., Badawi, R. D., Price, P. M., Jones, T. & Cherry, S. R. (2019), The effects of delay on the input function for early dynamics in total body parametric imaging, *in* '2019 IEEE Nuclear Science Symposium and Medical Imaging Conference (NSS/MIC)', IEEE, pp. 1–6.

Feng, T., Zhao, Y., Shi, H., Li, H., Zhang, X., Wang, G., Price, P. M., Badawi, R. D., Cherry, S. R. & Jones, T. (2021), 'Total-body quantitative parametric imaging of early kinetics of 18F-FDG', *J Nucl Med* **62**(5), 738–744.

Filippi, L., Dimitrakopoulou-Strauss, A., Evangelista, L. & Schillaci, O. (2022), 'Long axial field-of-view pet/ct devices: are we ready for the technological revolution?'.

Friedman, J., Hastie, T. & Tibshirani, R. (2001), *The elements of statistical learning*, Springer series in statistics New York.

Ganguly, D., Chakraborty, S., Balitanas, M. & Kim, T.-h. (2010), *Medical Imaging: A Review*, Springer Berlin Heidelberg, pp. 504–516.

Gong, K., Catana, C., Qi, J. & Li, Q. (2021), 'Direct reconstruction of linear parametric images from dynamic pet using nonlocal deep image prior', *IEEE Transactions on Medical Imaging* **41**(3), 680–689.

Gong, K., Guan, J., Kim, K., Zhang, X., Yang, J., Seo, Y., El Fakhri, G., Qi, J. & Li, Q. (2018), 'Iterative pet image reconstruction using convolutional neural network representation', *IEEE transactions on medical imaging* **38**(3), 675–685.

Graham, M. M. & Lewellen, B. L. (1993), 'High-speed automated discrete blood sampling for positron emission tomography', *Journal of Nuclear Medicine* **34**(8), 1357–1360.

Gu, F. (2023), Improved Statistical Quantitation of Dynamic PET Scans, PhD thesis, University College Cork.

Gu, F., Hernandez, F., O'Sullivan, F., Muzi, M., Eyal, S., Unadkat, J. & Mankoff, D. (2019*a*), Whole-body metabolic imaging of p-glycoprotein activity in pregnant macaques, *in* 'European Molecular Imaging Meeting'.

Gu, F., O'Sullivan, F., Muzi, M. & Mankoff, D. A. (2021*a*), 'Quantitation of multiple injection dynamic pet scans: an investigation of the benefits of pooling data from separate scans when mapping kinetics', *Physics in Medicine & Biology* **66**(13), 135010.

Gu, F. & Wu, Q. (2023), 'Quantitation of dynamic total-body pet imaging: recent developments and future perspectives', *Eur J Nucl Med Mol Imaging* .

Gu, F., Wu, Q. & O'Sullivan, F. (2021*b*), Image-domain bootstrapping of pet time-course data for assessment of uncertainty in complex regional summaries of mapped kinetics, *in* '2021 IEEE Nuclear Science Symposium and Medical Imaging Conference (NSS/MIC)', IEEE, pp. 1–3.

Gu, F., Wu, Q., O'Sullivan, F., Huang, J., Muzi, M. & Mankoff, D. A. (2019*b*), An illustration of the use of model-based bootstrapping for evaluation of uncertainty in kinetic information derived from dynamic pet, *in* '2019 IEEE Nuclear Science Symposium and Medical Imaging Conference (NSS/MIC)', IEEE, pp. 1–3.

Gu, F., Wu, Q., Wu, J., Hu, D., Xu, T., Cao, S., Zhou, Y. & Shi, H. (2022), 'Feasibility of standard and generalized patlak models for dynamic imaging of multiple organs using the uexplorer pet scanner', *Journal of Nuclear Medicine* **63**(Supplement 2), 3185–3185.

Gunn, R. N., Gunn, S. R. & Cunningham, V. J. (2001), 'Positron emission tomography compartmental models', *Journal of Cerebral Blood Flow & Metabolism* **21**(6), 635–652.

Gunn, R. N., Lammertsma, A. A., Hume, S. P. & Cunningham, V. J. (1997), 'Parametric imaging of ligand-receptor binding in pet using a simplified reference region model', *Neuroimage* **6**(4), 279–287.

Gunn, R. N., Sargent, P. A., Bench, C. J., Rabiner, E. A., Osman, S., Pike, V. W., Hume, S. P., Grasby, P. M. & Lammertsma, A. A. (1998), 'Tracer kinetic modeling of the 5-ht1areceptor ligand [carbonyl-11c] way-100635 for pet', *Neuroimage* **8**(4), 426–440.

Guo, Z., Li, X., Huang, H., Guo, N. & Li, Q. (2019), 'Deep learning-based image segmentation on multimodal medical imaging', *IEEE Transactions on Radiation and Plasma Medical Sciences* **3**(2), 162–169.

Häggström, I., Schmidtlein, C. R., Campanella, G. & Fuchs, T. J. (2019), 'Deeppet: A deep encoder–decoder network for directly solving the pet image reconstruction inverse problem', *Medical image analysis* **54**, 253–262.

Hawe, D. (2016), Statistical considerations in the kinetic analysis of PET-FDG brain tumour studies, PhD thesis, University College Cork.

Hawe, D., Hernández Fernández, F. R., O'Suilleabháin, L., Huang, J., Wolsztynski, E. & O'Sullivan, F. (2012), 'Kinetic analysis of dynamic positron emission tomography data using open-source image processing and statistical inference tools', *Wiley Interdisciplinary Reviews: Computational Statistics* **4**(3), 316–322.

Haynor, D. R. & Woods, S. D. (1989), 'Resampling estimates of precision in emission tomography', *IEEE Transactions on Medical Imaging* **8**(4), 337–343.

Hicks, R. J. (2023), 'So, you want to get into "total-body" pet/ct scanning? an installation guide for beginners!', *Cancer Imaging* **23**(1), 35.

Hoh, C. K. (2007), 'Clinical use of fdg pet', *Nuclear medicine and biology* **34**(7), 737–742.

HS, M. (2000), 'Reduced cerebral blood flow in white matter in ischaemic leukoaraiosis demonstrated using quantitative exogenous contrast based perfusion MRI', *J Neurol Neurosurg Psychiatry* **69**(1), 48–53.

Hu, H., Huang, Y., Sun, H., Zhou, K., Jiang, L., Zhong, J., Chen, L., Wang, L., Han, Y. & Wu, H. (2023), 'A proper protocol for routine 18f-fdg uexplorer total-body pet/ct scans', *EJNMMI Physics* **10**(1).

Hu, P., Zhang, Y., Yu, H., Chen, S., Tan, H., Qi, C., Dong, Y., Wang, Y., Deng, Z. & Shi, H. (2021), 'Total-body 18f-fdg pet/ct scan in oncology patients: how fast could it be?', *European journal of nuclear medicine and molecular imaging* **48**(8), 2384–2394.

Huang, J., Mou, T., O'Regan, K. & O'Sullivan, F. (2020), 'Spatial auto-regressive analysis of correlation in 3-d pet with application to model-based simulation of data', *IEEE Transactions on Medical Imaging* **39**(4), 964–974.

Huang, J. & O'Sullivan, F. (2014), 'An analysis of whole body tracer kinetics in dynamic pet studies with application to image-based blood input function extraction', *IEEE transactions on medical imaging* **33**(5), 1093–1108.

Huang, S., Barrio, J., Yu, D., Chen, B., Grafton, S., Melega, W., Hoffman, J., Satyamurthy, N., Mazziotta, J. & Phelps, M. (1991), 'Modelling approach for separating blood time activity curves in positron emission tomographic studies', *Physics in Medicine & Biology* **36**(6), 749.

Huang, S. C., Barrio, J. R. & Phelps, M. E. (1986), 'Neuroreceptor assay with positron emission tomography: equilibrium versus dynamic approaches', *J Cereb Blood Flow Metab* **6**(5), 515–21.

Huang, S.-C., Phelps, M. E., Hoffman, E. J., Sideris, K., Selin, C. J. & Kuhl, D. E. (1980), 'Noninvasive determination of local cerebral metabolic rate of glucose in man', *American Journal of Physiology-Endocrinology And Metabolism* **238**(1), E69–E82.

Huang, S., Carson, R., Hoffman, E., Carson, J., MacDonald, N., Barrio, J. & Phelps, M. (1983), 'Quantitative measurement of local cerebral blood flow in humans by positron computed tomography and 15o-water', *J Cereb Blood Flow Metab* **3**(2), 141–153.

Huang, Z., Wu, Y., Fu, F., Meng, N., Gu, F., Wu, Q., Zhou, Y., Yang, Y., Liu, X. & Zheng, H. (2022), 'Parametric image generation with the uexplorer total-body pet/ct system through deep learning', *European Journal of Nuclear Medicine and Molecular Imaging* pp. 1–11.

Huesman, R. (1977), 'The effects of a finite number of projection angles and finite lateral sampling of projections on the propagation of statistical errors in transverse section reconstruction', *Physics in Medicine and Biology* **22**(3), 511–521.

Ibaraki, M., Matsubara, K., Nakamura, K., Yamaguchi, H. & Kinoshita, T. (2014), 'Bootstrap methods for estimating pet image noise: experimental validation and an application to evaluation of image reconstruction algorithms', *Annals of nuclear medicine* **28**(2), 172–182.

Joe, H. (2014), *Dependence modeling with copulas*, CRC press.

Jones, T. & Townsend, D. W. (2017), 'History and future technical in-

novation in positron emission tomography', *Journal of Medical Imaging* **4**(1), 011013.

Kahn, D., Weiner, G., Ben-Haim, S., Boles Ponto, L. L., Madsen, M. T., Bushnell, D. L., Watkins, G. L., Argenyi, E. A. & Hichwa, R. D. (1994), 'Positron emission tomographic measurement of bone marrow blood flow to the pelvis and lumbar vertebrae in young normal adults', *Blood* **83**(4), 958–963.

Kak, A. C., Slaney, M. & Wang, G. (2002), 'Principles of computerized tomographic imaging', *Medical Physics* **29**(1), 107–107.

Kamasak, M. E., Bouman, C. A., Morris, E. D. & Sauer, K. (2005), 'Direct reconstruction of kinetic parameter images from dynamic pet data', *IEEE transactions on medical imaging* **24**(5), 636–650.

Karakatsanis, N. A., Casey, M. E., Lodge, M. A., Rahmim, A. & Zaidi, H. (2016), 'Whole-body direct 4d parametric pet imaging employing nested generalized patlak expectation–maximization reconstruction', *Physics in Medicine & Biology* **61**(15), 5456.

Karakatsanis, N. A., Zhou, Y., Lodge, M. A., Casey, M. E., Wahl, R. L., Zaidi, H. & Rahmim, A. (2015), 'Generalized whole-body patlak parametric imaging for enhanced quantification in clinical pet', *Physics in Medicine & Biology* **60**(22), 8643.

Katal, S., Eibschutz, L. S., Saboury, B., Gholamrezanezhad, A. & Alavi, A. (2022), 'Advantages and applications of total-body pet scanning', *Diagnostics* **12**(2), 426.

Kaufmann, P. A., Gnecchi-Ruscone, T., Yap, J. T., Rimoldi, O. & Camici, P. G. (1999), 'Assessment of the reproducibility of baseline and hyperemic myocardial blood flow measurements with 15o-labeled water and pet', *Journal of nuclear medicine* **40**(11), 1848–1856.

Keiding, S. (2012), 'Bringing physiology into pet of the liver', *Journal of Nuclear Medicine* **53**(3), 425–433.

Keramida, G., Potts, J., Bush, J., Verma, S., Dizdarevic, S. & Peters, A. M. (2014), 'Accumulation of 18f-fdg in the liver in hepatic steatosis', *American Journal of Roentgenology* **203**(3), 643–648.

Kety, S. S. & Schmidt, C. F. (1945), 'The determination ofcerebral blood øow in man by the use of nitrous oxide inlow concentrations.', *Am. J. Physiol.* **143**, 53–66.

Kety, S. S. & Schmidt, C. F. (1948), 'The nitrous oxide method for the quantitative determination of cerebral blood flow in man: theory, procedure and normal values', *The Journal of Clinical Investigation* **27**(4), 476–483.

Khalil, M. M. (2017), *Basic science of PET imaging*, Springer.

King, R. B., Raymond, G. M. & Bassingthwaighte, J. B. (1996), 'Modeling blood flow heterogeneity', *Annals of biomedical engineering* **24**(3), 352–372.

Knuuti, J., Tuisku, J., Kärpijoki, H., Iida, H., Maaniitty, T., Latva-Rasku, A., Oikonen, V., Nesterov, S. V., Teuho, J., Jaakkola, M. K., Klén, R., Louhi, H., Saunavaara, V., Nuutila, P., Saraste, A., Rinne, J. & Nummenmaa, L. (2023), 'Quantitative perfusion imaging with total-body pet', *Journal of Nuclear Medicine* **64**(Supplement 2), 11S–19S.

Kostakoglu, L., Duan, F., Idowu, M. O., Jolles, P. R., Bear, H. D., Muzi, M., Cormack, J., Muzi, J. P., Pryma, D. A. & Specht, J. M. (2015), 'A phase ii study of 3-deoxy-3-18f-fluorothymidine pet in the assessment of early response of breast cancer to neoadjuvant chemotherapy: results from acrin 6688', *Journal of Nuclear Medicine* **56**(11), 1681–1689.

Kotasidis, F. A., Tsoumpas, C. & Rahmim, A. (2014), 'Advanced kinetic modelling strategies: towards adoption in clinical pet imaging', *Clinical and Translational Imaging* **2**(3), 219–237.

Kucharczak, F., Loquin, K., Buvat, I., Strauss, O. & Mariano-Goulart, D. (2018), 'Interval-based reconstruction for uncertainty quantification in PET', *Physics in Medicine & Biology* **63**(3), 035014.

Kudomi, N., Koivuviita, N., Liukko, K., Oikonen, V. J., Tolvanen, T., Iida, H., Tertti, R., Metsärinne, K., Iozzo, P. & Nuutila, P. (2008), 'Parametric renal blood flow imaging using [15o]h2o and PET', *Eur J Nucl Med Mol Imaging* **36**(4), 683–691.

Kuntner, C. & Stout, D. (2014), 'Quantitative preclinical pet imaging: opportunities and challenges', *Frontiers in physics* **2**, 12.

Kutner, M., Nachtsheim, C., Neter, J. & Li, W. (2013), *Applied linear statistical models*, McGraw-Hill.

Lammertsma, A. A. (2017), 'Forward to the past: the case for quantitative pet imaging', *Journal of Nuclear Medicine* **58**(7), 1019–1024.

Lan, X., Huo, L., Li, S., Wang, J. & Cai, W. (2022), 'State-of-the-art of nuclear medicine and molecular imaging in china: after the first 66 years (1956–2022)'.

Lartizien, C., Aubin, J.-B. & Buvat, I. (2010), 'Comparison of bootstrap resampling methods for 3-d pet imaging', *IEEE transactions on medical imaging* **29**(7), 1442–1454.

Lau, J., Rousseau, E., Kwon, D., Lin, K.-S., Bénard, F. & Chen, X. (2020), 'Insight into the development of pet radiopharmaceuticals for oncology', *Cancers* **12**(5), 1312.

Lauritsen, K., Søndergaard, E., Luong, T., Møller, N. & Gormsen, L. C. (2020), 'Acute Hyperketonemia Does Not Affect Glucose or Palmitate Uptake in Abdominal Organs or Skeletal Muscle', *J Clin Endocrinol Metab* **105**(6), 1785–1790.

Leahy, R. M. & Qi, J. (2000), 'Statistical approaches in quantitative positron emission tomography', *Statistics and Computing* **10**(2), 147–165.

Lecomte, R. (2009), 'Novel detector technology for clinical pet', *European journal of nuclear medicine and molecular imaging* **36**(1), 69–85.

Lennon, H. & Yuan, J. (2019), 'Estimation of a digitised gaussian arma model by monte carlo expectation maximisation', *Computational Statistics and Data Analysis* **133**, 277–284.

Li, E. J., Spencer, B. A., Schmall, J. P., Abdelhafez, Y., Badawi, R. D., Wang, G. & Cherry, S. R. (2022*a*), 'Efficient delay correction for total-body pet kinetic modeling using pulse timing methods', *Journal of Nuclear Medicine* **63**(8), 1266–1273.

Li, E., Spencer, B., Abdelhafez, Y., López, J., Wang, G. & Cherry, S. (2022*b*), 'Total-body perfusion imaging using [11c]-butanol', *Journal of Nuclear Medicine* **63**(supplement 2), 2247–2247.

Li, F., Hicks, J. W., Yu, L., Desjardin, L., Morrison, L., Hadway, J. & Lee, T.-Y. (2020), 'Plasma radio-metabolite analysis of pet tracers for dynamic pet imaging: Tlc and autoradiography', *EJNMMI research* **10**(1), 1–12.

Li, J., Ni, B., Yu, X., Wang, C., Li, L., Zhou, Y., Gu, Y., Huang, G., Hou, J. & Liu, J. (2023), 'Metabolic kinetic modeling of [11c] methionine based on total-body pet in multiple myeloma', *European Journal of Nuclear Medicine and Molecular Imaging* pp. 1–9.

Li, W., Liu, H., Cheng, F., Li, Y., Li, S. & Yan, J. (2021), 'Artificial intelligence applications for oncological positron emission tomography imaging', *European Journal of Radiology* **134**, 109448.

Li, Y., Hu, J., Sari, H., Xue, S., Ma, R., Kandarpa, S., Visvikis, D., Rominger, A., Liu, H. & Shi, K. (2022*c*), 'A deep neural network for parametric image reconstruction on a large axial field-of-view pet', *European journal of nuclear medicine and molecular imaging* pp. 1–14.

Li, Z., Yipintsoi, T. & Bassingthwaighte, J. B. (1997), 'Nonlinear model for capillary-tissue oxygen transport and metabolism', *Annals of biomedical engineering* **25**(4), 604–619.

Liang, G., Zhou, J., Chen, Z., Wan, L., Wumener, X., Zhang, Y., Liang, D., Liang, Y. & Hu, Z. (2023), 'Combining deep learning with a kinetic model to predict dynamic pet images and generate parametric images', *EJNMMI Physics* **10**(1).

Lin, Y., Liu, E.-t. & Mou, T. (2022), Statistical characteristics of 3-d pet imaging: A comparison between conventional and total-body pet scanners, *in* 'Pattern Recognition and Computer Vision: 5th Chinese Conference, PRCV 2022, Shenzhen, China, November 4–7, 2022, Proceedings, Part II', Springer, pp. 240–250.

Liu, G., Hu, P., Yu, H., Tan, H., Zhang, Y., Yin, H., Hu, Y., Gu, J. & Shi, H. (2021*a*), 'Ultra-low-activity total-body dynamic PET imaging allows equal performance to full-activity PET imaging for investigating kinetic metrics of 18f-FDG in healthy volunteers', *European Journal of Nuclear Medicine and Molecular Imaging* **48**(8), 2373–2383.

Liu, G., Mao, W., Yu, H., Hu, Y., Gu, J. & Shi, H. (2023*a*), 'One-stop [18f] fdg and [68ga] ga-dota-fapi-04 total-body pet/ct examination with dual-

low activity: a feasibility study', *European Journal of Nuclear Medicine and Molecular Imaging* pp. 1–11.

Liu, G., Shi, Y., Hou, X., Yu, H., Hu, Y., Zhang, Y. & Shi, H. (2023*b*), 'Dynamic total-body pet/ct imaging with reduced acquisition time shows acceptable performance in quantification of [18f]fdg tumor kinetic metrics', *European Journal of Nuclear Medicine and Molecular Imaging* .

Liu, G., Xu, H., Hu, P., Tan, H., Zhang, Y., Yu, H., Li, X. & Shi, H. (2021*b*), 'Kinetic metrics of 18f-fdg in normal human organs identified by systematic dynamic total-body positron emission tomography', *European Journal of Nuclear Medicine and Molecular Imaging* **48**(8), 2363–2372.

Liu, G., Yu, H., Shi, D., Hu, P., Hu, Y., Tan, H., Zhang, Y., Yin, H. & Shi, H. (2021*c*), 'Short-time total-body dynamic pet imaging performance in quantifying the kinetic metrics of 18f-fdg in healthy volunteers', *European Journal of Nuclear Medicine and Molecular Imaging* pp. 1–11.

Logan, J. (2003), 'A review of graphical methods for tracer studies and strategies to reduce bias', *Nuclear medicine and biology* **30**(8), 833–844.

Logan, J., Fowler, J. S., Volkow, N. D., Wolf, A. P., Dewey, S. L., Schlyer, D. J., MacGregor, R. R., Hitzemann, R., Bendriem, B. & Gatley, S. J. (1990), 'Graphical analysis of reversible radioligand binding from time-activity measurements applied to [n-11c-methyl]-(-)-cocaine pet studies in human subjects', *Journal of Cerebral Blood Flow & Metabolism* **10**(5), 740–747.

Lu, W., Onofrey, J. A., Lu, Y., Shi, L., Ma, T., Liu, Y. & Liu, C. (2019), 'An investigation of quantitative accuracy for deep learning based denoising in oncological pet', *Physics in Medicine & Biology* **64**(16), 165019.

Lv, J., Yin, H., Yu, H., Liu, G. & Shi, H. (2022), 'The feasibility of ultralow-activity 18f-FDG dynamic PET imaging in lung adenocarcinoma patients through total-body PET/CT scanner', *Annals of Nuclear Medicine* **36**(10), 887–896.

Maitra, R. & O'Sullivan, F. (1998), 'Variability assessment in positron emission tomography and related generalized deconvolution models', *Journal of the American Statistical Association* **93**(444), 1340–1355.

Mankoff, D. A., Dunnwald, L. K., Gralow, J. R., Ellis, G. K., Charlop, A., Lawton, T. J., Schubert, E. K., Tseng, J. & Livingston, R. B. (2002), 'Blood flow and metabolism in locally advanced breast cancer: relationship to response to therapy', *Journal of Nuclear Medicine* **43**(4), 500–509.

Mankoff, D. A., Dunnwald, L. K., Gralow, J. R., Ellis, G. K., Schubert, E. K., Tseng, J., Lawton, T. J., Linden, H. M. & Livingston, R. B. (2003), 'Changes in blood flow and metabolism in locally advanced breast cancer treated with neoadjuvant chemotherapy', *Journal of Nuclear Medicine* **44**(11), 1806–1814.

Mankoff, D. A., Muzi, M. & Zaidi, H. (2006), Quantitative analysis in nuclear oncologic imaging, *in* 'Quantitative analysis in nuclear medicine imaging', Springer, New York, NY, USA, pp. 494–536.

Mankoff, D. A., Pantel, A. R., Viswanath, V. & Karp, J. S. (2019), 'Advances in pet diagnostics for guiding targeted cancer therapy and studying in vivo cancer biology', *Current Pathobiology Reports* **7**(3), 97–108.

Materne, R., Van Beers, E., Smith, A., Leconte, I., JAMART, J., DEHOUX, J.-P., KEYEUX, A. & HORSMANS, Y. (2000), 'Non-invasive quantification of liver perfusion with dynamic computed tomography and a dual-input one-compartmental model', *Clin Sci* **99**(6), 517–525.

Matsubara, K., Ibaraki, M., Nemoto, M., Watabe, H. & Kimura, Y. (2022), 'A review on ai in pet imaging', *Annals of Nuclear Medicine* pp. 1–11.

Matsunaga, K., Yanagawa, M., Otsuka, T., Hirata, H., Kijima, T., Kumanogoh, A., Tomiyama, N., Shimosegawa, E. & Hatazawa, J. (2017), 'Quantitative pulmonary blood flow measurement using 15o-h2o PET with and without tissue fraction correction: a comparison study', *EJNMMI Res* **7**(1).

Meier, P. & Zierler, K. L. (1954), 'On the theory of the indicator-dilution method for measurement of blood flow and volume', *Journal of applied physiology* **6**(12), 731–744.

Meikle, S. R., Matthews, J. C., Cunningham, V. J., Bailey, D. L., Livieratos, L., Jones, T. & Price, P. (1998), 'Parametric image reconstruction using spectral analysis of pet projection data', *Physics in Medicine & Biology* **43**(3), 651.

Meikle, S. R., Sossi, V., Roncali, E., Cherry, S. R., Banati, R., Mankoff, D., Jones, T., James, M., Sutcliffe, J. & Ouyang, J. (2021), 'Quantitative pet in the 2020s: a roadmap', *Physics in Medicine & Biology* **66**(6), 06RM01.

Meng, N., Zhang, M., Ren, J., Fu, F., Xie, B., Wu, Y., Li, Z., Dai, B., Li, Y., Feng, T., Xu, T. & Wang, M. (2023), 'Quantitative parameters of static imaging and fast kinetics imaging in 18f-fdg total-body pet/ct for the assessment of histological feature of pulmonary lesions', *Quantitative Imaging in Medicine and Surgery* **13**(9), 5579–5592.

Meyer, P. T., Elmenhorst, D., Bier, D., Holschbach, M. H., Matusch, A., Coenen, H. H., Zilles, K. & Bauer, A. (2005), 'Quantification of cerebral a1 adenosine receptors in humans using [18f] cpfpx and pet: an equilibrium approach', *Neuroimage* **24**(4), 1192–1204.

Mintun, M. A., Raichle, M. E., Kilbourn, M. R., Wooten, G. F. & Welch, M. J. (1984), 'A quantitative model for the in vivo assessment of drug binding sites with positron emission tomography', *Annals of Neurology: Official Journal of the American Neurological Association and the Child Neurology Society* **15**(3), 217–227.

Mou, T., Huang, J. & O'Sullivan, F. (2017), 'The gamma characteristic of reconstructed pet images: Implications for roi analysis', *IEEE transactions on medical imaging* **37**(5), 1092–1102.

Mullani, N. & Gould, K. (1983), 'First-pass measurements of regional blood flow with external detectors', *Journal of Nuclear Medicine* **24**(7), 577–581.

Mullani, N., Herbst, R., O'Neil, R., Gould, K., Barron, B. & Abbruzzese, J. (2008), 'Tumor blood flow measured by pet dynamic imaging of first-pass 18f-fdg uptake: A comparison with 15o-labeled water-measured blood flow', *Journal of Nuclear Medicine* **49**(4), 517–523.

Muzi, M., O'Sullivan, F., Mankoff, D. A., Doot, R. K., Pierce, L. A., Kurland, B. F., Linden, H. M. & Kinahan, P. E. (2012), 'Quantitative assessment of dynamic pet imaging data in cancer imaging', *Magnetic resonance imaging* **30**(9), 1203–1215.

Muzi, M., Spence, A., O'Sullivan, F., Mankoff, D., Wells, J., Grierson, J., Link, J. & Krohn, K. (2006), 'Kinetic analysis of 3′-deoxy-3′-18f-

fluorothymidine in patients with gliomas', *Journal of Nuclear Medicine* **47**(10), 1612–1621.

Nadig, V., Herrmann, K., Mottaghy, F. M. & Schulz, V. (2021), 'Hybrid total-body pet scanners—current status and future perspectives', *European journal of nuclear medicine and molecular imaging* pp. 1–15.

Nakajima, R., Abe, K., Kondo, T., Tanabe, K. & Sakai, S. (2015), 'Clinical role of early dynamic fdg-pet/ct for the evaluation of renal cell carcinoma', *European Radiology* **26**(6), 1852–1862.

Napieczynska, H., Kolb, A., Katiyar, P., Tonietto, M., Ud-Dean, M., Stumm, R., Herfert, K., Calaminus, C. & Pichler, B. J. (2018), 'Impact of the arterial input function recording method on kinetic parameters in small-animal pet', *Journal of Nuclear Medicine* **59**(7), 1159–1164.

Natterer, F. (2001), *The Mathematics of Computerized Tomography*, SIAM.

Nelder, J. & Wedderburn, R. (1972), 'Generalized linear models', *Journal of the Royal Statistical Society. Series A (General)* **135**(3), 370–384.

Niyas, S., Pawan, S., Kumar, M. A. & Rajan, J. (2021), 'Medical image segmentation using 3d convolutional neural networks: A review', *arXiv preprint arXiv:2108.08467* .

Nutt, R. (2002), 'The history of positron emission tomography', *Molecular Imaging & Biology* **4**(1), 11–26.

Oguro, A., Taniguchi, H., Koyama, H., Tanaka, H., Miyata, K., Takeuchi, K., Inaba, T., Nakahashi, H. & Takahashi, T. (1993), 'Quantification of human splenic blood flow (quantitative measurement of splenic blood flow with h2 15o and a dynamic state method: 1)', *Ann Nucl Med* **7**(4), 245–250.

Omidvari, N., Jones, T., Price, P. M., Ferre, A. L., Lu, J., Abdelhafez, Y. G., Sen, F., Cohen, S. H., Schmiedehausen, K. & Badawi, R. D. (2023), 'First-in-human immunopet imaging of covid-19 convalescent patients using dynamic total-body pet and a cd8-targeted minibody', *medRxiv* .

Omidvari, N., Jones, T., Price, P., Sen, F., Shacklett, B., Cohen, S., Badawi, R., Wilson, I. & Cherry, S. (2022), 'Total-body imaging of cd8+ t cells in patients recovering from covid-19 – a pilot study using the uexplorer

total-body pet', *Journal of Nuclear Medicine* **63**(supplement 2), 2327–2327.

Østergaard, L., Chesler, D. A., Weisskoff, R. M., Sorensen, A. G. & Rosen, B. R. (1999), 'Modeling cerebral blood flow and flow heterogeneity from magnetic resonance residue data', *Journal of Cerebral Blood Flow & Metabolism* **19**(6), 690–699.

Østergaard, L., Weisskoff, R. M., Chesler, D. A., Gyldensted, C. & Rosen, B. R. (1996), 'High resolution measurement of cerebral blood flow using intravascular tracer bolus passages. part i: Mathematical approach and statistical analysis', *Magnetic Resonance in Medicine* **36**(5), 715–725.

O'Sullivan, F. (1993), 'Imaging radiotracer model parameters in pet: a mixture analysis approach', *IEEE Transactions on Medical Imaging* **12**(3), 399–412.

O'Sullivan, F. (1995), 'A study of least squares and maximum likelihood for image reconstruction in positron emission tomography', *The Annals of Statistics* **23**(4), 1267–1300.

O'Sullivan, F. (2005), 'Locally constrained mixture representation of dynamic imaging data from pet and mr studies', *Biostatistics* **7**(2), 318–338.

O'Sullivan, F., Gu, F., Wu, Q. & O'Suilleabhain, L. D. (2021), 'A generalized linear modeling approach to bootstrapping multi-frame pet image data', *Medical Image Analysis* p. 102132.

O'Sullivan, F., Muzi, M., Mankoff, D. A., Eary, J. F., Spence, A. M. & Krohn, K. A. (2014), 'Voxel-level mapping of tracer kinetics in PET studies: A statistical approach emphasizing tissue life tables', *The Annals of Applied Statistics* **8**(2), 1065–1094.

O'Sullivan, F., Muzi, M., Spence, A. M., Mankoff, D. M., O'sullivan, J. N., Fitzgerald, N., Newman, G. C. & Krohn, K. A. (2009), 'Nonparametric residue analysis of dynamic pet data with application to cerebral fdg studies in normals', *Journal of the American Statistical Association* **104**(486), 556–571.

O'Sullivan, F., O'Sullivan, J. N., Huang, J., Doot, R., Muzi, M., Schubert, E., Peterson, L., Dunnwald, L. K. & Mankoff, D. M. (2017), 'Assessment of a

statistical aif extraction method for dynamic pet studies with 15 o water and 18 f fluorodeoxyglucose in locally advanced breast cancer patients', *Journal of Medical Imaging* **5**(1), 011010.

O'Sullivan, F. & Roy Choudhury, K. (2001), 'An analysis of the role of positivity and mixture model constraints in poisson deconvolution problems', *Journal of Computational and Graphical Statistics* **10**(4), 673–696.

O'Sullivan, F., Wu, Q., Gu, F., Shi, K., O'Suilleabhain, L., Xue, S. & Rominger, A. (2022), 'Mapping fdg tracer kinetics and their uncertainties via the bootstrap using data from a long-axial fov pet/ct scanner', *Journal of Nuclear Medicine* **63**(Supplement 2), 3220–3220.

Pantel, A. R., Viswanath, V., Daube-Witherspoon, M. E., Dubroff, J. G., Muehllehner, G., Parma, M. J., Pryma, D. A., Schubert, E. K., Mankoff, D. A. & Karp, J. S. (2020), 'Pennpet explorer: human imaging on a whole-body imager', *Journal of Nuclear Medicine* **61**(1), 144–151.

Pantel, A. R., Viswanath, V., Muzi, M., Doot, R. K. & Mankoff, D. A. (2022*a*), 'Principles of tracer kinetic analysis in oncology, part i: Principles and overview of methodology', *Journal of Nuclear Medicine* **63**(3), 342–352.

Pantel, A. R., Viswanath, V., Muzi, M., Doot, R. K. & Mankoff, D. A. (2022*b*), 'Principles of tracer kinetic analysis in oncology, part ii: examples and future directions', *Journal of Nuclear Medicine* **63**(4), 514–521.

Parsey, R. V., Slifstein, M., Hwang, D.-R., Abi-Dargham, A., Simpson, N., Mawlawi, O., Guo, N.-N., Van Heertum, R., Mann, J. J. & Laruelle, M. (2000), 'Validation and reproducibility of measurement of 5-ht1a receptor parameters with [carbonyl-11c] way-100635 in humans: comparison of arterial and reference tissue input functions', *Journal of Cerebral Blood Flow & Metabolism* **20**(7), 1111–1133.

Patlak, C. S. & Blasberg, R. G. (1985), 'Graphical evaluation of blood-to-brain transfer constants from multiple-time uptake data. generalizations', *Journal of Cerebral Blood Flow & Metabolism* **5**(4), 584–590.

Patlak, C. S., Blasberg, R. G. & Fenstermacher, J. D. (1983), 'Graphical evaluation of blood-to-brain transfer constants from multiple-time uptake data', *Journal of Cerebral Blood Flow & Metabolism* **3**(1), 1–7.

Peck, M., Pollack, H., Friesen, A., Muzi, M., Shoner, S., Shankland, E., Fink, J., Armstrong, J., Link, J. & Krohn, K. (2015), 'Applications of pet imaging with the proliferation marker [18f]-flt', *The quarterly journal of nuclear medicine and molecular imaging: official publication of the Italian Association of Nuclear Medicine (AIMN)[and] the International Association of Radiopharmacology (IAR),[and] Section of the Society of...* **59**(1), 95.

Pedersen, F., Bergström, M., Bengtsson, E. & Långström, B. (1994), 'Principal component analysis of dynamic positron emission tomography images', *European journal of nuclear medicine* **21**(12), 1285–1292.

Phelps, M., Huang, S., Hoffman, E., Selin, C., Sokoloff, L. & Kuhl, D. (1979), 'Tomographic measurement of local cerebral glucose metabolic rate in humans with (f-18) 2-fluoro-2-deoxy-d-glucose: validation of method', *Annals of Neurology: Official Journal of the American Neurological Association and the Child Neurology Society* **6**(5), 371–388.

Piert, M., Machulla, H., Jahn, M., Stahlschmidt, A., Becker, G. A. & Zittel, T. T. (2002), 'Coupling of porcine bone blood flow and metabolism in high-turnover bone disease measured by [15o]h2o and [18f]fluoride ion positron emission tomography', *Eur J Nucl Med Mol Imaging* **29**, 907–914.

Pouzot, C., Richard, J., Gros, A., Costes, N., Lavenne, F., Bars, D. L. & Guerin, C. (2013), 'Noninvasive quantitative assessment of pulmonary blood flow with 18f-fdg pet', *J Nucl Med* **54**(9), 1653–1660.

Prenosil, G. A., Sari, H., Fürstner, M., Afshar-Oromieh, A., Shi, K., Rominger, A. & Hentschel, M. (2022), 'Performance characteristics of the biograph vision quadra pet/ct system with a long axial field of view using the nema nu 2-2018 standard', *Journal of nuclear medicine* **63**(3), 476–484.

Qi, J. & Leahy, R. M. (2000), 'Resolution and noise properties of MAP reconstruction for fully 3-D PET', *IEEE transactions on medical imaging* **19**(5), 493–506.

R Core Team (2021), *R: A Language and Environment for Statistical Computing*, R Foundation for Statistical Computing, Vienna, Austria.

Rahmim, A., Lodge, M. A., Karakatsanis, N. A., Panin, V. Y., Zhou, Y., McMillan, A., Cho, S., Zaidi, H., Casey, M. E. & Wahl, R. L. (2019), 'Dynamic

whole-body pet imaging: principles, potentials and applications', *European journal of nuclear medicine and molecular imaging* **46**(2), 501–518.

Rahmim, A., Tang, J. & Zaidi, H. (2009), 'Four-dimensional (4d) image reconstruction strategies in dynamic pet: beyond conventional independent frame reconstruction', *Medical physics* **36**(8), 3654–3670.

Rahmim, A. & Zaidi, H. (2008), 'Pet versus spect: strengths, limitations and challenges', *Nuclear Medicine Communications* **29**(3), 193–207.

Rao, C. R. (1973), *Linear statistical inference and its applications*, John Wiley & Sons, New York, NY, USA.

Razifar, P. (2005), Novel approaches for application of principal component analysis on dynamic PET images for improvement of image quality and clinical diagnosis, PhD thesis, Acta Universitatis Upsaliensis.

Razifar, P., Sandström, M., Schnieder, H., Långström, B., Maripuu, E., Bengtsson, E. & Bergström, M. (2005), 'Noise correlation in PET, CT, SPECT and PET/CT data evaluated using autocorrelation function: a phantom study on data, reconstructed using FBP and OSEM', *BMC medical imaging* **5**(1), 5.

Reader, A. J., Corda, G., Mehranian, A., da Costa-Luis, C., Ellis, S. & Schnabel, J. A. (2020), 'Deep learning for pet image reconstruction', *IEEE Transactions on Radiation and Plasma Medical Sciences* **5**(1), 1–25.

Romano, J. P. & Wolf, M. (2017), 'Resurrecting weighted least squares', *Journal of Econometrics* **197**(1), 1 – 19.

Sachpekidis, C., Pan, L., Kopp-Schneider, A., Weru, V., Hassel, J. C. & Dimitrakopoulou-Strauss, A. (2022), 'Application of the long axial field-of-view pet/ct with low-dose [18f] fdg in melanoma', *European Journal of Nuclear Medicine and Molecular Imaging* pp. 1–10.

Samimi, R., Kamali-Asl, A., Geramifar, P., van den Hoff, J. & Rahmim, A. (2020), 'Short-duration dynamic fdg pet imaging: Optimization and clinical application', *Physica Medica* **80**, 193–200.

Sari, H., Eriksson, L., Mingels, C., Alberts, I., Casey, M. E., Afshar-Oromieh, A., Conti, M., Cumming, P., Shi, K. & Rominger, A. (2022*a*), 'Feasibility of using abbreviated scan protocols with population-based input functions

for accurate kinetic modeling of [18f]-fdg datasets from a long axial fov pet scanner', *European journal of nuclear medicine and molecular imaging* pp. 1–9.

Sari, H., Erlandsson, K., Marner, L., Law, I., Larsson, H. B., Thielemans, K., Ourselin, S., Arridge, S., Atkinson, D. & Hutton, B. F. (2018), 'Non-invasive kinetic modelling of pet tracers with radiometabolites using a constrained simultaneous estimation method: evaluation with 11c-sb201745', *EJNMMI research* **8**(1), 1–12.

Sari, H., Mingels, C., Alberts, I., Hu, J., Buesser, D., Shah, V., Schepers, R., Caluori, P., Panin, V. & Conti, M. (2022*b*), 'First results on kinetic modelling and parametric imaging of dynamic 18F-FDG datasets from a long axial FOV PET scanner in oncological patients', *Eur J Nucl Med Mol Imaging* pp. 1–13.

Scheuermann, J., Opanowski, A., Maffei, J., Thibeault, D. H., Karp, J., Siegel, B., Rosen, M. & Kinahan, P. (2013), 'Qualification of NCI-designated comprehensive cancer centers for quantitative PET/CT imaging in clinical trials', *Journal of Nuclear Medicine* **54**(supplement 2), 334–334.

Schierz, J.-H., Opfermann, T., Steenbeck, J., Lopatta, E., Settmacher, U., Stallmach, A., Marlowe, R. J. & Freesmeyer, M. (2013), 'Early dynamic 18f-fdg pet to detect hyperperfusion in hepatocellular carcinoma liver lesions', *Journal of Nuclear Medicine* **54**(6), 848–854.

Schuster, D., Kaplan, J., Gauvain, K., Welch, M. J. & Markham, J. (1995), 'Measurement of regional pulmonary blood flow with pet', *J Nucl Med* **36**(3), 371–377.

Seber, G. A. (2015), *The Linear Model and Hypothesis: A General Unifying Theory*, Springer International Publishing.

Slart, R. H., Tsoumpas, C., Glaudemans, A. W., Noordzij, W., Willemsen, A., Borra, R. J., Dierckx, R. A. & Lammertsma, A. A. (2021), 'Long axial field of view pet scanners: a road map to implementation and new possibilities', *European journal of nuclear medicine and molecular imaging* **48**(13), 4236–4245.

Slimani, L., Kudomi, N., Oikonen, V., Jarvisalo, M., Kiss, J., Naum, A.,

Borra, R., Viljanen, A., Sipila, H., Ferrannini, E., Savunen, T., Nuutila, P. & Iozzo, P. (2008), 'Quantification of liver perfusion with [15o]h2o-pet and its relationship with glucose metabolism and substrate levels', *J Hepatol* **48**(6), 974–982.

Snyder, D. L. (1984), 'Parameter estimation for dynamic studies in emission-tomography systems having list-mode data', *IEEE Transactions on Nuclear Science* **31**(2), 925–931.

Sokoloff, L., Reivich, M., Kennedy, C., Rosiers, M. D., Patlak, C., Pettigrew, K. e. a., Sakurada, O. & Shinohara, M. (1977), 'The [14c] deoxyglucose method for the measurement of local cerebral glucose utilization: theory, procedure, and normal values in the conscious and anesthetized albino rat 1', *Journal of neurochemistry* **28**(5), 897–916.

Spence, A. M., Muzi, M., Graham, M. M., O'Sullivan, F., Krohn, K. A., Link, J. M., Lewellen, T. K., Lewellen, B., Freeman, S. D. & Berger, M. S. (1998), 'Glucose metabolism in human malignant gliomas measured quantitatively with pet, l-[c-ll] glucose and fdg: Analysis of the fdg lumped constant', *Journal of Nuclear Medicine* **39**(3), 440–448.

Spence, A., Muzi, M., Graham, M., O'Sullivan, F., Link, J., Lewellen, T., Lewellen, B., Freeman, S., Mankoff, D., Eary, J. & Krohn, K. (2002), '2-[18f]fluoro-2-deoxyglucose and glucose uptake in malignant gliomas before and after radiotherapy: Correlation with outcome', *Clinical Cancer Research* **8**(4), 971–979.

Spencer, B. A., Berg, E., Schmall, J. P., Omidvari, N., Leung, E. K., Abdelhafez, Y. G., Tang, S., Deng, Z., Dong, Y. & Lv, Y. (2021), 'Performance evaluation of the uexplorer total-body pet/ct scanner based on nema nu 2-2018 with additional tests to characterize pet scanners with a long axial field of view', *Journal of Nuclear Medicine* **62**(6), 861–870.

Sun, T., Wu, Y., Wei, W., Fu, F., Meng, N., Chen, H., Li, X., Bai, Y., Wang, Z. & Ding, J. (2022), 'Motion correction and its impact on quantification in dynamic total-body 18f-fluorodeoxyglucose pet', *EJNMMI physics* **9**(1), 1–16.

Surti, S., Viswanath, V., Daube-Witherspoon, M. E., Conti, M., Casey, M. E. & Karp, J. S. (2020), 'Benefit of improved performance with state-of-the art

digital pet/ct for lesion detection in oncology', *Journal of Nuclear Medicine* **61**(11), 1684–1690.

Svensson, P.-E., Olsson, J., Engbrant, F., Bengtsson, E. & Razifar, P. (2011), 'Characterization and reduction of noise in dynamic pet data using masked volumewise principal component analysis', *Journal of Nuclear Medicine Technology* **39**(1), 27–34.

Takikawa, S., Dhawan, V., Spetsieris, P., Robeson, W., Chaly, T., Dahl, R., Margouleff, D. & Eidelberg, D. (1993), 'Noninvasive quantitative fluorodeoxyglucose pet studies with an estimated input function derived from a population-based arterial blood curve.', *Radiology* **188**(1), 131–136.

Tan, H., Cai, D., Sui, X., Qi, C., Mao, W., Zhang, Y., Liu, G., Yu, H., Chen, S. & Hu, P. (2022), 'Investigating ultra-low-dose total-body [18f]-fdg pet/ct in colorectal cancer: initial experience', *European Journal of Nuclear Medicine and Molecular Imaging* **49**(3), 1002–1011.

Tan, H., Gu, Y., Yu, H., Hu, P., Zhang, Y., Mao, W. & Shi, H. (2020), 'Total-body pet/ct: current applications and future perspectives', *American Journal of Roentgenology* **215**(2), 325–337.

Tan, H., Qi, C., Cao, Y., Cai, D., Mao, W., Yu, H., Sui, X., Liu, G. & Shi, H. (2023), 'Ultralow-dose [18f] fdg pet/ct imaging: demonstration of feasibility in dynamic and static images', *European Radiology* pp. 1–11.

Tanaka, E. & Murayama, H. (1982), Properties of statistical noise in positron emission tomography, *in* 'International Workshop on Physics and Engineering in Medical Imaging', International Society for Optics and Photonics, pp. 158–164.

Thie, J. A. (2004), 'Understanding the standardized uptake value, its methods, and implications for usage', *Journal of Nuclear Medicine* **45**(9), 1431–1434.

Tomasi, G., Turkheimer, F. & Aboagye, E. (2012), 'Importance of quantification for the analysis of pet data in oncology: review of current methods and trends for the future', *Molecular Imaging and Biology* **14**, 131–146.

Tonietto, M., Rizzo, G., Veronese, M. & Bertoldo, A. (2015), Modelling arterial input functions in positron emission tomography dynamic studies,

in '2015 37th annual international conference of the IEEE Engineering in Medicine and Biology Society (EMBC)', IEEE, pp. 2247–2250.

Tonietto, M., Rizzo, G., Veronese, M., Fujita, M., Zoghbi, S. S., Zanotti-Fregonara, P. & Bertoldo, A. (2016), 'Plasma radiometabolite correction in dynamic pet studies: insights on the available modeling approaches', *Journal of Cerebral Blood Flow & Metabolism* **36**(2), 326–339.

Torizuka, T., Tamaki, N., Inokuma, T., Magata, Y., Sasayama, S., Yonekura, Y., Tanaka, A., Yamaoka, Y., Yamamoto, K. & Konishi, J. (1995), 'In vivo assessment of glucose metabolism in hepatocellular carcinoma with fdg-pet', *Journal of Nuclear Medicine* **36**(10), 1811–1817.

Trench, W. F. (2013), 'Elementary differential equations with boundary value problems'.

Tsoumpas, C., Turkheimer, F. E. & Thielemans, K. (2008), 'Study of direct and indirect parametric estimation methods of linear models in dynamic positron emission tomography', *Medical Physics* **35**(4), 1299–1309.

Turkheimer, F. E., Hinz, R., Gunn, R. N., Aston, J. A., Gunn, S. R. & Cunningham, V. J. (2003), 'Rank-shaping regularization of exponential spectral analysis for application to functional parametric mapping', *Physics in Medicine & Biology* **48**(23), 3819.

van der Weijden, C. W., Mossel, P., Bartels, A. L., Dierckx, R. A., Luurtsema, G., Lammertsma, A. A., Willemsen, A. T. & de Vries, E. F. (2023), 'Non-invasive kinetic modelling approaches for quantitative analysis of brain pet studies', *European Journal of Nuclear Medicine and Molecular Imaging* pp. 1–15.

van Sluis, J., van Snick, J. H., Brouwers, A. H., Noordzij, W., Dierckx, R. A. J. O., Borra, R. J. H., Lammertsma, A. A., Glaudemans, A. W. J. M., Slart, R. H. J. A., Yaqub, M., Tsoumpas, C. & Boellaard, R. (2022), 'Shortened duration whole body 18f-FDG PET patlak imaging on the biograph vision quadra PET/CT using a population-averaged input function', *EJNMMI Physics* **9**(1).

Vandenberghe, S., Karakatsanis, N. A., Akl, M. A., Maebe, J., Surti, S., Dierckx, R. A., Pryma, D. A., Nehmeh, S. A., Bouhali, O. & Karp, J. S. (2023), 'The potential of a medium-cost long axial fov pet system for nuclear

medicine departments', *European Journal of Nuclear Medicine and Molecular Imaging* **50**(3), 652–660.

Vandenberghe, S., Mikhaylova, E., D'Hoe, E., Mollet, P. & Karp, J. S. (2016), 'Recent developments in time-of-flight pet', *EJNMMI physics* **3**(1), 1–30.

Vardi, Y., Shepp, L. & Kaufman, L. (1985), 'A statistical model for positron emission tomography', *Journal of the American statistical Association* **80**(389), 8–20.

Veronese, M., Bertoldo, A., Bishu, S., Unterman, A., Tomasi, G., Smith, C. B. & Schmidt, K. C. (2010), 'A spectral analysis approach for determination of regional rates of cerebral protein synthesis with the l-[1-11c] leucine pet method', *Journal of Cerebral Blood Flow & Metabolism* **30**(8), 1460–1476.

Veronese, M., Rizzo, G., Bertoldo, A. & Turkheimer, F. E. (2016), 'Spectral analysis of dynamic pet studies: a review of 20 years of method developments and applications', *Computational and mathematical methods in medicine* **2016**.

Vicini, P. & Bassingthwaighte, J. B. (2014), Chapter 17 - blood–tissue exchange modelling, *in* E. Carson & C. Cobelli, eds, 'Modelling Methodology for Physiology and Medicine (Second Edition)', second edition edn, Elsevier, Oxford, pp. 381 – 415.

Viswanath, V., Chitalia, R., Pantel, A. R., Karp, J. S. & Mankoff, D. A. (2021), 'Analysis of four-dimensional data for total body pet imaging', *PET clinics* **16**(1), 55–64.

Viswanath, V., Pantel, A. R., Daube-Witherspoon, M. E., Doot, R., Muzi, M., Mankoff, D. A. & Karp, J. S. (2020), 'Quantifying bias and precision of kinetic parameter estimation on the PennPET explorer, a long axial field-of-view scanner', *IEEE Transactions on Radiation and Plasma Medical Sciences* **4**(6), 735–749.

Viswanath, V., Sari, H., Pantel, A. R., Conti, M., Daube-Witherspoon, M. E., Mingels, C., Alberts, I., Eriksson, L., Shi, K. & Rominger, A. (2022), 'Abbreviated scan protocols to capture 18f-fdg kinetics for long axial fov pet scanners', *European journal of nuclear medicine and molecular imaging* pp. 1–11.

Votaw, J. R. & Shulman, S. D. (1998), 'Performance evaluation of the picocount flow-through detector for use in cerebral blood flow pet studies', *Journal of Nuclear Medicine* **39**(3), 509–515.

Vriens, D., de Geus-Oei, L.-F., Oyen, W. J. & Visser, E. P. (2009), 'A curve-fitting approach to estimate the arterial plasma input function for the assessment of glucose metabolic rate and response to treatment', *Journal of Nuclear Medicine* **50**(12), 1933–1939.

Wacholtz, E. H. (2011), 'History and development of pet', *ECEI, CEwebsources. http://www. cewebsource. com/coursePDFs/historyofPET. pdf (page consultée le 22 Février 2012)* .

Wahba, G. (1990), *Spline Models for Observational Data*, Society for Industrial and Applied Mathematics.

Wang, D., Zhang, X., Liu, H., Qiu, B., Liu, S., Zheng, C., Fu, J., Mo, Y., Chen, N., Zhou, R., Chu, C., Liu, F., Guo, J., Zhou, Y., Zhou, Y., Fan, W. & Liu, H. (2022*a*), 'Assessing dynamic metabolic heterogeneity in non-small cell lung cancer patients via ultra-high sensitivity total-body [18f]FDG PET/CT imaging: quantitative analysis of [18f]FDG uptake in primary tumors and metastatic lymph nodes', *European Journal of Nuclear Medicine and Molecular Imaging* **49**(13), 4692–4704.

Wang, G., Corwin, M. T., Olson, K. A., Badawi, R. D. & Sarkar, S. (2018), 'Dynamic pet of human liver inflammation: impact of kinetic modeling with optimization-derived dual-blood input function', *Physics in Medicine & Biology* **63**(15), 155004.

Wang, G., Fu, L. & Qi, J. (2008), 'Maximum a posteriori reconstruction of the patlak parametric image from sinograms in dynamic pet', *Physics in Medicine & Biology* **53**(3), 593.

Wang, G., Nardo, L., Jones, T., Cherry, S. R. & Badawi, R. D. (2021*a*), 'Total-body pet multiparametric imaging of cancer using a voxel-wise strategy of compartmental modeling', *Journal of Nuclear Medicine* .

Wang, G. & Qi, J. (2009), 'Generalized algorithms for direct reconstruction of parametric images from dynamic pet data', *IEEE transactions on medical imaging* **28**(11), 1717–1726.

Wang, G. & Qi, J. (2013), 'Direct estimation of kinetic parametric images for dynamic pet', *Theranostics* **3**(10), 802.

Wang, G., Rahmim, A. & Gunn, R. N. (2020), 'Pet parametric imaging: Past, present, and future', *IEEE Transactions on Radiation and Plasma Medical Sciences* **4**(6), 663–675.

Wang, H., Miao, Y., Yu, W., Zhu, G., Wu, T., Zhao, X., Yuan, G., Li, B. & Xu, H. (2022*b*), 'Improved clinical workflow for whole-body patlak parametric imaging using two short dynamic acquisitions', *Frontiers in Oncology* **12**.

Wang, H., Wu, Y., Huang, Z., Li, Z., Zhang, N., Fu, F., Meng, N., Wang, H., Zhou, Y. & Yang, Y. (2022*c*), 'Deep learning–based dynamic pet parametric ki image generation from lung static pet', *European Radiology* pp. 1–10.

Wang, J., Shao, Y., Liu, B., Wang, X., Geist, B. K., Li, X., Li, F., Zhao, H., Hacker, M. & Ding, H. (2021*b*), 'Dynamic 18f-fdg pet imaging of liver lesions: evaluation of a two-tissue compartment model with dual blood input function', *BMC Medical Imaging* **21**(1), 90.

Wang, T., Li, B., Shi, H., Li, P., Deng, Y., Wang, S., Luo, Q., Xv, D., He, J. & Wang, S. (2023*a*), 'Short-term pet-derived kinetic estimation for the diagnosis of hepatocellular carcinoma: a combination of the maximum-slope method and dual-input three-compartment model', *Insights into Imaging* **14**(1).

Wang, W. & Gindi, G. (1997), 'Noise analysis of map-em algorithms for emission tomography', *Physics in Medicine and Biology* **42**(11), 2215–2232.

Wang, Y., Li, E., Cherry, S. R. & Wang, G. (2021*c*), 'Total-body pet kinetic modeling and potential opportunities using deep learning', *PET clinics* **16**(4), 613–625.

Wang, Y., Nardo, L., Spencer, B., Abdelhafez, Y., Chaudhari, A., Badawi, R., Cherry, S. & Wang, G. (2022*d*), 'Multi-organ metabolic changes in covid-19 recovery measured with total-body dynamic 18f-fdg pet', *Journal of Nuclear Medicine* **63**(supplement 2), 2329–2329.

Wang, Y., Spencer, B. A., Schmall, J., Li, E., Badawi, R. D., Jones, T., Cherry, S. R. & Wang, G. (2023*b*), 'High-temporal-resolution lung kinetic modeling using total-body dynamic pet with time-delay and dispersion corrections', *Journal of Nuclear Medicine* .

Wang, Z., Wu, Y., Li, X., Bai, Y., Chen, H., Ding, J., Shen, C., Hu, Z., Liang, D., Liu, X., Zheng, H., Yang, Y., Zhou, Y., Wang, M. & Sun, T. (2022*e*), 'Comparison between a dual-time-window protocol and other simplified protocols for dynamic total-body 18f-FDG PET imaging', *EJNMMI Physics* **9**(1).

Watabe, H., Channing, M. A., Der, M. G., Adams, H. R., Jagoda, E., Herscovitch, P., Eckelman, W. C. & Carson, R. E. (2000), 'Kinetic analysis of the 5-ht2a ligand [11c] mdl 100,907', *Journal of Cerebral Blood Flow & Metabolism* **20**(6), 899–909.

Weber, M., Jentzen, W., Hofferber, R., Herrmann, K., Fendler, W. P., Rischpler, C., Umutlu, L., Conti, M., Costa, P. F., Sraieb, M. & Kersting, D. (2021), 'Evaluation of 18f-fdg pet/ct images acquired with a reduced scan time duration in lymphoma patients using the digital biograph vision', *BMC Cancer* **21**(1).

Weber, W. A., Schwaiger, M. & Avril, N. (2000), 'Quantitative assessment of tumor metabolism using fdg-pet imaging', *Nuclear medicine and biology* **27**(7), 683–687.

Wijngaarden, J. E., Huisman, M. C., Jauw, Y. W., van Dongen, G. A., Greuter, H. N., Schuit, R. C., Cleveland, M., Gootjes, E. C., Vugts, D. J. & Menke-van der Houven van Oordt, C. W. (2023), 'Validation of simplified uptake measures against dynamic patlak ki for quantification of lesional 89zr-immuno-pet antibody uptake', *European Journal of Nuclear Medicine and Molecular Imaging* pp. 1–9.

Wong, K.-P., Feng, D., Meikle, S. R. & Fulham, M. J. (2001), 'Simultaneous estimation of physiological parameters and the input function-in vivo pet data', *Ieee transactions on information technology in biomedicine* **5**(1), 67–76.

Wong, K.-P., Feng, D., Meikle, S. R. & Fulham, M. J. (2002*a*), 'Segmentation

of dynamic pet images using cluster analysis', *IEEE Transactions on nuclear science* **49**(1), 200–207.

Wong, K.-P., Meikle, S. R., Feng, D. & Fulham, M. J. (2002*b*), 'Estimation of input function and kinetic parameters using simulated annealing: application in a flow model', *IEEE Transactions on Nuclear Science* **49**(3), 707–713.

Wu, C., Honarmand, A., Schnell, S., Kuhn, R., Schoeneman, S. E., Ansari, S. A., Carr, J., Markl, M. & Shaibani, A. (2016), 'Age-related changes of normal cerebral and cardiac blood flow in children and adults aged 7 months to 61 years', *J Am Heart Assoc* **5**(1).

Wu, J., Liu, H., Ye, Q., Gallezot, J.-D., Naganawa, M., Miao, T., Lu, Y., Chen, M.-K., Esserman, D. A., Kyriakides, T. C., Carson, R. E. & Liu, C. (2021), 'Generation of parametric ki images for fdg pet using two 5min scans', *Medical Physics* **48**(9), 5219–5231.

Wu, Q., Gu, F., Gu, Y., Xu, T., Zhou, Y. & Shi, H. (2022*a*), 'Impact of equilibration time (t*) on patlak quantitation in dynamic total-body imaging using the uexplorer pet scanner', **63**(Supplement 2), 3184–3184.

Wu, Q., Gu, F., O'Suilleabhain, L. D., Sari, H., Xue, S., Shi, K., Rominger, A. & O'Sullivan, F. (2024*a*), 'Mapping 18f-fdg kinetics together with patient-specific bootstrap assessment of uncertainties: An illustration with data from a pet/ct scanner with a long axial field of view', *Journal of Nuclear Medicine* **65**(6), 971–979.

Wu, Q., Gu, F., Wu, Y., Zhou, Y. & Wang, M. (2022*b*), 'Assessment of compartmental models and delay estimation schemes for dynamic total-body pet imaging using uexplorer', *Journal of Nuclear Medicine* **63**(Supplement 2), 3186–3186.

Wu, Q., O'Sullivan, F., Muzi, M. & Mankoff, D. A. (2019), An exploration of the prognostic utility of shortened dynamic imaging protocols for pet-fdg scans, *in* '2019 IEEE Nuclear Science Symposium and Medical Imaging Conference (NSS/MIC)', IEEE, pp. 1–3.

Wu, Y., Feng, T., Shen, Y., Fu, F., Meng, N., Li, X., Xu, T., Sun, T., Gu, F. & Wu, Q. (2022*c*), 'Total-body parametric imaging using the patlak model: Feasibility of reduced scan time', *Medical Physics* .

Wu, Y., Feng, T., Zhao, Y., Xu, T., Fu, F., Huang, Z., Meng, N., Li, H., Shao, F. & Wang, M. (2022*d*), 'Whole-body parametric imaging of 18f-fdg pet using uexplorer with reduced scanning time', *Journal of Nuclear Medicine* **63**(4), 622–628.

Wu, Y., Fu, F., Meng, N., Wang, Z., Li, X., Bai, Y., Zhou, Y., Liang, D., Zheng, H., Yang, Y. et al. (2024*b*), 'The role of dynamic, static, and delayed total-body pet imaging in the detection and differential diagnosis of oncological lesions', *Cancer Imaging* **24**(1), 2.

Xiu, Z., Muzi, M., Huang, J. & Wolsztynski, E. (2022), 'Patient-adaptive population-based modeling of arterial input functions', *IEEE Transactions on Medical Imaging* .

Yao, S., Feng, T., Zhao, Y., Wu, R., Wang, R., Wu, S., Li, C. & Xu, B. (2021), 'Simplified protocol for whole-body patlak parametric imaging with 18f-fdg pet/ct: Feasibility and error analysis', *Medical physics* **48**(5), 2160–2169.

Yin, H., Liu, G., Hu, Y., Xiao, J., Mao, W., Lv, J., Yu, H., Lin, Q., Cheng, D. & Shi, H. (2023), 'Dynamic total-body pet/ct imaging reveals kinetic distribution of 68 ga-dotatate in normal organs', *Contrast Media & Molecular Imaging* **2023**.

Yu, H., Gu, Y., Fan, W., Gao, Y., Wang, M., Zhu, X., Wu, Z., Liu, J., Li, B. & Wu, H. (2023), 'Expert consensus on oncological [18f] fdg total-body pet/ct imaging (version 1)', *European Radiology* **33**(1), 615–626.

Zaidi, H. & Alavi, A. (2007), 'Current trends in pet and combined (pet/ct and pet/mr) systems design', *PET clinics* **2**(2), 109–123.

Zaidi, H. & El Naqa, I. (2021), 'Quantitative molecular positron emission tomography imaging using advanced deep learning techniques', *Annual Review of Biomedical Engineering* **23**, 249–276.

Zaidi, H. & Karakatsanis, N. (2017), 'Towards enhanced pet quantification in clinical oncology', *The British Journal of Radiology* **91**(1081), 20170508.

Zaker, N., Haddad, K., Faghihi, R., Arabi, H. & Zaidi, H. (2022), 'Direct inference of patlak parametric images in whole-body pet/ct imaging using

convolutional neural networks', *European journal of nuclear medicine and molecular imaging* **49**(12), 4048–4063.

Zanderigo, F., Parsey, R. V. & Ogden, R. T. (2015), 'Model-free quantification of dynamic pet data using nonparametric deconvolution', *Journal of Cerebral Blood Flow & Metabolism* **35**(8), 1368–1379.

Zhang, Q., Hu, Y., Zhou, C., Zhao, Y., Zhang, N., Zhou, Y., Yang, Y., Zheng, H., Fan, W., Liang, D. & Hu, Z. (2024), 'Reducing pediatric total-body pet/ct imaging scan time with multimodal artificial intelligence technology', *EJNMMI Physics* **11**(1).

Zhang, X., Cherry, S. R., Xie, Z., Shi, H., Badawi, R. D. & Qi, J. (2020*a*), 'Subsecond total-body imaging using ultrasensitive positron emission tomography', *Proceedings of the National Academy of Sciences* **117**(5), 2265–2267.

Zhang, X., Xie, Z., Berg, E., Judenhofer, M. S., Liu, W., Xu, T., Ding, Y., Lv, Y., Dong, Y. & Deng, Z. (2020*b*), 'Total-body dynamic reconstruction and parametric imaging on the uexplorer', *Journal of Nuclear Medicine* **61**(2), 285–291.

Zhang, Y., Dong, Y., Yu, W., Chen, S., Yu, H., Li, B. & Shi, H. (2023), 'Combined early dynamic 18f-fdg pet/ct and conventional whole-body 18f-fdg pet/ct in hepatocellular carcinoma', *Abdominal Radiology* **48**(10), 3127–3134.

Zhao, Y.-M., Li, Y.-H., Chen, T., Zhang, W.-G., Wang, L.-H., Feng, J., Li, C., Zhang, X., Fan, W. & Hu, Y.-Y. (2021), 'Image quality and lesion detectability in low-dose pediatric 18f-fdg scans using total-body pet/ct', *European journal of nuclear medicine and molecular imaging* **48**(11), 3378–3385.

Zhou, Y., Ye, W., Brašić, J. R. & Wong, D. F. (2010), 'Multi-graphical analysis of dynamic pet', *Neuroimage* **49**(4), 2947–2957.

Nomenclature

Δ	Delay
^{15}O	Oxygen-15
^{18}F	Fluorine-18
C_p	Arterial Input Function
C_T	Tissue Activity
iid	Independent Identically Distributed
K_1	Overall Flow
K_b	Blood Flow
K_d	In-Distribution Flow
K_i	Flux
K_{trans}	Transfer Constant
R	Residue Function
V_b	Blood Volume
V_d	In-Distribution Volume
1C	One Compartmental Model/Modeling
1D	One Dimension/Dimensional
2C	Two Compartmental Model/Modeling
2Ci	Two Irreversible Compartmental Model/Modeling
2Cr	Two Reversible Compartmental Model/Modeling

2D Two Dimension/Dimensional

3D Three Dimension/Dimensional

4D Four Dimension/Dimensional

ACF Auto-correlation Function

AIF Arterial Input Function

BBB Blood Brain Barrier

BGO Bismuth Germanium Oxide

CI Confidence Interval

COV or CV Coefficient of Variation

CT Computed Tomography

DCE Dynamic Contrast Enhanced

DGP Data Generation Process

DSC Dynamic Susceptibility Contrast

EM Expectation Maximization

FA Factor Analysis

FBP Filtered Backprojection

FDG Fluorodeoxyglucose

FFT Fast Fourier Transform

FLT Fluorothymidine

FOV Field of View

FWHM Full Width at Half Maximum

GAM Generalized Additive Model

GE General Electric

GLM Generalized Linear Model

IDIF Image-Derived Input Function

LABC Locally Advanced Breast Cancer

LAFOV Long Axial Field of View

LSO Lutetium Oxyorthosilicate

LYSO Lutetium-Yttrium Oxyorthosilicate

MBIF Model-Based Input Function

ML Maximum Likelihood

MR Magnetic Resonance

MRI Magnetic Resonance Imaging

MSE Mean Square Error

MTT Mean Transit Time

NPRM Non-Parametric Residue Mapping

OLS Ordinary Least Square

OSEM Ordered Subset Expectation Maximization

PBIF Population-Based Input Function

PBPM Population-Based Projection Model

PCA Principal Component Analysis

PET Positron Emission Tomography

QP Quadratic Programming

RMSE Root Mean Square Error

ROI Region of Interest

RSS Residual Sum of Squares

SA Spectral Analysis

SAFOV Short Axial Field of View

SAR Spatial Autoregressive

SD Standard Deviation

SE Standard Error

SNMMI Society of Nuclear Medicine and Molecular Imaging

SNR Signal-to-noise Ratio

SUV Standardized Uptake Value

SVD Singular Value Decomposition

TAC Time Activity Curve

TB Total-body

TOF Time of Flight

UCC University College Cork

UIH United Imaging Healthcare

VOI Volume of Interest

WLS Weighted Least Square

WRSS Weighted Residual Sum of Squares